Hybrid Photonic–Plasmonic Modes in Coated Whispering-Gallery Resonators

Carolin Klusmann

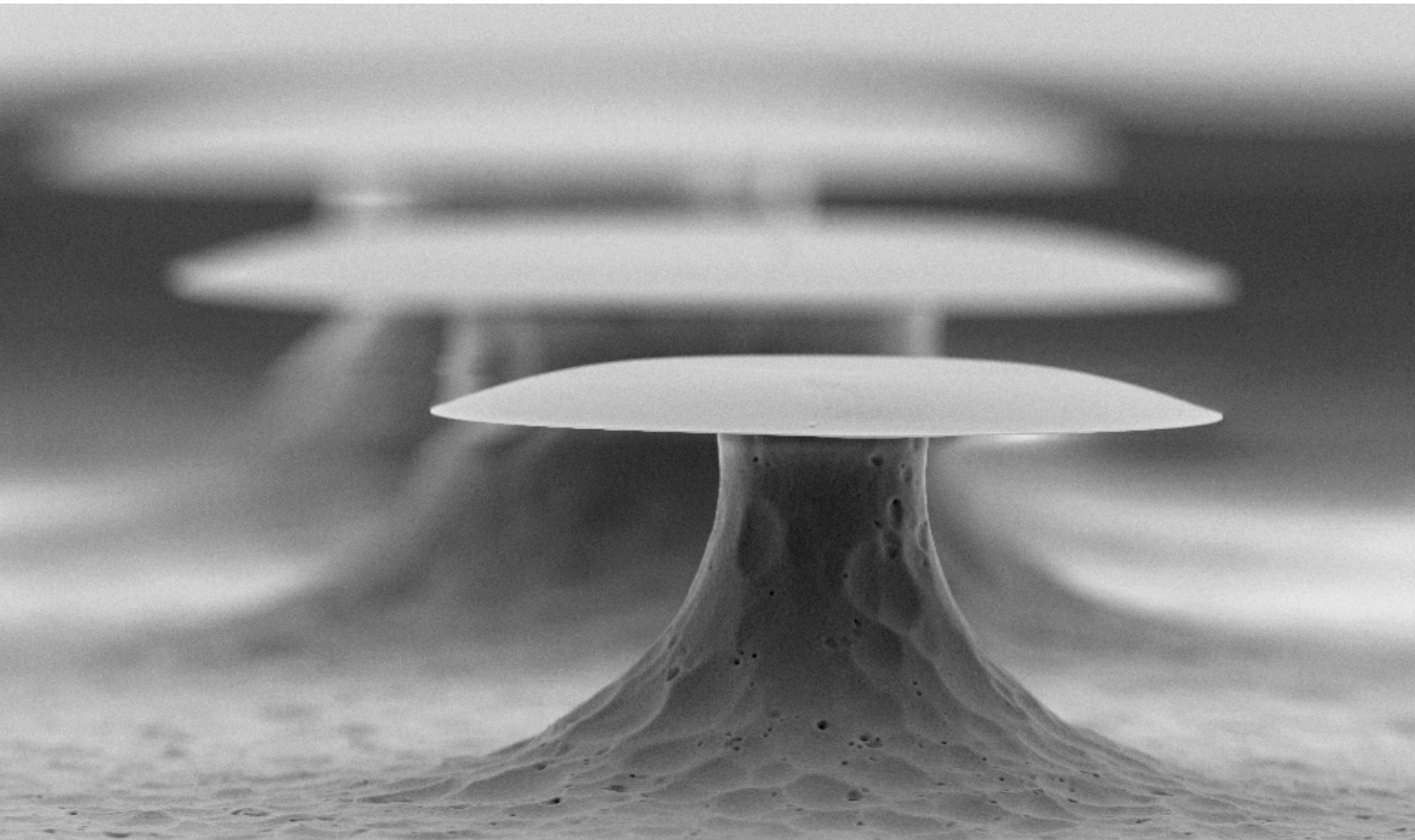

Hybrid Photonic–Plasmonic Modes in Coated Whispering-Gallery Resonators

Zur Erlangung des akademischen Grades eines
DOKTORS DER NATURWISSENSCHAFTEN
von der KIT-Fakultät für Physik
des Karlsruher Instituts für Technologie (KIT)

genehmigte

DISSERTATION

von

M.Sc. Carolin Klusmann
aus Karlsruhe

Tag der mündlichen Prüfung : 17.05.2019
Referent : Prof. Dr. Heinz Kalt
Korreferent : Prof. Dr. Carsten Rockstuhl

Prüfungskomission:

Prof. Dr. H. Kalt
Prof. Dr. C. Rockstuhl
Prof. Dr. D. Hunger
Prof. Dr. A. Mirlin
Prof. Dr. F. Bernlochner

Karlsruhe Institute of Technology (KIT)
Institute of Applied Physics
Wolfgang-Gaede-Straße 1
76131 Karlsruhe
Germany
AG Kalt: http://www.aph.kit.edu/kalt

Carolin Klusmann
carolin.klusmann@kit.edu carolin.klusmann@gmail.com

This work has been supported financially by the Karlsruhe School of Optics and Photonics.

http://www.ksop.de

Contents

1 Introduction **1**

2 Fundamentals of whispering-gallery-mode (WGM) resonators **5**
2.1 WGMs in optical microresonators 5
2.1.1 Optical modes in dielectric microspheres 6
2.1.2 Optical modes in dielectric microdisks 9
2.2 Figures-of-merit of WGM resonators 11
2.2.1 Free spectral range 11
2.2.2 Cavity mode volume 11
2.2.3 Quality factor (Q-factor) 12

3 Hybrid photonic–plasmonic WGM resonators: from the fabrication to the experimental extraction of their modal structure **15**
3.1 Fabrication of dielectric WGM resonator templates of various geometries . . 16
3.1.1 Ultra-high-Q silica microspheres 16
3.1.2 High-Q polymeric microdisks, -goblets, and -wedges 16
3.2 Integration of plasmonic nanostructures into polymeric WGM resonators . . 20
3.2.1 Fabrication of gold-nanoparticle-coated microdisks 21
3.2.2 Fabrication of silver-coated microwedges 22
3.3 Optical setups to extract the mode spectra of WGM resonators 22
3.3.1 Micro-photoluminescence spectroscopy setup 23
3.3.2 Fiber–coupling setup 24
3.4 Summary and conclusions 26

4 Sensitivity enhancement of WGM resonators via coupling to plasmonic nanoparticles (NPs) **29**
4.1 Sensing with hybrid WGM resonators 30
4.1.1 Sensing with WGMs 30
4.1.2 Sensing with plasmonic resonances 32
4.1.3 Hybrid WGM resonators for improved sensing performance 33
4.2 Coupled harmonic oscillator model for NP–WGM interaction 34
4.2.1 Theory of coupled harmonic oscillators 35
4.2.2 Properties of hybrid resonances 36

4.2.3 Sensitivity enhancement in the coupled system 39
4.2.4 Summary and conclusions 42
4.3 Multi-Mie simulations of a WGM microsphere coupled to an idealized plasmonic NP 42
4.3.1 Multi-Mie scattering theory of hybrid sensors 43
4.3.2 Drude-metal NPs with freely tunable optical parameters 45
4.3.3 Optical properties of the idealized hybrid system 47
4.3.4 Sensitivity enhancement in the idealized hybrid system 50
4.3.5 Summary and conclusions 51
4.4 Finite-element method simulations of polymeric microdisks coupled to densely packed gold NPs 52
4.4.1 Effective medium approach to simulate gold-NP-coated microdisks . 53
4.4.2 Optical properties of gold-NP-coated microdisks 60
4.4.3 Sensitivity enhancement in gold-NP-coated microdisks 63
4.4.4 Mimicking ultra-thin gold coatings in photonic devices by gold-NP composites 69
4.4.5 Summary and conclusions 70
4.5 Experiments on sensing performance of polymeric microdisk lasers coated with densely packed gold NPs 71
4.5.1 Lasing properties of gold-NP-coated microdisks 72
4.5.2 Bulk refractive index sensing with gold-NP-coated microdisks 75
4.5.3 Summary and conclusions 77
4.6 Summary and critical remark on hybrid NP–WGM resonators for bulk refractive index sensing 78

5 Plasmonic, dielectric, and hybrid modes in silver-coated polymeric microwedges 81
5.1 Benefits of metal-coated WGM resonators 82
5.2 Deducing general design guidelines for metal-coated resonators from fundamental properties of surface plasmon polaritons (SPPs) 83
5.2.1 Dispersion relation of SPPs at a plane metal–dielectric interface . . 83
5.2.2 Characteristic length scales of SPPs 84
5.2.3 Excitation of SPPs 87
5.2.4 Q-factors of SPPs 90
5.2.5 Conclusions 90
5.3 Simulation-based optimization of silver-coated polymeric WGM resonators . 91
5.3.1 Bent-waveguide approach for efficient mode modeling 91
5.3.2 Optimization of hybrid resonator design for efficient and selective mode excitation 93
5.4 Simulation of the modal characteristics of a fabricated silver-coated polymeric microwedge 99
5.4.1 Modal properties of plasmonic (SPP), dielectric (DE), and hybrid (HY) modes 99
5.4.2 Uncertainties in simulated spectral features 101

5.4.3 Mode filtering technique for unambiguous mode classification 102
5.5 Identification of SPP, DE, and HY modes in a silver-coated polymeric microwedge in fiber–coupling experiments 105
5.5.1 Polarization-dependent excitation scheme for preliminary mode classification 105
5.5.2 Selective excitation and classification of cavity eigenmodes using mode filtering 108
5.6 Summary and conclusions 111

6 Summary and perspective **113**

A Immobilization of gold nanoparticles on polymeric WGM resonators **119**

B Numerical modeling of fiber–resonator coupling **121**
B.1 Bent-waveguide approach to simulate fiber–resonator system 121
B.2 Calculation of fiber-position-dependent coupling efficiencies 123

List of Publications **127**

References **131**

Closing words **149**

Chapter 1

Introduction

With their pioneering work on the interaction of light and matter, James Clerk Maxwell and Albert Einstein set the foundation for the development of photonic concepts and devices with a huge impact on modern life. In this context, the invention of the laser in the 1960s [1] and the development of laser-based devices and applications played a vital role in improving our standard of living. Thanks to advances in semiconductor chip-technology, lasers became an integral part of everyday life with a wide field of applications ranging from Blu-ray players and computer printers over telecommunications [2] up to medical applications [3].

As in many other optical devices, light in a laser is confined via an optical resonator to enhance the intrinsically weak interaction of light and matter. Whereas the temporal confinement of light is characterized by the quality factor (Q-factor) of the cavity, the spatial confinement is quantified by its mode volume V. Therefore, the ratio Q/V is a key figure-of-merit of an optical resonator describing its capability to enhance light–matter interactions. Triggered by the growing demand to control light–matter interactions on the micro- and nanometer scale, sophisticated miniaturized resonators with ultra-high Q-factors in combination with small mode volumes have been developed [4–17]. Their fabrication was possible due to advances in micro- and nano-fabrication techniques enabling the down-scaling of photonic devices.
Among the proposed optical microresonators, whispering-gallery-mode (WGM) resonators emerged as promising platforms to boost and study light–matter interactions due to exceptionally high Q-factors up to 10^{10} in combination with small mode volumes of a few hundreds of cubic micrometers [8–12, 18, 19]. WGM resonators are curved dielectrics that confine light by means of repeated total internal reflection at the cavity boundary to form resonances, so-called WGMs. As they exhibit the highest Q/V-ratio measured to date [19], WGM resonators are employed in a broad field of photonic applications and fundamental research, such as cavity quantum electrodynamics (cQED) [10,20], non-linear optics [21–23], or the label-free and ultra-sensitive detection of biomolecules [24–27].

However, as the light confinement in WGM resonators relies on total internal reflection,

mode volumes are limited by diffraction, which ultimately restricts their performance.
Contrary to dielectric WGM resonators, plasmonic nanostructures have been shown to be capable of squeezing light into subwavelength dimensions, thus, breaking the diffraction barrier [28–31]. These cavities rely on the collective excitation of a metal's free electron gas which coherently interacts with a stimulating optical field to form resonances, so-called plasmon polaritons [32]. However, as metals are inherently lossy, the Q-factors of these cavities are typically far less than a hundred at optical frequencies and, hence, orders of magnitude smaller than those of WGM resonators.

Inspired by the complementary characteristics of WGM resonators and plasmonic cavities, optoplasmonic microcavities combining the high Q-factors of WGMs with the ultra-small mode volumes associated with plasmonic elements have been proposed to further enhance light–matter interactions [33, 34, 34–39]. They promise unprecedented performance, e.g., in sensing and cQED experiments [40]. However, to maintain the strong mode localization connected with plasmonic nanostructures while keeping plasmonic losses to a minimum, a careful design of the hybrid structures was shown to be critical [36, 37, 41].
Recently, ultra-high-Q silica microspheres coupled to single plasmonic nanoparticles (NPs) have brought single-molecule [33, 34, 34–37] and single-ion detection [38] into reach. These hybrid resonators exploit greatly enhanced optical near fields at the NP surface amplifying the inherently weak WGM signals induced by single adsorption events.
Other promising hybrid systems consist of WGM resonators coated with thin homogeneous metal films, allowing for the formation of surface plasmon polaritons (SPPs) at the metal–dielectric interface. Min *et al.*, e.g., demonstrated that SPP modes in a silver-coated silica microdisk possess significantly reduced mode volumes compared to purely dielectric WGMs while still exhibiting comparatively high Q-factors slightly above a thousand [39].
To further improve Q-factors while maintaining the small mode volumes associated with SPPs, metal-coated WGM resonators supporting hybrid photonic–plasmonic modes have been proposed. These modes emerge from the hybridization of purely dielectric modes with SPP modes and unite the low-loss characteristic of WGMs with the light-focusing characteristic of SPPs. Silica microtoroids coated with a silver nanoring [42], metal-coated microspheres [43], and metal-nanocapped microtubular cavities [44] are among the most promising cavity designs supporting hybrid modes with Q-factors exceeding a thousand and mode volumes as small as one cubic wavelength.

In this thesis, plasmonic elements are integrated into polymeric WGM resonators aiming to enhance light–matter interactions and increase their spectrum of application.
Compared to commonly exploited hybrid resonators made from silica, the usage of polymers as resonator material offers several advantages. High-Q polymeric WGM resonators can be fabricated at low cost and on a large scale on compact microchips using conventional lithographic techniques. Therefore, they are, e.g., highly attractive for biosensing applications where disposable lab-on-a-chip devices are of great interest [45]. On top of that, polymeric resonators can be easily doped with gain media to build low-threshold microlasers. Due to the presence of gain, the linewidth of WGMs in microresonators with integrated gain medium, so-called active resonators, is reduced compared to their

passive counterparts [46–49]. Thus, linewidth broadening of WGMs induced by the coupling to lossy plasmonic nanostructures can be partly compensated in active WGM resonators. Polymeric WGM resonators, hence, are promising templates to build hybrid photonic–plasmonic systems.
One goal of this thesis is to examine both theoretically and experimentally whether the coupling of plasmonic NPs to polymeric WGM resonators enhances their sensitivity toward minute changes in the refractive index of the surrounding medium. Special emphasize is put on providing a fundamental understanding of the interplay between plasmonic resonances and dielectric WGMs to derive general sensor design guidelines. The theoretical and experimental findings shall help to assess the potential of plasmonic-NP-coated WGM sensors as lab-on-a-chip devices for point-of-care diagnostics.
The other goal of this work is to design, fabricate, and optically characterize a metal-coated polymeric WGM resonator that supports purely dielectric, purely plasmonic, and hybrid photonic–plasmonic modes. It is shown that a high-Q polymeric WGM resonator with wedge-like geometry is an ideal template supporting the desired modes when coated with a thin silver layer from the top. Developing a strategy on how to efficiently and selectively excite the distinct cavity eigenmodes is at the heart of the investigation, as this is the key challenge in many applications.

Roadmap to the thesis

This thesis is structured as follows: **Chapter 2** serves as an introduction to dielectric whispering-gallery-mode (WGM) resonators. It addresses basic properties of WGMs and explains the working principle of WGM resonators. The modal properties of spherical and disk-like WGM microresonators are discussed and important figures-of-merit of WGM resonators are introduced.

Chapter 3 focuses on the fabrication of hybrid photonic–plasmonic WGM resonators and introduces the experimental setups and methods used to characterize their modal structure.

In **chapter 4**, a strategy is developed to improve the sensitivity of WGM resonators toward bulk refractive index changes by hybridizing WGMs and plasmonic resonances sustained by small metallic nanoparticles (NPs) coupled to the resonator surface. A coupled harmonic oscillator model is introduced and discussed to provide an intuitive picture for the interplay between plasmonic resonances and WGMs and the sensitivity enhancement in hybrid NP–WGM sensors. The results from the oscillator model are verified using exact analytical calculations of the optical and sensing properties of an idealized hybrid system comprised of a small WGM microsphere coupled to a single artificial plasmonic NP made from a Drude-metal. To examine the impact of the number density of plasmonic NPs on the sensitivity enhancement, finite-element method (FEM) simulations of a model hybrid system comprised of a polymeric microdisk covered by a huge number of randomly distributed spherical gold NPs are performed. Furthermore, the lasing and sensing properties of gold-NP-coated microdisks with integrated gain medium are charac-

terized experimentally on a micro-photoluminescence spectroscopy setup and sensitivity enhancement effects are discussed. The chapter is concluded with a critical remark on hybrid NP–WGM sensors for bulk refractive index sensing.

Chapter 5 is dedicated to the design and optical characterization of a metal-coated polymeric WGM resonator that supports plasmonic, dielectric and hybrid modes with high Q-factors and ultra-small mode volumes. Based on an analysis of basic properties of SPPs, general design guidelines for metal-coated resonators are derived. FEM simulations based on a numerically efficient bent-waveguide approach are introduced for cavity optimization. A silver-coated polymeric microwedge is shown to support all three distinct mode types which can be efficiently excited with the evanescent field of a tapered optical fiber. A mode classification scheme to selectively excite and unambiguously classify the distinct modes is developed and verified experimentally.

The main results of this thesis are summarized in **chapter 6** and a brief outlook on promising future research activities is given.

Chapter 2

Fundamentals of whispering-gallery-mode (WGM) resonators

In this chapter, the fundamentals of optical whispering-gallery-mode (WGM) resonators are addressed. After discussing the formation of optical resonance in rotationally symmetric dielectrics using a simple wave-optics approach, a rigorous description of optical modes sustained by spherical and disk-like WGM resonators, as investigated in this work, is provided using electromagnetic theory. In this context, similarities and differences in the modal properties of microspheres and -disks are worked out and important figures-of-merit (FOMs) of WGM resonators are introduced.

2.1 WGMs in optical microresonators

WGM resonators are optical microcavities with great potential in plenty of photonic applications ranging from ultra-sensitive label-free biosensing [50], through non-linear optics [21], to low-threshold lasing [51]. Their name can be dated back to Lord Rayleigh, who studied the characteristics of the acoustic whispering gallery in the dome of the St. Paul's Cathedral in London in the early 20th century [52]. He observed that a soft whisper spoken against the curved wall at one side of the dome could be clearly heard on the opposite side. Lord Rayleigh attributed this phenomenon to the repeated lossless reflection of sound waves at the wall of the dome.
The optical analogue to these acoustic waves was first proposed by Richtmyer in the 1930s [53], soon after Gustav Mie published his pioneering work on light scattering by dielectric spherical particles [54], known as Mie theory, which set the theoretical basis for the resonant characteristics within these particles. Following the same principle as their acoustic counterparts, Richtmyer demonstrated that electromagnetic waves can be guided

along the perimeter of curved dielectrics by means of repeated (total) internal reflection provided that the refractive index of the supporting dielectric structure exceeds that of the surrounding medium. Resonances, so-called whispering-gallery-modes, form inside these optical resonators if light interferes constructively with itself after one round-trip, leading to the build-up of a high circulating optical power within the cavity. For rotationally symmetric dielectrics the condition for constructive interference is fulfilled if the optical path of the light traveling along the resonator circumference equals a multiple integer m of the free-space wavelength λ. Denoting the cavity radius by R and the effective index of the resonant mode by n_{eff}, the resonance condition reads:

$$2\pi R n_{\text{eff}} = m\lambda, \quad \text{with } m \in \mathbb{Z}. \tag{2.1}$$

The so-called azimuthal mode number m in Eq. 2.1 quantifies the effective number of wavelengths along the resonator circumference. The effective mode index n_{eff} accounts for the fact that the (total) internal reflection at the curved cavity boundary is incomplete causing tunneling losses [55, 56] and the formation of an evanescent wave, which decays exponentially away from the interface into the surrounding medium. Therefore, the effective mode index n_{eff} of a WGM is always slightly smaller than the refractive index n_{R} of the resonator material.
Although Eq. 2.1 yields a first descriptive insight into the modal propagation of WGMs, it cannot describe the mode spectrum of a WGM resonator in a comprehensive manner. For instance, it does neither provide information about the spatial distribution of the electromagnetic fields of WGMs and their dependency on the refractive index of the surrounding medium, nor does it account for different polarization states of light. To rigorously describe optical modes in dielectric WGM resonators, Maxwell's equations have to be solved [57]. An analytic solution to Maxwell's equations exists, however, only for highly symmetric structures, such as microspheres or infinitely extended cylinders [58]. For more complex resonator geometries numerical simulations, such as finite-element method (FEM) simulations, must be performed to compute the electromagnetic field distributions of WGMs and their modal properties.

To provide a fundamental understanding of WGMs and analyze their functional dependency on relevant system parameters, we focus in the next section on the simplest WGM resonator geometry, a dielectric microsphere, and outline how to solve Maxwell's equations analytically.

2.1.1 Optical modes in dielectric microspheres

The electromagnetic problem of scattering by a single dielectric sphere embedded in a homogeneous background medium was first solved by Gustav Mie in 1908 [54]. Since then, several works on the electrodynamics of spherical dielectric particles have been published. In the following, we outline the basic steps in the computation of optical modes sustained by dielectric microspheres. For details, the reader is referred to [58, 59].

Exploiting the symmetry of the underlying problem and assuming piecewise homogeneous

and isotropic media, the optical modes of a dielectric sphere with radius R and permittivity $\epsilon_\mathrm{r}(\omega)=\epsilon_\mathrm{r}$ can be computed by solving the vector wave equation for the electric and the magnetic fields $\mathbf{E}(\mathbf{r},\omega)$ and $\mathbf{H}(\mathbf{r},\omega)$ in spherical coordinates (r,Θ,φ):

$$\nabla^2\mathbf{F}(\mathbf{r},\omega)+k_0^2\epsilon(\mathbf{r},\omega)\mathbf{F}(\mathbf{r},\omega)=0, \quad \text{with } \epsilon(\mathbf{r},\omega)=\begin{cases}\epsilon_\mathrm{r}, & r\leq R\\ \epsilon_\mathrm{m}, & r>R\end{cases}, \tag{2.2}$$

where $\mathbf{F}\in\{\mathbf{E},\mathbf{H}\}$. k_0 denotes the vacuum wave number, ϵ_m the background permittivity, and ∇^2 the Laplace operator in spherical coordinates. Analytic solutions to this vector differential equation can be found by defining a time-harmonic scalar function $\Psi=\Psi(r,\Theta,\varphi)e^{-i\omega t}$ that satisfies the scalar wave equation:

$$\nabla^2\Psi+k_0^2\epsilon(\mathbf{r},\omega)\Psi=0. \tag{2.3}$$

Using the separation of variables approach $\Psi(r,\Theta,\varphi)=\Psi_\mathrm{r}(r)\Psi_\Theta(\Theta)\Psi_\varphi(\varphi)$ and introducing the azimuthal and polar mode numbers m and l, respectively, yields the solution of the scalar wave equation (Eq. 2.3):

$$\Psi\sim e^{-i\omega t}\begin{pmatrix} j_l(k_0 n_\mathrm{R} r)\\ h_l^{(1)}(k_0 n_\mathrm{m} r)\end{pmatrix} P_l^m(\cos\Theta)e^{\pm im\varphi}, \tag{2.4}$$

where the upper line in Eq. 2.4 describes a wave inside the sphere ($|r|\leq R$) and the lower line an outgoing spherical wave outside the sphere ($|r|>R$). n_m denotes the background refractive index. The radial field Ψ_r is described by the spherical Bessel function $j_l(k_0 n_\mathrm{R} r)$ of first kind inside the sphere and the spherical Hankel function $h_l^{(1)}(k_0 n_\mathrm{m} r)$ outside the sphere. The latter can be approximated by a decaying exponential function, describing the evanescent tail of a WGM. The polar component Ψ_Θ is given by the associated Legendre polynomial $P_l^m(\cos\Theta)$ of first kind, the azimuthal eigenfunction Ψ_φ describing the equatorial behavior of the optical mode is sinusoidal. Allowed azimuthal mode numbers m for a given polar mode number l are in the range of $-l<m<l$, which leads to a $(2l+1)$-fold degeneracy of the azimuthal modes.

The solution Ψ of the scalar wave equation (Eq. 2.4) is used in a next step to generate two partial fields, the so-called vector spherical harmonics (VSHs) $\mathbf{M}(r,\Theta,\varphi)$ and $\mathbf{N}(r,\Theta,\varphi)$ [58, 59], which satisfy the vector wave equation and form an orthogonal base. The VSHs express fields with either the electric or the magnetic field being parallel to the sphere surface, i.e. TE- and TM-modes [57]. With the VSHs at hand, the solutions for the TE- and TM-modes in dielectric microspheres can be directly computed.

The electromagnetic field distributions and resonance wavelengths of the optical modes are determined by matching the tangential components of the electric and magnetic fields at the sphere boundary [59, 60], which leads to the following characteristic equation:

$$x\cdot\frac{[j_l(k_0 n_\mathrm{R} R)]'}{j_l(k_0 n_\mathrm{R} R)}=\frac{[h_l^{(1)}(k_0 n_\mathrm{m} R)]'}{h_l^{(1)}(k_0 n_\mathrm{m} R)}, \quad \text{with } \begin{cases} x=\frac{n_\mathrm{R}}{n_\mathrm{m}} & \text{for TE-modes}\\ x=\frac{n_\mathrm{m}}{n_\mathrm{R}} & \text{for TM-modes}\end{cases}, \tag{2.5}$$

where the prime denotes differentiation with respect to the argument inside the spherical Bessel and Hankel functions. Solving the transcendental equation (Eq. 2.5) leads to a

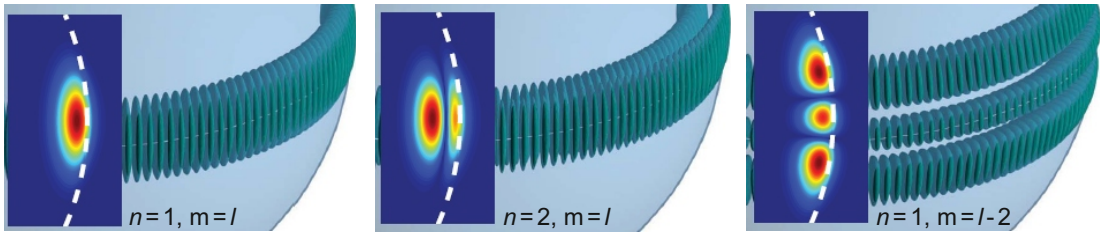

Figure 2.1: Visualization of WGMs in dielectric microspheres. Iso-intensity surfaces and simulated cross-sectional electric field intensity distributions (insets) of a fundamental WGM $m{=}l$ (left), a second-order radial mode $n{=}2$ (middle), and a WGM with azimuthal mode number $m{=}l{-}2$ (right) in a dielectric microsphere. Considered are modes with TE-polarization. Both the fundamental WGM and the higher-order modes are strongly localized at the equator of the sphere. A small part of the mode's field, the evanescent field, decays exponentially away from the sphere surface into the surrounding medium. Images taken from [50] and adapted.

family of modes, which can be classified using the polarization (TE or TM) and three mode numbers: the radial, the polar, and the azimuthal mode number n, l, and m, respectively. The radial mode number n specifies the number of intensity maxima in radial direction, the polar mode number l the $l{-}m{+}1$ maxima in polar direction, and the azimuthal mode number m counts the number of wavelengths along the perimeter of the sphere. Please note that owing to the spherical symmetry, many properties of WGMs in microspheres, such as the resonance frequency, are independent of the azimuthal mode number m. In a perfect sphere, modes differing only in the azimuthal mode numbers are, thus, energetically degenerate.
Among the multitude of modes supported by dielectric microspheres, WGMs correspond to modes with low radial mode number $n{=}1, 2, ...$ and large polar and azimuthal mode numbers. WGMs with one mode maximum in radial direction ($n{=}1$) and one maximum in the polar field distribution ($m{=}l$) are called fundamental modes. They possess the largest resonance wavelengths and the highest Q-factors in the system and are, thus, of particular relevance in most applications. Deriving a closed-form expression for the solution of Eq. 2.5 using analytical approximations shows that the resonance frequencies of WGMs sensitively depend on the size and the refractive index of the dielectric sphere, as well as on the refractive index of the surrounding medium [50, 61].

To illustrate the field distribution of WGMs and clarify the mode nomenclature, we show in Fig. 2.1 the cross-sectional electric field intensity distributions of a fundamental WGM $n{=}1$, $m{=}l$ (left), a second-order radial mode $n{=}2$, $m{=}l$ (middle), and a WGM with $n{=}1$ and azimuthal mode number $m{=}l{-}2$ supported by a dielectric microsphere. Both the fundamental WGM and the higher-order WGMs are strongly localized at the equator of the sphere, as expected for rays being totally reflected at the sphere boundary. Only a small part of the mode's electric field, the so-called evanescent field, penetrates into the surrounding medium. The evanescent field mediates the interaction of WGMs with their environment and is exploited in sensing applications to detect changes in the dielectric

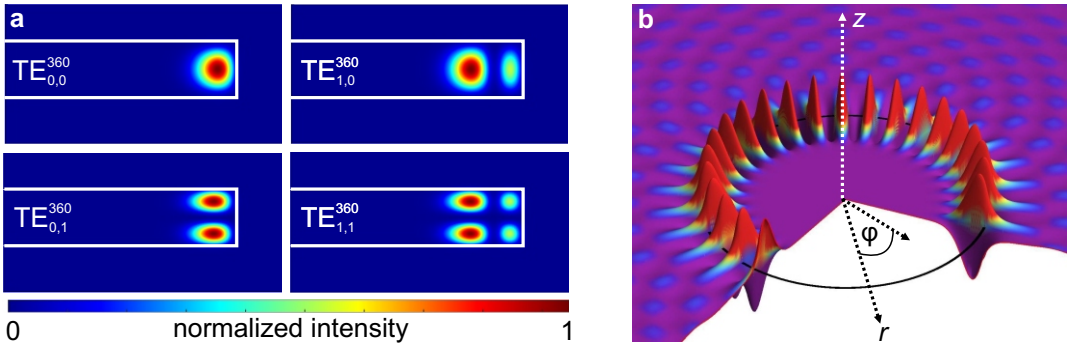

Figure 2.2: Visualization of WGMs in microdisks. (a) Simulated cross-sectional electric field intensity distributions of different TE-polarized WGMs and (b) the electric field distribution of a fundamental WGM with m=30 supported by a dielectric microdisk with 25 µm radius. WGMs supported by the microdisk show similar mode localization characteristics as corresponding WGMs in microspheres. Owing to the reduced symmetry of microdisks, the $2l$+1-fold degeneracy in the azimuthal mode number m, as encountered in perfect spheres, is lifted. Adapted from [64].

environment or to excite WGMs evanescently via tapered optical fibers or prisms.

2.1.2 Optical modes in dielectric microdisks

Having provided basic insight into the character of WGMs using an analytic theory for spherical microresonators, we proceed to look into the properties of WGMs in disk-like resonators.

As a consequence of the reduced symmetry of disks compared to spheres, the corresponding vector wave equation is not separable anymore and can, hence, not be solved analytically. Therefore, approximate expressions for the eigenfrequencies of WGMs in microdisks and their field distributions must be found. In the following, we outline an approach proposed by Borselli *et. al* which is based on an analytic, effective index approximation and allows to compute the mode spectra of microdisks with sufficient accuracy [62].
The key to find approximate analytic solutions lies in considering microdisks with thicknesses d much smaller than the resonator radius R ($d \ll R$), such that the actual three-dimensional problem can be reduced to two dimensions. As the vertical confinement of WGMs in these structures is similar to that in a slab waveguide of same thickness, the refractive index of the microdisk in the (r, φ)-plane can be approximated by that of the corresponding slab waveguide mode (n_{eff}). As a consequence, solutions to the wave vector equation fall into two classes: modes with electric field in the plane of the disk (TE-modes) and modes with electric field perpendicular to the plane of the disk (TM-modes) [63].[1]
The electromagnetic field distribution of thin microdisks can be approximated by solving

[1] Please note that the labelling of TE- and TM-modes in microdisks is inversed compared to that in microspheres [50].

the vector wave equation in cylindrical coordinates (r, φ, z) using the method of separation of variables. The solution for the z-component of the electromagnetic field in a disk-like resonator corresponds to that of a slab waveguide and can be found in many textbooks, e.g. in [65]. The corresponding field profile exhibits a harmonic dependency inside the microdisk and decays exponential away from the top and the bottom surface of the microdisk into the surrounding medium. Solutions for the azimuthal part of the field are proportional to $e^{\pm im\varphi}$ with the azimuthal mode number m already introduced above. The '$-$' and the '$+$' signs account for the energetically degenerate modes traveling clockwise (CW) and counterclockwise (CCW) along the perimeter of the microdisk, respectively. Please note that the azimuthal degeneracy of WGMs, as encountered in perfect spheres, is lifted due to the reduced symmetry of microdisks compared to microspheres. As a consequence, WGMs in microdisks are only twofold-degenerate (CW and CCW) in the azimuthal direction. As in the case of microspheres, the radial solutions inside the cavity are given by Bessel functions, those in the surrounding medium are given by Hankel functions of first kind. The latter can be approximated by a decaying exponential function with decay constant $\chi{=}k_0\sqrt{n_{\mathrm{eff}}^2{-}n_{\mathrm{m}}^2}$. The approximate resonance frequencies of the WGMs can be found by matching the tangential components of the fields inside and outside the disk at the microdisk surface [62].
In full analogy to their spherical counterparts, WGMs in microdisks can be classified by their polarization state (TE or TM) and three mode numbers: the azimuthal mode number m and the radial mode number n already introduced above, and the mode number n_{z}, which describes the number of intensity maxima in z-direction. Throughout the rest of this thesis, the following notation is used to label modes in disk-like resonators: $\mathrm{TE}_{n,n_{\mathrm{z}}}^{m}$, $\mathrm{TM}_{n,n_{\mathrm{z}}}^{m}$.

To assist the reader in visualizing WGMs in disk-like resonators, we show in Fig. 2.2 the simulated cross-sectional intensity distributions of different WGMs supported by a 1.2 µm thick PMMA microdisk with 25 µm radius (a) together with the electric field intensity distribution of a fundamental TE-mode with mode number $m{=}30$ supported by the same structure (b). The resonator rim is marked by a black line. As in the case of spherical WGM resonators, the WGMs sustained by the microdisk are strongly localized at the rim with an exponential tail penetrating into the surrounding medium.
The similarity in the modal structure of microspheres and -disks (see Fig. 2.1 and Fig. 2.2) is not surprising when considering the disk as a spherical segment obtained by cutting the sphere with a pair of parallel planes located around the equatorial plane of the sphere. However, a striking difference between both resonator geometries stems from the reduced symmetry of disks compared to spheres. Owing to the finite extension of microdisks in z-direction, resonance frequencies of WGMs become dependent on the thickness of the microdisk. In contrast, WGMs in perfect microspheres with same radial quantum number are energetically degenerate. Furthermore, for microdisks with thicknesses on the order of the wavelength of light, a significant part of the mode field penetrates through the top and the bottom surface of the disk into the surrounding medium. Compared to microspheres of same radius, the spatial overlap of WGMs with the surrounding is, thus, increased in microdisks. This property is, e.g., beneficial for sensing applications, but at the expense

of reduced quality factors (Q-factors).

2.2 Figures-of-merit of WGM resonators

In this section, we provide a brief overview of important FOMs of WGM resonators characterizing the optical density of states, as well as the spatial and temporal confinement of electromagnetic energy inside these structures. Among the introduced FOMs, the Q-factor and the mode volume V are of particular interest, as the ratio Q/V determines the strength of light–matter interactions encountered in WGM resonators.

2.2.1 Free spectral range

The free spectral range (FSR) of an optical microresonator is an important FOM describing the spectral distance between two consecutive longitudinal modes of same polarization with azimuthal mode numbers m and m+1. It can be directly inferred from the simple resonance condition of WGMs (Eq. 2.1) and can be expressed in terms of the resonator radius R, the effective mode index n_{eff} and the free-space wavelength λ as follows [62]:

$$FSR = \frac{\lambda^2}{2\pi R n_{\text{eff}} + \lambda} \approx \frac{\lambda^2}{2\pi R n_{\text{eff}}}, \tag{2.6}$$

where the approximation in Eq. 2.6 is valid for $R \gg \lambda$.

2.2.2 Cavity mode volume

The cavity mode volume V quantifies the spatial confinement of WGMs and is commonly defined as the ratio of the total energy of an optical mode to its maximum energy density [66, 67]:

$$V = \frac{\int u(\mathbf{r}) d^3\mathbf{r}}{\max\{u(\mathbf{r})\}}, \quad \text{with } u(\mathbf{r}) = \frac{\mathrm{d}}{\mathrm{d}\omega}\{\omega\epsilon_0\epsilon(\mathbf{r},\omega)\}\,|\mathbf{E}(\mathbf{r})|^2 + \mu_0\,|\mathbf{H}(\mathbf{r})|^2\,, \tag{2.7}$$

where $u(\mathbf{r})$ is the electromagnetic energy density for dispersive media [68].
Typically, the mode volume of WGM resonators is given in units of µm^3 or cubic wavelengths $(\lambda/n_{\text{R}})^3$. As mode volumes of WGMs in purely dielectric WGM resonators are limited by diffraction, they are notably larger than one cubic wavelength [69]. A promising approach to circumvent the diffraction barrier and squeeze WGMs into subwavelength volumes exploits the light-focusing characteristic of plasmonic nanostructures coupled to WGM resonators (see chapter 5).

2.2.3 Quality factor (Q-factor)

As WGM resonators are open systems with electromagnetic fields leaking into the surrounding medium, light will inherently decay – even in ideal resonators with vanishing absorption losses and smooth boundaries. One of the most important FOMs quantifying the temporal confinement of WGMs inside the cavity and characterizing the extent of dissipation in resonant systems is the Q-factor.
The Q-factor of an optical mode with eigenfrequency ω_0 is defined as the ratio of energy E_{st} stored in the cavity to the energy E_{diss} dissipated per electric field oscillation period [57]:

$$Q = 2\pi \frac{E_{\mathrm{st}}}{E_{\mathrm{diss}}} = \omega_0 \tau, \tag{2.8}$$

where the decay constant τ corresponds to the lifetime of the photons in the cavity. Experimentally, the Q-factor of a WGM can be determined in two different ways. As the energy stored in the cavity decays exponentially with time, one method for Q-factor determination relies on measuring the temporal decay of the energy using cavity-ring down spectroscopy [62]. An alternative, experimentally less challenging method to determine the Q-factor of a WGM relies on measuring its spectral linewidth. As WGMs exhibit a Lorentzian-shaped intensity distribution in frequency domain with full width at half maximum (FWHM) $\delta\omega_0{=}\omega_0/Q$ [57], the Q-factor

$$Q = \frac{\omega_0}{\delta\omega_0} \approx \frac{\lambda_0}{\delta\lambda_0}, \tag{2.9}$$

of a WGM can be easily determined from transmission measurements by scanning the wavelength of a tunable pump laser across the resonance (see section 3.3.2).

In WGM resonators, the total Q-factor is limited by multiple intrinsic loss mechanisms Q_{int}^{-1}, such as radiation losses Q_{rad}^{-1}, scattering losses Q_{scat}^{-1}, and absorption losses Q_{abs}^{-1}, and external losses Q_{ext}^{-1} arising from the coupling to an input waveguide or a prism. The total Q-factor is determined by the individual loss contributions according to [62, 70]:

$$\frac{1}{Q} = \frac{1}{Q_{\mathrm{int}}} + \frac{1}{Q_{\mathrm{ext}}} = \frac{1}{Q_{\mathrm{rad}}} + \frac{1}{Q_{\mathrm{scat}}} + \frac{1}{Q_{\mathrm{abs}}} + \frac{1}{Q_{\mathrm{ext}}}. \tag{2.10}$$

In the following, we briefly analyze the origin of the individual intrinsic loss contributions in Eq. 2.10 and discuss the limits they impose on the intrinsic Q-factors of the WGM resonators fabricated in this work.

Radiation losses

Radiation losses in WGM resonators originate from the fact that (total) internal reflection of light at the cavity boundary is incomplete and inevitably results in the loss of optical energy by radiation. In the particle picture of light, these radiation losses can be explained by the tunneling of photons through an effective potential barrier whose height

is determined by the curvature of the resonator and the refractive index contrast between cavity and surrounding medium [55, 56]. Increasing the cavity radius or the refractive index contrast leads to reduced tunneling rates of photons through the potential barrier and, thus, higher radiation-limited Q-factors Q_{rad}. For resonators made from poly(methyl methacrylate) (PMMA) with cavity radii R>15 µm, radiation-limited Q-factors in air are as high as 10^{16} at wavelengths in the visible spectral range [71]. In water, Q_{rad} is strongly reduced due to the lower refractive index contrast, but still on the order of 10^8. For the resonators fabricated in this work with radii R>15 µm, radiation losses play a negligible role compared to the other intrinsic loss mechanisms.

Scattering losses

Scattering losses due to residual surface inhomogeneities are usually the major contribution to the total loss in dielectric WGM resonators [72]. As the evanescent field of a WGM decays exponentially away from the cavity surface, it is extremely sensitive to surface imperfections, such as surface roughness or defects caused during the fabrication process, or dust particles deposited within the sensing volume of a WGM. These surface inhomogeneities act as scattering centers for light causing the decay of optical energy. For PMMA microdisks structured lithographically using electron-beam lithography, the limited precision of the manufacturing process restricts their Q-factors typically to values of $\sim 10^4 - 10^5$ [73]. The associated scattering losses from defects can be reduced by applying a post-lithographic thermal reflow process, which smoothens the cavity surface and increases the cavity Q-factors by up to two orders of magnitude (see section 3.1.2). An alternative strategy to increase the scattering-loss-limited Q-factors Q_{scat} relies on effectively pushing the modal profile away from the lithographically-induced imperfections at the cavity surface by either increasing the cavity radius [62] or by using sophisticated resonator designs [39, 74], such as microwedges with shallow wedge angles (see section 3.1.2).

Absorption losses

Absorption losses in WGM resonators are determined by the optical properties of the materials from which the cavity is made. The respective absorption-limited Q-factor Q_{abs} at the operation wavelength λ can be approximated as:

$$Q_{\mathrm{abs}} \approx \frac{2\pi n'_{\mathrm{R}}}{\alpha\lambda}, \tag{2.11}$$

where n'_{R} denotes the real part of the refractive index of the resonator material and α the corresponding absorption coefficient.
Due to low absorption losses of PMMA at optical frequencies [75], absorption-limited Q-factors of purely PMMA resonators reach values as high as 10^8 in the visible and 10^6 in the near-IR [73, 76]. The contribution of absorption losses to the total intrinsic Q-factor of purely polymeric WGM resonators is, hence, comparatively small. The situation is,

however, different when incorporating plasmonic nanostructures into the polymeric WGM resonators. Due to the high absorption of metals, absorption-limited Q-factors of hybrid photonic–plasmonic resonators are reduced by several orders of magnitude compared to their purely polymeric counterparts. The intrinsic Q-factors of hybrid resonators, thus, become metal-loss limited (see chapters 4 and 5 for details).

Chapter 3

Hybrid photonic–plasmonic WGM resonators: from the fabrication to the experimental extraction of their modal structure

This chapter focuses on the fabrication of hybrid photonic–plasmonic WGM resonators, as investigated in this work, and introduces the methods to experimentally characterize their modal properties.

At the beginning of the chapter, we briefly discuss the fabrication of WGM microspheres made from silica, which are a prominent template for the implementation of hybrid resonators – owing to ultra-high Q-factors. Inspired by their limited integrability into photonic circuits, we motivate using polymers as resonator material. We present the well-established lithographic fabrication process of high-Q polymeric microdisks and microgoblets on a silicon pedestal and introduce a novel type of polymeric WGM resonator with wedge-like geometry. Its sophisticated resonator design enables the formation of purely photonic, plasmonic, and hybrid photonic–plasmonic modes with high Q-factors and small mode volumes when coated with a thin silver layer from the top.
We then present two distinct approaches to integrate plasmonic nanostructures into polymeric template resonators. In this context, we discuss the fabrication of polymeric microdisks coated by randomly distributed and densely packed spherical gold nanoparticles (NPs) and silver-coated polymeric microwedges. The sensing capabilities of gold-NP-coated microdisks are studied in chapter 4. The modal characteristics of silver-coated polymeric microwedges are investigated in chapter 5.
Afterwards, the micro-photoluminescence spectroscopy (µ-PL) setup and the fiber–coupling setup to extract the mode spectra of WGM resonators with and without integrated gain medium, respectively, are introduced. A short summary and concluding remarks are provided at the end of the chapter.

3.1 Fabrication of dielectric WGM resonator templates of various geometries

Dielectric WGM resonators can be fabricated from a wide range of materials, such as silica [24, 33], silicon nitride [77], diverse semiconductors (GaAs [78], InP [79]), crystalline materials [80], or polymers [51, 73] and can be implemented in a variety of geometries. Spheres [25], disks [51], toroids [9], goblets [73], or rings [81] are under the most prominent WGM geometries. Depending on the material choice and resonator geometry, the complexity of the fabrication process, the integrability, as well as the achievable Q-factors can differ significantly. In general, the exact resonator choice depends on the field of application.
To build high-performance hybrid photonic–plasmonic resonators, a high-Q template resonator is indispensable. Both commonly used silica WGM microspheres, which exhibit the highest Q-factors measured to date, and lithographically structured polymeric WGM resonators of various geometries, as fabricated in this work, meet this requirement. In the following, we detail the fabrication of these high-Q dielectric WGM resonators with focus on polymeric WGM resonators.

3.1.1 Ultra-high-Q silica microspheres

The fabrication of silica microspheres is illustrated in Fig. 3.1. Microspheres made from silica can be easily fabricated by melting the tip of a conventional single-mode optical fiber with the aid of a high-power carbon dioxide (CO_2) heating laser, which is precisely focused onto the cleaned and cleaved fiber end [82]. Depending on the diameter of the optical fiber and the laser intensity, microspheres with diameters ranging from ten to hundred micrometers and ultra-smooth surfaces can be fabricated. Owing to extremely low optical losses of silica in the visible and near-infrared together with an extraordinary smooth cavity surface, Q-factors of silica microspheres reach values up to 10^{10} [18].
As silica microspheres are inherently biocompatible, possess the simplest possible three-dimensional geometry together with ultra-high Q-factors, they are an ideal template for hybrid photonic–plasmonic resonators. In combination with individual plasmonic NPs attached to their surface, they have, e.g., proven their potential in single-molecule [24] and even single-ion [38] sensing, as detailed in chapter 4. Despite their outstanding optical properties, the major drawback of silica microspheres is their limited integrability into photonic circuits.

3.1.2 High-Q polymeric microdisks, -goblets, and -wedges

Contrary to silica microspheres, WGM resonators made from polymers offer high integrability into photonic circuits at low cost. High-Q polymeric WGM resonators can be fabricated on planar chips using electron beam (e-beam) lithography or UV-lithography

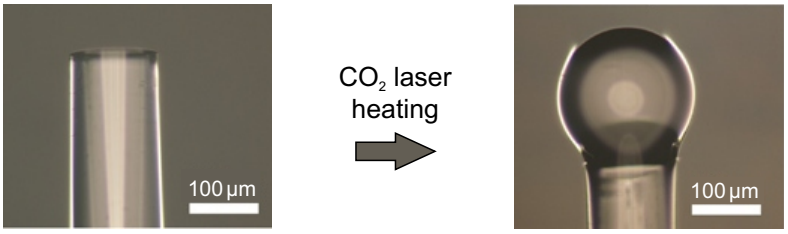

Figure 3.1: Fabrication of ultra-high-Q silica microspheres. Focusing a high-power carbon dioxide (CO_2) laser onto a cleaned and cleaved end of a conventional single-mode optical fiber produces a silica microsphere resonator with ultra-high Q-factor up to 10^{10} [18]. Although silica microspheres exhibit outstanding optical properties, their major drawback is the limited integrability into photonic circuits. Images taken from [82] and adapted.

together with conventional etching techniques. In contrast to silica microspheres, whose fabrication relies on a serial reflow process with a CO_2 heating laser, polymeric WGM resonators can be fabricated in parallel, which is a prerequisite for a large-scale production. Furthermore, and contrary to silica resonators, gain media can be easily integrated into polymeric matrices, which is the foundation to implement WGM microlasers. In this work, poly(methyl methacrylate) (PMMA) is used as resonator material owing to low absorption losses in the visible and near-IR [83].

In the following, the lithographic fabrication of PMMA resonators with disk-, goblet-, and wedge-like geometry on a silicon substrate is discussed. Special emphasize is put on the fabrication of polymeric microwedges, which were developed in close cooperation with Patrick Forster during his master's thesis [84]. Detailed fabrication parameters of polymeric microwedges can be found in [84,85], the fabrication of microdisks and microgoblets is detailed in [73].

Fabrication of PMMA microdisks and -goblets

Polymeric WGM microdisks and -goblets with and without integrated gain medium are fabricated using a well-established fabrication process developed at the Institute of Applied Physics (APH, KIT), which is schematically depicted in Fig. 3.2.

For the fabrication of passive polymeric microdisks and -goblets without integrated gain medium, the thermoplastic positive photoresist PMMA (*PMMA 950k, MicroChem Corp.*) is spin-coated in a first step on top of a silicon substrate and baked on a hotplate to remove residual solvents. For the fabrication of active WGM resonators, the laser dye pyrromethene 597 (PM597) is added at a concentration of 25 µmol/g PMMA to the photoresist prior to spin-coating. Spin-coating parameters are chosen in both cases such that the resulting PMMA layer has a thickness of 1.2 µm. E-beam lithography is then used to structure microdisks into the photoresist [Fig. 3.2(a)]. The exposed parts of the resist are removed in a subsequent chemical developing process, which yields microdisks lying on

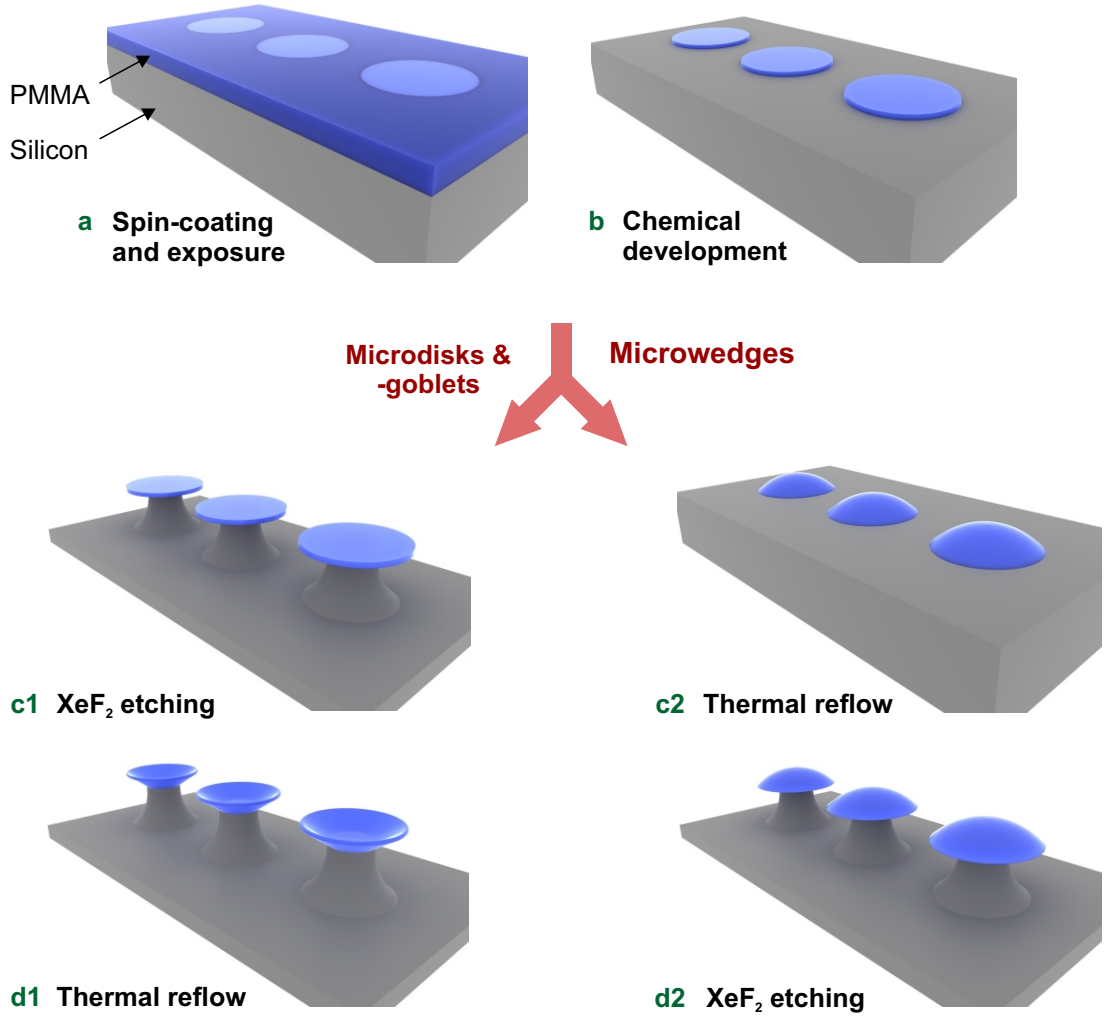

Figure 3.2: Fabrication of high-Q polymeric WGM resonators with disk-, goblet-, and wedge-like geometry. (a) PMMA is spin-coated on top of a silicon substrate and structured using e-beam lithography. (b) Subsequent chemical development of the exposed resist results in PMMA microdisks lying on the silicon substrate. (c1) To obtain free-standing microdisks, the silicon underneath the resonator rims is isotropically etched with XeF_2. (d1) An optional thermal reflow process after etching smoothens the cavity surface and transforms the microdisks into microgoblets. (c2) To obtain resonators with wedge-like geometry, the thermal reflow process is applied to the microdisks lying on the silicon substrate prior to etching with XeF_2 (d2). The thermal reflow process is pivotal for the fabrication of microwedges as it transforms the cylindrical geometry of microdisks into the desired wedge-like geometry while simultaneously smoothening the cavity surface. Both aspects are critical to build template resonators enabling the formation of high-Q plasmonic, photonic, and hybrid photonic–plasmonic modes when coated with a thin silver layer from the top.

the silicon substrate [Fig. 3.2(b)]. In a next step, the silicon is selectively and isotropically etched with XeF_2 to obtain free-standing microdisks on a silicon pedestal [Fig. 3.2(c1)]. Q-factors of the microdisks are typically around $5{\cdot}10^4$ at a wavelength λ=630 nm [73]. To further increase the cavity Q-factors, a post-lithographic surface-tension-induced reflow process can be applied [Fig. 3.2(d1)]. Heating the microdisks to temperatures above the glass-transition temperature of PMMA (T_g=105 °C) leads to a smoothing of the resonator surface. As a result of notably reduced surface scattering losses, Q-factors typically increase by up to two orders of magnitude [73]. The increase in the cavity's Q-factor during the thermal reflow process is accompanied by a shape change of the WGM resonators from a disk- to a goblet-like geometry. This process is driven by minimizing the system's surface energy [86]. Owing to different thermal expansion coefficients of PMMA and silicon, mechanical stress, induced between the spin-coated PMMA layer and the silicon substrate during the baking process prior to e-beam patterning, is released. This effect results in a tilt-up of the rims of the microdisks, whose central parts remain attached to the silicon pedestal.

Fabrication of PMMA microwedges

In the following, we introduce a novel type of polymeric WGM resonator with wedge-like geometry, which is well-engineered to support high-Q modes of plasmonic nature when coated with a thin silver layer from the top (see chapter 5). Its fabrication is inspired by the fabrication of polymeric microgoblets and graphically illustrated in Fig. 3.2.

The first two steps in the fabrication of polymeric microwedges are the same as for microdisks and -goblets. Spin-coating parameters of PMMA are chosen such that microdisks with a thickness of $\sim$1$-$2 µm lying on top of the silicon substrate result after e-beam exposure and chemical development [Fig. 3.2(b)]. The subsequent thermal reflow process is at the heart of the fabrication process and critical to obtain the desired wedge-like resonator geometry together with a smooth cavity surface [Fig. 3.2(c2)]. When heated to temperatures well above the glass-transition temperature T_g of PMMA, the rims of the cylindrical microdisks start melting and form microlenses with pronounced wedges as a result of minimizing the surface energy [87,88]. The exact shape of the resulting microwedges critically depends on the reflow temperature T_R, but also on the diameter and thickness of the former microdisks, and on process parameters, such as exposure energy.
For given microdisks, the inclination angle can be precisely controlled by adjusting the reflow temperature T_R. The impact of the reflow temperature on the resulting wedge shape is demonstrated in Fig. 3.3, which depicts scanning electron micrographs of two free-standing WGM microwedges, which have been subjected to reflow temperatures T_R=170 °C (left) and T_R=210 °C (middle) prior to etching with XeF_2 [Fig. 3.2(d2)]. As clearly visible from the expanded views of the resonator edges (right), increasing the reflow temperature results in shallower wedge angles. Simultaneously, the thickness of the resonators in their central region increases with increasing reflow temperature as a result of volume conservation. Starting point for both resonators shown in Fig. 3.3 was a 1.3 µm thick microdisk

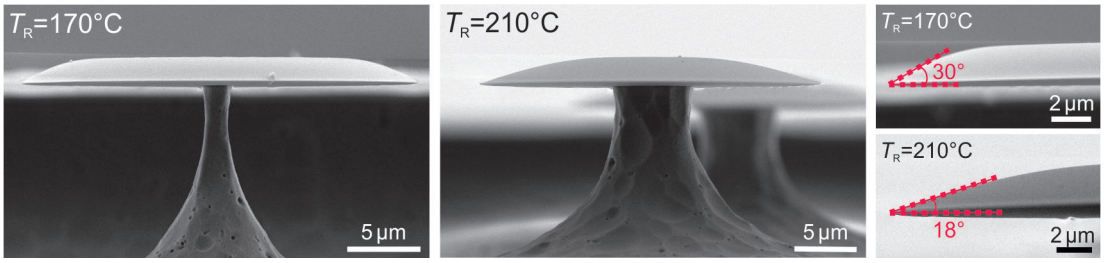

Figure 3.3: Influence of reflow temperature T_R on wedge angle. The inclination angle of microwedges can be precisely controlled by adjusting the temperature during the reflow process. Higher reflow temperatures result in shallower wedge angles. Heating a cylindrical microdisk with 1.3 µm thickness to T_R=170 °C results in a wedge angle of ∼30 ° (left), heating to T_R=210 °C results in a wedge angle of ∼18 ° (middle). Expanded views of the resonator edges are shown on the right.

with a radius of 15 µm.
Q-factors on the order of 10^5 are measured for the polmyeric microwedges at wavelengths around 1500 nm [see Fig. 3.6(b)]. As the Q-factors are close to the absorption-limited Q-factor (Q_{abs}≈$3{\cdot}10^5$) [89], they demonstrate the high quality of the fabricated microwedges and hint to small surface-scattering losses.

As a smooth resonator surface is a prerequisite to obtain high-quality metal coatings and enable a low-loss propagation of surface plasmon polaritons (SPPs) at the metal-dielectric interface, the surface roughness of the top surface of the polymeric wedge-like template resonators was characterized using atomic force microscopy (AFM). The AFM measurements reveal an arithmetic surface roughness of only 400 pm [84], which confirms the high quality of the fabricated samples. The low surface roughness together with the high Q-factors predestine polymeric microwedges for the application as hybrid photonic–plasmonic resonators supporting high-Q modes with SPP character.

3.2 Integration of plasmonic nanostructures into polymeric WGM resonators

In this section, we present means to combine the proposed high-Q polymeric template resonators with plasmonic nanostructures. After addressing how to covalently attach high number densities of spherical gold NPs to the surface of polymeric microdisks, we detail the technical means to coat polymeric microwedges with thin, smooth and homogeneous silver films.

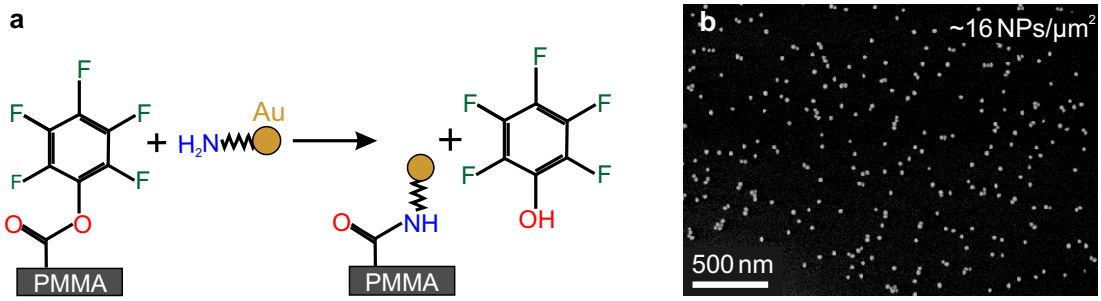

Figure 3.4: Covalent attachment of gold NPs to the surface of PMMA microdisks. (a) The PMMA surface is activated with a reactive pentafluorophenyl ester (PFP-ester) using CVD prior to NP immobilization (left). Immersing the activated PMMA sample into a suspension with amine-terminated colloidal gold NPs (yellow) results in the covalent binding of gold NPs to the CVD-modified PMMA surface (right). The amine groups (blue) in the functionalization layer surrounding the gold NPs react with the PFP-ester to form stable amide bonds. (b) The scanning electron micrograph depicting a small excerpt of the top surface of a hybrid microdisk proves the successful immobilization of gold NPs. The gold NPs distribute randomly on the resonator surface with a resulting surface density of ∼16 NPs/ µm^2 in the present case.

3.2.1 Fabrication of gold-nanoparticle-coated microdisks

To coat PMMA microdisks with a huge number of randomly distributed spherical gold NPs, we rely on self-assembly techniques. As gold-NP-coated microdisks are intended to operate as sensors (see chapter 4), a covalent binding of gold NPs to the resonator surface is indispensable to assure a proper and reliable sensing performance. However, as PMMA is chemically inert, direct coupling of gold NPs to the microdisk surface is not possible due to the lack of suitable functional groups. To covalently attach gold NPs to PMMA microdisks, thus, the cavity surface has to be activated appropriately.

In this work, the PMMA surface is activated by depositing a ∼50 nm thick polymeric layer containing chemically addressable functional groups onto the PMMA microdisk surface using chemical vapor deposition (CVD) polymerization, as graphically illustrated in Fig. 3.4(a). The thin film coatings made from poly[(4-pentafluorophenyl ester-p-xylylene)-co-(p-xylylene)] were fabricated at the Institute of Functional Interfaces (Institut für Funktionelle Grenzflächen, IFG) at KIT by Dr. Meike König. Details regarding CVD polymerization are provided in [90–93]. As the reactive pentafluorophenyl ester (PFP-ester) in the polymeric coating can readily react with primary amines to form stable amide bonds [94], amine-functionalized gold NPs with 25 nm radius (*NanopartzTM Inc., Loveland, CO, USA*) are chosen as the plasmonic component in the hybrid system.
When immersing the CVD-modified polymeric microdisks into the suspension containing the colloidal gold NPs, the amine groups in the ∼2 to 4 nm thick polymeric functionalization layer surrounding the gold NPs covalently bind to the PFP-ester groups in the CVD coating, as schematically illustrated in Fig. 3.4(a). As visible from the scanning electron micrograph in Fig. 3.4(b), which depicts a small excerpt of the top surface of a hybrid microdisk, this reaction results in the desired anchoring of the amine-functionalized gold

NPs on the microdisk surface. The spherical gold NPs are seen to be largely isolated from each other and distributed randomly on the microdisk surface with a surface density of $\sim$16 NPs/ µm^2 in the present case. By controlling the immersion time and the concentration of the gold NPs in the suspension during the self-assembly process, the resulting number density of gold NPs on the resonator surface can be adjusted. A protocol for the gold-NP-immobilization procedure is provided in appendix A.

3.2.2 Fabrication of silver-coated microwedges

For the fabrication of high-performance silver-coated polymeric microwedges, as studied in chapter 5, two main aspects have to be considered.
First, the deposited thin silver films must be as smooth as possible to enable a low-loss propagation of SPP modes at the silver–polymer interface. Second, the utilized deposition method must ensure that only the top surface of the polymeric microwedges is coated with silver. Owing to the small penetration depth of the evanescent field of SPPs into silver at wavelengths in the near-infrared (see section 5.2.2), this requirement is critical to access the distinct cavity eigenmodes of silver-coated microwedges evanescently by means of a tapered optical fiber approached to the cavity from below. E-beam physical vapor deposition (PVD) is chosen as coating method in this work, as it meets these requirements and allows to precisely control the resulting silver-film thickness. For details regarding the deposition method, the reader is referred to [95].

To produce hybrid microwedges, the lithographically structured polymeric microwedges are coated in a final fabrication step with a $\sim$100 nm thick silver film from the top using PVD [96]. The thickness of the deposited silver layer is measured in-situ with a piezoelectric crystal. A chamber pressure of 10^{-6} mbar and a slow silver evaporation rate of 1 Å/s is chosen "to prevent collision-induced deposition of silver atoms at the bottom surface of the resonator" [85]. AFM measurements reveal a low arithmetic surface roughness of $1-2$ nm of the deposited silver layer [84], which indicates the high quality of the produced silver films.

3.3 Optical setups to extract the mode spectra of WGM resonators

In this section, the optical setups used to characterize active and passive WGM resonators are introduced. Active resonators are optically characterized on a micro-photoluminescence spectroscopy (µ-PL) setup, which allows remote excitation and collection of WGM signals using free-space optics. Cavity Q-factors and the mode spectra of passive resonators without gain medium are determined on an optical fiber–coupling setup, which relies on the evanescent coupling between the eigenmode of a tapered optical fiber and the cavity eigenmodes.

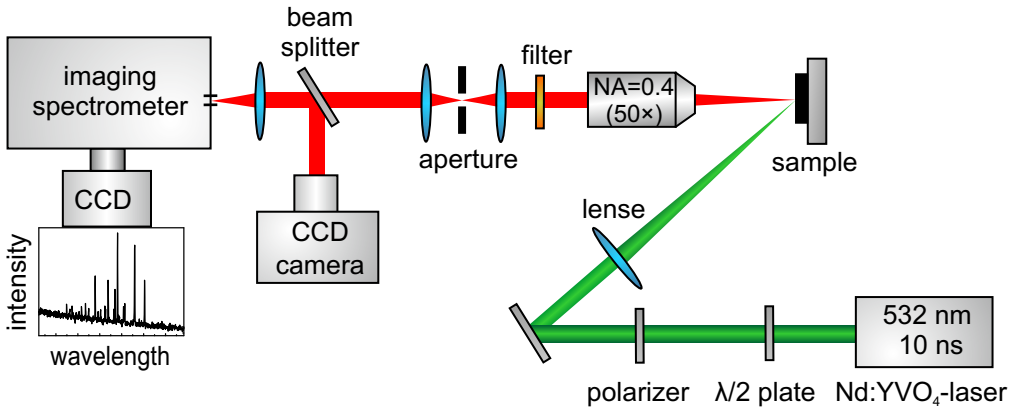

Figure 3.5: Micro-photoluminescence spectroscopy setup for the optical characterization of dye-doped WGM resonators. Light of a 532 nm pump laser is focused onto active resonators to excite the integrated laser dyes. A part of the emitted light is monitored onto a CCD camera to obtain a spatially resolved image of the sample, another part is imaged onto the entrance slit of a spectrometer equipped with a CCD camera for spectral analysis. When optically pumping the resonators above their lasing threshold, sharp lasing modes emerge in the recorded PL-spectra. Based on [71].

3.3.1 Micro-photoluminescence spectroscopy setup

Active resonators with integrated laser dye PM597 are optically characterized on the µ-PL setup depicted in Fig. 3.5.

A frequency-doubled Nd:YVO4 laser (*InnoLas Photonics, nanio*) emitting pulses with 10 ns pulse duration at a wavelength of 532 nm close to the absorption maximum of the laser dye PM597 is used as a pump source. The pulsed laser operation is needed to prevent triplet formation and, hence, quenching of the laser dye PM597 [97–99]. The repetition rate of the pump pulses can be varied using a frequency generator. In this work, a repetition rate of 20 Hz is chosen to excite the resonators. The pump energy is adjusted using a half-wave plate in combination with a variable linear polarizer and measured with a power meter.
To excite the laser dyes inside the cavity, the green laser beam is loosely focused onto the top surface of the resonators under an angle of ∼45 °. The fluorescence of the dye molecules is then collected with a microscope objective with 50-fold magnification and a numerical aperture of 0.42. As the fluorescence light in the µ-PL setup is collected perpendicular to the resonator plane, only scattered light is collected from the sample. Therefore, the detection mechanism relies strongly on surface imperfections or dust deposited on the resonator surface that scatter light toward the detector. A long-pass filter in the detection pass separates the red-shifted fluorescence signal from the exciting laser light. A beam splitter in the detection path is used to monitor 30% of the emitted light onto a charge coupled device (CCD) camera and obtain a spatially resolved image of the sample. 70% of the fluorescence light is imaged onto the entrance split of a grating spectrometer (*Acton*

Research Corporation, Spectra-Pro500, f=50 cm) equipped with a CCD camera (*Andor, iDus420, 256x1024 pixel*) for spectral analysis. For pump powers above the lasing threshold, WGMs manifest themselves as spectrally sharp lasing peaks in the PL-spectrum, which superimpose on the fluorescence background of the laser dye. Three different gratings with 150 lines/mm, 1200 lines/mm or 2400 lines/mm are available to record PL-spectra, which result in a spectral resolution of approximately 700 pm, 70 pm, and 35 pm, respectively, for an entrance-slit width of 30 µm and wavelengths around 600 nm [100].

3.3.2 Fiber–coupling setup

Contrary to active WGM resonators, the direct excitation of WGMs in passive WGM resonators via free-space coupling is in general not feasible. Extremely small radiation losses of WGM resonators with diameters exceeding a few tens of micrometers together with their rotational symmetry prevent an efficient exchange of electromagnetic energy between WGMs and the surrounding [101, 102]. Hence, indirect means have to be identified to efficiently couple light into WGMs and extract light from WGMs experimentally. Commonly used approaches to access WGMs in passive resonators rely on external evanescent field couplers, such as prisms [103, 104] or tapered fibers [105, 106], which mediate the coupling to WGMs via the optical near-field. In this work, tapered optical fibers are used as external couplers, which provide coupling efficiencies up to 99.95% [107].

Tapered optical fibers are manufactured in a home-built setup using the so-called flame brushing technique, which relies on locally heating a conventional single-mode fiber with a flame while pulling the fiber ends apart [108,109]. When tapered down to a waist diameter on the order of the wavelength of light, the fundamental mode of the former single-mode fiber, which is guided by the refractive index difference between fiber core and cladding, is converted into an air-guided taper mode [66]. In the tapered area, the tapered-fiber's eigenmode significantly overlaps with the surrounding, which is a prerequisite for coupling to WGMs. Details regarding the manufacturing process of tapered fibers can be found in [108].

The fiber–coupling setup used to extract the mode spectrum of passive resonators is depicted in Fig. 3.6 (left). Coupling into WGMs is achieved by launching light of a narrow-linewidth (<100 kHz) continuously tunable diode laser (*DLC CTL 1500, Toptica, Germany*) into a tapered optical fiber (*Corning SMF-28*), which is brought into close proximity to the resonator rim where the WGMs are confined. To control the relative alignment between fiber and resonator and, hence, the modal overlap, the fiber is mounted on a five-axis piezoelectric stage with an encoded resolution of 20 nm. The positioning of the fiber with respect to the resonator can be checked with the aid of two CCD cameras, which provide a top and a side view of the fiber–resonator system. The transmission through the fiber is recorded with a photodiode and monitored onto a digital oscilloscope while performing a wavelength scan over the 1460-1570 nm wavelength range. Provided that phase-matching is fulfilled, WGMs manifest themselves as Lorentzian-shaped dips in the transmission spectrum. Their Q-factors can be calculated from the full width at half

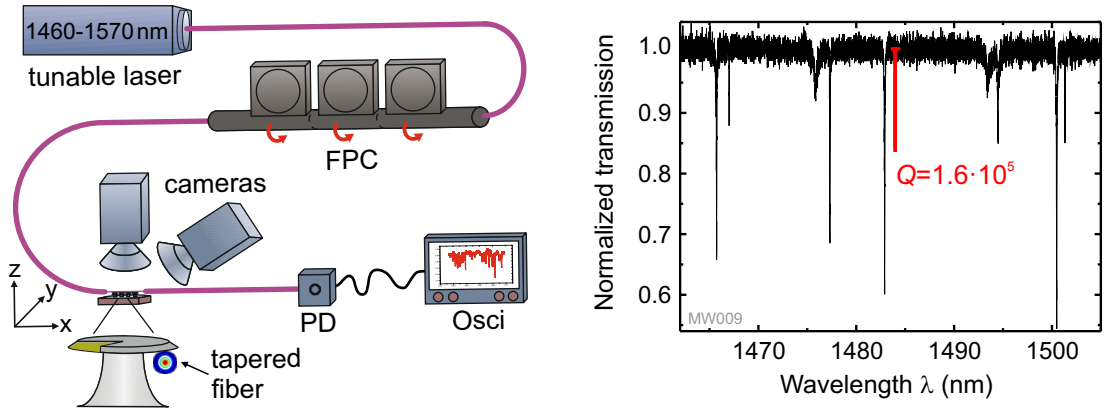

Figure 3.6: Fiber–coupling setup to extract the mode spectra of passive WGM resonators. *Left:* Light of a tunable laser is launched into a tapered single-mode optical fiber, which is brought into close proximity to the resonator rim. The transmission through the fiber is recorded with a photodiode (PD) and monitored onto a digital oscilloscope while performing a wavelength scan. Coupling of the fiber eigenmode to WGMs is manifested in Lorentzian-shaped dips in the transmission spectrum. A manual fiber polarization controller (FPC) allows controlling the polarization of the input laser light. Taken from [85]. *Right:* Typical transmission spectrum of a polymeric WGM microwedge. Q-factors on the order of 10^5 close to the absorption-limited Q-factor at wavelengths around 1500 nm confirm the high quality of the fabricated samples.

maximum (FWHM) of the respective dips in the transmission spectrum using Eq. 2.9. A typical transmission spectrum of a polymeric microwedge with a Q-factor on the order of 10^5 is shown in Fig. 3.6 (right).

To control the input laser polarization, a manual fiber polarization controller (FPC) is integrated into the fiber–coupling setup. Relying on stress-induced birefringence, the FPC allows to continuously transform any arbitrary input polarization into any desired output polarization by rotating its paddles acting as quarter- and half-wave plates. Optimal coupling into a specific eigenmode occurs if the polarization vectors of the exciting fiber field and the cavity mode coincide, leading to a minimal transmission at the resonance wavelength of the mode. Experimentally, the fiber–resonator coupling efficiency can be determined from the absolute depth of the respective Lorentzian-shaped dip in a normalized transmission spectrum, as illustrated in Fig. 3.7 for a cavity eigenmode centered around 1555 nm. Fitting the resonance with a Lorentzian function (blue line) yields the baseline intensity I_0 and the minimal transmitted intensity I_{min} as fit parameters, from which the absolute depth of the Lorentzian and, hence, the fiber–resonator coupling efficiency c can be extracted:

$$c := 1 - \frac{I_{\mathrm{min}}}{I_0}. \tag{3.1}$$

Adjusting the input laser polarization allows to selectively excite orthogonally polarized WGMs and provides additional insight into the complex mode spectra of WGM resonators. In section 5.5.1, we demonstrate that controlling the polarization of the exciting fiber field

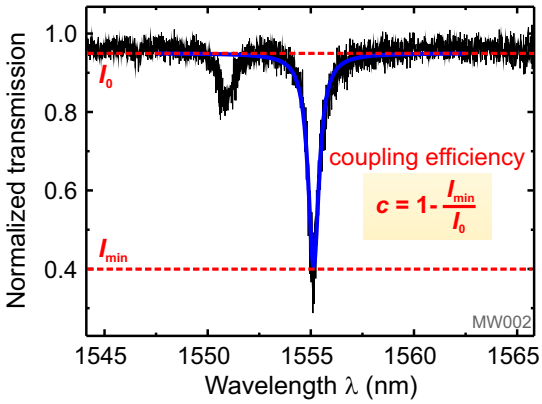

Figure 3.7: Fiber–resonator coupling efficiencies c are determined experimentally from the absolute depth of a Lorentzian-shaped dip in a normalized fiber transmission spectrum. For the cavity eigenmode centered around 1555 nm, the Lorentzian fit (blue solid line) yields a coupling efficiency c=0.57. Taken from [85].

is critical to distinguish between dielectric modes and modes with SPP character in silver-coated wedge-like WGM resonators.

3.4 Summary and conclusions

In this chapter, the fabrication of hybrid photonic-plasmonic WGM resonators, as investigated in this work, was addressed and the optical setups used to extract their modal structure were introduced.

We emphasized that a high-Q WGM resonator template with a smooth cavity surface is needed to implement high-performance hybrid resonators. Frequently studied silica microspheres with ultra-high Q-factors were introduced as a first prominent template resonator. Constrained by their limited integrability into photonic circuits, we highlighted the advantages of polymers as resonator material and introduced lithographically structured polymeric WGM resonators of various geometries. Inspired by the well-established lithographic fabrication process of PMMA microdisks and -goblets on a silicon substrate, we introduced a novel type of polymeric WGM resonator with wedge-like geometry, whose sophisticated resonator design enables the formation of dielectric, plasmonic, and hybrid photonic–plasmonic modes with high Q-factors and small mode volumes when coated with a thin silver layer from the top. As in the case of microgoblets, a post-lithographic thermal reflow process is at the heart of the fabrication of polymeric microwedges. It smoothens the polymer surface and transforms the lithographically structured polymeric microdisks into the desired wedge-like geometry due to surface tension. High Q-factors on the order of 10^5 at wavelengths around 1500 nm close to the absorption-limited Q-factor together with a low arithmetic roughness of the resonator surface of only 400 pm proved the high optical quality of the fabricated microwedges. These properties make the polymeric microwedges

ideal resonator templates for hybrid photonic–plasmonic resonators.

We proceeded to detail the technical means to integrate plasmonic nanostructures into polymeric WGM resonators and discussed the fabrication of two distinct types of hybrid resonators: polymeric microdisks coated with huge numbers of spherical gold nanoparticles (NPs) and silver-coated polymeric microwedges.
As gold-NP-coated microdisks are operated as sensors in section 4.5, we emphasized the need to covalently attach the gold NPs to the resonator surface to ensure a reliable sensing performance. Successful covalent attachment of amine-functionalized gold NPs was achieved by modifying the chemically inert PMMA surface of the microdisks via chemical vapor deposition (CVD) polymerization and relying on self-assembly techniques. The gold NPs were shown to distribute randomly and well isolated from each other on the surface of the CVD-modified PMMA microdisks.
Homogeneous 100 nm thick silver films with the required smoothness needed for a low-loss propagation of SPP modes were deposited onto polymeric microwedges using electron-beam physical vapor deposition. To make the distinct cavity eigenmodes supported by silver-coated microwedges accessible with the evanescent field of a tapered optical fiber, only the top surface of the polymeric microwedges was coated with silver. AFM measurements revealed a low arithmetic surface roughness of the silver coatings of only 1-2 nm. The high quality of the fabricated silver-coated microwedges is confirmed by Q-factor measurements in section 5.5, which yield values for the Q-factors of plasmonic and hybrid photonic–plasmonic modes close to the theoretical predictions.

At the end of the chapter, the micro-photoluminescence spectroscopy (µ-PL) setup and the optical fiber–coupling setup used to extract the modal structure of WGM resonators with and without integrated gain medium, respectively, were introduced.
Despite reduced excitation and collection efficiencies compared to the fiber–coupling setup, the µ-PL setup is appealing due to its simplicity. As WGM signals can be easily excited and collected using free-space optics, this setup is extremely attractive for real-life applications, especially when an operation in aqueous environment is required.
The comparatively complex optical fiber–coupling setup utilizing tapered optical fibers as external evanescent field couplers is used to extract the mode spectra of passive resonators and determine their Q-factors. Emphasize was put on the possibility to control the input laser polarization together with the relative position of the input fiber relative to the resonator, which is, e.g., the foundation to efficiently and selectively excite dielectric, plasmonic, and hybrid modes in silver-coated wedge-like WGM resonators (see section 5.5).

Chapter 4

Sensitivity enhancement of WGM resonators via coupling to plasmonic nanoparticles (NPs)

Optical sensing with WGM resonators gained considerable attention in recent years. Due to high Q-factors in combination with relatively small mode volumes, WGM resonators exhibit unprecedented sensitivity toward micro- and nanoscale objects. Recirculation of light inside the cavity leads to multiple interactions of WGMs with their surrounding resulting in large detection signals. However, since WGMs are strongly confined inside the resonator, only a small part of their evanescent field can probe the surrounding, which inherently limits their sensing performance. To further boost the sensitivity of WGM resonators, hence, means have to be identified to push the mode distribution further outside the resonator.

In this chapter, we present a strategy to increase the spatial overlap of WGMs with the surrounding. Our approach to boost the sensitivity of WGM resonators makes use of strongly enhanced optical near-fields connected with plasmonic nanoparticles (NPs) coupled to the WGM resonator surface.
After motivating the concept of hybrid photonic–plasmonic sensors in section 4.1, a simple model of two coupled harmonic oscillators (HO-model) is introduced in section 4.2 to provide a basic understanding of the interaction between WGMs and plasmonic resonances sustained by metallic NPs. An analytic formula for the bulk refractive index sensitivity, an important figure-of-merit (FOM) of a sensor, is derived and general design guidelines for hybrid sensors are deduced from it. The results of the HO-model are verified in section 4.3 with exact calculations of an idealized hybrid system comprised of a small WGM microsphere coupled to a single artificial plasmonic NP made from a Drude-metal. Modeling the plasmonic NP as an idealized NP with freely tunable optical properties allows to study the optical and sensing properties of hybrid resonators in a fundamental manner. In section 4.4, the impact of the number density of plasmonic NPs on the sensitivity

enhancement in hybrid WGM resonators is studied. To this end, finite-element method (FEM) simulations of a state-of-the-art polymeric microdisk coated with densely packed spherical gold NPs are performed. To efficiently simulate the hybrid system, the layer of gold NPs surrounding the microdisk is treated at the level of an effective medium. The optical and sensing properties of gold-NP-coated microdisks are discussed and related to comparable hybrid systems with ultra-thin homogeneous gold coatings. In section 4.5, results of BRIS measurements on active polymeric microdisks coated with large numbers of spherical gold NPs are presented and discussed. The chapter is concluded with a summary and a critical remark on hybrid NP–WGM sensors for bulk refractive index sensing.

4.1 Sensing with hybrid WGM resonators

In recent years, the development of micro- and nanoscale sensing technologies based on photonic concepts has experienced an enormous progress [24,110–112]. The advances were mainly triggered by the growing demand for highly sensitive and rapid label-free detection schemes that enable an early disease diagnosis or the detection of single biomolecules, such as viruses, DNA, or proteins.
Within the broad field of optical sensors, high-Q dielectric WGM resonators [24, 27, 33] and plasmon resonance sensors [112–114] emerged as promising sensing platforms. The prime sensing strategy of both sensor types relies on monitoring the spectral shift of the system's resonance induced upon minute changes in the dielectric environment [115]. An important FOM characterizing their sensing performance is the ratio of sensitivity to resonance linewidth, where the sensitivity can be quantified via the so-called bulk refractive index sensitivity (BRIS) [116, 117]. The BRIS is a measure for the spatial overlap of a WGM with the surrounding and is defined as the magnitude of the resonance wavelength shift $\Delta\lambda_{\mathrm{res}}$ induced upon small uniform changes Δn_{m} in the refractive index of the surrounding medium [118]:

$$BRIS = \frac{\Delta\lambda_{\mathrm{res}}}{\Delta n_{\mathrm{m}}}. \tag{4.1}$$

In the following, we investigate the sensing performance and the sensing principles of WGM sensors and plasmon resonance sensors and motivate the concept of hybrid photonic–plasmonic sensors.

4.1.1 Sensing with WGMs

Since WGMs exhibit an evanescent tail which decays exponentially away from the cavity surface into the surrounding, they are sensitive to chemical–physical changes in the resonator environment. Adsorption of biomolecules or minute changes in the refractive index of the surrounding medium disturb the optical mode profile and alter the effective refractive index n_{eff} of the WGM. According to the resonance condition (Eq. 2.1), the

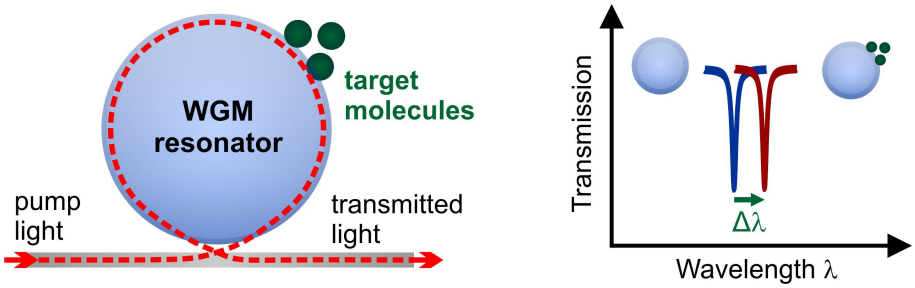

Figure 4.1: Illustration of the sensing principle of WGM resonators. Molecules adsorbing to the surface of a WGM resonator or minute changes in the background refractive index induce a spectral shift of the cavity eigenmode, which can be monitored in real-time by recording the transmission through a tapered optical fiber evanescently coupled to the WGM resonator. Owing to high Q-factors of WGMs up to $\sim 10^{10}$ tiny spectral shifts of a few attometers associated with the binding of single molecules can be resolved [10]. Adapted from [24].

change in n_{eff} translates to a spectral shift of a WGM, which can be used as sensor signal. In WGM biosensing, this sensing principle is widely known as 'reactive sensing principle' and is the most commonly used sensing strategy. It is graphically illustrated in Fig. 4.1. Alternatively, resonance broadening [26, 27, 50] or mode splitting [119–121] in the case of ultra-high-Q WGMs can be exploited to detect binding events of small particles entering the evanescent field of a WGM. For details regarding the different sensing techniques the reader is referred to the review articles [50, 122].

WGM resonators derive their excellent sensing performance from high Q-factors in combination with relatively small modal volumes. Long photon lifetimes lead to the build-up of high circulating intensities inside the cavity and result in multiple interactions of a WGM with its surrounding. Besides strong light–matter interactions, WGM sensors benefit from the high accuracy with which the spectral position of a WGM can be detected [50, 123]. Considering the shot noise limit as fundamental limit of detection, the accuracy with which the spectral position of an optical resonance can be determined is proportional to its Q-factor [50, 123]. Due to the high Q-factors of WGMs, which can reach values as high as $\sim 10^{10}$ [18], tiny wavelength shifts of a few attometers associated with the binding of single molecules can be resolved [24]. However, to properly determine such tiny shifts in an optical measurement, sophisticated measurement techniques are indispensable to suppress any source of noise and achieve a high signal-to-noise ratio [121, 124].
The sensing performance of high-Q WGM resonators is, however, limited by the low intrinsic sensitivity of WGMs. The latter results from the fact that WGMs in high-Q resonators are strongly confined inside the cavity. Therefore, only a small part of the WGM's mode field interacts with the surrounding, limiting the BRIS of purely dielectric WGM resonators to values between 30-200 nm per refractive index unit (RIU) [125–128].

These considerations hint to the tradeoff between high spectral resolution and sensitivity present in sensor systems. Whereas sharp resonances enable the detection of tiny objects, induced resonance shifts are very small due to the strong confinement of high-Q resonances

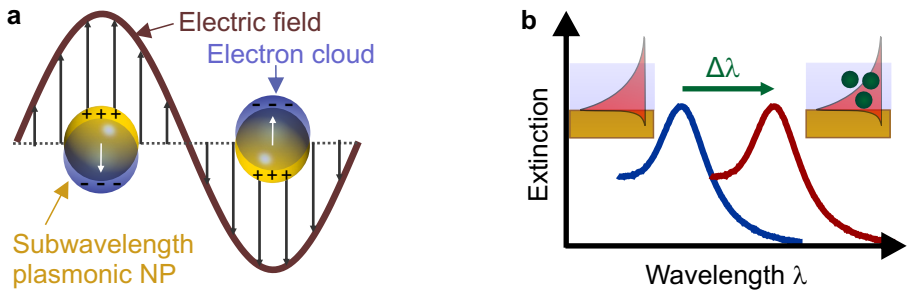

Figure 4.2: Excitation of LSPRs in metallic NPs (a) and illustration of sensing principle of LSPR sensors (b). LSPRs are collective oscillations of the conduction band electrons of subwavelength metallic NPs which coherently interact with a stimulating electric field, generating a peak in the absorption or scattering spectrum. LSPR sensors exploit the evanescent field of LSPRs to detect changes in the plasmon resonance wavelength induced upon minute changes in the dielectric environment. LSPR sensors possess a high intrinsic sensitivity but a comparatively low spectral resolution. Adapted and modified from [131].

inside the cavity and their observation requires complex measurement techniques.

4.1.2 Sensing with plasmonic resonances

Contrary to dielectric WGM sensors, biosensors based on plasmonic resonances derive their excellent sensing performance from the high intrinsic sensitivity connected with plasmonic resonances.

Plasmonic resonances are collective oscillations of the free electron gas of metallic structures which coherently interacts with a stimulating electromagnetic field [32]. At optical frequencies, the conduction electrons of a metal can sustain both surface charge density oscillations confined to an extended metal-dielectric interface, widely known as surface plasmon polaritons (SPPs), and volume charge density oscillations confined to subwavelength metallic NPs, so-called localized surface plasmon resonances (LSPRs), as depicted in Fig. 4.2(a). Due to the subwavelength confinement of electron oscillations, the excitation of plasmonic nanostructures results in strongly localized and greatly enhanced electromagnetic fields at the metal surface [129]. The associated evanescent fields decay exponentially away from the metal interface and are exploited in sensing experiments to probe the surrounding environment in close proximity to the metal–dielectric interface. Similar to WGM sensors, plasmon resonance sensors detect biomolecular binding events or minute changes in the refractive index of the surrounding medium by monitoring spectral shifts of the plasmonic resonance [32, 130], as illustrated in Fig. 4.2(b) for a metallic NP.

The strong field enhancement, superior field confinement compared to WGMs and the fact that the resonance frequency of oscillating plasmons is extremely sensitive to slight changes in the dielectric environment are responsible for the high intrinsic sensitivity of plasmonic nanostructures. For SPP sensors, BRIS values up to 7120 nm/RIU are reported [132],

which exceed those of purely dielectric WGM resonators by more than one order of magnitude. BRIS values of LSPR sensors strongly depend on the shape, the aspect ratio and the morphology of the underlying nanostructure [133]. Whereas smooth colloidal gold nanoparticles with a diameter of 30 nm possess BRIS values of ∼80 nm/RIU [134], the BRIS of nanocrescents or plasmonic nanostructures with properly engineered shape and dispersion can reach values as high as ∼1000 nm/RIU [131, 135, 136]. The generally reduced BRIS values of LSPR sensors can be mainly attributed to the shorter decay length of LSPRs compared to SPPs leading to reduced sensing volumes [137]. However, as metallic NPs confine the enhanced near field to a volume comparable to that of typical biomolecules, LSPR sensors outperform SPP sensors in applications where single-molecule sensitivity is required. Recently, gold nanorods were proven to be capable of detecting single proteins and even monitoring their molecular dynamics [138, 139]. However, as in the case of single-molecule sensing with WGMs, the signal-to-noise ratio in the experiment was very low, thus, still leaving room for improvement.

Although plasmon resonance sensors possess high intrinsic BRIS values, their sensing performance suffers a lot from the low Q-factors of plasmonic resonances. Due to large ohmic losses in the metal, Q-factors of plasmonic nanostructures are typically far less than a hundred at optical frequencies [31, 140–142], leading to a low spectral resolution.

4.1.3 Hybrid WGM resonators for improved sensing performance

Inspired by the tradeoff between high sensitivity and high signal resolution present in the two addressed types of optical sensors, a promising concept to push sensing applications forward can be seen in combining dielectric WGM resonators with plasmonic nanostructures in a single hybrid photonic–plasmonic biosensor. Whereas the plasmonic component in the hybrid sensor shall boost the wavelength shift induced by changes in the dielectric environment by providing strongly enhanced electromagnetic fields, the high-Q WGM component shall ensure that the induced shift can be properly resolved. The major challenge in the design of hybrid sensors, however, lies in simultaneously preserving the high Q-factors of WGMs and the strong mode localization connected with plasmonic resonances. Recently, several approaches have been proposed to combine the best of the two 'worlds' in a hybrid photonic–plasmonic sensor [34, 37, 143–146].

One approach to enhance the sensitivity of WGM resonators while keeping metal-related losses to a minimum relies on coating rotationally symmetric WGM resonators with a thin homogeneous metal layer that allows for the formation of SPP modes at the metal–dielectric interface [39, 121, 147]. For dielectric ring resonators coated with metallic nanodisks or -stripes deposited along the ring's circumference BRIS values between 200-500 nm/RIU have been theoretically predicted for operation wavelengths in the near-IR [148–153]. Compared to their purely dielectric counterparts, the BRIS was increased by a factor of ∼4. Another promising hybrid structure for bulk refractive index sensing is a silicon ring surrounded by silver layers which are separated by a narrow air gap from the ring itself [154]. Due to a high electric field accumulation in the air gap between the

two silver layers, BRIS values as high as 700 nm/RIU have been measured. Whereas high Q-factors on the order of 10^3 have been predicted theoretically, in the experiment they dropped to values below 300.

An alternative approach to boost the sensitivity of WGM resonators while simultaneously maintaining high Q-factors makes use of locally enhanced light–matter interactions in the vicinity of plasmonic NPs coupled to the surface of WGM resonators [34–36]. The proposed structures were employed in single-molecule sensing and specifically engineered to push detection limits down to the single-molecule [33] and single-ion level [38]. Greatly enhanced optical near-fields together with the strong polarizability of plasmonic NPs gave rise to greatly enhanced WGM shifts in these structures. For instance, binding of a single RNA virus to an adequately aligned gold nanoshell coupled to a silica microsphere was shown to enhance the WGM shift by a factor of ∼70 compared to when the virus binds to the surface of the bare dielectric WGM resonator [33]. In the case of a single atomic ion interacting with a gold NR on the microsphere surface even a 1000-fold signal enhancement was achieved over a non-hybrid WGM resonator [38]. Hybrid NP–WGM resonators were also successfully employed in monitoring interactions of single ligand molecules at the NP interface in situ and in real-time [155].
To keep scattering losses in the proposed structures to a minimum, only a single or a few plasmonic NPs were attached to the surface of the WGM resonators. Besides, a careful choice of the operation wavelength was shown to be indispensable to preserve the high Q-factors necessary for single-molecule resolution [36, 37, 41]. After the incorporation of plasmonic NPs, Q-factors dropped by up to two orders of magnitude to values between 10^5-10^6 [36–38, 156, 157]. But, due to strongly enhanced wavelength shifts in these structures, less sophisticated measurement techniques could be employed to monitor the binding events associated with single molecules, which is advantageous from a practical point of view.

Throughout the rest of this chapter, we present and discuss an alternative approach to improve the sensing capabilities of WGM resonators. We consider a sensing scheme that measures tiny changes in the refractive index of the surrounding medium and analyze whether the locally enhanced light–matter interactions in the vicinity of plasmonic NPs can be also exploited to enhance the sensitivity of WGM resonators toward bulk refractive index changes.

4.2 Coupled harmonic oscillator model for NP–WGM interaction

To optimize the performance of hybrid NP–WGM resonators as bulk refractive index sensors, it is essential to understand the interplay between WGMs and plasmonic modes sustained by metallic NPs. Although proposed theoretical frameworks based on generalized Lorenz Mie theory [146] and level repulsion [41] have proven to, e.g., accurately predict spectral resonance shifts induced by a plasmonic NP perturbing the optical WGM

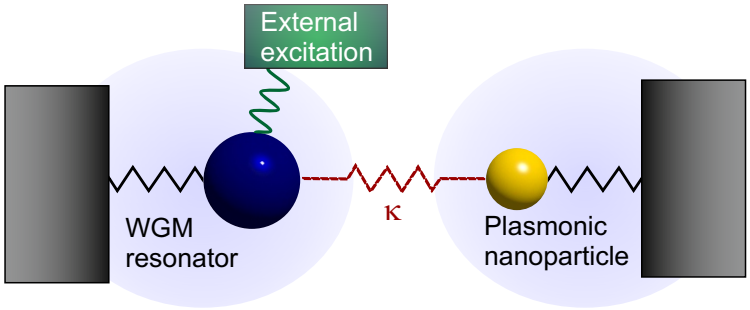

Figure 4.3: Schematic illustration of the coupled harmonic oscillator model to describe the NP–WGM interaction in hybrid resonators. A weakly damped HO representing the WGM resonator (blue) is coupled to a strongly damped HO representing the plasmonic NP (yellow) via the coupling constant κ. The WGM-HO is directly driven by an external time-harmonic force, the NP-HO is only excited via the coupling to the WGM-HO.

resonator, they cannot provide a descriptive insight into the coupling between plasmonic and dielectric modes due to their complexity.
Therefore, we develop in this section a simple model of two coupled harmonic oscillators (HOs) to provide an intuitive picture for the NP–WGM interaction. This simple model turns out to capture fundamental aspects of hybrid sensors (see section 4.3) and provides basic insight into the mechanisms underlying the sensitivity enhancement in these systems. After introducing the theory of coupled HOs in section 4.2.1, we discuss the properties of hybrid resonances in the coupled system in section 4.2.2. We proceed in section 4.2.3 to derive an analytic formula for the BRIS of the hybrid system and deduce general sensor design guidelines from it. A brief summary and conclusions are given at the end of the section.

The calculations presented in this section are based on a matlab code developed by Steffen A. Schmid during his master's thesis [158] under supervision of Radius N. S. Surydharma from the Institute of Theoretical Solid States Physics (TFP) at KIT and me.

4.2.1 Theory of coupled harmonic oscillators

The model of two coupled HOs has been widely used to explain many phenomena in an intuitive manner, such as Fano resonances [159] or level repulsion [160]. Here, we use the model of two coupled HOs to describe the interaction between a LSPR supported by a metallic NP and a WGM supported by a dielectric microresonator.

To examine the NP–WGM interaction, we model the WGM and the LSPR as two damped HOs with resonance frequencies ω_{WGM} and ω_{NP} and damping constants Γ_{WGM} and Γ_{NP}, respectively. The damping constants account for energy losses in the optical resonators. Due to large ohmic losses in the metal, Q-factors of plasmonic resonances are small compared to those of WGMs. Therefore, the NP damping constant Γ_{NP} is significantly larger

than the damping constant Γ_{WGM} of the WGM, i.e. $\Gamma_{\mathrm{NP}} \gg \Gamma_{\mathrm{WGM}}$. As in typical experiments, the coupled system is excited by driving the WGM oscillator (WGM-HO) with an external time-harmonic field $x(t)=x^0_{\mathrm{ext}}\exp(i\omega_0 t)$ with excitation frequency ω_0 and amplitude x^0_{ext}. The oscillator representing the plasmonic NP (NP-HO) is solely excited via the leakage of the WGM-HO, as graphically illustrated in Fig. 4.3. The electromagnetic coupling between NP-HO and WGM-HO, enabling the transfer of energy between both oscillators, is modeled via the coupling constant κ.
The dynamic of the hybrid system is governed by the following differential equations:

$$\ddot{x}_{\mathrm{WGM}} + \Gamma_{\mathrm{WGM}}\dot{x}_{\mathrm{WGM}} + \omega^2_{\mathrm{WGM}}x_{\mathrm{WGM}} - \kappa x_{\mathrm{NP}} = x^0_{\mathrm{ext}}e^{i\omega_0 t} \tag{4.2a}$$

$$\ddot{x}_{\mathrm{NP}} + \Gamma_{\mathrm{NP}}\dot{x}_{\mathrm{NP}} + \omega^2_{\mathrm{NP}}x_{\mathrm{NP}} - \kappa x_{\mathrm{WGM}} = 0. \tag{4.2b}$$

We analyze the system in the time-harmonic limit and seek for steady-state solutions of the form:

$$x_{\mathrm{WGM}}(t) = x^0_{\mathrm{WGM}}e^{i\omega_0 t} \tag{4.3a}$$

$$x_{\mathrm{NP}}(t) = x^0_{\mathrm{NP}}e^{i\omega_0 t}. \tag{4.3b}$$

Inserting this ansatz into the equations of motion (Eq. 4.2) results in two coupled linear equations for the complex oscillator amplitudes x^0_{WGM} and x^0_{NP} of WGM-HO and NP-HO, respectively:

$$\begin{pmatrix} x^0_{\mathrm{WGM}} \\ x^0_{\mathrm{NP}} \end{pmatrix} = \begin{pmatrix} \omega^2_{\mathrm{WGM}} - \omega_0^2 + i\Gamma_{\mathrm{WGM}}\omega_0 & -\kappa \\ -\kappa & \omega^2_{\mathrm{NP}} - \omega_0^2 + i\Gamma_{\mathrm{NP}}\omega_0 \end{pmatrix}^{-1} \cdot \begin{pmatrix} x^0_{\mathrm{ext}} \\ 0 \end{pmatrix}. \tag{4.4a}$$

Nontrivial solutions of this inhomogeneous system of equations are determined by inverting the matrix in Eq. 4.4 numerically for varying excitation frequencies ω_0. The resonance frequency ω_{res} of the WGM-HO in the coupled system is given by the frequency for which the modulus $\left|x^0_{\mathrm{WGM}}\right|$ of the WGM oscillator amplitude is maximal. The respective Q-factor is inferred from the full width half maximum (FWHM) of the Lorentzian-shaped oscillator amplitude.

In the following, the influence of the properties of the NP-HO and the coupling strength on the response of the WGM-HO in the coupled system is calculated as a function of the resonance frequency detuning $\Delta\omega = \omega^0_{\mathrm{WGM}} - \omega^0_{\mathrm{NP}}$ between both oscillators. ω^0_{WGM} and ω^0_{NP} denote the natural frequencies of the uncoupled WGM- and NP-HO and are given by $(\omega^0_{\mathrm{WGM}})^2 = \omega^2_{\mathrm{WGM}} - \Gamma^2_{\mathrm{WGM}}$ and $(\omega^0_{\mathrm{NP}})^2 = \omega^2_{\mathrm{NP}} - \Gamma^2_{\mathrm{NP}}$. Different detunings $\Delta\omega$ are implemented by varying the natural frequency of the NP-HO with respect to that of the WGM-HO. With regard to the experiments, the simulation results of the coupled HO-model are presented in the wavelength domain, i.e. plotted as a function of the resonance wavelength detuning $\Delta \equiv \lambda^0_{\mathrm{NP}} - \lambda^0_{\mathrm{WGM}}$ between the natural resonance wavelengths of the NP-HO and the WGM-HO.

4.2.2 Properties of hybrid resonances

To gain first insight into the NP–WGM interaction, we plot in Fig. 4.4(a) the modulus of the oscillator amplitudes $\left|x^0_{\mathrm{NP}}\right|$ and $\left|x^0_{\mathrm{WGM}}\right|$ of NP-HO (red) and WGM-HO (black) at

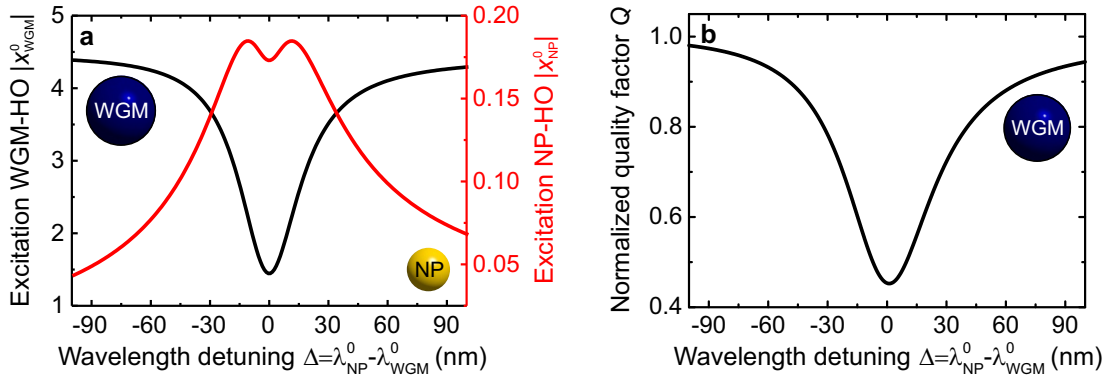

Figure 4.4: Impact of wavelength detuning $\Delta=\lambda^0_{\mathrm{NP}}-\lambda^0_{\mathrm{WGM}}$ on (a) the excitation $\left|x^0_{\mathrm{WGM}}\right|$ and $\left|x^0_{\mathrm{NP}}\right|$ of WGM-HO (black) and NP-HO (red) and (b) the Q-factor of the WGM-HO at the resonance wavelength λ_{res} of the hybrid system [161]. For $\Delta=0$, energy is efficiently transferred from the WGM-HO to the lossy NP-HO, leading to a global minimum in the excitation of the WGM-HO and its Q-factor. As the NP-HO is indirectly driven via the coupling to the WGM-HO, its excitation reveals a local minimum for $\Delta=0$ and two local maxima for slightly detuned resonances $|\Delta|>0$.

the resonance wavelength λ_{res} of the hybrid system versus the wavelength detuning Δ. The functional dependency of the Q-factor of the WGM-HO in the coupled system on the detuning Δ is shown in Fig. 4.4(b).

As the NP-HO is indirectly driven via the coupling to the WGM-HO, its excitation $\left|x^0_{\mathrm{NP}}\right|$ is notably smaller than the excitation $\left|x^0_{\mathrm{WGM}}\right|$ of the WGM-HO. For large absolute detunings $|\Delta|$, the excitation of the directly driven WGM-HO is maximal while being minimal for the indirectly driven NP-HO due to a vanishing spectral overlap between the resonances of both HOs. For zero detuning ($\lambda^0_{\mathrm{NP}}=\lambda^0_{\mathrm{WGM}}$), energy is efficiently transferred from the weakly damped WGM-HO to the strongly damped NP-HO giving rise to a global minimum in the excitation of the WGM-HO and its Q-factor. Contrary to the WGM-HO, the excitation of the NP-HO increases toward $|\Delta|\to 0$ with a local minimum at zero detuning. This circumstance can be interpreted as follows: If the NP-HO was uncoupled, its oscillator amplitude would be maximal if excited directly at its resonance wavelength. But, the NP-HO in the hybrid system is indirectly driven via the coupling to the WGM-HO whose amplitude is, however, minimal at zero detuning. Therefore, the excitation $\left|x^0_{\mathrm{NP}}\right|$ of the NP-HO reveals a local minimum at zero detuning and two local maxima slightly red and blue shifted from $\Delta=0$.

These results point out the tradeoff between maximizing the excitation of the NP-HO and simultaneously maximizing the Q-factor of the WGM-HO in the coupled system. Whereas the excitation of the NP-HO is maximal close to zero detuning, the WGM-HO's Q-factor is most strongly degraded there due to huge losses induced by coupling to the low-Q NP-HO. Operating a hybrid system slightly detuned from the resonance case $|\Delta|=0$, thus, seems to be favorable to keep linewidth broadening of WGMs at a moderate level while still being able to notably excite the plasmonic component in the hybrid system.

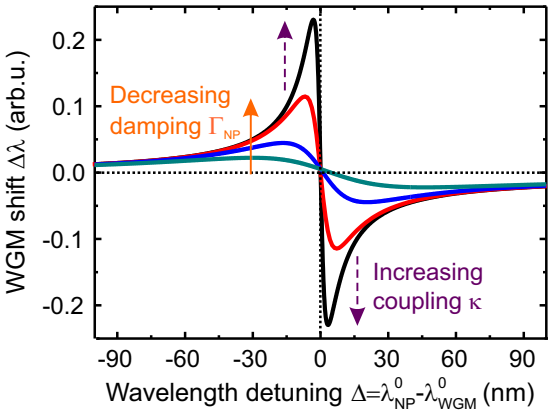

Figure 4.5: Resonance wavelength shift $\Delta\lambda$ of the WGM-HO induced upon coupling to NP-HOs with different damping constants Γ_{NP} as a function of the wavelength detuning $\Delta{=}\lambda^0_{\mathrm{NP}}{-}\lambda^0_{\mathrm{WGM}}$ [161]. The induced shift $\Delta\lambda$ strongly depends on the detuning Δ and the damping of the NP-HO. Whereas NP-HOs with resonance wavelengths blue detuned from the WGM-HO ($\lambda^0_{\mathrm{NP}}{<}\lambda^0_{\mathrm{WGM}}$) spectrally shift the resonance wavelength of the WGM-HO toward longer wavelenghts, the coupling to red detuned NP-HOs ($\lambda^0_{\mathrm{NP}}{>}\lambda^0_{\mathrm{WGM}}$) leads to a shift toward shorter wavelengths. The weaker the damping of the NP-HO and the larger the coupling strength κ, the larger is the induced shift.

To evaluate how the coupling to the NP-HO affects the resonance wavelength of the WGM-HO, we plot in Fig. 4.5 the resonance wavelength shift $\Delta\lambda$ of the WGM-HO induced by the NP-HO as a function of the detuning Δ and for different NP damping constants Γ_{NP}. The resonance wavelength shift $\Delta\lambda$ is evaluated with respect to the natural resonance wavelength λ^0_{WGM} of the uncoupled WGM-HO, i.e. $\Delta\lambda{=}\lambda_{\mathrm{res}}{-}\lambda^0_{\mathrm{WGM}}$.
From Fig. 4.5, a strong dependency of the induced WGM shift $\Delta\lambda$ on the detuning is obvious. Whereas NP-HOs with resonance wavelengths blue detuned from the WGM-HO ($\lambda^0_{\mathrm{NP}}{<}\lambda^0_{\mathrm{WGM}}$) spectrally shift the resonance of the WGM-HO toward longer wavelengths ($\Delta\lambda{>}0$), NP-HOs with resonance wavelengths red detuned with respect to the WGM-HO ($\lambda^0_{\mathrm{NP}}{>}\lambda^0_{\mathrm{WGM}}$) shift the resonance of the WGM-HO toward shorter wavelengths ($\Delta\lambda{<}0$). In the limit of large negative detunings, the induced WGM shift $\Delta\lambda$ approaches zero. In contrast, for large positive detunings $\lambda^0_{\mathrm{NP}}{\gg}\lambda^0_{\mathrm{WGM}}$, off-resonant coupling leads to a non-vanishing spectral shift of the WGM-HO's resonance toward slightly shorter wavelengths. For $\Delta{=}0$, the spectral position of the WGM-HO remains unaffected.
Figure 4.5 furthermore reveals that the magnitude of the induced wavelength shift $\Delta\lambda$ strongly depends on the damping constant Γ_{NP} of the NP-HO. The stronger the damping of the NP-HO coupled to the WGM-HO, the smaller is the induced WGM shift $\Delta\lambda$ and the less pronounced are the features in Fig. 4.5. On top of that, increasing the damping of the NP-HO shifts the extrema in $\Delta\lambda(\Delta)$ toward larger absolute detunings.
Evaluating the effect of the coupling strength κ on the resonance shift of the WGM-HO shows that varying κ effectively leads to a rescaling of the curves $\Delta\lambda(\Delta)$ [158], as indicated by the purple arrows in Fig. 4.5. The larger the coupling strength, the larger is the response of the WGM-HO to the coupling to the NP-HO and, hence, the modulus of the induced

shift $|\Delta\lambda|$. For $\kappa \to 0$, the induced resonance wavelength shift $\Delta\lambda$ vanishes, as expected for a system of uncoupled HOs.

The results obtained so far from the model of coupled HOs provide valuable guidelines for the design of sensing experiments which aim to detect individual plasmonic NPs. To maximize the WGM shift induced by a plasmonic NP, an operational WGM wavelength slightly red detuned with respect to the plasmonic resonance should be selected. The higher the quality of the plasmonic resonance and the higher the NP–WGM coupling strength, the larger is the induced WGM shift. In an experimental hybrid NP–WGM sensor, the coupling strength is mainly determined by the spatial overlap of the evanescent fields of the plasmonic NP and the exciting WGM and the optical properties of the resonators.

4.2.3 Sensitivity enhancement in the coupled system

Based on the results obtained so far, we derive in the following an analytic formula for the BRIS of the hybrid system which provides elementary insight into what governs the sensitivity of hybrid NP–WGM resonators and allows deducing general sensor design guidelines.

Within the formalism of two coupled HOs, the resonance wavelength λ_{res} of the WGM-HO in the coupled system can be expressed as the sum of the resonance wavelength λ^0_{WGM} of the uncoupled WGM-HO and the resonance wavelength shift $\Delta\lambda$ of the WGM-HO induced by coupling to the NP-HO. As $\Delta\lambda$ depends on both the wavelength detuning $\Delta = \lambda^0_{\mathrm{NP}} - \lambda^0_{\mathrm{WGM}}$ between the two HOs and the coupling strength κ (see section 4.2.2), the hybrid system's resonance wavelength λ_{res} can be written as follows:

$$\lambda_{\mathrm{res}} = \lambda^0_{\mathrm{WGM}} + \Delta\lambda(\Delta, \kappa). \tag{4.5}$$

According to Eq. 4.1, the BRIS of the hybrid system is, hence, given by:

$$BRIS_{\mathrm{HY}} = \frac{d\lambda_{\mathrm{res}}}{dn_{\mathrm{m}}}. \tag{4.6}$$

To derive an explicit expression for the BRIS of the hybrid system, one has to consider that changing the refractive index n_{m} of the surrounding medium alters the resonance wavelengths λ^0_{WGM} and λ^0_{NP} of the isolated WGM-HO and NP-HO. The induced resonance wavelength shifts of the uncoupled HOs are determined by the BRIS values $BRIS_{\mathrm{WGM}}$ and $BRIS_{\mathrm{NP}}$ of the respective oscillators according to:

$$d\lambda^0_{\mathrm{WGM}} = BRIS_{\mathrm{WGM}} \cdot dn_{\mathrm{m}} \tag{4.7a}$$

$$d\lambda^0_{\mathrm{NP}} = BRIS_{\mathrm{NP}} \cdot dn_{\mathrm{m}}. \tag{4.7b}$$

As the BRIS of a plasmonic NP is typically larger than that of a dielectric WGM resonator, variations in the background refractive index n_{m} alter the detuning Δ between both HOs. Furthermore, altering n_{m} simultaneously affects the coupling strength κ between NP and WGM. Considering these effects and combining Eq. 4.7 with Eq. 4.5, the BRIS of the

hybrid system can be expressed as follows:

$$BRIS_{\mathrm{HY}} = BRIS_{\mathrm{WGM}} + \frac{\partial \Delta\lambda}{\partial \Delta}(BRIS_{\mathrm{NP}} - BRIS_{\mathrm{WGM}}) + \frac{\partial \Delta\lambda}{\partial \kappa} \cdot \frac{\partial \kappa}{\partial n_{\mathrm{m}}}. \tag{4.8}$$

According to Eq. 4.8, the BRIS of the hybrid system is modified compared to the BRIS of the uncoupled WGM-HO by the second and third term in Eq. 4.8, which we denote by detuning term and coupling term, respectively. The detuning term accounts for the fact that the relative detuning Δ between WGM-HO and NP-HO is altered when changing the background refractive index n_{m}. The coupling term describes additional changes in the BRIS due to variations in the coupling strength κ induced by altering n_{m}. It cannot be fully described within the simple model of two coupled HOs. According to the full-wave simulations presented in section 4.3, the coupling term is, however, expected to only lead to minor modifications in the BRIS of the hybrid system. Therefore, we focus in the following on discussing the dominant role of the detuning term on the BRIS enhancement.

Eq. 4.8 reveals that the detuning term is proportional to the difference in the BRIS values of NP-HO and WGM-HO. Therefore, only NP-HOs with a BRIS much larger than that of the WGM-HO notably modify the BRIS of the WGM-HO. For NP-HOs whose BRIS equals that of the WGM-HO no change in BRIS is induced upon coupling.
From Eq. 4.8 we furthermore see that the functional dependency of the detuning term on the wavelength detuning Δ is governed by the derivative of the resonance wavelength shift $\Delta\lambda$ of the WGM-HO induced by coupling to the NP-HO with respect to the detuning Δ. To closer examine this dependency, we plot the respective derivative $\partial\Delta\lambda/\partial\Delta$ in Fig. 4.6 versus the detuning Δ considering NP-HOs with different damping constants Γ_{NP}. The derivative $\partial\Delta\lambda/\partial\Delta$ is seen to be strongly dispersive, as expected from Fig. 4.5, and either positive or negative. Depending on the detuning Δ, the BRIS of the WGM-HO is, hence, either enhanced or reduced due to the interaction with the NP-HO. How can we understand this effect?
According to Eq. 4.8 and given that $BRIS_{\mathrm{NP}} > BRIS_{\mathrm{WGM}}$, the BRIS of the hybrid system is reduced compared to the BRIS of the uncoupled WGM-HO for detuning regions Δ for which $\partial\Delta\lambda/\partial\Delta < 0$, i.e. for detunings spectrally located between the two extrema in $\Delta\lambda(\Delta)$ (see Fig. 4.5). The reduction in BRIS in this detuning region is the result of two opposing effects. On the one hand, increasing the background refractive index n_{m} shifts the resonances of both HOs toward longer wavelengths. As the BRIS of the NP-HO is, however, larger than that of the WGM-HO, the resonance of the NP-HO experiences a larger red shift than the resonance of the WGM-HO. Increasing n_{m}, thus, increases the relative detuning Δ. As $\partial\Delta\lambda/\partial\Delta$ is negative in the spectral region between the two extrema in $\Delta\lambda(\Delta)$ (see Fig. 4.5), the increase in detuning Δ effectively shifts the resonance of the WGM-HO toward shorter wavelengths. This effect counteracts the actual WGM red shift and is responsible for the reduction in BRIS. Please note that the BRIS of the WGM-HO in the hybrid system is maximally reduced over that of the isolated WGM-HO for zero resonance wavelength detuning.
Contrary to the situation considered above, the coupling to the NP-HO is beneficial for the BRIS of the WGM-HO if the coupled system is operated at detunings Δ for which the

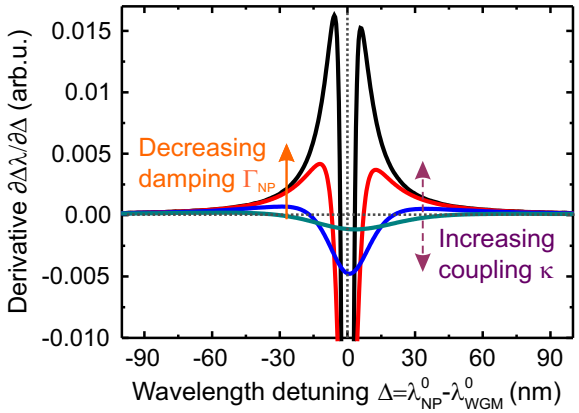

Figure 4.6: Derivative $\partial\Delta\lambda/\partial\Delta$ of the resonance wavelength shift $\Delta\lambda$ of the WGM-HO induced upon coupling to the NP-HO for different wavelength detunings $\Delta{=}\lambda^0_{\mathrm{NP}}{-}\lambda^0_{\mathrm{WGM}}$ and varying damping factors Γ_{NP} [161]. $\partial\Delta\lambda/\partial\Delta$ describes modifications in the BRIS of a hybrid NP-WGM sensor over a bare WGM sensor. Depending on the detuning Δ, the coupling of the NP-HO to the WGM-HO can either lead to an enhancement or a reduction in BRIS. A maximal BRIS enhancement is observed for NP-HOs with resonance wavelengths slightly blue detuned from the WGM-HO. The higher the Q-factor of the NP-HO and the higher the coupling strength κ, the larger are the enhancement effects.

derivative $\partial\Delta\lambda/\partial\Delta$ is positive, i.e. for detunings blue- and red shifted from the maximum and the minimum in $\Delta\lambda(\Delta)$, respectively (see Fig. 4.5). Due to the positive slope of $\Delta\lambda(\Delta)$, the actual red shift of the resonance of the WGM-HO due to the increase in n_{m} is now accompanied by an effective red shift due to the increased relative detuning Δ. Both effects leading to a red shift of the WGM-HO's resonance wavelength add up constructively in this detuning region and, thus, lead to an enhancement in BRIS. A maximal BRIS enhancement is achieved when operating the hybrid system at detunings corresponding to the turning point blue shifted from the maximum in $\Delta\lambda(\Delta)$ for which the derivative $\partial\Delta\lambda/\partial\Delta$ exhibits its maximal positive value.
Let's now briefly discuss the impact of the damping constant Γ_{NP} of the NP-HO and the coupling strength κ on the BRIS of the coupled system. According to Fig. 4.6, the BRIS of the hybrid system is larger, the weaker the damping of the NP-HO and the larger the coupling strength (indicated by purple arrows). For strongly damped NP-HOs or small coupling strengths, the beneficial effect of the NP-HO on the BRIS of the WGM-HO almost vanishes. Please note that variations in the coupling strength do not alter the optimal detuning corresponding to the maximal BRIS enhancement, but only lead to a rescaling of the curves shown in Fig. 4.6. Contrary, variations in the damping of the NP-HO affect the optimal operation conditions of the hybrid sensor.

The results obtained from the HO-model suggest to use plasmonic NPs with high-quality resonances, high BRIS values, and resonance wavelengths slightly blue detuned from the operational WGM to maximally enhance the BRIS of a dielectric WGM resonator.

4.2.4 Summary and conclusions

The simple model of two coupled harmonic oscillators (HOs) derived in this section provides elementary insight into the coupling process between WGMs and plasmonic resonances sustained by metallic NPs and succeeds in mapping out a strategy on how to boost the sensitivity of dielectric WGM resonators.
The HO-model predicts that both the optical properties of a WGM, i.e. its Q-factor and spectral resonance position, and the BRIS strongly depend on the resonance wavelength detuning between WGM and plasmonic resonance. Depending on the relative detuning, the coupling of a plasmonic NP to a WGM resonator is shown to spectrally shift the operational WGM either toward longer or shorter wavelengths. It is furthermore shown that the BRIS of a WGM resonator can be enhanced or reduced via the coupling to a plasmonic NP. A maximal BRIS enhancement is predicted for operational WGM wavelengths slightly red detuned from the plasmonic resonance. The enhancement in BRIS is demonstrated to sensitively depend also on the properties of the plasmonic NP, i.e. its Q-factor and BRIS. The HO-model suggests that only metallic NPs with high-quality plasmonic resonances and high BRIS values notably exceeding that of the operational WGM significantly enhance the sensitivity of a WGM resonator toward bulk refractive index changes.
Please note that the optical properties of the plasmonic NP and the WGM resonator are not captured in the simple-HO model. Therefore, the HO-model can only make qualitative statements about the optical response of WGMs to the coupling to plasmonic NPs and associated sensitivity enhancement effects. To quantify the respective effects, exact calculations or numerical simulations of hybrid NP–WGM resonators are needed (see sections 4.3 and 4.4).

4.3 Multi-Mie simulations of a WGM microsphere coupled to an idealized plasmonic NP

To prove the concept of using plasmonic NPs to enhance the sensitivity of a WGM resonator and verify the results obtained from the coupled harmonic oscillator model (HO-model), full electromagnetic simulations of hybrid NP–WGM sensors based on exact calculations using multi-Mie simulations are performed and presented in this section. To study the coupling between plasmonic NPs and WGMs in a fundamental manner, an idealized hybrid system comprised of a dielectric WGM microsphere with 2 µm radius coupled to an artificial plasmonic NP made from a metal with Drude permittivity is considered. Modeling the plasmonic NP as an idealized Drude-metal NP allows to freely tune the optical properties of the plasmonic resonance and to analyze the impact of the plasmonic resonance wavelength and linewidth on the optical and sensing properties of WGMs individually.

After introducing the multi-Mie scattering formalism used to simulate the electromagnetic properties of hybrid NP–WGM sensors in section 4.3.1, we introduce in section 4.3.2 the concept of the Drude-metal NPs (DNPs). We proceed to discuss consequences of the

coupling between DNPs and WGMs and present simulation results for the optical and sensing properties of the idealized hybrid system in sections 4.3.3 and 4.3.4, respectively. Throughout the section, we relate the multi-Mie simulation results to those obtained from the simple HO-model. The excellent qualitative agreement between both formalisms shows that the mechanisms underlying the sensitivity enhancement in hybrid systems are already well captured by the simple HO-model. A short summary and concluding remarks are given at the end of the section.

The simulations presented in this section were performed by Steffen A. Schmid during his master's thesis [158] and are based on a multiple-scattering algorithm documented in [162,163]. Radius N. S. Surydharma from the Insitute of Theoretical Solid State Physics (TFP) at KIT, with whom I supervised Steffen A. Schmid, notably contributed to the results presented in this section by assisting Steffen A. Schmid in adapting the algorithm to the specific problem of electromagnetic scattering by a hybrid NP–WGM resonator.

4.3.1 Multi-Mie scattering theory of hybrid sensors

In the following, we outline the multi-Mie scattering formalism used to analytically calculate the electromagnetic response of hybrid NP–WGM sensors comprised of a dielectric WGM microsphere with a single spherical plasmonic NP attached to its surface. For details regarding this formalism, the interested reader is referred to [162, 164].

The multi-Mie scattering formalism describes the electromagnetic scattering by an aggregate of arbitrarily arranged and mutual interacting spheres of arbitrary sizes made from homogeneous, linear, local and isotropic materials. It resorts to the analytic framework of the classical Mie theory for a single isolated sphere [54] and makes use of an addition theorem for vector spherical harmonics (VSHs) to account for the mutual interaction of the spheres in the cluster [164]. In full analogy to Mie theory for an isolated sphere, solving the electromagnetic scattering problem of a cluster of spheres in the framework of multi-Mie theory requires relating incident fields to scattered fields. To this end, we consider time-harmonic electric fields $\mathbf{E}(\mathbf{r},\omega)$ oscillating at angular frequency ω and assume that the cluster of spheres is embedded in a homogeneous, nonabsorbing background medium. Exploiting the spherical symmetry of each constituent in the cluster, the incident, internal and scattered fields of each sphere j in the cluster can be expanded into a series of VSHs $\mathbf{M}(r^j,\Theta^j,\varphi^j)$ and $\mathbf{N}(r^j,\Theta^j,\varphi^j)$, which represent TE- and TM-polarized fields [57]. Using VSHs as the basis set, the electric field $\mathbf{E}^j_{\mathrm{inc}}(r,\Theta,\varphi,\omega)$ incident onto sphere j and the electric field $\mathbf{E}^j_{\mathrm{sca}}(r,\Theta,\varphi,\omega)$ scattered from the sphere can be expanded as follows:

$$\mathbf{E}^j_{\mathrm{inc}}(\mathbf{r},\omega) = \sum_{n=1}^{N}\sum_{m=-n}^{n} p^j_{nm}(\omega)\mathbf{N}_{nm}(r^j,\Theta^j,\varphi^j) + q^j_{nm}(\omega)\mathbf{M}_{nm}(r^j,\Theta^j,\varphi^j) \tag{4.9}$$

$$\mathbf{E}^j_{\mathrm{sca}}(\mathbf{r},\omega) = \sum_{n=1}^{N}\sum_{m=-n}^{n} a^j_{nm}(\omega)\mathbf{N}_{nm}(r^j,\Theta^j,\varphi^j) + b^j_{nm}(\omega)\mathbf{M}_{nm}(r^j,\Theta^j,\varphi^j). \tag{4.10}$$

$[p^j_{nm}(\omega), q^j_{nm}(\omega)]$ and $[a^j_{nm}(\omega), b^j_{nm}(\omega)]$ are the expansion coefficients for the incident and

the scattered field, respectively. For a given illumination, they fully describe the interaction of light with the scatterer. n and m are the quantum numbers of the respective multipole moments, N denotes the maximal multipolar order considered in the expansion. From now on, we skip the frequency dependency to simplify the notation.
Applying the boundary conditions at the surface of sphere j and exploiting the orthogonality of the VSHs, the scattering coefficients (a^j_{nm}, b^j_{nm}) can be expressed in terms of the expansion coefficients (p^j_{nm}, q^j_{nm}) of the incident field and the physical properties of the sphere, i.e. its radius and refractive index, which are encoded in the so-called Mie-coefficient of the corresponding isolated sphere. Importantly and contrary to the case of an isolated sphere, the total field $\mathbf{E}^j_{\text{inc}}$ impinging onto sphere j in the cluster is a superposition of the external incident field $\mathbf{E}_{\text{ext}}$ and the field $\mathbf{E}_{\text{sca}}(l, j)$ scattered from all other spheres $l{\neq}j$ in the cluster:

$$\mathbf{E}^j_{\text{inc}} = \mathbf{E}_{\text{ext}} + \sum_{l \neq j} \mathbf{E}_{\text{sca}}(l, j). \tag{4.11}$$

To relate the expansion coefficients of the total incident field to the scattered field from sphere j, it is necessary to transform the VSHs from the spherical coordinate system centered about the origin of sphere l to the one centered about sphere j. This transformation, denoted by (l, j) in Eq. 4.11, can be accomplished using an addition theorem of VSHs (Eq. 4 and 5 in [163]). One finally obtains a set of self-consistent equations for the complex valued scattering coefficients a^j_{nm} and b^j_{nm}, which can be solved numerically using the so-called T-matrix formalism. The T-matrix is unique to a scatterer and describes how an incident electric field is scattered by a given object. The total field scattered by the cluster can be obtained by superimposing the scattered fields from all spheres in the cluster.
With the scattering coefficients and the expansion coefficients of the external incident field at hand, all physical quantities of interest can be directly computed, e.g., local electric fields, scattering or extinction cross sections. In this work, the scattering cross section of the WGM sphere in the hybrid NP–WGM cluster is of particular interest, as it determines the spectrum of the hybrid resonator. An explicit expression for the scattering cross section is provided in [164].

To efficiently compute the scattering response, we exploit that the plasmonic NP coupled to the WGM microsphere is small compared to the wavelength of light, which allows to approximate its spectral resonance features by an electric dipole resonance ($N{=}1$) [58]. The complexity of the linear system of equations for the scattering coefficients can be further reduced by localizing the plasmonic NP in the $x{-}y$ plane, i.e. attaching it to the equator of the microsphere. Here, the dominant modes are the fundamental modes ($n{=}m$) and we can, hence, safely assume that the interaction of the plasmonic NP with modes with mode numbers $n{\neq}m$ can be neglected.

4.3.2 Drude-metal NPs with freely tunable optical parameters

In the following, we briefly look into the resonant character of plasmonic NPs made from real metals and motivate why artificial NPs made from a Drude-metal are an excellent choice to systematically study hybrid sensors. In this context, we discuss the optical and sensing properties of the DNPs used below to boost the sensitivity of a small dielectric WGM microsphere.

Optical response of plasmonic NPs made from real metals

For plasmonic NPs being small compared to the wavelength of the incident light, the optical response to a stimulating light field can be well described within an electrostatic approximation [58]. Their resonant character becomes evident from the frequency-dependency of far-field quantities, such as the scattering cross section. For a subwavelength plasmonic NP with radius R_{NP} and complex permittivity $\epsilon_{\mathrm{NP}}(\lambda)$ embedded in a homogeneous background medium with permittivity ϵ_{m}, the scattering cross section C_{sca} in the quasi-static limit is given by [58]:

$$C_{\mathrm{sca}} \approx \frac{8}{3}\pi k_0^4 R_{\mathrm{NP}}^6 \left| \frac{\epsilon_{\mathrm{NP}}(\lambda) - \epsilon_{\mathrm{m}}}{\epsilon_{\mathrm{NP}}(\lambda) + 2\epsilon_{\mathrm{m}}} \right|^2 . \tag{4.12}$$

Resonances occur if the real part of the denominator in Eq. 4.12 vanishes, which is the case for $\mathrm{Re}[\epsilon_{\mathrm{NP}}(\lambda)]{=}{-}2\epsilon_{\mathrm{m}}$. This condition is known as the Fröhlich condition. For gold and silver NPs, the LSPR occurs in the visible region of the electromagnetic spectrum. Resonance tuning in a given dielectric environment is achieved by controlling the NP size and shape [165]. For spherical gold NPs in water, e.g., an increase in the NP radius from 10 to 50 nm spectrally shifts the plasmonic resonance wavelength from ∼520 nm to ∼570 nm. Due to increased absorption losses with increasing NP dimension, the red shift of the plasmonic resonance is, however, accompanied by a Q-factor reduction. Therefore, the optical properties of plasmonic NPs made from real metals cannot be tuned independently of each other, which prevents studying the individual impact of the plasmonic resonance wavelength and linewidth on the electromagnetic response of WGMs in a hybrid resonator.

Optical properties and sensitivity of DNPs

To systematically analyze the NP–WGM interaction and provide fundamental insight into processes governing the sensitivity enhancement in hybrid systems, we therefore model the plasmonic NP as an idealized NP made from an artificial metal with Drude-permittivity [57]:

$$\epsilon_{\mathrm{Drude}}(\omega) = 1 - \frac{\omega_{\mathrm{p}}^2}{\omega^2 + i\gamma\omega}. \tag{4.13}$$

Eq. 4.13 describes the optical response of freely moving conduction electrons in the bulk material to an applied time-harmonic electromagnetic field with angular frequency ω.

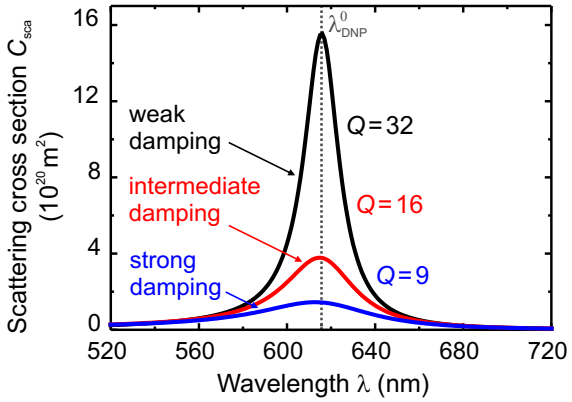

Figure 4.7: Simulated scattering cross section C_{sca} of weakly (black), intermediately (red), and strongly (blue) damped DNPs in air with 25 nm radius and resonance wavelength λ^0_{DNP}=616 nm [166]. Increasing the damping of the DNPs leads to a resonance broadening and a reduced optical response. From the full width at half maximum of the scattering peak, the Q-factors of the DNPs with weak, intermediate, and strong damping are determined to be 32, 16, and 9, respectively.

Damping due to collisions among the free electron is considered via the damping factor γ. $\omega_{\mathrm{p}}=\frac{ne^2}{m_{\mathrm{eff}}\epsilon_0}$ denotes the bulk plasma frequency of a metal with electron density n, electron charge e, effective electron mass m_{eff}, and free space permittivity ϵ_0. Contrary to real plasmonic NPs, the resonance wavelength and linewidth of the plasmonic resonance of a DNP can be tuned independently of each other via the Drude parameters ω_{p} and γ. The possibility to freely tune the spectral position of DNPs over the entire spectral range while keeping the NP dimension and the Q-factor constant makes DNPs ideal candidates to fundamentally study the coupling between plasmonic resonances and WGMs.

To provide insight into the resonant character of DNPs, we calculate their scattering cross section C_{sca} using Mie theory for an isolated sphere in the electrostatic approximation [58]. We consider DNPs with a radius of 25 nm and varying damping factors γ_1=1·10^{14}, γ_2=5·10^{14}, and γ_3=1·10^{15} corresponding to weak, intermediate, and strong damping, respectively. Air (n_{m}=1) is considered as surrounding medium and a plane wave is used to excite the DNPs.
To study the influence of the damping factor on the optical response of DNPs, we show in Fig. 4.7 the scattering cross sections C_{sca} of a weakly (black), an intermediately (red), and a strongly (blue) damped DNP. For better comparability, all three curves are centered around the same wavelength λ=616 nm. Please note that spectral tuning of the plasmonic resonance can be easily achieved by simply varying the Drude parameter ω_{p} without affecting the resonance linewidth. Coupling of the DNP to the incoming light field is seen to result in a Lorentzian-shaped peak in the scattering cross section. Increasing the damping factor γ leads to a resonance broadening and a reduced optical response. At resonance, C_{sca} is proportional to the inverse of the plasmonic resonance linewidth. This behavior corresponds to that of a damped harmonic oscillator driven by an external field and justifies modeling plasmonic NPs as harmonic oscillators – as done in section 4.2. From the

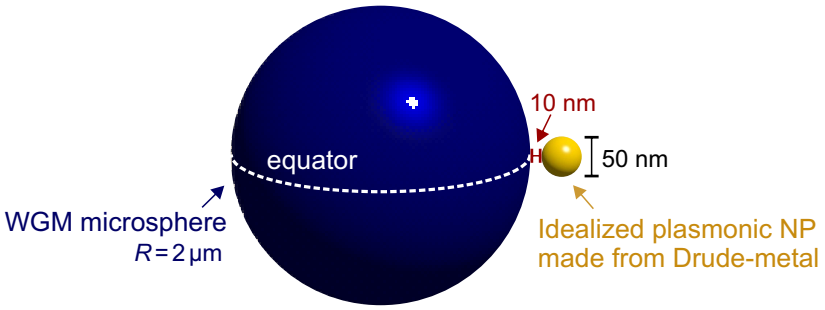

Figure 4.8: Schematic illustration of the idealized hybrid sensor composed of a dielectric WGM microsphere (blue) with 2 µm radius coupled to single idealized plasmonic NP (yellow) with 25 nm radius made from a Drude-metal. For computational reasons, the DNP is located at a 10 nm surface-to-surface distance at the equator of the WGM microsphere (white dashed line) where the fundamental WGMs are localized.

spectral width of the plasmonic resonances shown in Fig. 4.7, the Q-factors of the DNPs with weak, intermediate, and strong damping are determined to be 32, 16, 9, respectively.

To determine the sensitivity of isolated DNPs to slight changes in the background refractive index n_m, we track their resonance wavelengths λ^0_DNP corresponding to the maximum in C_sca while varying n_m. Fitting a linear function to the data $\lambda^0_\mathrm{DNP}(n_\mathrm{m})$ yields a BRIS of ∼300 nm/RIU, which is a factor of ∼5 larger compared to the BRIS of the isolated dielectric microsphere the DNPs will be coupled to.

4.3.3 Optical properties of the idealized hybrid system

To study the NP–WGM interaction, we rigorously simulate the idealized hybrid system composed of a dielectric WGM microsphere with 2 µm radius and refractive index n_R=1.49 coupled to a single DNP with 25 nm radius using the multi-Mie scattering formalism introduced in section 4.3.1. To maximize the mode overlap between WGM and plasmonic resonance and, hence, the NP–WGM coupling strength, the DNP is attached to the equator of the WGM microsphere where the fundamental modes are localized. Due to computation issues, the DNP is not directly attached to the surface of the WGM sphere, but a 10 nm surface-to-surface distance apart, as illustrated in Fig. 4.8.
In the following, we analyze the interaction of a single fundamental WGM with the plasmonic resonance of a DNP. We restrict the discussion to a TM-polarized WGM with the electric field distribution being mainly radial in character, azimuthal mode number m=25, resonance wavelength λ≈616 nm and Q-factor Q≈2400. TE-modes with the electric field pointing in a direction parallel to the sphere surface can be treated in full analogy. Since TE-modes show qualitatively the same functional dependency like TM-modes when coupled to plasmonic NPs, they are not specifically considered here. However, we'd like to point out that compared to TM-modes, TE-modes in spherical resonators show a reduced

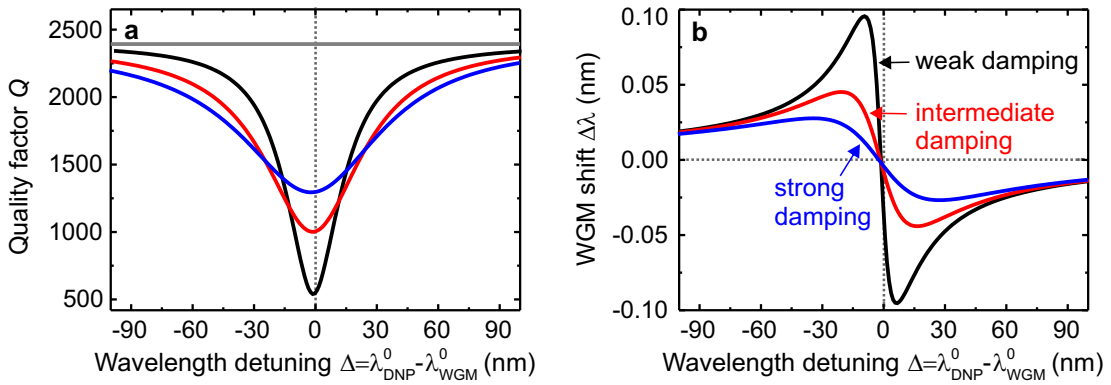

Figure 4.9: Q-factor degradation (a) and resonance wavelength shift $\Delta\lambda$ (b) of a fundamental WGM (m=25) in the investigated microsphere induced upon coupling to a single DNP for different wavelength detunings $\Delta=\lambda^0_{\mathrm{DNP}}-\lambda^0_{\mathrm{WGM}}$ and DNP damping factors [strong (blue), intermediate (red), weak damping (black)] [166]. In line with the predictions from the coupled HO-model, the Q-factor of the hybrid WGM is maximally degraded if the resonance wavelengths of WGM and DNP coincide (Δ=0) and approaches that of an isolated WGM (horizontal gray line) for large absolute detunings. The functional dependency of the induced WGM shift $\Delta\lambda$ on the wavelength detuning Δ and the DNP damping is in excellent qualitatively accordance with the coupled-HO results. DNPs with resonance wavelengths slightly blue detuned from the operational WGM induce a maximal red shift. The higher the Q-factor of the DNP, the larger is the induced WGM shift.

spatial mode overlap with their surrounding. Consequently, effects related to the coupling of NPs are reduced. As in the experiment, where the plasmonic NP is excited via the leakage of the WGM, we model the exciting field in the multi-Mie simulations with the electromagnetic field of the considered WGM itself.
As coupling of a DNP to the WGM sphere breaks the spherical symmetry, the degeneracy of the clock- and counterclockwise propagating WGMs is lifted [41, 167]. For ultra-high-Q WGMs, this effect can give rise to the phenomenon of mode splitting [46]. However, for the underlying hybrid system, broadening of the WGM due to absorption and scattering losses introduced by the lossy DNP exceeds the amount of mode splitting. Therefore, mode splitting cannot be resolved in the investigated system. Instead, coupling of the DNP to the WGM resonator only induces a broadening and a spectral shift of WGMs [168].

In analogy to the analysis presented in section 4.2, we study the optical response of the considered WGM to the coupling to DNPs with varying damping factors γ as a function of the resonance wavelength detuning $\Delta=\lambda^0_{\mathrm{DNP}}-\lambda^0_{\mathrm{WGM}}$ between plasmonic resonance and WGM. To this end, the plasmonic resonance of the DNP coupled to the WGM sphere is spectrally shifted with respect to the WGM while keeping the resonance linewidth of the DNP fixed.
Figure 4.9(a) shows the Q-factor of the hybrid WGM as a function of the wavelength detuning Δ for weakly (black), intermediately (red), and strongly (blue) damped DNPs. The functional dependency of the WGM's Q-factor on the detuning is qualitatively in excellent accordance with the results obtained from the simple HO-model [Fig. 4.4(b)].

As predicted by the HO-model, the Q-factor of the hybrid WGM is maximally degraded for zero resonance wavelength detuning and approaches that of the isolated WGM in the limit of large absolute detunings. Increasing the Q-factor of the plasmonic resonance leads to sharper features in Fig. 4.9(a) and a reduced Q-factor for zero detuning.

To gain further insight into the optical response of the WGM microsphere to the coupling to a single DNP, we plot in Fig. 4.9(b) the WGM wavelength shift $\Delta\lambda{=}\lambda_{\mathrm{HY}}{-}\lambda^{0}_{\mathrm{WGM}}$ induced upon coupling to DNPs with varying damping factors γ as a function of the resonance detuning Δ. λ_{HY} denotes the resonance wavelength of the hybrid WGM.
Comparing the multi-Mie simulation results for the induced WGM shift $\Delta\lambda$ in Fig. 4.9(b) with the corresponding results obtained from the simple HO-model (Fig. 4.5) reveals a perfect qualitative agreement. The dispersive behavior of the induced WGM shift, i.e. its functional dependency on the detuning Δ, is seen to be well reproduced. Depending on the detuning, coupling of the WGM to the DNP shifts the WGM either toward longer or shorter wavelengths. A maximal red (blue) shift of the WGM is observed for DNPs with their plasmonic resonance being slightly blue (red) detuned from the exciting WGM. As predicted by the HO-model, increasing the NP damping lowers the magnitude of the induced WGM shift while simultaneously shifting the maximum and minimum values of $\Delta\lambda$ toward larger absolute detunings. For the DNPs considered here, the induced WGM shifts $\Delta\lambda$ range from $\sim$25 pm in the case of strongly damped DNPs (blue) to $\sim$100 pm for weakly damped DNPs (black).

Combining the results for the induced WGM shift $\Delta\lambda$ with the results for the hybrid system's Q-factor allows identifying two distinct coupling regimes [41].
For zero detuning, the coupling of a DNP to a WGM does not affect the spectral position of the WGM. Instead, coupling to the DNP only leads to a drastic broadening of the WGM, as electromagnetic energy is efficiently transferred from the WGM to the lossy DNP for $\Delta{=}0$. Coupling in this regime can be, therefore, referred to as purely resistive. Away from zero detuning, the coupling of the DNP to the WGM sphere induces a non-vanishing spectral shift whose magnitude and sign is determined by the exact value of the resonance detuning Δ. In this regime, coupling is, hence, not only resistive but also partly reactive. For practical applications of hybrid NP–WGM resonators, e.g. when operated as a biosensor, reactive coupling should dominate over resistive coupling. In line with the results obtained from the HO-model, the above considerations, thus, suggest to operate hybrid NP–WGM resonators at wavelengths slightly red detuned from the plasmonic resonance.

We'd like to note that the multi-Mie simulation results presented here underestimate effects related to the NP–WGM coupling. This is first of all due to the fact that in contrast to experiments, where NPs are directly attached to the WGM sphere surface, the DNPs in the simulations are attached a 10 nm distance apart from the WGM sphere surface. Since the evanescent field of the WGM decays exponentially away from the resonator surface, the increased distance of the DNP to the WGM sphere results in a reduced mode overlap of WGM and NP field and, thus, a reduced coupling strength. Furthermore, treating the DNP coupled to the WGM sphere within an electrostatic approximation additionally leads to reduced values for the NP-WGM coupling strength [169]. Even though the DNP

coupled to the WGM sphere is much smaller than the excitation wavelength, the strong field gradient associated with the rapid fall off of the WGM field away from the resonator surface can lead to a notable decay of the WGM across the DNP [169]. The assumption of a homogeneous field penetrating the DNP is, therefore, only limitedly valid. Omitting higher order multipole contributions is shown in [169] to result in reduced values for the NP-WGM coupling strength.
Both effects combined therefore slightly underestimate the NP–WGM coupling strength. According to section 4.2, however, reducing the coupling strength only leads to a rescaling of the physical quantities related to the NP–WGM coupling, i.e. it lowers the induced WGM shift and the BRIS of the hybrid system. For the purpose of this section, which aims at qualitatively comparing the multi-Mie results with the results from the simple HO-model, it is, hence, sufficient to be aware of these effects.

4.3.4 Sensitivity enhancement in the idealized hybrid system

To check whether the design guidelines derived from the HO-model correctly predict the optimal operation conditions for hybrid NP–WGM sensors, we calculate the BRIS of the hybrid DNP–WGM system in the following as a function of the resonance wavelength detuning Δ using the multi-Mie scattering algorithm.
To this end, the idealized hybrid system is simulated in different dielectric environments with refractive indices between n_{m}=1.0 and n_{m}=1.001 while tracking the resonance wavelength λ_{HY} of the fundamental TE-polarized WGM with mode number m=25. The BRIS of the hybrid WGM is obtained from the resonance wavelength shift induced per change in refractive index unit (RIU). In analogy to the figures presented in section 4.2.3 and to account for the influence of the DNP damping, we plot the BRIS of the hybrid WGM in Fig. 4.10 versus the detuning Δ and for varying DNP damping factors γ. The horizontal grey dashed line in Fig. 4.10 serves as a reference line marking the BRIS of the corresponding WGM supported by the isolated microsphere ($\sim$60 nm/RIU). The comparison with Fig. 4.6 reveals that the simple HO-model captures the main physics of hybrid sensors.
As predicted by the HO-model, the detuning Δ determines whether the coupling of the WGM to the plasmonic resonance leads to an enhancement or a reduction in BRIS. A maximum BRIS enhancement is again observed for WGMs with resonance wavelengths slightly red detuned with respect to the plasmonic resonance. In line with the results obtained from the HO-model, the optimal detuning corresponds to the turning point blue shifted with respect to the maximum in the WGM shift $\Delta\lambda(\Delta)$ with its exact value being determined by the Q-factor of the plasmonic NP. The higher the Q-factors of the plasmonic NPs coupled to the WGM microsphere, the larger is the BRIS enhancement. Whereas the coupling of WGMs to weakly damped DNPs gives rise to strongly pronounced effects in the BRIS of the hybrid system and a maximal increase in BRIS by $\sim$1 nm/RIU (BRIS enhancement of $\sim$1 %), coupling to a strongly damped DNP leads to much less pronounced effects with an almost vanishing positive effect on the BRIS. For zero detuning, the BRIS of the hybrid system exhibits a global minimum and is, hence, maximally reduced compared

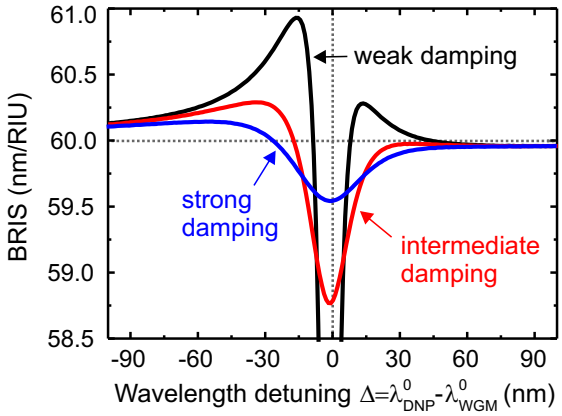

Figure 4.10: Functional dependency of the BRIS of the investigated hybrid DNP–WGM microsphere on the wavelength detuning $\Delta=\lambda^0_{\mathrm{DNP}}-\lambda^0_{\mathrm{WGM}}$ and the damping factor of the DNP [166]. Considered is a fundamental WGM with azimuthal mode number m=25. The BRIS of an isolated WGM in the bare dielectric microsphere is marked by the horizontal dashed line. Depending on the detuning Δ, the BRIS of the WGM sphere is either increased or decreased due to the coupling to the DNP. A maximal increase in BRIS is observed for weakly damped DNPs with resonance wavelengths slightly blue detuned from the WGM. The results are in perfect accordance with the predictions from the coupled HO-model.

to that of the bare dielectric WGM sphere.

Please note that the simulation results for the BRIS of the hybrid DNP–WGM resonator presented in Fig. 4.10 arise from the superposition of two effects discussed in section 4.2.3. First, they consider that the relative detuning between DNP and WGM is altered when changing the background refractive index. The respective contribution to the BRIS was seen to be captured in the detuning term. Second, they consider that the coupling strength between DNP and WGM is simultaneously affected when changing n_{m}. This effect was seen to contribute to the resulting BRIS via the coupling term, whose functional dependency on the detuning could not be derived within the formalism of two coupled HOs. As the detuning term derived from the HO-model was seen to be almost perfectly symmetric with respect to the y-axis Δ=0, the slight asymmetry observed in the multi-Mie simulation results for the BRIS of the hybrid system in Fig. 4.10 might be attributed to contributions from the coupling term.

4.3.5 Summary and conclusions

The multi-Mie simulation results of the optical and sensing properties of the idealized hybrid system composed of a small dielectric microsphere and an artificial plasmonic NP made from a Drude-metal are in excellent accordance with those obtained from the simple HO-model in section 4.2. They, hence, underpin the strength of the simple HO-model in providing a basic and intuitive understanding of the interplay between WGMs and plas-

monic resonances sustained by metallic NPs.
The physical insights obtained from both the HO-model and the multi-Mie simulations of the idealized hybrid sensor system provide general guidelines on how to boost the sensitivity of bare dielectric WGM resonators by exploiting the plasmonic enhancement associated with metallic NPs. In particular, they point up the most relevant design parameters for hybrid sensors and demonstrate that the detuning between plasmonic resonance and exciting WGM together with the Q-factor of the plasmonic resonance play a crucial role when optimizing the performance of a hybrid sensor. High-Q plasmonic NPs with resonance wavelengths slightly blue detuned from the operational WGM wavelength are shown to maximally boost the sensitivity of a WGM resonator when immobilized within the sensing region of a WGM.

Please note that although the multi-Mie simulations presented in this section are capable of quantifying sensitivity enhancement effects, the simulation results cannot be directly transferred to experimental hybrid sensor systems. This is first due to the fact that the plasmonic NPs considered in the idealized hybrid system are made from an artificial metal whose optical properties differ from those of real metals. In particular, as the Q-factors of the considered DNPs exceed those of plasmonic NPs made from, e.g., silver or gold, the predicted sensitivity enhancement is expected to overestimate that encountered in realistic hybrid sensors. Second, the WGM sphere considered in the multi-Mie simulations is considerably smaller than typical WGM resonators employed in experiments (see section 3.1). Keeping the size of the WGM sphere small was, however, indispensable to efficiently simulate hybrid resonators and perform large parameter sweeps. To quantify the BRIS of experimentally relevant hybrid sensor systems and assess the impact of the number density of plasmonic NPs on the BRIS enhancement, numerical simulations of gold-NP-coated polymeric microdisks are performed in the next section.

4.4 Finite-element method simulations of polymeric microdisks coupled to densely packed gold NPs

Motivated by the previous findings, we analyze in this section whether the sensing capability of a state-of-the-art polymeric WGM microdisk (see section 3.1.2) can be notably improved via the coupling to a high number density of randomly distributed plasmonic NPs.
For simplicity and with regard to an easy handling in experiment, we consider spherical gold NPs as the plasmonic component in the hybrid NP–WGM system. Gold is well suited for sensing experiments due to its high chemical stability. Spherically symmetric NPs are selected as their optical response is invariant with respect to the polarization direction of the exciting WGM field. Contrary to anisotropic NP geometries with an intrinsic polarization dependence, this eliminates the need to control the NP orientation relative to the exciting WGM field to ensure an optimal sensing performance.
To simulate the gold-NP-coated microdisks, we rely on an effective medium concept, i.e.

we model the densely packed spherical gold NPs surrounding the WGM microdisk as a layer made from a homogeneous medium with effective properties. "This effective treatment of the layer of metallic NPs allows for an efficient tuning of its properties and is the key to investigate resonator systems with huge NP densities" [170].

After introducing the theoretical and numerical framework to simulate gold-NP-coated microdisks in section 4.4.1, we study in section 4.4.2 the impact of an effective plasmonic shell with moderate gold NP filling fraction on the optical properties of WGMs. We proceed in section 4.4.3 to analyze its impact on the BRIS of the WGM microdisk and extend the discussion to plasmonic shells with higher NP densities. We identify optimal operation conditions and gold NP filling fractions leading to the best sensing performance. In section 4.4.4, we show that ultra-thin homogeneous gold coatings on dielectrics can be mimicked by a random assembly of spherical gold NPs. A summary and concluding remarks are given at the end of the section.

The results presented in this section have been developed in close collaboration with Radius N. S. Suryadharma from the Institute of Theoretical Solid State Physics (TFP). Parts of the results presented in this chapter were published in [170].

4.4.1 Effective medium approach to simulate gold-NP-coated microdisks

In the previous section, it was shown that the coupling of a WGM sustained by a small dielectric WGM microsphere to the plasmonic resonance of a single metallic NP can give rise to the formation of hybrid photonic–plasmonic resonances with superior sensitivity compared to their bare dielectric counterparts. As the analysis was, however, based on an idealized hybrid system with the plasmonic component made from an artificial Drude metal and the dielectric component being much smaller than typical WGM resonators, a direct transfer of the simulation results to realistic sensor systems was not possible.
Although the multi-Mie simulations presented in section 4.3 can be easily adapted to the problem of scattering by a small central dielectric microsphere surrounded by a few plasmonic NPs made from real metals, computational costs grow immensely when increasing the WGM dimension or the number of plasmonic NPs. For WGM resonators with radii on the order of tens of micrometers covered with densely packed plasmonic NPs, solving the scattering problem in a self-consistent manner is, thus, not feasible at all. Therefore, and to include the impact of the NP density on the sensitivity enhancement in hybrid systems, an effective treatment of the NP layer is indispensable.

In the following, we introduce the effective medium approach used to model the layer of densely arranged plasmonic NPs covering the WGM microdisk and detail the technical means to simulate the hybrid microdisk using FEM simulations. We focus on a model hybrid system comprised of a state-of-the-art polymeric WGM microdisk with 25 µm radius, 1.2 µm thickness, and permittivity ϵ_{d}=2.25, surrounded by spherical gold NPs with 25 nm radius, as sketched in Fig. 4.11. Such a hybrid system can be easily implemented using bottom-up approaches which rely on the self-assembly of plasmonic NPs around the

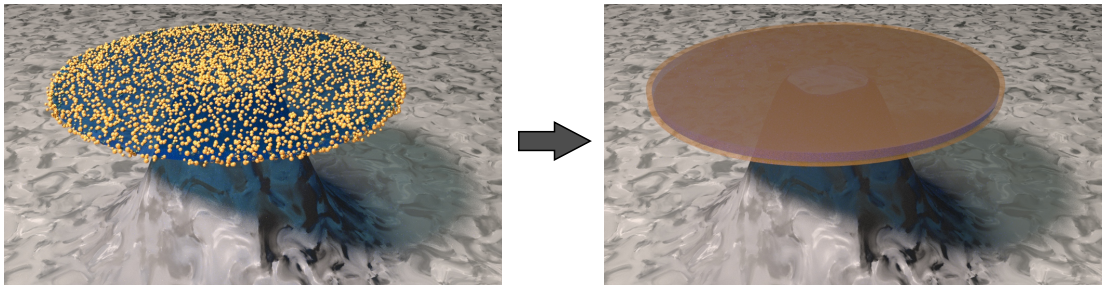

Figure 4.11: Graphical illustration of the effective medium approach to model gold-NP-coated microdisks. The investigated hybrid system consists of a polymeric microdisk covered by randomly distributed and densely packed spherical gold NPs (left). To efficiently simulate the hybrid microdisk, the gold-NP layer is treated at the level of an effective medium and modeled as a homogeneous coating to which effective properties are assigned (right). Taken from [170] and adapted.

dielectric WGM microdisk [171,172]. With regard to the application as sensor, the hybrid system is simulated in water (ϵ_{m}=1.77).

Clausius-Mossotti effective medium theory

To efficiently simulate the optical properties of the hybrid microdisk, we make use of an effective medium approach. To this end, we consider the gold NP layer surrounding the WGM microdisk as a two-component mixture made from identical spherical gold NPs with permittivity $\epsilon_{\mathrm{NP}}(\lambda)$ embedded in water. Since the spherical inclusions are small compared to the wavelength of light, the interaction of the gold NP layer with light can be statistically well described by means of an average dielectric function [58]. Consequently, the random assembly of densely packed gold NPs surrounding the WGM microdisk can be modeled as a homogeneous coating layer made from a medium with effective permittivity $\epsilon_{\mathrm{eff}}(\lambda)$, as graphically illustrated in Fig. 4.11. According to the Clausius-Mossotti effective medium theory, the effective permittivity $\epsilon_{\mathrm{eff}}(\lambda)$ of the NP composite can be calculated from the properties of its constituents, namely the polarizability $\alpha_{\mathrm{NP}}(\lambda)$ of a single spherical gold NP, the background permittivity ϵ_{m}, and the gold NP filling fraction f [173]:

$$\epsilon_{\mathrm{eff}}(\lambda) = \epsilon_{\mathrm{m}} \frac{3 + 2f\alpha_{\mathrm{NP}}(\lambda)}{3 - f\alpha_{\mathrm{NP}}(\lambda)}, \tag{4.14}$$

where f is defined as the number of gold NPs per unit volume. To fully include absorption and scattering losses associated with the individual lossy gold NPs in the effective plasmonic shell, we calculate the polarizability $\alpha_{\mathrm{NP}}(\lambda)$ of a single spherical gold NP not in the quasi-static approximation, but directly from Mie theory [174]:

$$\alpha_{\mathrm{NP}}(\lambda) = \frac{\sqrt{12\pi}i}{cZk} \frac{\eta^2 j_l(\eta x)[x l_1(x)]' - j_l(x)[\eta x j_l(\eta x)]'}{j_l(\eta x)[x h_l^{(1)}(x)]' - h_l^{(1)}(x)[\eta x j_l(\eta x)]'}. \tag{4.15}$$

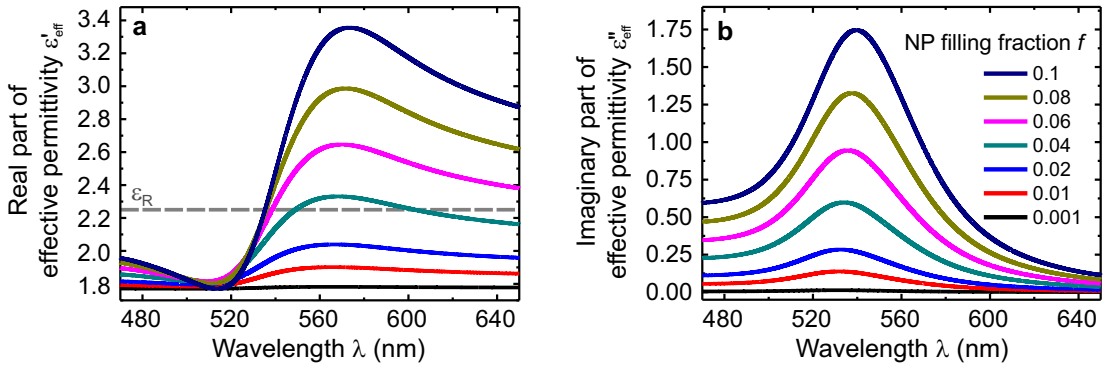

Figure 4.12: Dependency of the real (a) and imaginary parts (b) of the complex effective permittivity ϵ_{eff} of a homogeneous medium made from spherical gold NPs with 25 nm radius embedded in water (ϵ_{m}=1.77) on the wavelength λ and the NP filling fraction f [174]. The real and imaginary parts of the effective permittivity exhibit a strong Lorentzian dispersion around the plasmonic resonance of a single gold NP in water (λ^0_{Au}=538 nm). Adjusting the gold NP filling fraction allows to efficiently and widely tune the effective permittivity. The horizontal gray dashed line marks the permittivity of the resonator material (ϵ_{R}=2.25). Taken from [170] and adapted.

Z denotes the background impedance, k the wavenumber in the surrounding medium, and c_0 the speed of light in vacuum. j_l and $h_l^{(1)}$ are the first-order spherical Bessel and Hankel functions of first kind [175], $\eta=\sqrt{\epsilon_{\text{NP}}/\epsilon_{\text{m}}}$, and $x=\omega/c_0\sqrt{\epsilon_{\text{m}}}R$, where ω denotes the angular frequency. The prime denotes the differentiation with respect to the argument inside the Bessel and Hankel functions.

We'd like to mention that the predictions of the Mie simulations regarding the spectral response of a single gold NP strongly depend on the plugged-in dielectric function for gold [176]. We use in the simulations bulk values for the gold permittivity determined experimentally by Johnson and Christy [177] and, thus, neglect size-dependent corrections to the dielectric function arising from enhanced electron-surface collisions in small NPs [176, 178, 179]. Finite size effects become significant if the size of the NP is smaller or comparable to the electron mean free path being 42 nm in gold [180] and translate to an increased imaginary part of the gold permittivity. Since the size of the considered gold NP is slightly larger than the mean free path of the conduction electrons, the simulation results for the optical response of a WGM and the sensitivity enhancement presented in the following sections can be considered as an upper bound.

Optical properties and tunability of effective plasmonic shell

To get insight into the optical properties of plasmonic shells made from spherical gold NPs and to demonstrate that the respective effective permittivity can be efficiently tuned by varying the gold NP filling fraction, we plot in Fig. 4.12(a) the real and imaginary parts (b) of the effective permittivity of plasmonic shells with varying NP filling fractions

f versus the wavelength λ. The plasmonic resonance wavelength λ^0_{Au} of a single gold NP with 25 nm radius in water is spectrally located at a wavelength of 538 nm, as determined from the respective scattering cross section.
Both the real part $\epsilon'_{\mathrm{eff}}(\lambda)$ and the imaginary part $\epsilon''_{\mathrm{eff}}(\lambda)$ of the effective permittivity possess a Lorentzian dispersion around the plasmonic resonance associated with the single gold NP. The larger the NP filling fraction in the effective plasmonic shell, the stronger is the dispersion in the real part and the larger are the absorption and scattering losses in the shell, which are encoded in the imaginary part of the effective permittivity. In the limit of a vanishing NP filling fraction, the real part of the effective permittivity approaches the constant background permittivity ϵ_{m}=1.77. For larger NP filling fractions, $\epsilon'_{\mathrm{eff}}(\lambda)$ is modulated on top of the background permittivity with a local minimum (maximum) slightly blue (red) shifted from the plasmonic resonance wavelength of the single gold NP. Please note that the real part of the effective permittivity of plasmonic shells with NP filling fractions above $f{\approx}0.04$ ($\sim$30 NPs/µm^2) exceeds that of the polymeric microdisk (horizontal grey dashed line) on the long-wavelength side of the plasmonic resonance.
The results plotted in Fig. 4.12 show that the effective permittivity of the plasmonic shell wrapping the dielectric WGM microdisk can be efficiently and widely tuned by simply adjusting the NP filling fraction.

Contrary to the artificial Drude-metal NPs considered in section 4.3, the optical response of spherical gold NPs to an external excitation deviates from a perfect Lorentzian. This is due to the fact that in addition to free electrons also interband transitions connected with the oscillation of bound electrons significantly contribute to the dielectric function of gold for wavelengths below 650 nm [181]. Such additive contributions to the dielectric function of gold arise on the one hand from the excitation of electrons from the top of the d band to states above the Fermi level in the conduction band. These transitions lead to modifications in the dielectric function of gold in the visible at wavelengths λ<516.6 nm. On the other hand, energetic-lower lying transitions from the 5d-band to unoccupied states in the 6sp-band above the Fermi energy give rise to additive contributions in the red spectral region below λ=688.8 nm [176]. Both interband contributions lead to a deviation of the gold NP's scattering response from a perfect Lorentzian and are furthermore responsible for spectrally shifting the plasmonic resonance into the visible.

FEM simulations of hybrid microdisks

Treating the large number of gold NPs attached to the surface of the WGM microdisk at the level of an effective medium allows to efficiently simulate the optical properties and the sensing capabilities of the hybrid system. Since rotational symmetry is preserved when modeling the densely packed NPs as a homogenous coating with an effective permittivity, numerically efficient 2D simulations of the hybrid system can be performed.
To compute the eigenmodes of the hybrid microdisk and determine its optical and sensing properties, we perform FEM simulations using the commercially available software package JCMsuite [182]. The provided eigenmode solver allows to directly compute the resonance

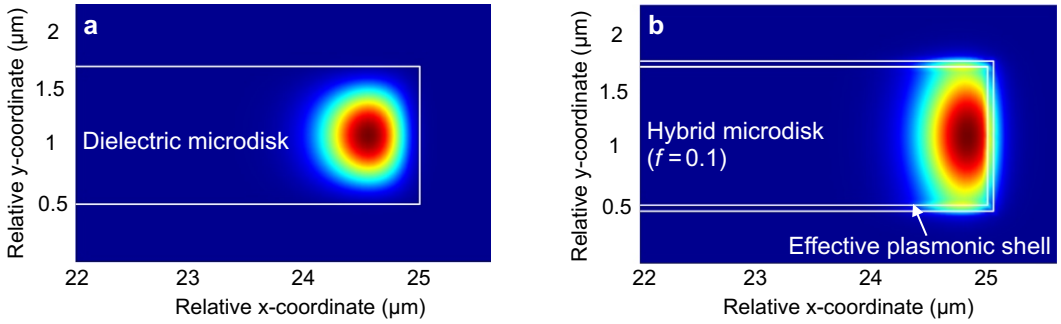

Figure 4.13: Impact of an effective plasmonic shell on the WGM field distribution in microdisks. Cross-sectional electric field intensity distributions of fundamental TE-modes (m=392) sustained by a bare microdisk (a) and a microdisk wrapped by a plasmonic shell with gold NP filling fraction f=0.1 (∼80 NPs/μm^2) (b). Due to the presence of the effective plasmonic coating, the WGM is pushed further toward the resonator rim. The resulting increased mode overlap with the surrounding is responsible for the sensitivity enhancement in hybrid microdisks. (b) taken from [170].

frequency and linewidth of a hybrid mode from its complex eigenfrequency ω=ω'+$i\omega''$, which is the simulation output. The resonance frequency is given by the real part ω' of the complex eigenfrequency, the linewidth by its imaginary part ω''. From the real and imaginary parts of ω the Q-factor of the eigenmode can be calculated according to:

$$Q = \frac{\omega'}{2\omega''}. \tag{4.16}$$

To illustrate the effect of the effective plasmonic coating on the WGM field distribution, we show in Fig. 4.13 the cross-sectional electric field intensity distributions of fundamental TE-modes (m=392) sustained by a bare microdisk (a) and a hybrid microdisk with gold NP filling fraction f=0.1 (∼80 NPs/μm^2) (b). The white double line in Fig. 4.13(b) marks the boundary of the plasmonic shell wrapping the dielectric microdisk. The thickness of the plasmonic shell is 50 nm and corresponds to the diameter of a single gold NP. The plasmonic shell wrapping the microdisk is seen to effectively push the WGM further toward the outer rim of the microdisk, thus, increasing the spatial overlap of the WGM with the surrounding. This effect is responsible for the sensitivity enhancement encountered in gold-NP-coated microdisks (see section 4.4.3).

We want to stress at this point that the effective medium approach presented in this section is not capable of describing the phenomenon of mode splitting. The deposition of plasmonic NPs onto the microdisk surface introduces coupling between initially degenerate clockwise and counterclockwise propagating WGMs which causes mode splitting if the coupling is strong enough. To exclude that mode splitting plays a role in the current system and to justify using the effective medium theory to model the gold NPs around the WGM microdisk, we performed basic back-of-the-envelope calculations [121, 168]. From these calculations, we inferred that the linewidth broadening due to absorption and scattering losses brought into the system by the lossy gold NPs exceeds the amount of mode splitting.

Since linewidth broadening is the dominant effect, mode splitting cannot be resolved in the investigated parameter regime and the effective medium approach is, hence, well suited to describe the coupling between WGMs and huge numbers of spherical gold NPs.

Verification of the effective medium approach

In the following, we verify using the Clausius-Mossotti effective medium theory to model the randomly distributed gold NPs surrounding the WGM microdisk and discuss its scope of application.
The Clausius-Mossotti relation is well known to be valid only for NP filling fractions much smaller than unity, i.e. for $f \lesssim 0.15$ [183, 184]. Above a certain NP filling fraction, coupling between neighboring NPs becomes significant, giving rise to anisotropic effects if the NPs are arranged in a monolayer [184, 185]. As a result of the absence of coupling partners in the direction perpendicular to the plane of the gold NPs, electromagnetic interparticle interactions in densely packed NP monolayers become strongly dependent on the polarization direction of the incident light [185]. This effect related to a geometrical anisotropy cannot be described with the Clausius-Mossotti effective medium theory.

To demonstrate that anisotropy effects play, however, a negligible role for the NP filling fractions considered in this section and to ensure that the effective medium treatment accurately describes the physics showing up in the considered hybrid microdisks, we compare in the following simulation results of a hybrid WGM resonator obtained from the effective medium approach with those obtained from exact calculations based on multi-Mie theory [186].
As discussed above, a rigorous simulation of the investigated hybrid microdisks is not feasible due to the large resonator size and the high number density of gold NPs immobilized on the microdisk surface. Thus, for reasons of comparability, we consider in the following the largest possible hybrid system we can simulate using the multi-Mie scattering formalism, which is a spherical polymeric WGM resonator with 1.5 µm radius (ϵ_d=2.25) surrounded by 248 randomly distributed spherical gold NPs with 25 nm radius. This number of gold NPs translates to a NP filling fraction of f=0.011 and is close to the NP filling fractions considered throughout this section. For the simulations based on an effective medium approach, we therefore model the 248 gold NPs as a 50 nm thick homogeneous layer enclosing the WGM microsphere with an effective permittivity defined by Eq. 4.14 using f=0.011. Simulations of the hybrid system are performed in two different dielectric environments (ϵ_m=1.0 and ϵ_m=1.014). The simulations consider that changing the background refractive index spectrally shifts the plasmonic resonance of a single gold NP and, hence, alters the material properties of the plasmonic shell.
To include the role of possible anisotropy effects, we excite the hybrid WGM microsphere in both simulation approaches with two polarizations, namely TE- and TM-polarized WGMs with mode number m=18, and compare their scattering response. The simulation results for the scattered power of the TE-mode and the TM-mode are plotted in Fig. 4.14(a) and Fig. 4.14(b), respectively, as a function of the wavelength λ for two different back-

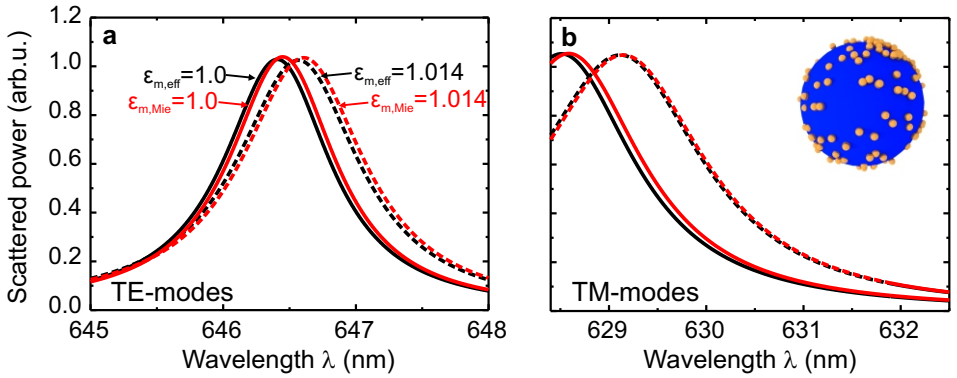

Figure 4.14: Verification of the effective medium approach. Scattered power of TE- (a) and TM-modes (b) with azimuthal mode number m=18 supported by a dielectric microsphere (ϵ_R=2.25) with 1.5 µm radius surrounded by 248 randomly distributed gold NPs with 25 nm radius (see inset) [186]. The red curves are obtained by rigorously simulating the hybrid microsphere using exact calculations based on multi-Mie theory, the black curves are obtained by treating the gold NPs at the level of an effective medium (f=0.011). Simulations are performed in two different dielectric environments [ϵ_m=1.0 (solid curves) and ϵ_m=1.014 (dashed curves)]. The excellent accordance between both simulation approaches and both polarizations demonstrates that the effective medium approach accurately describes the hybrid system. Taken from [170] and adapted.

ground permittivities ϵ_m=1.0 (solid line) and ϵ_m=1.014 (dashed line). The black curves in Fig. 4.14 correspond to results obtained by treating the gold NPs surrounding the WGM microsphere at the level of an effective medium, the red curves are obtained from the exact calculations based on multi-Mie theory. From Fig. 4.14 an excellent accordance between both simulation approaches and both polarizations is obvious.
The slight differences in the spectral position of the WGMs (maxima in scattered power) for the two distinct simulation approaches is a result of the averaging nature of the effective medium theory. In the exact calculation based on the multi-Mie scattering formalism each constituent in the cluster is described individually. The simulation outcome, therefore, depends on the exact spatial arrangement of the spherical gold NPs in the cluster. Slight modifications in the configuration of the NPs in the hybrid cluster, thus, lead to slightly different eigenfrequencies of the considered WGM. In contrast, when treating the gold NPs surrounding the WGM sphere at the level of an effective medium, one merely averages over all possible NP configurations and does not consider the exact structure of the hybrid system. Therefore, and due to the fact that we considered only one particular NP arrangement in the exact Mie calculations, it is obvious that the resonance curves in Fig. 4.14 slightly differ for both simulation approaches.
In the light of these facts, the effective medium approach can be considered as a powerful tool to describe experimental systems containing randomly distributed NPs. Such random distributions result, in particular, when depositing NPs via self-assembly techniques onto the surface of dielectrics. As the exact arrangement of the NPs in such systems is mostly unknown and as the effective medium theory accounts exactly for this situation, it is justified and furthermore obvious to treat the random assembly of gold NPs at the level of

an effective medium.
To underpin the validity of the effective medium treatment even further, we additionally compare the BRIS values of the considered TE- and TM-modes in the hybrid system obtained from both simulation approaches. The BRIS of a particular WGM is deduced from the spectral shift of the respective maximum in the scattered power in Fig. 4.14 induced upon changing the background refractive index. From the exact calculations using multi-Mie theory, we so obtain BRIS values of 21 nm/RIU for the TE-mode, and 83 nm/RIU for the TM-mode. The simulations based on the effective medium approach yield the same value for the BRIS of the TE-mode. The BRIS of the TM-mode is with 85 nm/RIU slightly larger (less than 3%) compared to the value obtained from the exact calculation. Nevertheless, the accordance for the BRIS values obtained from both simulation approaches and polarizations is excellent and, thus, confirms the validity of the effective medium treatment.

The above analysis shows that the simulations based on the effective medium approach accurately describe the optical response and the sensitivity for both TE- and TM-modes. Therefore, coupling between neighboring gold NPs is negligible for the comparatively low NP filling fraction considered here and we can safely exclude that anisotropy effects play a notable role in the parameter regime investigated in this work. Very good agreement between both simulation approaches can be expected up to NP filling fractions f=0.15 [183] which is larger than the highest NP filling fraction considered in this section.

4.4.2 Optical properties of gold-NP-coated microdisks

Having set the theoretical framework to simulate hybrid microdisks with large numbers of randomly distributed gold NPs, we investigate in this section the optical response of WGMs to the presence of an effective plasmonic shell with moderate NP filling fraction f=0.023 corresponding to a NP surface density of approximately $\sim$19 NPs/µm^2.

To this end, we calculate the Q-factor degradation and the WGM shift induced upon coupling to the plasmonic shell as a function of the wavelength detuning $\Delta=\lambda^0_{\mathrm{Au}}-\lambda^0_{\mathrm{WGM}}$ between the plasmonic resonance wavelength λ^0_{Au} of the plasmonic shell and the resonance wavelength λ^0_{WGM} of the exciting WGM sustained by the bare dielectric microdisk. The wavelength detuning is implemented in the FEM simulations by varying the operational wavelength with respect to the plasmon resonance wavelength. For this purpose, fundamental WGMs of varying azimuthal mode numbers m with resonance wavelengths between 470 nm and 650 nm are used to evanescently excite the plasmonic shell. The range of operation wavelengths is chosen to fully cover the plasmonic resonance. For reasons already discussed in 4.3.3, we focus on fundamental WGMs with the electric field being polarized in the plane of the microdisk, i.e. TE-modes.
On the basis of Fig. 4.15, which shows the Q-factor (red curve) of hybrid WGMs of different azimuthal mode numbers together with the respective resonance wavelength shift $\Delta\lambda$ (black curve) induced upon coupling to the plasmonic shell for different detunings Δ, we closer examine the interaction of WGMs with the plasmonic resonance of the shell

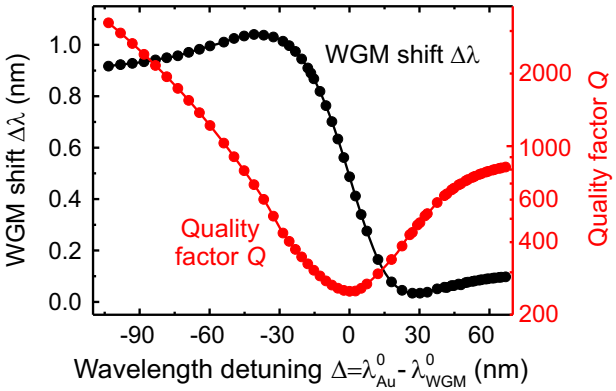

Figure 4.15: Optical response of fundamental TE-modes in the investigated microdisk to the presence of a plasmonic shell with gold NP filling fraction f=0.023 for different wavelength detunings $\Delta=\lambda^0_{\mathrm{Au}}-\lambda^0_{\mathrm{WGM}}$. Both the Q-factor (red) and the resonance wavelength shift $\Delta\lambda$ (black) of a WGM induced upon coupling to the plasmonic shell strongly depend on the detuning Δ. Strong resistive coupling for Δ=0 maximally degrades the Q-factor. A maximal WGM red shift is predicted for WGMs with resonance wavelengths slightly red detuned from the plasmonic resonance. Published in [170] in a different form.

material. The induced WGM shift $\Delta\lambda$ is determined from the difference in the resonance positions of a WGM after and before introducing the plasmonic shell wrapping the polymeric microdisk. As expected from the fundamental studies on the NP–WGM interaction in sections 4.2 and 4.3, both the Q-factor of the hybrid modes and the induced WGM shift $\Delta\lambda$ strongly depend on the resonance detuning Δ. Their functional dependency on the detuning agrees qualitatively well with the predictions from the HO-model and the multi-Mie simulations of an idealized hybrid system.

From Fig. 4.15 we see that the coupling of WGMs to the plasmonic shell strongly reduces their Q-factors. Whereas simulated Q-factors of WGMs supported by the bare polymeric microdisk are on the order of 10^7, they are reduced by more than four orders of magnitude due to the presence of the plasmonic shell. The strong reduction in Q-factor is a result of the large imaginary part of the effective permittivity of the plasmonic shell in the considered wavelength range [see Fig. 4.12(a)]. As dielectric losses can be neglected compared to plasmonic losses and as the radiation-limited Q-factor is orders of magnitude larger than the respective metal-loss limited Q-factor Q_{plasmon}, the total Q-factor of the hybrid microdisk is metal-loss-limited ($Q^{-1}\approx Q^{-1}_{\mathrm{plasmon}}$).
In accordance with the results from the HO-model and the multi-Mie simulations of idealized DNP-WGM resonators, the strongest Q-factor degradation is observed for operational WGM wavelengths close to the plasmonic resonance. Due to strong resistive coupling in this regime, Q-factors are reduced to values below 300. Contrary to the predictions from the simplified models, the Q-factor of the hybrid microdisk is asymmetric with respect to Δ=0. For large absolute detunings, the Q-factors of WGMs with resonance wavelengths blue detuned from the plasmonic resonance (Δ>0) experience a stronger degradation as

compared to red detuned WGMs ($\Delta<0$). According to the discussion in section 4.4.1, this asymmetry in the spectral response can be traced back to the contribution of interband transitions to the optical properties of gold [181]. Since their contribution to the effective permittivity of the plasmonic shell is stronger for wavelengths on the short-wavelength side of the gold NP resonance compared to the long-wavelength side, WGMs with resonance wavelengths blue detuned from the plasmonic resonance experience a stronger damping compared to red detuned WGMs.

Whereas the Q-factor of the hybrid modes is mainly determined by the imaginary part of the effective permittivity of the plasmonic shell, the functional dependency of the induced WGM shift $\Delta\lambda$ on the detuning Δ is governed by the dispersive character of the real part of the effective permittivity. This can be understood as follows: The larger the real part of the effective shell permittivity, the further the WGM is pushed toward the rim of the microdisk. As the plasmonic shell is, however, only 50 nm thick, this simultaneously leads to an increased spatial overlap of the WGM with the surrounding, resulting in a reduced effective refractive index of the considered WGM. Therefore, increasing the real part of the effective permittivity of the plasmonic shell spectrally shifts the WGM toward longer wavelengths [187]. From the comparison between Fig. 4.15 and Fig. 4.12(a) it is, hence, obvious why WGMs red detuned with respect to the plasmonic resonance ($\Delta<0$) experience larger spectral shifts compared to blue detuned WGMs ($\Delta>0$). In accordance with the results from the simple HO-model and the multi-Mie simulations, the maximal red shift of a WGM ($\Delta\lambda_{\mathrm{max}}\approx 1$ nm) is observed when operating the hybrid system at slight negative detunings ($\Delta\approx -40$ nm) for which $\epsilon'_{\mathrm{eff}}(\lambda)$ is close to its maximal value.
Please note that the coupling of WGMs to the plasmonic shell in the present system shifts the WGMs always toward longer wavelengths – independently of the detuning. This observation is not in compliance with the results from the HO-model and the multi-Mie simulations with idealized plasmonic NPs, which predict a blue shift of WGMs for positive detunings. This discrepancy can be, again, attributed to the specific material properties of gold. In contrast to the idealized DNPs, where only free-electrons contribute to the metal's optical properties, the additional contributions of interband transitions to the optical properties of gold NPs effectively cause a red shift of the WGMs which superimposes the negative effect on the WGM shift caused by the free electrons in gold. For wavelengths below the plasmon resonance of gold, this combined effect results in an overall red shift of the WGMs.

Combining the simulation results for the induced WGM shifts and the Q-factors of the hybrid WGMs implies operating the gold-NP-coated microdisk at wavelengths slightly red detuned with respect to the plasmonic resonance of a single gold NP. This result is the outcome of balancing between resistive effects causing linewidth broadening and reactive effects causing WGM shifts. It is in excellent accordance with the predictions from the HO-model (section 4.2) and the multi-Mie simulations of an idealized hybrid system considering artificial plasmonic NPs made from a Drude-metal (section 4.3). Although the simplified models are seen to correctly describe relevant aspects of the NP–WGM interaction, the simulations of the realistic hybrid system presented in this section show the importance of

considering the optical properties of real metals to fully describe and quantify the optical response of WGMs to the coupling to plasmonic NPs.

4.4.3 Sensitivity enhancement in gold-NP-coated microdisks

In the following, we analyze to which extent the sensitivity of a bare dielectric microdisk can be increased by covering it with an effective plasmonic shell made from a huge number of randomly distributed gold NPs.
We first consider the hybrid microdisk introduced above with a fixed, moderate gold NP filling fraction f=0.023 and analyze the functional dependency of its BRIS on the resonance wavelength detuning $\Delta=\lambda^0_{\mathrm{Au}}-\lambda^0_{\mathrm{WGM}}$. The analysis aims to identify optimal operational conditions for hybrid microdisk sensors. Based on these findings, we then investigate the impact of the gold NP filling fraction in the plasmonic shell on the achievable BRIS enhancement in hybrid microdisks. For this purpose, FEM simulations of hybrid microdisks with varying NP filling fractions ranging from f=0.001 ($\sim$1 NP/µm^2) up to f=0.1 ($\sim$80 NPs/µm^2) are performed. We demonstrate that the strong Q-factor degradation of the hybrid modes with increasing number density of gold NPs effectively counteracts the sensitivity gain and, hence, ultimately limits the sensing performance of gold-NP-coated microdisks.

Impact of resonance wavelength detuning on sensitivity enhancement in hybrid microdisks

To illustrate the impact of the operational WGM wavelength on the BRIS of hybrid microdisks, we plot in Fig. 4.16(a) the BRIS of WGMs with different azimuthal mode numbers m supported by the model hybrid microdisk with NP filling fraction f=0.023 (red dotted line) against the resonance wavelength detuning Δ. The BRIS values of the corresponding WGMs in the bare dielectric microdisk (black dotted line) serve as reference. The BRIS of a particular WGM is calculated by tracking its resonance wavelength while increasing the background permittivity stepwise from ϵ_{m}=1.77 to ϵ_{m}=1.78. Changes in the effective permittivity of the plasmonic shell when altering the dielectric environment are considered in each simulation step.
As expected from both the HO-model and the multi-Mie simulations with idealized plasmonic NPs, the BRIS of the hybrid microdisk is modified over the BRIS of its bare dielectric counterpart. Depending on the resonance detuning Δ, coupling to the plasmonic shell either increases or decreases the BRIS of a particular WGM.
To quantify the BRIS enhancement due to the presence of the effective plasmonic shell, we introduce the dimensionless BRIS enhancement factor η, defined as the ratio of the BRIS of a hybrid WGM to the BRIS of the corresponding isolated WGM. This factor corrects for the monotonic increase in BRIS of isolated WGMs with increasing wavelength. Plotting the BRIS enhancement factor η for the investigated hybrid microdisk in Fig. 4.16(b)

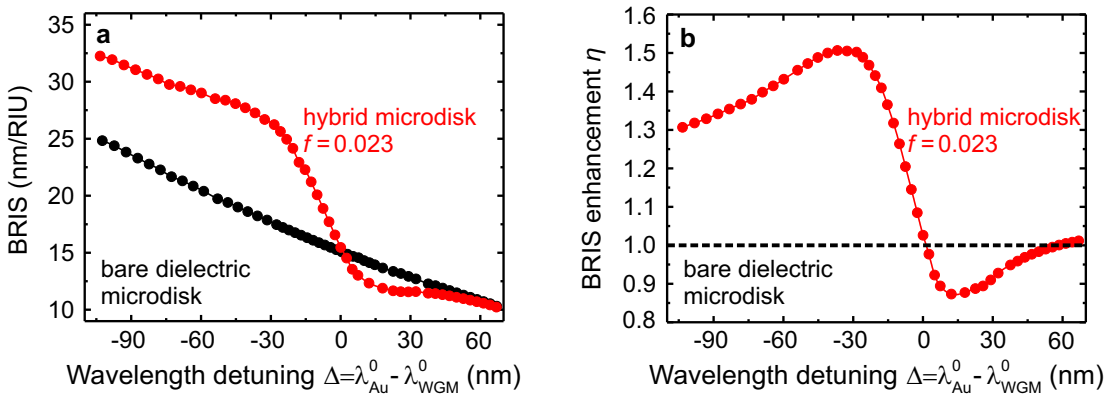

Figure 4.16: Sensitivity enhancement in a hybrid microdisk with gold NP filling fraction f=0.023. (a) Functional dependency of the BRIS of the hybrid microdisk (red) and the corresponding bare microdisk (black) on the resonance wavelength detuning $\Delta=\lambda^0_{\mathrm{Au}}-\lambda^0_{\mathrm{WGM}}$. (b) The ratio of the BRIS of a hybrid WGM to the BRIS of the corresponding isolated WGM defines the BRIS enhancement factor η. Due to an optimal balance between linewidth broadening and sensitivity gain, the BRIS of the hybrid microdisk is maximally enhanced over its bare dielectric counterpart (black dashed line) for a detuning $\Delta\approx-36$ nm. Published in [170] in a different form.

against the resonance wavelength detuning Δ (red dotted line), thus, allows to isolate the net effect of the coupling between WGM and plasmonic shell on the sensitivity enhancement. The black dashed line represents the case of a bare dielectric microdisk (η=1).
In accordance with the predictions from the HO-model (see Fig. 4.6) and the multi-Mie simulations of an idealized hybrid system (see Fig. 4.10), coupling of a WGM with same resonance wavelength as the plasmonic shell does not alter the BRIS. Although the sensitivity of the plasmonic shell is in itself maximal when excited directly at its resonance, strong resistive coupling at zero detuning counteracts the potential sensitivity gain. Away from zero detuning, coupling of WGMs with resonance wavelengths red (blue) detuned with respect to the plasmonic resonance enhances (reduces) the BRIS of the hybrid microdisk over its bare dielectric counterpart. The maximum enhancement in BRIS (η=1.5) is predicted for slight negative detunings $\Delta\approx-36$ nm. This detuning value defines the optimal operation wavelength for the hybrid microdisk when used as bulk refractive index sensor and corresponds to approximately half the plasmonic resonance linewidth.

Superiority of plasmonic shell over all-dielectric high-index coating in sensing applications

Before analyzing the role of the gold NP filling fraction on the BRIS of hybrid microdisks, we'd like to emphasize that covering the polymeric microdisk with an effective plasmonic shell outperforms a comparable system where only a thin high-index dielectric film is deposited onto the microdisk surface.
The reason for this is as follows: In the case of a bare lossless dielectric coating, only the spectral position of a WGM is altered when changing the background permittivity.

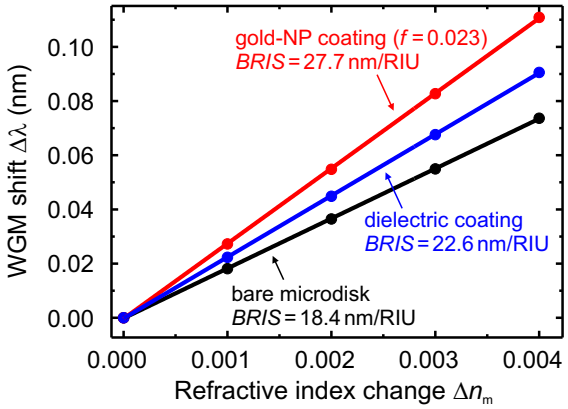

Figure 4.17: Simulated WGM wavelength shift $\Delta\lambda$ of a TE-mode (m=392) induced by changes Δn_m in the background refractive index for a gold-NP-coated microdisk with NP filling fraction f=0.023 and effective permittivity ϵ_eff=1.7975+0.0097i (red) and a microdisk with comparable high-index dielectric coating with permittivity ϵ_diel=1.7975 (blue). The simulation results for a bare microdisk without any coating serve as reference (black). The slope of a linear function fitted to the simulation results yields the respective BRIS values. Covering the microdisk with an effective plasmonic shell outperforms a comparable system with a high-index dielectric coating.

The material properties of the resonator system itself remain unaltered. In the case of a microdisk covered with an effective plasmonic shell, the material properties of the coating depend, however, also on the dielectric environment. Altering the refractive index of the surrounding medium, hence, affects both the spectral position of a WGM and the material properties of the resonator system.

To demonstrate that both effects combined lead to a superior sensing performance, we compare the BRIS of the model hybrid microdisk with gold NP filling fraction f=0.023 with the BRIS of a comparable bare dielectric system for which the plasmonic shell is replaced by a lossless high-index dielectric coating of same thickness. For optimal comparability, the real part of the bare dielectric coating is chosen such that it equals the real part of the effective permittivity of the plasmonic shell (ϵ'_eff=1.7975). To ensure an optimal sensing performance of the hybrid microdisk, we consider in the FEM simulations a TE-polarized WGM with mode number m=392 corresponding to the optimal detuning $\Delta\approx-36$ nm.

Figure 4.17 depicts the simulation results for the WGM wavelength shift $\Delta\lambda$ induced upon changing the background refractive index n_m for the hybrid microdisk (f=0.023) with effective permittivity ϵ_eff=1.7975+0.0097i (red) and the microdisk with comparable high-index dielectric coating (blue). The simulation result for a bare dielectric microdisk without any coating is depicted in black and serves as reference. The BRIS-values for the considered resonators are deduced from the slope of a linear function fitted to the simulation results. The BRIS of the hybrid microdisk (27.7 nm/RIU) is seen to exceed the BRIS of a bare dielectric microdisk with lossless high-index dielectric coating (22.6 nm/RIU) by more than 20%, which demonstrates the superior sensing performance of the microdisk

with effective plasmonic coating.

Impact of gold NP filling fraction on sensitivity enhancement in hybrid microdisks

The simulation results for the BRIS of the model hybrid microdisk with a plasmonic shell of fixed gold NP filling fraction presented above showed that the operation wavelength must be deliberately chosen to notably enhance its BRIS over that of a bare dielectric microdisk. Exciting the plasmonic shell evanescently with WGMs red detuned ($\Delta\approx-36\,\mathrm{nm}$) with respect to the plasmonic resonance was seen to result in a maximal sensitivity enhancement of $\sim$1.5. The BRIS enhancement was, however, at the cost of a strongly degraded Q-factor. As the key performance parameters for sensing, namely the Q-factor and the BRIS of the hybrid modes, are expected to critically depend also on the gold NP filling fraction, we calculate both quantities in the following for a large range of NP filling fractions between f=0.001 ($\sim$1 NP/µm^2) and f=0.1 ($\sim$80 NPs/µm^2) to identify optimal sensor design parameters.
Whereas the BRIS of a hybrid mode is expected to increase monotonically with increasing gold NP filling fraction due to the larger real part of the effective permittivity [see Fig. 4.12(a)], its Q-factor is expected to decrease with increasing NP filling fraction due to the larger imaginary part of the effective permittivity [see Fig. 4.12(b)]. These opposing trends in the key parameters for sensing, thus, require balancing between high sensitivity on the one hand and high spectral resolution on the other hand. On the basis of Fig. 4.18, which depicts the FEM simulation results for the Q-factor (red triangles) and the BRIS (red solid line) of a hybrid microdisk as a function of the NP filling fraction f, we present in the following a strategy on how to identify the optimal gold NP filling fraction leading to the best sensing performance. We consider hybrid microdisks of fixed geometry and use again TE-polarized WGMs with mode number m=392 corresponding to the optimal detuning $\Delta\approx-36\,\mathrm{nm}$ to excite the plasmonic shells.
As expected, the BRIS of the considered WGM in the hybrid microdisk increases monotonically with increasing NP filling fraction, whereas its Q-factor decreases rapidly with increasing f. For the lowest gold NP filling fraction considered here (f=0.001), the optical properties of the plasmonic shell are almost constant over the entire spectral region and close to that of the surrounding medium [see Fig. 4.12(a)]. Both the Q-factor and the BRIS of the hybrid WGM are close to that of a WGM supported by a bare dielectric microdisk. With increasing NP filling fraction f, the real part of the effective permittivity of the plasmonic shell is increased compared to the background permittivity and finally exceeds the permittivity of the polymeric resonator material for f>0.04 (grey dashed horizontal line in Fig. 4.14). As a consequence, the WGM is pushed further toward the resonator edge, resulting in an increased mode overlap with the surrounding and an increased BRIS. For the highest NP filling fraction considered here (f=0.1), a sensitivity enhancement by almost half an order of magnitude over the BRIS of the bare dielectric microdisk is predicted. The beneficial effect of the sensitivity enhancement due to an increased number of

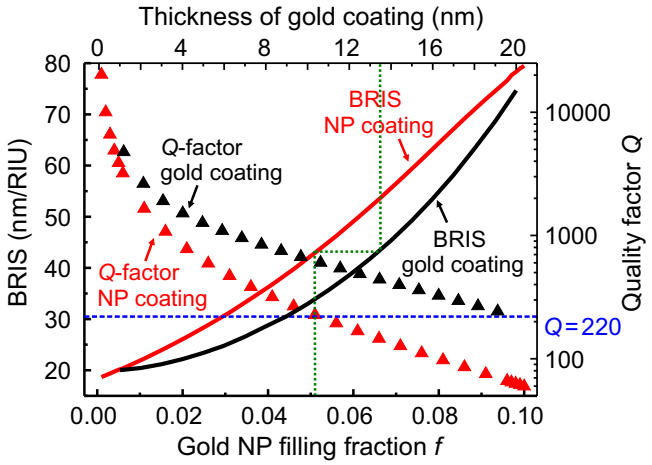

Figure 4.18: Comparison of Q-factor (triangles) and BRIS (solid lines) of a microdisk with different effective plasmonic coatings (red) with those of a microdisk with ultra-thin homogeneous gold coatings of varying thicknesses (black). A TE-mode (m=392) is considered in both cases. The increase in BRIS with increasing gold NP filling fraction f and gold film thickness is at the expense of a strongly degraded Q-factor. The lowest tolerable Q-factor in the system is ∼220 (horizontal blue line), restricting the BRIS enhancement in gold-NP-coated microdisks to a factor of ∼2. The similarity in the key performance parameters for sensing in both hybrid systems suggests that ultra-thin gold coatings can be mimicked by effective-medium coatings made from randomly assembled gold NPs (indicated by green dotted line). Adapted from [170].

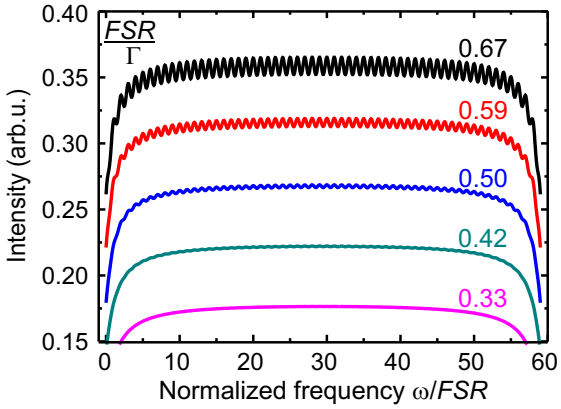

Figure 4.19: Impact of ratio r between FSR and linewidth Γ of a WGM on the peak visibility. Plotted is the superposition of multiple equally shaped Lorentzians, spectrally separated by a fixed FSR, versus the normalized frequency ω/FSR for increasing ratios r (bottom to top). Two neighboring Lorentzians can be clearly and individually resolved for $r\gtrsim 0.59$, which translates to Q-factors $Q>220$. Taken from [170].

gold NPs is, however, at the expense of the cavity's Q-factor. For hybrid microdisks with NP filling fractions close to $f=0.1$, the respective Q-factors drop to values notably below a hundred. This effect drastically lowers the sensor's spectral resolution and ultimately limits its performance.

To assure a proper performance of WGM sensors, fundamental WGMs of the same polarization with consecutive mode numbers m and $m+1$ must be resolved individually. To identify the lowest tolerable Q-factor in the hybrid system for which two WGMs spectrally separated by their free spectral range (FSR) can be just resolved, we define the ratio $r=FSR/\Gamma$ between free spectral range FSR and linewidth Γ of a WGM. Plotting the superposition of multiple equally shaped Lorentzians, spectrally separated by a fixed FSR, in Fig. 4.19 versus the normalized frequency ω/FSR for increasing ratios r (bottom to top) allows to make statements about the maximal permissible WGM linewidth Γ. As expected, increasing the resonance linewidth Γ translates to a reduced peak visibility. As visible from Fig. 4.19, two neighboring peaks in the spectrum can be well resolved above a threshold ratio $r\gtrsim 0.59$. For the investigated hybrid microdisks with a FSR of $\sim$1.5 nm in the considered wavelength range, this threshold value restricts permissible linewidths Γ to less than $\sim$2.5 nm, which corresponds to Q-factors $Q>220$ (horizontal blue dashed line in Fig. 4.19). To assure a proper sensing performance of hybrid microdisks, the maximal gold NP filling fraction in the plasmonic shell should, therefore, not exceed values $f\gtrsim 0.05$ ($\sim$40 NPs/µm^2). This in turn implies that the maximal achievable sensitivity enhancement in the present structure is restricted to a factor of $\sim$2.

We'd like to stress that standard parameters for the dielectric microdisk have been used throughout the analysis and neither the photonic nor the plasmonic component in the considered hybrid system have been subjected to an optimization process. Optimizing

the cavity geometry and using alternative plasmonic NPs with superior optical properties compared to spherical gold NPs, such as high-Q silica-silver core-shell NPs, is expected to further improve the sensing performance of the hybrid system. Such an optimization is, however, beyond the scope of this work.

4.4.4 Mimicking ultra-thin gold coatings in photonic devices by gold-NP composites

In this section, we highlight analogies in the optical and sensing properties between dielectric microdisks wrapped by an effective plasmonic shell and hybrid systems comprised of the same dielectric core but coated with an ultra-thin gold film instead. Motivated by the extremely challenging fabrication of ultra-smooth and homogenous gold films with thicknesses <20 nm [171,188] on curved dielectrics, we map out a strategy on how to mimic such thin gold coatings by randomly distributed gold NPs forming an effective medium. Replacing ultra-thin gold films by effective medium coatings made from randomly distributed plasmonic NPs is expected to be of practical relevance, as such effective NP layers can be easily fabricated by means of self-assembly [171, 172].

To compare both hybrid systems, we calculate the Q-factors and the BRIS of TE-polarized WGMs with mode number m=392 sustained by microdisks with homogeneous gold coatings of varying thicknesses using FEM simulations. We add the respective simulation results for the Q-factor (black triangles) and the BRIS (black solid line) to Fig. 4.18 for gold film thicknesses between 1 and 20 nm to directly relate gold film thicknesses to gold NP filling fractions.
The functional dependency of both key performance parameters for sensing on the gold film thickness is seen to correspond well to that observed for NP-coated microdisks with varying gold NP filling fractions. These similarities imply that ultra-thin gold coatings with thicknesses <20 nm can be mimicked and replaced by effective media made from randomly distributed gold NPs. To make the connection between both systems clearer, we focus on a gold-NP-coated microdisk with gold NP filling fraction f=0.051 and illustrate, using Fig. 4.18, how to map this system to a comparable system with homogeneous gold coating. The considered NP-coated microdisk exhibits a BRIS of 43 nm/RIU and a Q-factor $Q\approx$230 close to the lowest tolerable Q-factor. As indicated by the green dashed line in Fig. 4.18, a similar BRIS is obtained when replacing the plasmonic shell by a homogeneous gold coating with ∼13.5 nm thickness. Compared to the NP-coated microdisk, the Q-factor of the WGM in the hybrid system with homogeneous gold coating is slightly increased owing to reduced scattering losses in a smooth gold film.
We'd like to note that the proposed gold film thickness of ∼13.5 nm needed to achieve a similar sensing performance as in the case of a plasmonic shell with f=0.051 must be considered as an upper limit. This is due to the fact that we used experimentally determined bulk values for the gold permittivity in the FEM simulations [177] and neglected additional contributions to the dielectric function of gold due to enhanced electron-surface collisions present in very thin gold films (see also section 4.4.1) [189, 190]. Since the con-

sidered gold film thicknesses are, however, significantly smaller than the electron mean free path in gold, nonlocal effects and enhanced surface scattering in the ultra-thin gold films are expected to notably increase the imaginary part of the gold permittivity over its respective bulk value [178, 179]. As a consequence of the additional thickness-dependent losses, even smaller gold film thicknesses than those deduced from Fig. 4.18 are, thus, necessary to make the sensing performance of gold-coated microdisks comparable to that of gold NP-coated microdisks.

The simulation results presented here show that dielectric microdisks coated with smooth and homogeneous gold films with thicknesses <20 nm exhibit similar optical and sensing properties like dielectric microdisks coated with an effective plasmonic shell. Whereas the fabrication of ultra-thin gold films with the homogeneity and smoothness required for practical applications is a big challenge [189, 190], effective plasmonic layers made from randomly distributed gold NPs can be easily deposited on arbitrarily shaped dielectrics using self-assembly techniques. The simulation results, therefore, "[...] provide a powerful guideline for the design of novel hybrid photonic–plasmonic devices exhibiting similar optical properties like hybrid systems with ultra-thin metal coatings but overcoming fabrication challenges related to the realization of gold films on micrometer-sized non-planar dielectric substrates. In our case, ultra-thin homogeneous gold coatings with thickness <15 nm can be well mimicked with randomly distributed gold NPs with a diameter of 50 nm forming an effective plasmonic shell" [170].

4.4.5 Summary and conclusions

In this section, we analyzed theoretically and numerically whether the BRIS of a state-of-the-art polymeric microdisk can be notably improved by coating it with a huge number of randomly distributed spherical gold NPs.

To efficiently simulate gold-NP-coated microdisks, the densely packed gold NPs on the microdisk surface were treated at the level of an effective medium, i.e. modeled as a smooth homogeneous layer with an effective permittivity. It was shown that the effective permittivity of the plasmonic shell can be easily and widely tuned in the visible spectral region by simply adjusting the gold NP filling fraction. This property was the key to study the optical and sensing properties of hybrid microdisks for a large range of gold NP filling fractions.
Performing FEM simulations of a hybrid microdisk wapped by a plasmonic shell with moderate gold NP filling fraction, we demonstrated that the spectral resonance position, Q-factor, and BRIS of a WGM strongly depend on the resonance wavelength detuning between the operational WGM and the plasmonic resonance of the effective plasmonic shell. In excellent accordance with the predictions from the simple HO-model in section 4.2 and the multi-Mie simulations in section 4.3, operating the hybrid microdisks at wavelengths red detuned with respect to the plasmonic resonance by approximately half the plasmon resonance linewidth leads to a maximal BRIS enhancement. The optimal detuning was the outcome of balancing between sensitivity gain and linewidth broadening. Despite the

remarkably good correspondence with the simplified theoretical models, the FEM simulation results of the realistic hybrid sensor presented in this section, pointed out the need to consider the optical properties of real metals to correctly predict and quantify effects showing up in hybrid systems.
The BRIS of hybrid WGMs was shown to increase monotonically with increasing NP filling fraction due to the increased real part of the shell's effective permittivity, leading to an increased mode overlap with the surrounding. As the imaginary part of the plasmonic shell's effective permittivity was, however, simultaneously increased, the beneficial effect on the BRIS of the hybrid system due to the larger number of gold NPs was accompanied by a strong Q-factor reduction. This effect drastically lowered the hybrid sensor's spectral resolution and ultimately limited its sensing performance. A proper sensing performance was predicted for hybrid microdisks with Q-factors $\gtrsim$220 corresponding to gold NP filling fractions f<0.05. For this largest tolerable NP filling fraction, a BRIS enhancement by a factor of $\sim$2 was demonstrated. Replacing the gold NPs in the hybrid system by plasmonic NPs with higher Q-factors, such as silica–silver core–shell NPs, is expected to further boost the BRIS.
The investigated NP-coated microdisks were demonstrated to possess similar optical and sensing properties like microdisks coated with ultra-thin homogeneous gold films with thicknesses below $\sim$20 nm. As the fabrication of ultra-thin homogeneous gold films on curved dielectrics is a big challenge, we outlined a strategy on how to mimick such thin gold films by an effective medium made from randomly distributed gold NPs. Since gold-NP composites can be fabricated with ease using self-assembly techniques, the proposed effective medium approach is expected to pave the way for novel hybrid devices whose performance was so far restricted by the achievable smoothness and homogeneity of ultra-thin gold coatings.

4.5 Experiments on sensing performance of polymeric microdisk lasers coated with densely packed gold NPs

In this section, we investigate experimentally whether the BRIS of a standard polymeric microdisk can be measurably enhanced via the coupling to a large number of randomly distributed gold NPs – as predicted theoretically.
The FEM simulations of gold-NP-coated microdisks in the previous section showed that the increase in BRIS due to an increasing number of gold NPs on the microdisk surface is accompanied by a strong Q-factor degradation. The reduction in Q-factor drastically lowers the hybrid sensor's spectral resolution and imposes an upper bound on the achievable BRIS enhancement. To overcome the respective limitations imposed by linewidth broadening to a certain extent, we use active gold-NP-coated microdisks with integrated gain medium in the sensing experiments. Contrary to their passive counterparts, the linewidth of WGMs in active microdisks is reduced when operated above the lasing threshold [46,47], which improves the spectral resolution.

At the beginning of this section, we briefly discuss the lasing properties of PM597-doped PMMA microdisks and investigate how their lasing wavelength and lasing threshold are affected by the coupling to densely packed gold NPs. Optically characterizing hybrid microdisk lasers with different packing densities of gold NPs on the micro-photoluminescence spectroscopy (µ-PL) setup, we determine in section 4.5.1 the largest tolerable gold NP filling fraction for which lasing operation in water is possible. In this context, we evaluate whether lasing in the respective hybrid microdisk occurs at a wavelength close to the predicted optimal operational wavelength corresponding to a maximal BRIS enhancement. We proceed in section 4.5.2 to quantify the BRIS enhancement for the hybrid microdisk with largest tolerable gold NP filling fraction in BRIS measurements and discuss the result. At the end of the section, a summary and concluding remarks are provided.

4.5.1 Lasing properties of gold-NP-coated microdisks

Standard PMMA microdisks (radius: 25 µm, thickness: 1.2 µm) doped with the laser dye pyrromethene 597 (PM597) serve as resonator templates for the implementation of gold-NP-coated WGM sensors (see section 3.1.2). Spherical gold NPs with 25 nm radius are covalently attached in a high number density to the resonator surface using the immobilization scheme presented in section 3.2.1 to ensure a reliable sensing performance. A normalized absorption spectrum of the gold NPs in aqueous solution is shown in Fig. 4.20(a). The plasmonic resonance of the gold NPs, as determined from the peak in the absorption spectrum, is located at a wavelength λ=532 nm.
In the following, we analyze the impact of the gold NP filling fraction on the lasing wavelength and lasing threshold and investigate whether lasing in gold-NP-coated microdisks occurs at wavelengths close to the predicted optimal operational wavelength, i.e. red detuned from the plasmonic resonance by ∼36 nm (see section 4.4.3).

Lasing condition

For lasing in a resonator to occur, the optical gain per round-trip has to overcome the round-trip losses at the lasing wavelength [191]. This condition imposes a lower bound on the number density of dye molecules which have to be excited into the first singlet state from which stimulated emission occurs. Defining γ as the ratio of the number density of dye molecules excited into the first singlet state to the total number density n_t of dye molecules, the minimal fraction γ=$n_\mathrm{S1}/n_\mathrm{t}$ of dye molecules which need to be excited to achieve lasing operation is given by the following threshold condition [192]:

$$\gamma(\lambda) \geq \frac{\frac{2\pi n_\mathrm{R}}{\lambda Q n_\mathrm{t}} + \sigma_\mathrm{a}(\lambda)}{\sigma_\mathrm{a}(\lambda) + \sigma_\mathrm{e}(\lambda)}. \tag{4.17}$$

$\sigma_\mathrm{a}(\lambda)$ and $\sigma_\mathrm{e}(\lambda)$ in Eq. 4.17 denote the absorption and emission cross sections of the laser dye, respectively, n_R the refractive index of the cavity, and Q its Q-factor. The global minimum in $\gamma(\lambda)$ determines the wavelength at which lasing occurs. Eq. 4.17 shows that

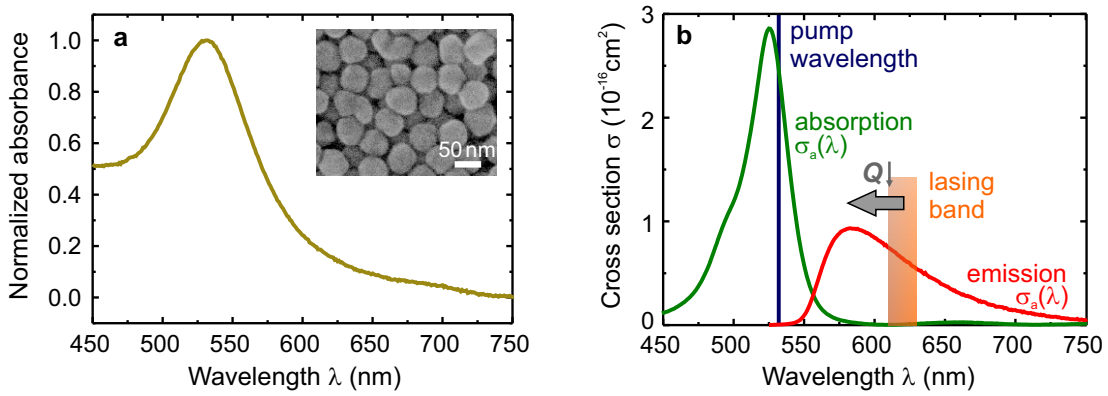

Figure 4.20: (a) Measured normalized absorption spectrum of colloidal gold NPs with 25 nm radius in water. The plasmonic resonance, as determined from the peak in the absorption spectrum, is spectrally located at a wavelength $\lambda \approx 532$ nm. The inset shows a scanning electron micrograph of densely packed gold NPs on a PMMA substrate. (b) Absorption (green) and emission (red) cross sections of a $\sim$1 µm thick PM597-doped PMMA film. Data taken from [100]. With decreasing Q-factor of the cavity, e.g. due to the incorporation of gold NPs, the lasing band (orange) in active microdisks shifts from the long-wavelength side of the emission curve toward the maximum in $\sigma_e(\lambda)$ (indicated by arrow).

both the lasing wavelength and the corresponding lasing threshold $P_{\text{thresh}} \propto \gamma$ [97] critically depend on the number density of dye molecules and the cavity's Q-factor. The lasing threshold is defined as the minimal pump power flux required to achieve laser emission at a specific wavelength.

For the standard PM597-doped microdisks with Q-factors on the order of $10^4 - 10^5$ in aqueous environment, lasing is typically observed at wavelengths between $\sim$610 nm and $\sim$630 nm [51]. The respective lasing band is marked in Fig. 4.20(b), where we show the absorption (green) and emission (red) cross sections of PM597 embedded in a $\sim$1 µm thick PMMA film [100, 193]. As the result of an optimal balance between emission and reabsorption, lasing in bare PM597-doped PMMA microdisks occurs at wavelengths red-shifted with respect to the maximum in $\sigma_e(\lambda)$. However, if the Q-factor of the cavity decreases, e.g. due to the incorporation of lossy gold NPs, the lasing band shifts toward regions with higher gain to overcome the increased losses in the cavity. This effect results in a blue shift of the lasing modes toward the maximum in the emission cross section of PM597 at $\lambda = 588$ nm, as indicated in Fig. 4.20(b), and is accompanied by an increase in the lasing threshold.

These considerations suggest that lasing in gold-NP-coated PM597-doped microdisks occurs at wavelengths red detuned from the plasmonic resonance of a single gold NP [see Fig. 4.20(a)] and close to the optimal operational wavelength $\lambda_{\text{opt}} \approx 570$ nm for which a maximal BRIS enhancement is predicted [see Fig. 4.16(b)]. Therefore, coupling of the lasing modes to the gold NPs is expected to result in the desired BRIS enhancement. However, owing to the strong decrease in Q-factor due to the incorporation of densely

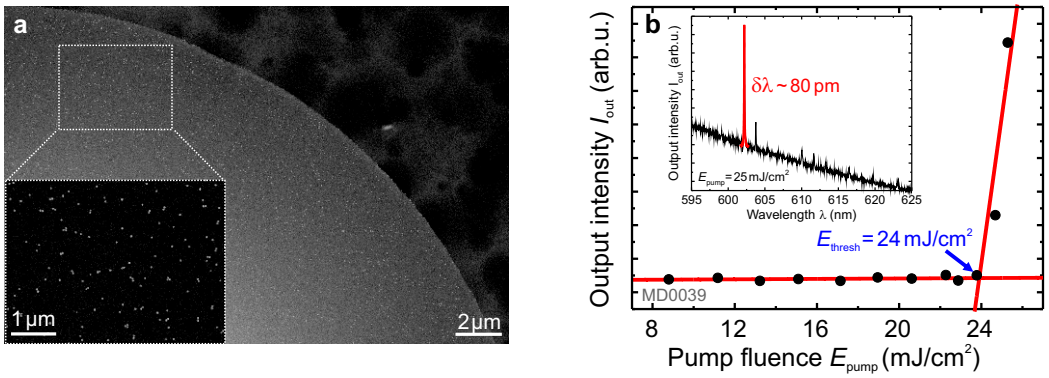

Figure 4.21: (a) Scanning electron micrograph showing a hybrid microdisk with largest tolerable gold NP filling fraction f_{max}≈0.009 (∼7 NPs/µm^2) from the top. (b) Characteristic input–output curve to determine the lasing threshold of the hybrid microdisk. The onset of lasing is marked by the kink. The lasing threshold is determined from the intersection of the two red lines (E_{thresh}∼24 mJ/cm^2 per pulse). The inset shows an emission spectrum for a pump fluence slightly above the lasing threshold. The lasing mode appearing at lowest pump power is marked in red.

packed gold NPs, the lasing threshold of gold-NP-coated microdisks is expected to be notably increased over that of bare polymeric microdisks.

Experimental characterization of lasing properties of hybrid microdisks

To asses the largest tolerable gold NP filling fraction for which laser emission in water is possible for the pump power available in the experiment, the lasing performance of hybrid microdisks with gold NP filling fractions between f≈0.003 and f≈0.015 was characterized on the µ-PL setup introduced in section 3.3.1. Determining the largest tolerable gold NP filling fraction is of particular interest, as it imposes an upper limit on the achievable BRIS enhancement in the present system.

With regard to the application as sensors, the gold-NP-coated microlasers are placed in a sample chamber which is integrated into the µ-PL setup and filled with water. Lasing modes are observed for hybrid microdisks with gold NP filling fractions up to f_{max}≈0.009 (∼7 NPs/µm^2). The gold NP filling fractions are determined from scanning electron micrographs of the investigated samples by counting the number of gold NPs on the top surface and the rim of the microdisks. A scanning electron micrograph of the hybrid microdisk with largest tolerable gold NP filling fraction f_{max}≈0.009 is depicted in Fig. 4.21(a).
To determine the lasing threshold of the respective hybrid microdisk, the green pump laser is loosely focused onto the top surface of the hybrid microdisk (spot size ∼0.013 mm^2) and PL-spectra are acquired while step-wise increasing the power of the pump laser. Plotting the integrated intensity of the lasing mode appearing at the lowest pump power as a function of the pump fluence E_{pump} per pulse results in the characteristic input-output curve shown in Fig. 4.21(b). The onset of lasing is marked by the kink. The lasing threshold

E_{thresh} of the hybrid microdisk is determined from the intersection of the two red lines to be 24 mJ/cm^2 per pulse. Compared to its bare dielectric counterpart with a lasing threshold of 80 µJ/cm^2 in water, the lasing threshold of the considered gold-NP coated microdisk is increased by a factor of ∼300 due to huge plasmonic losses brought into the system by the gold-NP-coating.
A lasing spectrum recorded for a pump fluence of 25 mJ/cm^2 per pulse is shown in the inset of Fig. 4.21(b). The lasing mode appearing at lowest pump power is marked in red and spectrally located at a wavelength λ=602 nm. According to the results presented in Fig. 4.16(b), a BRIS enhancement can be expected for the respective lasing mode, although the lasing wavelength slightly differs from the optimal operational wavelength. We'd like to note that the linewidth of the lasing mode is with $\delta\lambda\approx$80 pm ($Q\approx$7300) notably smaller than the predicted linewidth of $\delta\lambda\approx$150 pm ($Q\approx$4000) which would be observed in the respective passive cavity without gain medium (see Fig. 4.18). As expected, the spectral resolution of the active hybrid microdisk is, thus, improved compared to its passive counterpart without integrated laser dye.

4.5.2 Bulk refractive index sensing with gold-NP-coated microdisks

To quantify the BRIS of the hybrid microdisk with largest tolerable gold NP filling fraction $f_{\text{max}}\approx$0.009 and quantify the enhancement in sensitivity due to the incorporation of the gold-NP coating, BRIS measurements on the respective hybrid microdisk and its bare dielectric counterpart are performed.

During the BRIS measurement, the sample chamber containing the chip with the considered hybrid microdisk is filled alternately with water and water-glycerol mixtures of increasing refractive indices while continuously recording lasing spectra. Tracking the spectral position of a lasing mode over time reveals a step-wise spectral shift toward longer wavelengths as soon as a high-index water-glycerol mixture flows into the sample chamber. Plotting the induced WGM shift $\Delta\lambda$ versus the refractive index change Δn_{m} of the surrounding produces Fig. 4.22. From the slope of a linear regression (red line) fitted to the data points, the BRIS of the hybrid microdisk is determined to be 43 nm/RIU with an error bound of ±2 nm/RIU, as obtained from the standard error of the linear regression. This value for the BRIS of the hybrid microdisk with gold NP filling fraction $f_{\text{max}}\approx$0.009 can be considered as an upper bound for the achievable sensitivity in experiments with active hybrid microdisks in the present setup.
Due to the high pump powers necessary to bring the gold-NP coated microdisk into the lasing regime, photobleaching of the laser dye constitutes a major problem during the BRIS measurement. On the one hand, photobleaching leads to a gradual blue shift of the WGMs, which counteracts the actual WGM red shift induced by increasing the refractive index n_{m} of the background medium. On the other hand, it drastically limits the number of acquisition cycles and, thus, the sensor's performance. When pumped with a repetition rate of 20 Hz and a pump fluence of 25 mJ/cm^2 per pulse, lasing modes in active resonators typically disappear within a few acquisition cycles.

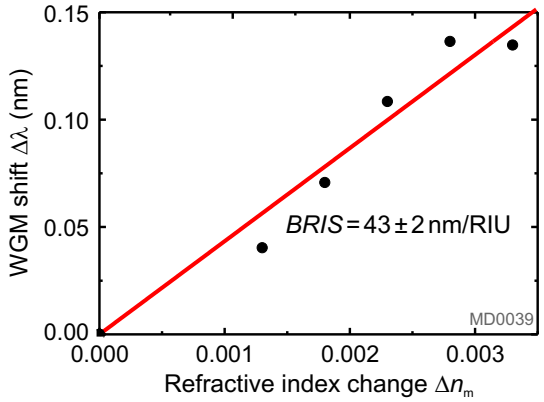

Figure 4.22: Relative resonance wavelength shift $\Delta\lambda$ of a WGM in the hybrid microdisk with largest tolerable gold NP filling fraction $f \approx 0.009$ induced upon changing the refractive index n_{m} of the surrounding medium. The slope of a linear function (red) fitted to the WGM shift $\Delta\lambda$ when plotted versus the change Δn_{m} in background refractive index determines the BRIS of the hybrid microdisk (43±2 nm/RIU). As the predicted BRIS enhancement factor for the investigated hybrid microdisk is on the order of the measurement error, the beneficial effect of the NP-WGM coupling on the BRIS could not be verified experimentally.

To evaluate whether the coupling of the gold NPs to the WGM microdisk leads to the desired sensitivity enhancement, we relate the BRIS of the hybrid microdisk with gold NP filling fraction $f_{\mathrm{max}} \approx 0.009$ to the BRIS of its bare dielectric counterpart. The BRIS of the PMMA microdisk prior to the gold-NP immobilization is determined to be 41 nm/RIU. Therefore, no enhancement in sensitivity due to the coupling to the gold NPs is observed within the limits of the measurement accuracy.

To explain this finding, we take a closer look into the FEM simulation results for a hybrid microdisk with gold NP filling fraction $f_{\mathrm{max}} \approx 0.009$ (see section 4.4).
From Fig. 4.18(b) we can deduce that even under optimal excitation conditions only an enhancement in BRIS by a factor of 1.14 can be expected for the respective hybrid microdisk. This value corresponds to an absolute increase in BRIS by 2.7 nm/RIU. Considering that the gold NPs used in the experiment are, according to the manufacturer specifications, surrounded by a $\sim$2−4 nm thick dielectric functionalization layer, even smaller beneficial effects on the BRIS can be expected. The thin functionalization layer surrounding the gold NPs effectively screens the gold NP's evanescent field from the surrounding, which reduces the NP–WGM coupling strength and the BRIS of spherical gold NPs by $\sim$15−20% compared to bare gold NPs without dielectric coating [158]. According to the results obtained in section 4.2.3, both effects lower the BRIS of the hybrid microdisk. Furthermore, the operation conditions for the hybrid microdisk in the experiment slightly differ from the optimum. Therefore, the enhancement in BRIS is, according to the results shown in Fig. 4.18(a), expected to be further reduced by $\sim$7% compared to the case of an optimal detuning.
All effects combined make clear that the beneficial effect of the gold NPs on the BRIS is even for the active hybrid microdisk with largest tolerable NP filling fraction quite small

and on the order of the measurement error. Therefore, the predicted enhancement in BRIS due to the coupling to the spherical gold NPs could not be verified experimentally.

4.5.3 Summary and conclusions

In this section, it was investigated experimentally whether the coating of polymeric microdisks with huge numbers of randomly distributed spherical gold NPs measurably enhances their BRIS – as predicted theoretically by the FEM simulations in section 4.4.

To partly compensate for the linewidth broadening of WGMs induced by coupling to the lossy gold-NP coating and improve the hybrid sensor's spectral resolution, active PMMA microdisks with integrated laser dye pyrromethene 597 (PM597) were used as resonator templates. Compared to their passive counterparts without gain medium, WGMs in active resonators exhibit a reduced linewidth when operated above the lasing threshold which facilitates measuring tiny bulk refractive index changes. To ensure a reliable sensing performance, the gold NPs were covalently attached to the microdisk surface using self-assembly techniques. The lasing and sensing properties of the gold-NP-coated microdisks in aqueous environment were characterized on a micro-photoluminescence spectroscopy setup.
It was shown that the lasing performance of active gold-NP-coated microdisks tremendously degrades with increasing number density of gold NPs on the microdisk surface due to strongly increased plasmonic losses. For the pump power available in the experiment, lasing operation was achieved up to a modest gold NP filling fraction $f{\approx}0.009$ ($7\,\mathrm{NPs}/\,\mu\mathrm{m}^2$). For the respective hybrid microdisk, the lasing threshold $E_{\mathrm{thresh}}{=}24\,\mathrm{mJ/cm^2}$ was increased by two orders of magnitude compared to its bare dielectric counterpart. As high pump powers were needed for the laser action, photobleaching of the laser dye was a major problem that strongly degraded the device performance.
BRIS measurements on the hybrid microdisk with gold NP filling fraction $f{\approx}0.009$ and its bare dielectric counterpart were performed to assess the maximal BRIS enhancement achievable with the present experimental system. The beneficial effect of the gold-NP coating on the BRIS of the WGM microdisk could, however, not be verified experimentally. This observation was explained by the fact that the predicted BRIS enhancement factor $\eta{=}1.14$ for the investigated hybrid microdisk is quite small and on the order of the measurement error.

The experimental results presented in this section made clear that the huge losses in gold NPs ultimately limit the performance of active gold-NP-coated microdisks as bulk refractive index sensors. As a result of strongly increased lasing thresholds with increasing number density of gold NPs on the microdisk surface, high pump powers are needed to achieve lasing operation in hybrid microdisks with gold NP filling fractions for which a notable enhancement in sensitivity can be expected. However, for such high pump powers photobleaching of the integrated laser dye PM597 is strongly pronounced. This effect drastically shortens the operational lifetime of the hybrid sensors and makes active hybrid microdisks, therefore, rather unsuitable for practical applications. The way out of this dilemma can be seen in using plasmonic NPs with significantly higher-quality reso-

nances and higher BRIS values to boost the BRIS of the hybrid system into a regime where enhancement effects can be accessed even with modest pump powers. Up to now, the spectrum of available plasmonic materials and NP geometries which meet these requirements is, however, severely restricted. Advances in material science are, thus, indispensable to make hybrid NP–WM sensors competitive with their bare dielectric counterparts. So far, the disadvantages of the plasmonic components, i.e. the huge plasmonic losses, dominate by far the beneficial effects on the BRIS resulting from strongly enhanced fields at the NP's surface.

4.6 Summary and critical remark on hybrid NP–WGM resonators for bulk refractive index sensing

In this chapter, it was studied both theoretically and experimentally whether the sensitivity of dielectric WGM resonators can be enhanced by hybridizing WGMs with plasmonic resonances sustained by small metallic nanoparticles (NPs) coupled to the resonator surface. The strategy to boost the sensitivity relied on pushing the WGM's field distribution outside the resonator to enhance its interaction with the surrounding. The so-called bulk refractive index sensitivity (BRIS), a measure for the spatial overlap of a WGM with the surrounding, was used to quantify the sensitivity.

A fundamental analysis of hybrid NP–WGM sensors using a simple formalism of two coupled harmonic oscillators and full-wave simulations of an idealized hybrid system based on multi-Mie scattering theory demonstrated that the BRIS of a WGM resonator can be enhanced via the coupling to a single plasmonic NP. The associated enhancement effects were shown to sensitively depend on the resonance wavelength detuning between the plasmonic resonance and the operational WGM, and the properties of the plasmonic NP in the hybrid system, namely its Q-factor and BRIS. A maximal BRIS enhancement was predicted for plasmonic NPs with resonance wavelengths slightly blue detuned from the operational WGM. The respective optimal detuning was the outcome of balancing between sensitivity gain and WGM linewidth broadening induced by coupling to the lossy metallic NPs. It was, however, shown that a significant BRIS enhancement occurs only for plasmonic NPs with comparatively high-quality resonances and high BRIS values notably exceeding the BRIS of the underlying WGM resonator.
Finite-element method (FEM) simulations of a hybrid sensor composed of a polymeric microdisk coated with randomly distributed and densely packed spherical gold NPs provided insight into the role of the number of gold NPs on the BRIS enhancement. It was demonstrated that the BRIS of gold-NP-coated microdisks increases monotonically with increasing number density of gold NPs on the microdisk surface. The beneficial effect on the BRIS due to the increased number density of gold NPs was, however, seen to be at the cost of a strongly degraded Q-factor, which drastically lowered the sensor's spectral resolution and ultimately restricted its sensing performance. For the largest tolerable gold NP filling fraction $f \approx 0.05$ ($\sim 40\,\mathrm{NPs}/\,\mu\mathrm{m}^2$) for which a proper sensing performance of the

hybrid microdisks was ensured, a BRIS enhancement by a factor of ∼2 was predicted. Sensing experiments on gold-NP-coated microdisks with integrated gain medium confirmed that the huge losses in gold NPs are the major problem in hybrid sensors, ultimately limiting the device performance. For the largest tolerable gold NP filling fraction $f \approx 0.009$ ($\sim 7\,\mathrm{NPs}/\,\mu\mathrm{m}^2$) for which lasing operation in water was possible, the BRIS enhancement was quite small and on the order of the measurement error. Therefore, the beneficial effect of the gold-NP coating on the BRIS of WGM microdisks could not be verified experimentally.

The theoretical and experimental results presented in this chapter suggest that the coupling of gold NPs to WGM resonators is, so far, not beneficial to improve their performance as bulk refractive index sensors. Although the incorporation of huge numbers of gold NPs into WGM resonators can improve the BRIS by a factor of ∼2, this modest enhancement in sensitivity cannot compensate for the strong WGM Q-factor degradation by several orders of magnitude induced upon coupling to the lossy gold-NP coating. As the performance of a sensor is quantified via the ratio of sensitivity to resonance linewidth, the performance of the proposed gold-NP-coated WGM microdisks in bulk refractive index sensing is, thus, at the moment worse than that of a bare dielectric WGM resonator. Advances in material science are needed to make plasmonic-NP-coated WGM resonators in the future competitive with their bare dielectric counterparts for what concerns bulk refractive index sensing. In particular, the fabrication of novel plasmonic nanostructures with higher-quality resonances and higher intrinsic BRIS values is critical to notably boost the sensitivity of hybrid resonators while simultaneously improving their Q-factors.

Chapter 5

Plasmonic, dielectric, and hybrid modes in silver-coated polymeric microwedges

In this chapter, we systematically study both theoretically and experimentally the modal characteristics of a silver-coated polymeric wedge-like WGM resonator. This novel type of resonator is carefully engineered to support distinct types of modes: pure surface plasmon polariton (SPP) modes, pure dielectric (DE) modes, and hybrid photonic–plasmonic (HY) modes with Q-factors exceeding a thousand and ultra-small modal volumes of only a few cubic micrometers. Providing insight into the largely disparate properties of the distinct eigenmodes and developing a strategy on how to access the individual resonant modes in experiments in a controlled manner is at the heart of this chapter.

After highlighting the potential of metal-coated WGM resonators in photonic applications, we examine in section 5.2 SPPs propagating along a plane metal–dielectric interface. From their dispersion relation, we deduce first guidelines for the design of metal-coated WGM resonators. We proceed in section 5.3 to introduce numerically efficient bent-waveguide simulations to model hybrid WGM resonators and identify a cavity design which ensures the existence of SPP, DE, and HY modes and guarantees that all three mode types can be efficiently and selectively excited by means of a tapered optical fiber. In this context, we highlight the need for a template WGM resonator with wedge-like geometry. We then simulate in section 5.4 the mode spectrum of a fabricated silver-coated polymeric microwedge and work out differences in the modal properties of SPP, DE, and HY modes. Motivated by uncertainties in the simulated spectral features, we develop a mode classification scheme to unambiguously identify resonances observed in fiber transmission spectra. Performing bent-waveguide simulations which explicitly include the coupling to the input fiber and applying coupled-mode theory, we develop an experimental procedure based on mode filtering to reliably classify modes in silver-coated microwedges. In section 5.5, we map the theoretical results to the experiment and demonstrate that the proposed mode filtering

technique was successfully applied in fiber–coupling experiments to categorize and selectively excite SPP, DE, and HY modes in silver-coated polymeric microwedges. A summary and concluding remarks are given at the end of the chapter.

The results presented in this chapter were developed in close cooperation with Patrick Forster during his master's thesis [84] and with the doctoral student Jens Oppermann from the Institute of Theoretical Solid State Physics (TFP) at KIT with whom I supervised Patrick Forster. The bent-waveguide simulations presented in this chapter to efficiently simulate the modal properties of silver-coated WGM resonators and the coupling to a tapered optical fiber are based on a code developed by Jens Oppermann during his master's thesis at TFP [194]. The code was adapted to the specific problem of coupling between a straight fiber and a silver-coated polymeric wedge-like WGM resonator mainly by Patrick Forster. Parts of the presented results are published in [85].

5.1 Benefits of metal-coated WGM resonators

Due to their high Q-factors in combination with relatively small mode volumes V, WGM resonators have attracted considerable attention not only in photonic applications, where they are used as ultra-sensitive biosensors [24, 120] or low-threshold microlasers [11, 195–197], but also in fundamental research to study nonlinear optics [23, 198, 199] or cavity quantum electrodynamics [20, 200–203]. However, as the mode volumes of WGMs in purely dielectric resonators are limited by diffraction to typically a few hundred cubic wavelengths [69] and as the strength of light–matter interactions is proportional to the ratio Q/V, their performance in these fields is ultimately restricted.
To further boost light–matter interactions in WGM resonators, thus, strategies have to be developed to break the diffraction limit. Here, SPP cavities come into play. They rely on the collective excitation of a metal's free electron gas, which coherently interacts with an incoming electromagnetic field. This light–matter interaction leads to the formation of SPPs which propagate along metal–dielectric interfaces and are accompanied by strongly enhanced and localized electromagnetic fields [32]. Owing to the light-focusing characteristic of SPPs, electromagnetic energy in SPP cavities can be squeezed down to nanometric volumes [204–206]. However, there is a price to pay for breaking the diffraction barrier. Owing to large ohmic losses in the metal, Q-factors of SPP cavities are typically $\ll 100$ at wavelengths in the visible and near-infrared [31, 140–142] and, thus, several orders of magnitude smaller than those of dielectric WGM resonators.
Inspired by the complementary characteristics of purely dielectric and purely SPP cavities, a promising strategy to increase the Q/V-ratio of common WGM resonators can be seen in combining the ultra-small mode volumes of SPPs with the high Q-factors of DE modes [39, 42, 147, 207–213]. Min *et al.* demonstrated, e.g., that SPP modes supported by a silver-coated silica microdisk provide notably reduced mode volumes compared to purely dielectric WGMs [39]. Although Q-factors of the SPP eigenmodes were close to the theoretical loss-limited Q-factor, they were still only slightly above a thousand and, hence, notably smaller than for their dielectric counterparts.

To further increase the Q-factors while simultaneously preserving the small mode volumes connected with SPPs, resonator designs allowing for the formation of HY modes have been proposed, such as silica WGM microtoroids coated with a silver nanoring [42], metal-coated microspheres [43], or metal-nanocapped microtubular cavities [44]. These structures were shown to support HY modes with Q-factors >1000 and mode volumes as small as one cubic wavelength and, thus, successfully combine the advantages of dielectric and plasmonic modes.

5.2 Deducing general design guidelines for metal-coated resonators from fundamental properties of surface plasmon polaritons (SPPs)

Optimizing the performance of photonic devices relying on the excitation of SPP modes requires understanding the peculiarities of these surface modes. In this section, we provide essential insight into the physical properties of SPPs by examining their dispersion relation. We study SPPs propagating along a plane metal–dielectric interface and deduce first guidelines for the design of metal-coated resonators. The analysis of characteristic length scales, effective mode indices, and Q-factors of SPPs helps identifying a suitable coating metal and an operational wavelength regime for which SPP modes in metal-coated WGM resonators possess the highest possible Q-factors and can be excited with the evanescent field of a tapered optical fiber.

5.2.1 Dispersion relation of SPPs at a plane metal–dielectric interface

The dispersion relation of SPPs describes how the angular frequency ω is connected to the wave vector component k_{SPP} of SPPs parallel to the interface along which they propagate. It can be found by seeking for eigenmodes of Maxwell's equation which are localized at the metal–dielectric interface with electromagnetic fields decaying exponentially into both half-spaces and which fulfill the boundary conditions. In the following, we focus on surface modes propagating in x-direction along a plane metal–dielectric interface located at z=0, as graphically illustrated in Fig. 5.1(a). The lower half-space (z<0) with complex permittivity $\epsilon_2(\omega)=\epsilon_2'(\omega)+i\epsilon_2''(\omega)$ represents the metallic medium, the upper half-space (z>0) with permittivity $\epsilon_1(\omega)$ the dielectric for which we neglect absorption losses. To simplify the notation, we drop the frequency dependency of the permittivities from now on. The dispersion relation of SPPs is given by [181]:

$$k_{\mathrm{SPP}} = k_{\mathrm{SPP}}' + ik_{\mathrm{SPP}}'' = k_0\sqrt{\frac{\epsilon_1\epsilon_2}{\epsilon_1+\epsilon_2}}, \tag{5.1}$$

where $k_0=\omega/c_0$ denotes the vacuum wave number. Due to the absorbing nature of metals, the SPP wave number k_{SPP} in Eq. 5.1 is complex with real part k_{SPP}' and imaginary part

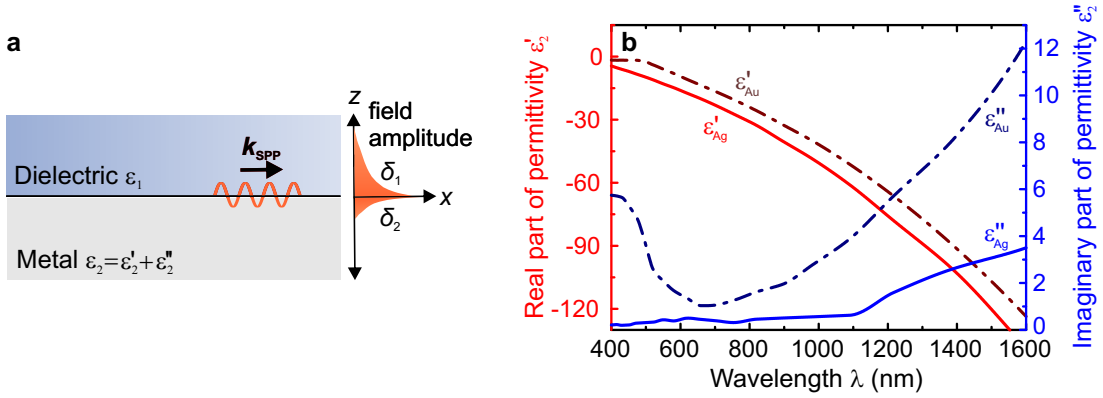

Figure 5.1: (a) Schematic illustration of SPPs propagating along a plane interface between a metallic half-space with complex permittivity ϵ_2 and a dielectric half-space with real permittivity ϵ_1. SPPs are accompanied by strongly enhanced and localized electromagnetic fields which decay exponentially away from the interface, as sketched on the right-hand section. The penetration depths δ_1 and δ_2 characterize the decay of the z-component of the SPP electric field amplitude into the dielectric and the metal, respectively. (b) Large negative real parts (red) of the permittivities of silver (solid lines) and gold (dashed) together with small imaginary parts (blue) at optical frequencies are a prerequisite for the formation of SPPs. Data taken from [177].

k''_{SPP}.

For an interface mode to exist, the wave vector component k_{SPP} parallel to the interface must be real to ensure propagation of the associated waves along the interface. Additionally, the normal components $k_{j,z}=\sqrt{\epsilon_j^2/(\epsilon_1+\epsilon_2)}k_0$ [181] of the wave vector must be purely imaginary in both the dielectric (j=1) and the metal half-space (j=2) to account for the 'bound' nature of SPPs. Assuming that the metal's imaginary part ϵ_2'' is small compared to the metal's real part ϵ_2', i.e. $|\epsilon_2''|\ll|\epsilon_2'|$, it follows from these requirements that the real parts must be of opposite sign if SPP modes are to be guided by the interface. Since the permittivity ϵ_1 of dielectrics is real and positive and common metals such as silver or gold exhibit a large negative real part ϵ_2' of their permittivity together with a small imaginary part ϵ_2'' at optical frequencies, localized surface modes can exist at such metal–dielectric interfaces. It can be shown that SPPs are inherently TM-polarized [214], i.e. the magnetic field is polarized tangential and the electric field mainly normal to the interface. This peculiarity of SPPs will be important in the experiments on silver-coated microwedges to distinguish between modes with plasmonic character and DE modes (see section 5.5).

5.2.2 Characteristic length scales of SPPs

To select a suitable coating metal for polymeric WGM resonators which ensures a low-loss propagation of SPPs at optical frequencies, we first examine the propagation length of SPPs. We then introduce the SPP penetration depths into the metal and the dielectric half-

space as additional relevant length scales for the design of metal-coated WGM resonators.

SPP propagation length

The SPP propagation length δ_{SPP} quantifies the distance SPPs propagate along the metal–dielectric interface until their intensity is attenuated to 1/e. It can be directly obtained from the imaginary part of the SPP wave vector, which characterizes the damping of the mode and is responsible for the exponential decay of the SPP's electric field amplitude [see Fig. 5.1(a)]. It is given by:

$$\delta_{\mathrm{SPP}} = \frac{1}{2k''_{\mathrm{SPP}}} \approx \frac{1}{k_0}\frac{(\epsilon'_2)^2}{\epsilon''_2}, \tag{5.2}$$

where the approximation in Eq. 5.2 is valid for low-loss metals, i.e. $|\epsilon''_2| \ll |\epsilon'_2|$. Since photonic devices relying on SPPs benefit from long SPP propagation lengths, metals with a large negative real part ϵ'_2 and a small imaginary part ϵ''_2 of the permittivity in the wavelength range of interest are required, according to Eq. 5.2, to ensure a good performance. Among metallic elements, silver and gold fulfill these requirements in the visible and near-infrared and are one of the best-performing materials for plasmonic applications in this wavelength regime, as they exhibit much weaker damping rates compared to other metals. The real (red) and imaginary parts (blue) of the permittivities of silver (solid lines) and gold (dashed) are plotted in Fig. 5.1(b) versus the wavelength λ. They have been interpolated from the data sets from Johnson and Christy [177]. The reduced imaginary part of the permittivity of silver compared to gold suggests using silver as coating material for WGM resonators, as it leads to longer SPP propagation lengths. Therefore and with regard to the experimental system, we focus throughout the rest of this section on SPPs propagating along a plane silver–polymer interface. A real, constant permittivity ϵ_1=2.25 is assumed for the polymer.

To identify a suitable wavelength regime for which SPP propagation lengths are maximal, we plot in Fig. 5.2(a) the propagation length δ_{SPP} of SPPs supported by the plane silver–polymer interface versus the free space wavelength λ. The SPP propagation length δ_{SPP} is seen to increase from $\sim$0.6 µm at λ=400 nm to $\sim$400 µm at λ=1600 nm. As the SPP propagation length imposes an upper limit on the size of hybrid photonic–plasmonic devices, increased SPP propagation lengths at longer wavelength favor the excitation of SPPs at wavelengths in the near-infrared over the visible spectral range. However, due to the absorbing nature of metals, even in the near-infrared the propagation lengths of SPPs are severely restricted. To ensure a proper performance of silver-coated WGM resonators in the experiment, their resonator radii must be, thus, chosen such that SPP modes propagate at least several times around the resonator circumference before their energy is dissipated into heat.

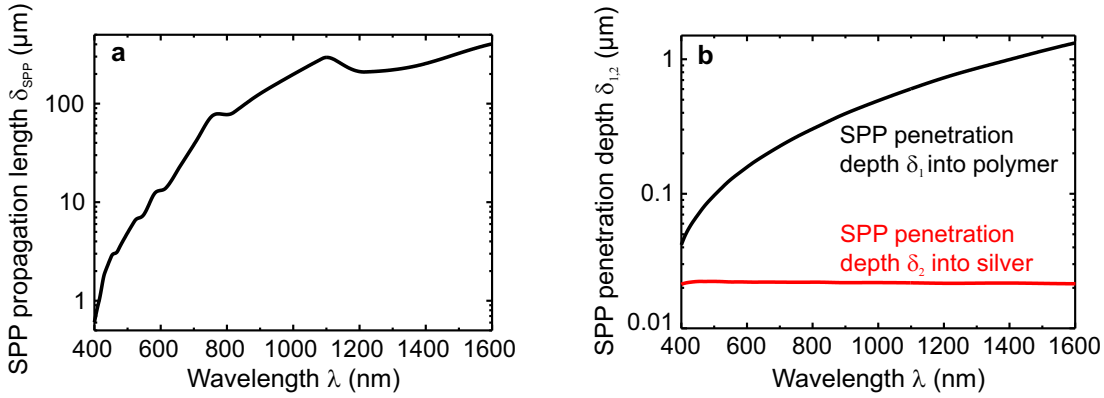

Figure 5.2: Characteristic length scales of SPPs sustained at a polymer–silver interface. (a) Longer SPP propagation lengths δ_{SPP} at longer wavelengths λ favor exciting SPP modes in the near-IR. (b) The SPP penetration depth δ_2 into the silver half-space is with ∼20 nm largely independent of λ and notably smaller than the penetration depth δ_1 into the polymer half-space. Although SPPs increasingly loose their light-focusing characteristic with increasing wavelength, the larger penetration depth into the polymer at longer wavelength is critical to efficiently excite SPP modes in silver-coated WGM resonators with a tapered-fiber eigenmode.

SPP penetration depth

The SPP penetration depth describes the decay of the SPP electric fields into the dielectric or the metal half-space and is defined as the distance normal to the metal–dielectric interface at which the electric field amplitude in the respective medium is decreased by 1/e of its maximal value at the interface.

The penetration depth δ_1 into the dielectric quantifies the length scale over which SPP modes can interact with their surrounding. It is not only important for sensing applications, but also plays a significant role when exciting SPPs in silver-coated WGM resonators by means of a tapered optical fiber. Only if the SPP evanescent fields notably penetrate through the polymeric resonator body into the surrounding medium, efficient coupling of SPP modes to a fiber mode is possible. The penetration depth δ_2 into the silver half-space characterizes the field decay into the metal. It provides a measure for the maximal thickness of silver films up to which SPPs supported on both sides of the film can interact with each other or with light totally reflected in an adjacent prism [215].

The SPP penetration depths δ_1 and δ_2 can be obtained from the SPP wave numer k_{SPP} when considering that the total wave vector $\epsilon_j k_0$ in the dielectric (j=1) and the silver (j=2) half-space is given by $\epsilon_j k_0^2 = k_{\mathrm{SPP}}^2 + k_{j,z}^2$. Assuming again that $|\epsilon_2''| \ll |\epsilon_2'|$, the 1/e decay lengths of the SPP's electric fields δ_1 and δ_2 into the dielectric and the silver are given by:

$$\delta_1 = \frac{1}{k_0}\sqrt{\left|\frac{\epsilon_2' + \epsilon_1}{(\epsilon_1)^2}\right|} \qquad \delta_2 = \frac{1}{k_0}\sqrt{\left|\frac{\epsilon_2' + \epsilon_1}{(\epsilon_2')^2}\right|}. \tag{5.3}$$

From Fig. 5.2(b), where we plot the SPP penetration depths δ_1 and δ_2 into the polymer and the silver half-space as a function of the free space wavelength λ, we see that the

penetration depth into silver is considerably smaller compared to the penetration into the polymer and is with $\delta_2 \approx 20\,\text{nm}$ largely independent of λ. Contrary, the penetration depth into the polymer half-space strongly depends on the wavelength and increases from $\delta_1 \approx 40\,\text{nm}$ at $\lambda = 400\,\text{nm}$ to $\delta_1 \approx 1.3\,\mu\text{m}$ at $\lambda = 1600\,\text{nm}$.

In the near-infrared, the SPP penetration depth δ_1 into the polymer is seen to exceed typical WGM resonator thicknesses of $\sim 1\,\mu\text{m}$ and, in particular, those of polymeric microwedges in the edge region (see section 3.1.2). In the latter case, the SPP mode's evanescent field is, thus, expected to notably overlap with the eigenmode of a tapered fiber approached to the silver-free bottom-surface of the WGM resonator from below (see section 5.4.3). As a large evanescent field overlap is a prerequisite for an efficient fiber–resonator coupling, operation wavelengths in the near-infrared are critical to efficiently excite SPP modes in silver-coated WGM resonators.

5.2.3 Excitation of SPPs

To couple light into SPP modes, both energy and momentum conservation must be fulfilled. To check whether both conditions can be fulfilled using a fiber–coupling scheme and to see how SPP modes can be excited experimentally, we study in the following the dispersion diagram of SPPs sustained at a plane silver–polymer interface, which is plotted in Fig. 5.3(a). For simplicity, we consider only the real part of the silver permittivity in the calculation of k_{SPP}.

Figure 5.3 reveals that the SPP mode lies close to – but always below – the light line $\omega = c_0 k_0$ (green line) in vacuum at low angular frequencies corresponding to wavelengths in the visible and near-infrared (highlighted in blue and red, respectively). c_0 denotes the speed of light in vacuum. As SPPs are predominantly light-like in this wavelength regime, their wavelength $\lambda_{\text{SPP}} = 2\pi/k'_{\text{SPP}}$ is only slightly shorter than the wavelength of the exciting light of same angular frequency. SPPs are, hence, well described as polaritons. With increasing angular frequency ω, the SPP mode bends away from the light line and approaches asymptotically the surface plasmon resonant frequency ω_{res} (horizontal dashed black line), whose spectral position is determined by the pole in the dispersion relation (Eq. 5.1). The avoided crossing obvious from Fig. 5.3 manifests that SPPs arise from the hybridization of surface plasmons and light. Please note that at frequencies close to ω_{res}, the SPP wavelength λ_{SPP} is significantly shorter than the corresponding wavelength of the excitation light, which means that SPPs can efficiently squeeze down light to subwavelength scales here. As the SPP wavelength is a measure for the mode localization, SPPs increasingly lose their subwavelength confinement character with increasing wavelength, which directly translates to increased mode volumes. This observation is in accordance with the results for the SPP penetration depth δ_1 into the polymer plotted in Fig. 5.2(b), which characterizes the mode confinement perpendicular to the silver–polymer interface. Importantly, as the SPP wave vector is always larger than the wave vector of a photon of same frequency propagating in free space, SPPs cannot be excited directly by means of free-space light. Instead, a momentum-enhancing scheme such as grating coupling [216, 217],

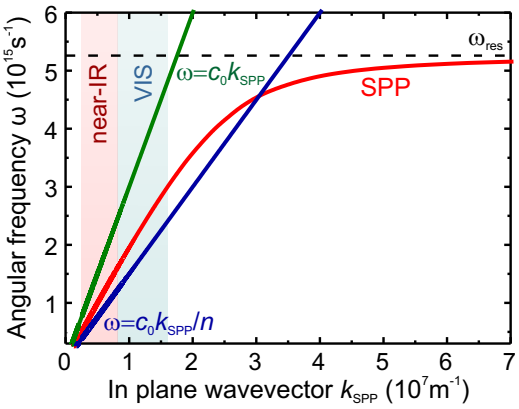

Figure 5.3: Excitation of SPPs. Dispersion relation of SPPs at a plane polymer–silver interface (red) together with the light line in vacuum (green) and in a dielectric with refractive index n=1.45 (blue). ω_{res} denotes the surface plasmon resonant frequency. As the SPP dispersion relation lies always below the light line in vacuum at optical frequencies, SPPs cannot be excited directly using free-space light. Instead, a momentum-enhancing scheme is necessary to increase the exciting light's wavevector component parallel to the interface and excite SPPs. In this work, a near-field coupling scheme utilizing the evanescent field of a tapered fiber is used to tilt the light line and couple light into SPP modes.

prism coupling [218, 219] or near-field coupling [220, 221] is necessary to increase the exciting light's wavevector component parallel to the interface over its free-space value and intersect the light line with the SPP dispersion relation. In this work, we make use of a near-field coupling scheme utilizing the evanescent field of a tapered optical fiber to tilt the light line and couple light into SPP modes.

Evanescent excitation of SPPs via tapered fiber

To investigate whether phase matching between a SPP mode and a tapered-fiber eigenmode can be fulfilled and to identify an optimal wavelength regime for mode excitation, we relate the effective refractive indices of SPPs in the following to those of tapered optical fibers.

Effective mode indices of tapered optical fibers at a given wavelength strongly depend on the fiber radius R_{F} in the tapered region. Plotting simulated values for the effective refractive index n_{F} of a conventional single mode fiber in Fig. 5.4(a) versus the fiber radius R_{F} for input wavelengths λ=600 nm (red) and λ=1500 nm (black) points out the range of accessible fiber mode indices.
Whereas comparatively thin fibers with radii R_{F}<500 nm exhibit effective mode indices n_{F} close to unity, n_{F} rapidly increases with increasing fiber radius until the bulk refractive index of silica ($n_{\mathrm{SiO_2}}$≈1.45) is approached (green dashed line), from which the fiber is

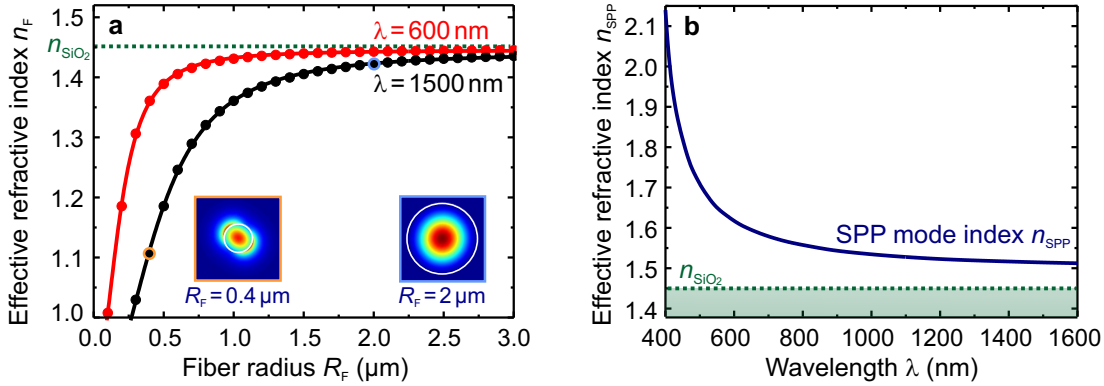

Figure 5.4: Evanescent excitation of SPPs using tapered fibers. (a) Effective refractive indices n_F of tapered-fiber eigenmodes for varying fiber radii R_F and input wavelengths λ=600 nm (red) and λ=1500 nm (black). Effective fiber mode indices increase with increasing fiber radius until they approach the bulk refractive index n_{SiO_2} of silica from which the fiber is made (green dashed line). The larger the fiber radius, the smaller is the evanescent field overlap of the fiber mode with the surrounding (see insets). (b) Effective refractive indices n_{SPP} of SPPs propagating along a plane silver–polymer interface are close to fiber mode indices only in the near-IR. Phase-matching requires excitation wavelengths in the near-IR to couple light from a fiber into SPP modes.

made. The increase in fiber mode index with increasing fiber radius is accompanied by a significant reduction in the spatial overlap of the fiber's evanescent field with the surrounding, as visible from the insets in Fig. 5.3(a), where the cross-sectional electric field intensity distributions of two optical fibers with radii R_F=0.4 µm (left) and R_F=2.0 µm (right) are plotted for an input wavelength λ=1500 nm.

The effective refractive index n_{SPP} of SPPs sustained at a plane metal–dielectric interface is determined by the real part of the SPP wave number and can be calculated as follows:

$$n_{SPP} = \frac{k'_{SPP}}{k_0} \approx \sqrt{\epsilon_1}\left(1 - \frac{\epsilon_1}{2\epsilon'_2}\right), \tag{5.4}$$

where the approximation $|\epsilon''_2| \ll |\epsilon'_2|$ and $|\epsilon'_2| \ll |\epsilon_1|$ is made. Eq. 5.4 shows that the dispersive character of SPPs in the low-loss limit is mainly determined by the permittivity ϵ_1 of the dielectric.

To predict a wavelength regime for which phase matching between SPPs and a fiber eigenmode is best fulfilled, we plot the effective refractive indices n_{SPP} of SPPs sustained at the plane silver–polymer interface in Fig. 5.4(b) versus the free space wavelength λ (red line). Increasing the wavelength lowers the effective mode indices of SPPs from n_{SPP}>2.0 at λ=400 nm toward n_{SPP}≈1.5 at wavelengths in the near-infrared.

As effective mode indices of SPPs at the silver–polymer interface are close to accessible fiber mode indices only in the near-infrared, phase matching requires using pump wavelengths in the near-infrared to excite SPPs evanescently by means of a tapered optical fiber. However, even in this wavelength regime, phase matching cannot be perfectly fulfilled, as the SPP mode indices still slightly exceed those of tapered optical fibers.

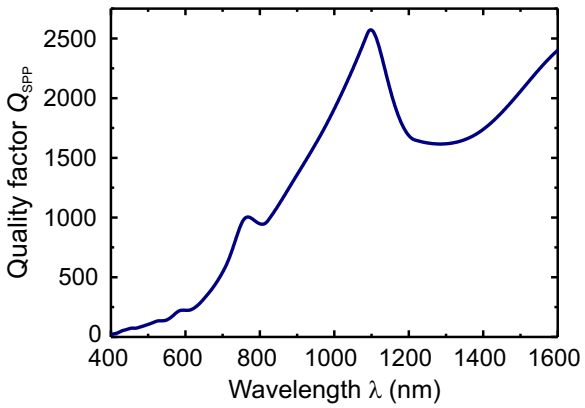

Figure 5.5: Impact of excitation wavelength λ on the Q-factor of SPPs sustained at a plane silver–polymer interface. Higher Q-factors at longer wavelengths favor exciting SPP modes at wavelengths in the near-IR over the visible spectral range.

5.2.4 Q-factors of SPPs

We conclude the discussion about the properties of SPPs propagating along a plane silver-polymer interface with examining their Q-factors. Although Q-factors of SPPs strongly depend on the specific geometry of the underlying photonic structure, the Q-factors of SPPs sustained at a plane metal–dielectric interface can be considered as a generic limiting case. Assuming that the dielectric is weakly dispersive, the Q-factors of SPPs sustained at the plane metal–dielectric interface in the low-loss limit are given by [222]:

$$Q_{\mathrm{SPP}} = \frac{k'_{\mathrm{SPP}}}{2k''_{\mathrm{SPP}}} \approx \frac{(\epsilon'_2)^2}{\epsilon''_2}. \tag{5.5}$$

From Eq. 5.5 we see that the Q-factors of SPPs are solely determined by the metal's permittivity. Plotting the Q-factors Q_{SPP} of SPPs sustained at the silver–polymer interface in Fig. 5.5 versus the wavelength λ shows that the Q-factors tend to increase with increasing wavelength with a local maximum at $\lambda{\approx}1100\,\mathrm{nm}$. Whereas the Q-factors of SPPs for wavelengths $\lambda{<}600\,\mathrm{nm}$ are less than $\sim$200, they approach values exceeding a thousand in the near-infrared. Increased Q-factors of SPPs at longer wavelengths, thus, provide an additional argument for operating silver-coated WGM resonators in the near-infrared, whose total Q-factor is metal-loss limited.

5.2.5 Conclusions

The results presented in this section show that silver is a suitable coating metal for WGM resonators due to comparably weak damping rates at optical frequencies, enabling a low-loss propagation of SPP modes. Operation wavelengths in the near-infrared are seen to be critical to largely fulfill phase matching between SPP modes and the fundamental mode of

a tapered optical fiber used to evanescently excite SPP modes in silver-coated polymeric microwedges (see section 5.5). Despite increased mode volumes, the longer propagation lengths, larger field penetration depths into the dielectric and increased Q-factors of SPPs in the near-infrared compared to wavelengths in the visible spectral range are furthermore beneficial from an experimental point of view.

However, as optical properties of SPPs also depend on the underlying geometry, the simple model of SPPs sustained at a plane interface between two semi-infinite metal and dielectric half-spaces can only provide first basic guidelines for the design of metal-coated WGM resonators. As it is not capable of describing effects related to the finite thickness of the silver coating layer and the polymeric resonator body, the optical properties of SPP modes supported by silver-coated WGM resonators are expected to deviate from those calculated here. Whereas strong deviations are expected for silver films being notably thinner than the SPP penetration depth into silver ($\delta_2 \approx 20\,\mathrm{nm}$), the optical properties of SPP modes in silver-coated WGM resonators are expected to approach those calculated here in the limit of thick silver coatings and polymeric resonator bodies being thick compared to the penetration depth into the polymer.
To analyze the impact of the exact resonator geometry and the silver film thickness on the modal properties of silver-coated WGM resonators, we introduce in the next section a numerical framework based on the finite-element method (FEM) to efficiently model modes in silver-coated WGM resonators.

5.3 Simulation-based optimization of silver-coated polymeric WGM resonators

Based on numerically efficient FEM simulations using a bent-waveguide approach, we identify in this section a promising polymeric WGM resonator template which supports SPP, DE, and HY modes when coated with a thin silver layer from the top.

After introducing the bent-waveguide approach for efficient mode modeling in section 5.3.1, we discuss in section 5.3.2 why a wedge-like resonator geometry is indispensable for the existence of SPP, DE, and HY modes and to efficiently and selectively excite them by means of a tapered optical fiber. In this context, we study the impact of the exact geometry of the underlying polymeric microwedge and the silver coating thickness on the optical properties of SPP, DE, and HY modes. The results presented in this section build the foundation for the later experiments.

5.3.1 Bent-waveguide approach for efficient mode modeling

To gain insight into the modal characteristics of silver-coated polymeric WGM microresonators, FEM simulations using the commercially available software JCMsuite are performed [182].

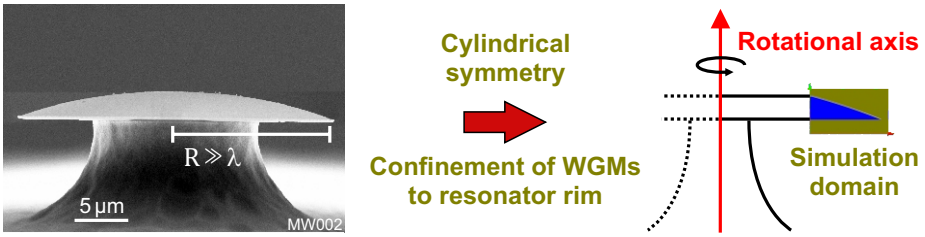

Figure 5.6: Schematic illustration of the bent-waveguide approach for mode modeling. Exploiting the cylindrical symmetry of WGM resonators and the confinement of WGMs to the resonator rim allows to drastically reduce the size of the simulation domain. Modeling the resonator rim as a bent waveguide being concentric around the rotational axis of the resonator allows performing numerically efficient 2D-simulations. Adapted from [85].

As polymeric WGM resonators with typically tens of micrometers in diameter are large compared to the wavelength of light and a high local resolution is required to properly resolve the mode profiles of WGMs, their numerical treatment is challenging. The task of simulating the full three-dimensional structure gets even more demanding when introducing a thin silver layer with a thickness of a few up to a hundred nanometers on top of the resonator surface. To accurately account for local field enhancements at the silver–polymer interface, extremely fine meshes are needed for the computation, leading to tremendous computational costs. With the computational resources available, a rigorous 3D simulation of silver-coated WGM resonators is, therefore, not feasible.

To significantly reduce simulation costs while still being able to accurately describe modes supported by silver-coated WGM resonators, we exploit their cylindrical symmetry together with the fact that WGMs are localized at the rim of the resonator. Exploiting the rotational symmetry of WGM resonators allows to reduce the simulation domain from three to two dimensions (see also section 4.4.1). Considering additionally that WGMs are spatially confined only to a small region close to the resonator rim allows to further significantly reduce the simulation domain, as graphically illustrated in Fig. 5.6. Instead of simulating the whole 3D structure, it is, hence, sufficient to consider only the resonator rim in the simulations, which "can be modeled as a bent waveguide forming a concentric ring around the rotational axis of the resonator" [85].

With this approach, the eigenmodes of a WGM resonator can be described by a set of dissipative eigenmodes of a bent waveguide [194, 223–225]. Using the propagation-mode solver provided by JCMsuite, these modes are fully characterized by their complex effective refractive index n_{eff} and their cross-sectional field distribution, which is the FEM-simulation outcome. Using the resonance condition for WGMs (Eq. 2.1) and requiring that both the amplitude and the phase of the mode's field have to be reproduced after each round trip through the loop, the resonance wavelength λ_m and the Q-factor Q_m of a mode with azimuthal mode number m can be directly calculated from the complex effective refractive

index $n_{\text{eff}}=n'_{\text{eff}}+in''_{\text{eff}}$ [223]:

$$\lambda_m = \frac{2\pi R}{m} n'_{\text{eff}}, \tag{5.6}$$

$$Q_m = \frac{n'_{\text{eff}}}{2n''_{\text{eff}}}, \tag{5.7}$$

where $m \in \mathbb{Z}$. For an arbitrarily chosen input wavelength, the resonance condition is in general not fulfilled and $m \notin \mathbb{Z}$. To account for the dispersive character of n_{eff}, Eq. 5.6 is therefore solved in a self-consistent manner by iterating over the input wavelength until a resonance λ_m is hit. The accuracy in determining the spectral resonance position of a WGM is chosen such that the error is smaller than the resonance linewidth.

5.3.2 Optimization of hybrid resonator design for efficient and selective mode excitation

With the numerically efficient bent-waveguide simulations at hand, we now turn to the task of identifying an optimal hybrid WGM resonator design that supports SPP, DE, and HY modes and ensures that all modes can be efficiently and selectively excited with the evanescent field of a tapered optical fiber. The optimization process focuses on resonator geometries which can be fabricated lithographically on a polymer basis, i.e. WGM resonators with disk-, goblet-, and wedge-like geometry (see section 3.1). Falling back to the findings from section 5.2, wavelengths in the near-infrared around 1500 nm are used to simulate the silver-coated WGM resonators of various geometries and air is considered as surrounding medium. The permittivity values for silver and PMMA provided by Johnson and Christy [177] and Beadie [226], respectively, are used to consider the materials' dispersive character.

Impact of cavity geometry on mode spectrum of silver-coated WGM resonators

On the basis of Fig. 5.7, which shows the cross-sectional electric field intensity distributions of different first order modes supported by silver-coated WGM resonators with disk- (left), goblet- (middle), and wedge-like geometry (right), we examine in the following which of these resonators fulfills the above target requirements best. For the moment, we focus on silver coatings with a thickness of 100 nm. The resonators are coated from the top with a thin silver layer to ensure that the distinct cavity eigenmodes can be accessed evanescently with a tapered optical fiber approached to the silver-free bottom surface of the resonators from below. In the case of the disk- and goblet-like WGM resonators not only the top resonator surface is coated with silver, but also the side surfaces. This is due to the fact that experimentally, where silver is deposited onto the WGM resonators using physical vapor deposition, one cannot prevent that silver atoms deposit also on the side surfaces of these structures.

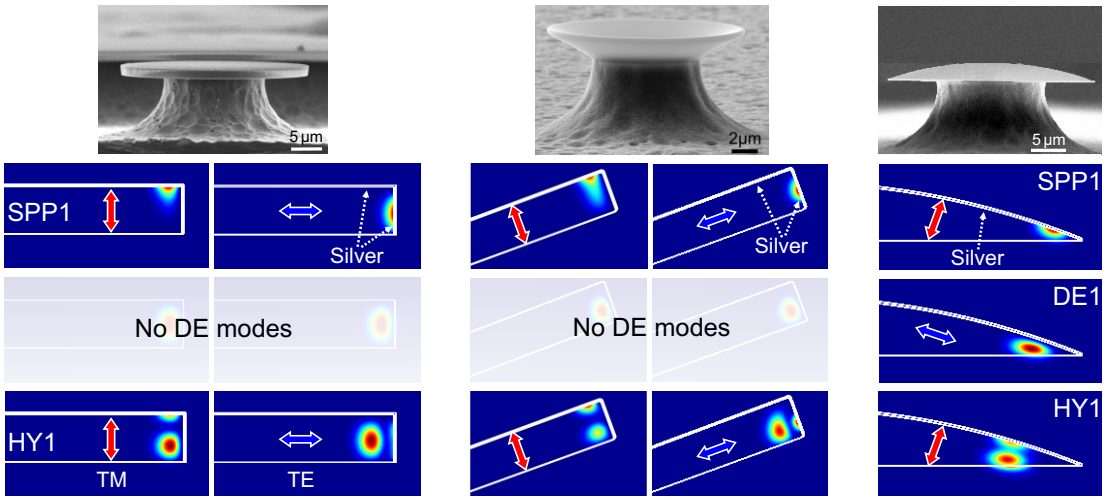

Figure 5.7: Modal structure of silver-coated polymeric WGM resonators of varying geometries. Comparing the cross-sectional electric field intensity distributions of first order modes supported by a silver-coated PMMA microdisk (left), -goblet (middle), and -wedge (right) shows that only the wedge-like WGM resonator supports SPP (top), DE (middle), and HY modes (bottom). The electric field vectors of the cavity eigenmodes are indicated by arrows. Silver-coated microdisks and -goblets do not support purely DE modes because TM- (red arrow) and TE-polarized (blue arrow) DE modes in these structures couple to SPP modes localized at the resonators' top and side surfaces, respectively, to form HY modes. The wedge-like geometry is seen to effectively push the distinct resonator modes into the surrounding and is responsible for spatially separating their centers of gravity. Both effects pave the way for an efficient and selective excitation of SPP, DE, and HY modes with the evanescent field of a tapered optical fiber.

According to their distinct localization and polarization characteristics (indicated by arrows), we can classify the cavity eigenmodes shown in Fig. 5.7 into three groups. The eigenmodes in the top panel of Fig. 5.7, which are localized at the silver–polymer interface and are polarized perpendicular to the interface are first order SPP (SPP1) modes. These modes are supported by all three resonator types. The eigenmode shown in the middle panel of Fig. 5.7, which is only existent in the wedge-like resonator, is a first order DE (DE1) mode. It is localized mainly in the PMMA and polarized parallel to the silver–polymer interface. The eigenmodes shown in the bottom of Fig. 5.7, which are again supported by all three resonator types, are first order HY (HY1) modes. Due to their SPP character, these modes are TM-polarized and combine the mode localization characteristic of DE and SPP modes.
From Fig. 5.7 we can conclude that only the silver-coated WGM resonator with wedge-like geometry supports SPP, DE, and HY modes. In silver-coated microdisks and -goblets, the DE modes with polarizations parallel (TE-modes) and perpendicular (TM-modes) to the resonator plane readily couple to SPP modes sustained at the side and the top silver-polymer interfaces, respectively, to form HY modes. Contrary, in silver-coated microwedges only DE modes with a polarization perpendicular to the silver layer can hybridize with the inherently TM-polarized SPP modes sustained at the top silver–polymer interface. Due to the absence of a coupling partner for the DE modes with a polarization parallel to the interface, the hybrid microwedge supports all three mode types.
A further advantage of the hybrid microwedge over the resonators with disk- and goblet geometries is that the distinct eigenmodes get effectively 'pushed' away from the silver–polymer interface owing to the inclined resonator edge. This effect results in an increased evanescent field overlap of the distinct mode types with the surrounding and a spatial separation of their centers of gravity, which is extremely beneficial from an experimental point of view. Whereas the increased evanescent field overlap with the surrounding paves the way for an efficient excitation of the distinct modes with the evanescent field of a tapered optical fiber, the spatial separation of the modes is the foundation to selectively address them (see section 5.5.2). These considerations show that a polymeric WGM resonator with wedge-like geometry is an ideal template to build a hybrid system that supports SPP, DE, and HY modes.

By analyzing the impact of the exact resonator geometry on the modal properties of the distinct mode types, we motivate in the following why the fabricated silver-coated microwedge shown in the scanning electron micrograph in Fig. 5.7 with resonator radius r_{edge}=14.6 µm, wedge angle Θ=21.6°, and silver coating thickness t=103 nm is a promising experimental platform. The analysis focuses on modes with SPP character and aims at identifying optimal cavity design parameters for which the Q-factors of the respective modes are as high as possible and for which phase matching of the distinct eigenmodes with a tapered-fiber eigenmode is largely fulfilled. The geometrical dimensions of the fabricated silver-coated microwedge in Fig. 5.7 serve as starting point for the parameter optimization and only selected parameters are swept through.

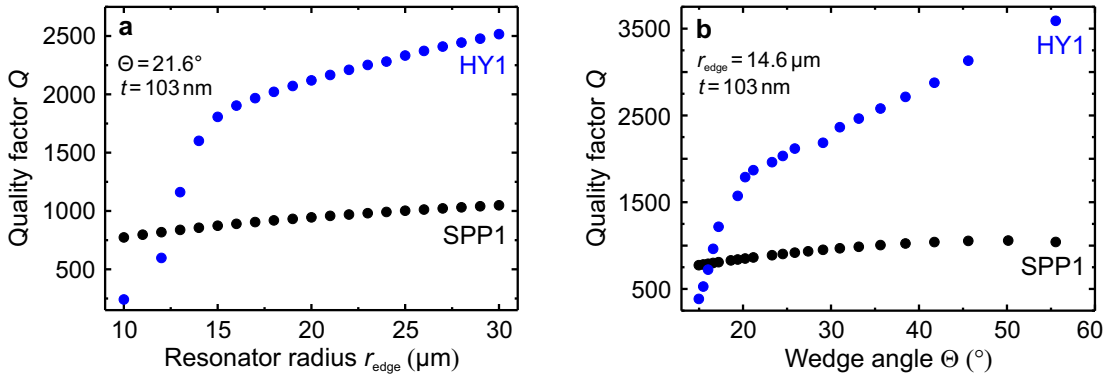

Figure 5.8: Impact of resonator radius r_{edge} (a) and wedge angle Θ (b) on the Q-factors of SPP1 and HY1 modes in silver-coated polymeric microwedges. The Q-factors of the modes with SPP character increase with increasing resonator radius and wedge angle. Owing to the strong localization of the SPP1 mode at the silver–PMMA interface, its Q-factor is less sensitive to variations in cavity geometry compared to the HY1 mode. For resonator radii $r_{\mathrm{edge}} \lesssim 15\,\mu\mathrm{m}$ and wedge angles $\Theta \lesssim 20°$ the HY1 mode gets strongly pushed into the surrounding, which results in a rapid Q-factor decay in this parameter regime.

Impact of resonator radius on modal properties of silver-coated microwedges

From Fig. 5.8(a), where the Q-factors of the SPP1 (black) and HY1 modes (blue) are plotted versus the resonator radius r_{edge}, it is visible that the Q-factors of both modes monotonically increase with increasing resonator radius. Q-factors exceeding 2500 are predicted for the HY1 mode, Q-factors slightly above 1000 are predicted for the SPP1 mode. Whereas the Q-factor of the SPP1 mode increases only moderately in the investigated parameter regime, the Q-factor of the HY1 mode rapidly increases when increasing the resonator radius toward $r_{\mathrm{edge}} \approx 15\,\mu\mathrm{m}$. For resonator radii $r_{\mathrm{edge}} < 15\,\mu\mathrm{m}$, the HY1 mode is strongly 'pushed' into the surrounding medium, leading to a rapid Q-factor decay.
To achieve reasonably high Q-factors for the HY1 mode, resonator radii of silver-coated polymeric microwedges should, thus, not drop below values of $r_{\mathrm{edge}} \approx 15\,\mu\mathrm{m}$. But, owing to the finite propagation length of SPPs [see Fig. 5.2(a)], resonator radii should also not exceed values larger than $\sim 20\,\mu\mathrm{m}$ to ensure that the SPP modes propagate several times around the resonator circumference before their energy is dissipated into heat.

Impact of wedge angle on modal properties of silver-coated microwedges

Performing bent-waveguide simulations of silver-coated polmyeric microwedges for varying wedge angles shows that wedge angles $\Theta \lesssim 60°$ are critical for the existence of SPP, DE, and HY modes. For larger wedge angles, the resonators do not support purely DE modes, as they readily couple to SPP modes sustained at the top and the inclined side surface of the micowedges to form HY modes.

Reducing the wedge angle is seen to effectively 'push' the distinct cavity eigenmodes into the surrounding. Although the increased evanescent field overlap with the surrounding is beneficial to efficiently excite the cavity eigenmodes with the evanescent field of a tapered optical fiber, it negatively affects the modes' Q-factors, as visible from Fig. 5.8(b), where the Q-factors of the SPP1 (black) and HY1 modes (blue) are plotted versus the wedge angle Θ. Whereas only a slight decrease in Q-factor is observed for the SPP1 mode due to its strong localization at the silver–polymer interface, the HY1 mode's Q-factor degrades rapidly for wedge angles $\Theta \lesssim 20°$ owing to a strongly increased mode overlap with the surrounding. For wedge angles $\Theta < 15°$, the Q-factors of the HY1 mode are less than 400 and, hence, even lower than those of the SPP1 modes. These considerations hint to the tradeoff between maximizing the Q-factor of the distinct eigenmodes and simultaneously maximizing the field overlap with an exciting tapered-fiber eigenmodes.

Impact of silver coating thickness on modal properties of silver-coated WGM microwedges

In the following, we analyze the impact of the silver coating thickness on the effective refractive indices of SPP1, DE1, and HY1 modes and the Q-factors of the modes with SPP character.
To study the dispersive behavior of SPP1, DE1, and HY1 modes under variations of the silver coating thickness and check whether the distinct modes can be excited with a tapered optical fiber, we plot their effective refractive indices n_{eff} in Fig. 5.9(a) versus the silver coating thickness t. The three distinct mode types are seen to differ in their effective mode indices and their dispersive behavior, which indicates their distinct nature. Whereas the effective refractive index of the DE1 mode (red) is with $n_{\text{eff}} \approx 1.3$ almost invariant against variations in the silver layer thickness, the SPP1 mode (black) shows a strong dispersion for silver coatings being thinner than the SPP penetration depth $\delta_2 \approx 20\,\text{nm}$ into silver (see section 5.2.2). For such thin silver films, a significant part of the SPP1 mode's evanescent field penetrates through the silver coating into the surrounding air, as visible from the left inset in Fig. 5.9(a), where the electric field intensity distribution of a SPP1 mode is shown exemplarily for a 10 nm thick silver coating. Furthermore, the SPP1 mode is seen to be strongly localized at the interface, a property that is reflected in an increased effective mode index. Although the tighter confinement of the SPP modes together with the strong field enhancement at the silver–air interface in the case of thin silver coatings is beneficial, e.g., for sensing applications, their comparatively high effective refractive indices ($n_{\text{eff}} > 1.5$) prevent the excitation of SPP modes by means of a tapered optical fiber. To access SPP modes in silver-coated microwedges evanescently with a tapered-fiber eigenmode, silver coating thicknesses exceeding the SPP penetration depth δ_2 into silver are necessary, according to Fig. 5.9(a), to bring their effective refractive indices into a regime where phase matching between fiber and resonator mode is largely fulfilled. For such comparatively thick silver coatings, the SPP1 mode is localized at the inner silver–polymer interface, as visible from the right inset in Fig. 5.9(a), and the effective refractive index ($n_{\text{eff}} \approx 1.48$) approaches the one calculated for SPPs propagating along

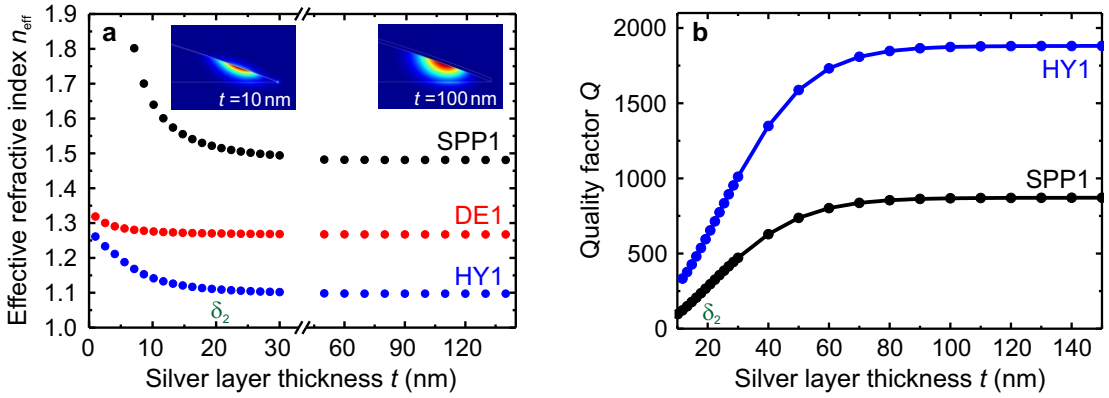

Figure 5.9: Impact of silver layer thickness t on effective refractive indices n_{eff} and Q-factors of SPP1, DE1, and HY1 modes supported by the investigated microwedge [227]. (a) Differences in the dispersive behavior of the cavity eigenmodes under variations in the silver layer thickness indicate the distinct nature of the modes. For silver layer thicknesses smaller than the penetration depth δ_2 into silver, the effective refractive index of the SPP1 mode is highly sensitive to variations in t. The insets show the cross-sectional electric field intensity distributions of a SPP1 mode for t=10 nm (left) and t=100 nm (right). For thin silver layers, the SPP1 mode is strongly confined at the interface, which is reflected in an increased effective mode index. (b) Higher Q-factors of the modes with SPP character for thicker silver layers together with the saturation behavior favor coating polymeric microwedges with silver layers with $t \gtrsim 70$ nm. (a) Adapted from [85].

a plane silver–polymer interface (see section 5.2). The fact that the HY1 mode (blue) exhibits an intermediate dispersive behavior and an effective mode index saturating at the same silver coating thickness as that of the SPP1 mode shows that it indeed emerges from the hybridization of a DE and a SPP mode. Owing to the large field overlap of the HY1 mode with the surrounding, the HY1 mode exhibits the smallest effective mode index among the three distinct mode types, approaching $n_{\text{eff}} \approx 1.1$ for thick silver coatings.
These results demonstrate that silver coatings being thick compared to the penetration depth of SPPs into silver are indispensable to access all three mode types in silver-coated microwedges evanescently with a tapered optical fiber. Whereas phase matching between a fiber eigenmode and the DE1 and HY1 modes can be fulfilled for all considered silver coating thicknesses, a phase-matched excitation of the SPP1 can only be achieved for comparatively thick silver layers.

An additional argument for coating the polymeric microwedges with a comparatively thick silver layer is provided by Fig. 5.9(b), where the Q-factors of the modes with plasmonic character are plotted versus the silver coating thickness t.
The Q-factors of both the SPP1 and the HY1 mode increase monotonically with increasing silver layer thickness until they reach saturation at silver layer thicknesses beyond $t \approx 70$ nm. The higher Q-factors for thicker silver coatings together with the fact that the modal properties of the SPP1 and the HY1 mode are invariant against slight deviations in the thickness of the deposited silver film far above the saturation threshold favor coating the

resonators with silver films with thicknesses $t \gtrsim 70\,\text{nm}$.
We'd like to note that although the mode volumes of SPP1 and HY1 modes slightly increase with increasing silver film thickness until they saturate beyond $t \approx \delta_2 \approx 20\,\text{nm}$, the increase in Q-factor dominates over the increase in mode volume. Therefore, silver layers above the saturation threshold are also beneficial to maximize the Q/V-ratio of SPP1 and HY1 modes supported by silver-coated microwedges.

Conclusions

The results presented in this section show that phase matching of SPP modes in silver-coated polymeric microwedges with a tapered-fiber eigenmode in the near-infrared can only be largely fulfilled for silver coatings being thick compared to the SPP penetration depth $\delta_2 \approx 20\,\text{nm}$ into silver. From an experimental point of view, the deposition of silver layers with thicknesses $t \gtrsim 70\,\text{nm}$ is beneficial, as the optical properties of SPP, DE, and HY modes are robust against uncertainties in the deposited silver layer thickness in this regime. Wedge angles $20° \lesssim \Theta \lesssim 60°$ ensure the existence of all three mode types, while cavity radii $r_{\text{edge}} \gtrsim 15\,\mu\text{m}$ are critical for the high optical quality of the modes.
In the light of these facts, the silver-coated microwedge shown in the scanning electron micrograph in Fig. 5.7 with resonator radius $r_{\text{edge}} = 14.6\,\mu\text{m}$, wedge angle $\Theta = 21.6°$, and silver coating thickness $t = 103\,\text{nm}$ is an ideal platform to study the modal properties of SPP, DE, and HY modes in fiber–coupling experiments. Throughout the rest of this chapter, we focus on this structure.

5.4 Simulation of the modal characteristics of a fabricated silver-coated polymeric microwedge

In this section, we provide a comprehensive insight into the modal properties of the silver-coated polymeric microwedge and develop an experimental procedure based on mode filtering to selectively excite and unambiguously identify SPP, DE, and HY modes in fiber transmission spectra.

5.4.1 Modal properties of plasmonic (SPP), dielectric (DE), and hybrid (HY) modes

Based on Fig. 5.10, where we show the intensity distributions (left) and vector plots of the cross-sectional electric field (right) of all experimentally relevant modes supported by the investigated microwedge, we identify SPP, DE, and HY modes and work out differences in their modal properties. We focus on a set of modes with resonance wavelengths λ_m around 1550 nm. The resonance positions λ_m together with the Q-factors and mode volumes V of the respective modes are listed in Fig. 5.10.
The upper two modes in Fig. 5.10 being localized at the silver–polymer interface with

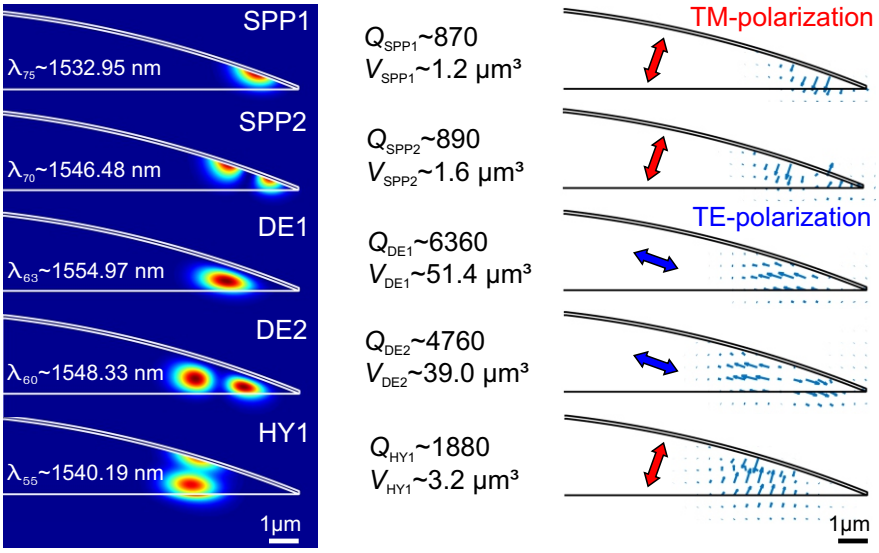

Figure 5.10: Intensity distributions (left) and vector plots (right) of the electric field of SPP1, SPP2, DE1, DE2, and HY1 modes with resonance wavelengths λ_m around 1550 nm supported by the investigated hybrid microwedge. The distinct mode localization and polarization characteristics together with differences in the Q-factors and mode volumes V, as calculated from the electromagnetic energy density (Eq. 2.7), indicate the distinct nature of the various cavity eigenmodes. Taken from [85].

one and two modal maxima in radial direction can be identified as first- and second order SPP modes (SPP1 and SPP2), respectively. In accordance with SPPs propagating along a plane silver–PMMA interface, these modes are TM-polarized. The subsequent two modes depicted in Fig. 5.10 are mainly localized inside the polymeric resonator body. Together with the fact that they are polarized parallel to the silver–polymer interface, it can be concluded that these modes are of purely dielectric nature. According to their field distribution, they can be identified as the first- and second-order DE modes (DE1 and DE2). The mode depicted in the bottom of Fig. 5.10 with one modal maximum close to the silver–PMMA interface and one modal maximum close to the bottom surface of the microwedge unites the mode localization characteristic of SPP and DE modes. As this mode is mainly polarized perpendicular to the silver–polymer interface, hinting to its SPP character, it can be identified as the HY1 mode. Although higher-order HY modes exist in principle, they cannot be excited experimentally owing to their small effective refractive indices close to unity. Therefore, they are not considered in Fig. 5.10.
Comparing the intensity distributions of the different eigenmodes, we notice that the centers of gravity of the modes increasingly shift from the resonator edge toward the rotational axis of the resonator when moving from the top to the bottom in Fig. 5.10. Whereas the SPP1 mode is localized closest to the resonator edge, the HY1 mode is localized furthest inside the resonator. The spatial separation of the different eigenmodes in the silver-coated microwedge together with their distinct polarization characteristics is the foundation to

selectively address them with the evanescent field of a tapered fiber (see section 5.5.2).
The different nature of SPP, DE, and HY modes manifests itself additionally in important figures-of-merit, such as the Q-factor and the mode volume V. In accordance with our expectation, the SPP modes exhibit with $Q{\approx}900$ the lowest Q-factors in the system due to large ohmic losses in the metal. Owing to the light-focusing character of SPPs, the SPP1 and SPP2 modes exhibit with $V{\approx}1.2\,\mu m^3$ and $V{\approx}1.6\,\mu m^3$, however, also the smallest mode volumes. Their mode volumes are on the order of a cubic wavelength and, thus, significantly smaller than the mode volumes of the low-loss DE1 and DE2 modes ($V{\approx}51.4\,\mu m^3$ and $V{\approx}39.0\,\mu m^3$). Since the DE1 and DE2 modes are mainly localized inside the PMMA, their Q-factors ($Q{\approx}6400$ and $Q{\approx}4800$) exceed those of the SPP modes by an order of magnitude. The HY1 mode is, finally, seen to successfully combine the low-loss characteristic of the DE modes with the light-focusing characteristic of SPP modes, which is reflected in intermediate values for the Q-factor ($Q{\approx}1900$) and an ultra-small mode volume of only $V{\approx}3.2\,\mu m^3$, which is close to the value obtained for SPP modes.
We'd like to emphasize that the calculation of the mode volumes relies, according to Eq. 2.7, on the electromagnetic field energy density $u(\mathbf{r})$ in dispersive media, whose electric component is proportional to the derivative of $\omega\epsilon(\mathbf{r},\omega)$ with respect to the angular frequency ω. Since silver is strongly dispersive at optical frequencies, the volume integral in Eq. 2.7 is governed by the field components of an eigenmode in the silver layer. A larger field penetration of an eigenmode into the silver layer, hence, translates to a reduced mode volume. The differences in the mode volumes of the distinct eigenmodes are, thus, not apparent from Fig. 5.10, where only the electric field intensity distribution and not the electromagnetic energy density of the modes is plotted.

The systematic analysis of the modal characteristic of the fabricated silver-coated polymeric microwedge shows that the hybrid resonator supports various mode types with largely disparate properties. Differences in the spectral resonance positions, Q-factors, polarization characteristics, and mode localization can be identified as experimentally relevant criteria to distinguish between the various modes observed in fiber transmission spectra.

5.4.2 Uncertainties in simulated spectral features

However, as the simulated values for the resonance positions λ_m and Q-factors of the cavity eigenmodes are highly sensitive to slight deviations in the resonator geometry and the material properties, an unambiguous identification of resonances in fiber transmission spectra solely based on a quantitative comparison between simulated and experimentally observed spectral features is challenging. Uncertainties in the resonator dimension, as extracted from scanning electron micrographs, together with uncertainties in the literature values for the silver permittivity [228–231] translate to significant errors in the calculated resonance wavelengths and Q-factors of the cavity modes.
Whereas uncertainties in the tabulated values of the silver permittivity most strongly affect the modes with SPP character, leading easily to errors in the calculated Q-factors of

the SPP modes of a few hundred in the near-IR, uncertainties in the extracted resonator geometry drastically affect the resonance positions of all mode types. For instance, errors in the resonator radius of ±50 nm (±3 pixel in the scanning electron micrograph) lead to deviations in the calculated resonance positions of $\delta\lambda_m \approx \pm 5$ nm for all mode types. Errors in the wedge angle of $\delta\Theta \approx \pm 2°$ have an even larger impact on the calculated resonance positions and influence the spectral positions of SPP, DE, and HY modes to a different degree. Whereas the smallest error in the resonance wavelength is observed for the SPP1 modes ($\delta\lambda_m \approx \pm 13$ nm), the resonance wavelengths of the HY1 modes are with errors as high as $\delta\lambda_m \approx \pm 32$ nm, which is almost twice the free spectral range, most strongly affected by uncertainties in Θ [84].
Considering these large errors in the simulated spectral features makes clear that modes observed in fiber transmission spectra cannot be unambiguously identified by simply comparing simulated and measured spectral resonance positions and Q-factors. Instead, a reliable mode classification scheme which is robust against slight deviations in the resonator geometry and material parameters is needed to unequivocally assign the resonances.

5.4.3 Mode filtering technique for unambiguous mode classification

By performing FEM simulations of the silver-coated microwedge which explicitly include the coupling to a tapered fiber and applying coupled-mode theory (CMT), we developed a reliable mode classification scheme based on mode filtering to unambiguously identify the various eigenmodes observed in fiber transmission spectra [232]. Instead of quantitatively comparing simulated and experimentally determined mode properties, the proposed mode classification scheme exploits qualitative differences in the mode localization and propagation to classify the modes. Therefore, it is robust against slight deviations in resonator geometry and material properties. In analogy to the experiment, the fiber in the FEM simulations is positioned underneath the silver-free bottom surface of the resonator to evanescently excite the distinct cavity eigenmodes, as illustrated in Fig. 5.11. The simulation approach used to model the joint fiber–resonator sytem is detailed in the appendix B.1.

To efficiently excite the cavity eigenmodes of a WGM resonator with the evanescent field of a tapered fiber, two conditions need to be fulfilled. First, the effective refractive index of the fundamental fiber mode and the cavity mode of interest must match to ensure a coherent energy transfer between both systems. Second, the evanescent field of the fiber mode must substantially overlap with the evanescent field of the considered cavity eigenmode. Therefore, both the radius of the input fiber and its position relative to the modal maximum of the cavity mode must be carefully adjusted.
However, the distinct eigenmodes supported by the model silver-coated microwedge differ in their effective mode indices n_{eff} and their mode localization characteristic (see Fig. 5.10). Whereas the SPP1 mode has an effective mode index around n_{eff}=1.48, the mode indices of the DE1 mode (n_{eff}=1.27) and the HY1 mode (n_{eff}=1.1) are notably smaller in the considered wavelength range. Consequently, phase matching cannot be simultaneously

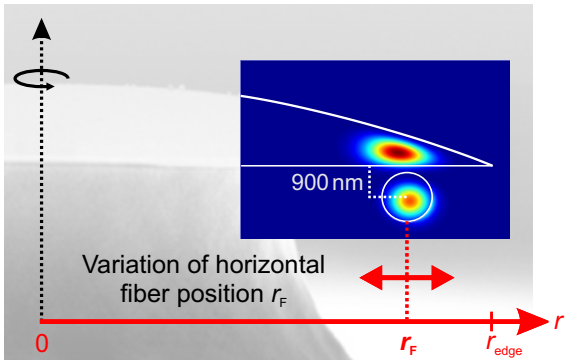

Figure 5.11: Illustration of the joint fiber–resonator system used to compute fiber–resonator coupling efficiencies for varying horizontal fiber positions r_F. The fiber in the FEM simulations is moved horizontally underneath the silver-free bottom surface of the hybrid microwedge at a constant vertical distance of 900 nm between the fiber axis and the bottom surface of the resonator. Tuning the horizontal fiber position r_F with respect to the resonator edge is the key to selectively address and classify the distinct cavity eigenmodes.

optimized for SPP, DE, and HY modes for a given input fiber. Furthermore, since the centers of gravity of the distinct eigenmodes are localized at different radial positions, accessible resonator modes and associated fiber–resonator coupling efficiencies are expected to strongly depend on the horizontal position of the fiber relative to the resonator edge. Assuming that coupling into SPP, DE, and HY modes is possible for the same input fiber, moving the fiber horizontally underneath the resonator from the resonator edge toward its rotational axis should, thus, result in a successive excitation of SPP1, SPP2, DE1, DE2, and HY1 modes, respectively.

To verify that tuning of the horizontal fiber position is the key to unambiguously classify the resonator modes, we derive in the appendix B.2 a method to compute the power P transferred from an input fiber to the distinct cavity eigenmodes as a function of the horizontal fiber position r_F. The transferred power P serves as a measure for the fiber–resonator coupling efficiency and is proportional to the dip depth of Lorentzian-shaped resonances observed in fiber transmission spectra.
Plotting the power P transferred from an input fiber with a radius of 700 nm into distinct eigenmodes with resonance wavelengths around 1500 nm versus the horizontal fiber position r_F produces Fig. 5.12(a). The selected fiber radius corresponds to a typical fiber radius used in the experiment. Moving the fiber horizontally underneath the resonator at a constant vertical distance of 900 nm between the fiber axis and the bottom surface of the resonator from the resonator edge r_{edge}=14.6 µm toward its rotation axis (r_F=0 µm) is seen to result in a successive excitation of the SPP1, SPP2, DE1, DE2, and HY1 modes, respectively. As expected from the values for the fiber–resonator coupling constants κ calculated in the appendix B.2, the DE1 mode is most strongly excited. From Fig. 5.12(a) it is expected, that all the five distinct modes can be observed experimentally in fiber transmission spectra using an input fiber with a radius around 700 nm.

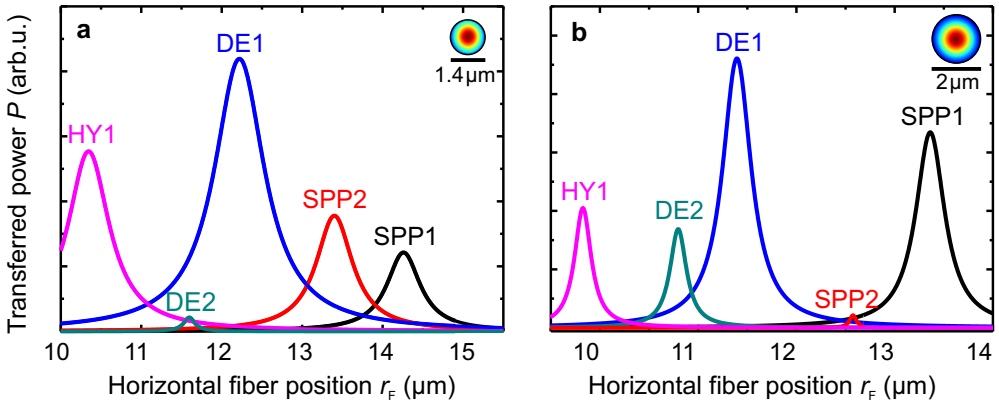

Figure 5.12: Calculated power P transferred from fibers with radii R_F=700 nm (a) and R_F=1 µm (b) to distinct cavity eigenmodes of the investigated silver-coated microwedge for varying horizontal fiber positions r_F [232]. Moving the fiber underneath the resonator from the resonator edge r_{edge}=14.6 µm toward the rotation axis (r_F=0 µm) results in a selective and successive excitation of SPP1, SPP2, DE1, DE2, and HY1 modes, respectively. Increasing the fiber radius alters the relative coupling efficiencies, but not the order of appearance of the modes when tuning the fiber position, which is the basis for a reliable mode classification in fiber–coupling experiments.

To analyze the influence of the fiber radius on the phase-matched excitation of the distinct cavity eigenmodes, we plot in Fig. 5.12(b) the results for the transferred power P for an input fiber with a radius of 1 µm. The comparison with Fig. 5.12(a) reveals that increasing the fiber radius favors the excitation of the SPP1 mode and the DE2 mode, while lowering the coupling into the HY1 and the SPP2 modes. The DE1 mode is again seen to dominate over the other modes supported by the silver-coated model microwedge. Furthermore, increasing the fiber radius is seen to shift the point of maximal coupling for all modes toward smaller horizontal fiber positions r_F. However, and this is the basis for a reliable mode classification in experiments, the order of appearance when moving the fiber from the resonator edge toward the rotation axis remains unaffected.

The results presented in this section suggest that SPP, DE, and HY modes can be efficiently excited with the evanescent field of a tapered fiber using operation wavelengths in the near-infrared. Owing to differences in the modal overlap and phase matching, the fiber–resonator coupling efficiencies differ among the distinct eigenmodes supported by the silver-coated microwedge and their relative excitation strength is determined by the fiber radius. Tuning the horizontal fiber position with respect to the resonator edge is seen to result in a selective excitation of the individual eigenmodes supported by the silver-coated microwedge, which paves the way for a clear assignment of modes observed in fiber transmission spectra.

5.5 Identification of SPP, DE, and HY modes in a silver-coated polymeric microwedge in fiber–coupling experiments

Exploiting the largely disparate properties of SPP, DE, and HY modes and relying on the mode filtering technique developed in the previous section, we analyze the modal properties of the model silver-coated polymeric microwedge in this section experimentally. Utilizing the orthogonality of the polarization of DE modes and modes with SPP character in combination with Q-factor differences, we first present results of polarization-dependent measurements to gain first experimental insight into the mode spectrum of the hybrid microwedge. We then follow the proposed mode filtering technique to unambiguously classify the resonator modes and demonstrate the existence of SPP, DE, and HY modes. The measurements are performed on the fiber-coupling setup introduced in section 3.3.2. To ensure sufficient phase matching between the fundamental fiber mode and the distinct resonator eigenmodes, an input fiber tapered down to a radius of approximately 700 nm is used (see section 5.3.1), which is positioned underneath the silver-free bottom surface of the resonator. The radius of the tapered fiber in the coupling region is estimated from top-view micrographs during the experiments.

5.5.1 Polarization-dependent excitation scheme for preliminary mode classification

As controlling the input laser polarization plays the key role to discriminate between DE modes and modes with SPP character in the experiment, we detail in the following the technical means to identify an optimal input laser polarization state that maximizes the coupling into a specific eigenmode (see also section 3.3.2).
Provided that phase matching between the fiber and the resonator mode is fulfilled and that the horizontal fiber position is properly adjusted, optimal fiber–resonator coupling occurs if the polarization vectors of the exciting fiber field and the resonator mode coincide. If the wavelength of the tunable laser hits the mode's resonance wavelength, the complete power is transferred from the fiber into the resonator mode. The respective Lorentzian-shaped dip observed in the fiber transmission spectrum is then most strongly pronounced. Deviations from the optimal input fiber polarization reduce the fiber–resonator coupling efficiency and lead to higher transmitted intensities at the cavity mode's resonance wavelength and less pronounced dips in the transmission spectrum.
The optimal polarization of the exciting fiber field can be determined by manually rotating the paddles of the fiber polarization controller (FPC) integrated in the fiber–coupling setup until the transmitted intensity at the resonance wavelength of the considered cavity mode is minimal. We'd like to emphasize that the exact polarization state of the exciting field in the tapered fiber region cannot be deduced from the paddle configuration of the FPC owing to the high sensitivity of the fiber polarization toward slight bending and twisting of the fiber. Such mechanical effects might, in particular and inevitably, lead to stress-

induced rotations of the polarization of the fiber field in regions between the tapered area and the fiber end where the transmission through the fiber is recorded. Therefore, conclusions regarding the direction of the polarization vector of the exciting fiber field in the coupling region cannot be drawn. Nevertheless, statements about the relative change of the polarization angle of the fiber field during a fiber–coupling experiment can be made once the fiber is fixed on the optical table. In particular, rotations of the exciting fiber field by 90°, as needed to optimally couple light either into DE modes or modes with SPP character, can be identified.

Let's now turn to the results of the polarization-sensitive excitation of the eigenmodes supported by the model silver-coated microwedge. To demonstrate that controlling the polarization of the exciting fiber field allows to discriminate between DE modes on the one hand and modes with SPP character on the other hand and to provide insight into a variety of supported eigenmodes, we show in Fig. 5.13 normalized fiber transmission spectra for three different input laser polarization states (black, red, and blue arrows) recorded at two different horizontal fiber positions $r_F \approx 13.75\,\mu m$ (highlighted in gray) and $r_F \approx 11.50\,\mu m$ (highlighted in orange).
For the fiber positioned at $r_F \approx 13.75\,\mu m$ close to the resonator edge and the input polarization state denoted by two black crossed arrows, two distinct mode types with significantly differing linewidths are observed in the transmission spectrum (black curve), "which repeat spectrally according to their free spectral ranges" [85]. Rotating the polarization angle of the exciting fiber field is seen to alter the relative excitation of both mode types. Whereas optimal coupling for the broad resonances with Q-factors around 600 (red curve) is obtained for the polarization state denoted by the red arrow, optimal coupling into the spectrally sharp resonances with Q-factors up to $\sim$3000 (blue curve) occurs if the polarization vector of the exciting fiber field is rotated by 90° (blue arrow) with respect to the optimal polarization angle identified for the spectrally broad resonances. Due to the orthogonality of the polarizations of both mode types, maximizing the fiber–resonator coupling efficiency for one mode type leads to the complete disappearance of the other mode type in the transmission spectrum. Recalling that DE modes in the silver-coated microwedge are polarized orthogonal to the modes with SPP character (see Fig. 5.10) and considering the observed Q-factor differences of both mode types, we can now make statements about the input fiber polarization.
Using the vector plots of the electric fields of the distinct cavity eigenmodes depicted in Fig. 5.10, we can conclude that the polarization vector of the exciting fiber field maximizing the coupling into the spectrally broad resonances with SPP character (red arrow) points in a direction perpendicular to the silver–polymer interface, whereas the one optimally exciting the spectrally sharp DE modes is parallel to the silver–polymer interface (blue arrow). The polarization state denoted by the black crossed arrows corresponds to a polarization angle of the fiber field in-between the two optimal polarization angles, thus, leading to the excitation of both mode types. Due to deviations from the optimal coupling conditions, the coupling into both mode types is, however, reduced for this input polarization state, which is reflected in less pronounced dips in the normalized transmission spectrum.

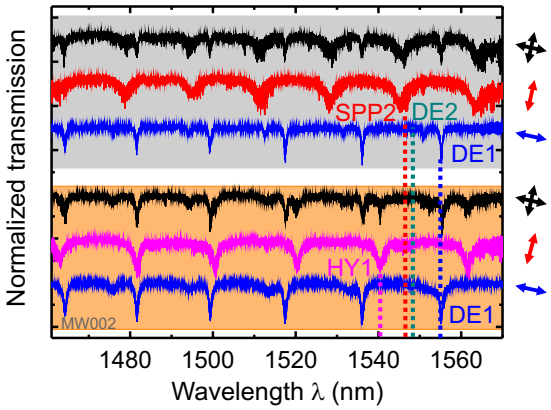

Figure 5.13: Polarization-dependent excitation of eigenmodes supported by the investigated silver-coated microwedge. Normalized transmission spectra are recorded for three different polarizations of the exciting fiber field (black, red, and blue arrows) and two horizontal fiber positions r_F=13.75 µm (gray) and r_F=11.5 µm (orange). Controlling the input laser polarization allows to discriminate between modes with SPP character and DE modes. Input laser polarizations perpendicular to the silver–polymer interface (red arrow) result in an optimal coupling to either SPP modes (red) or HY1 modes (magenta) – depending on the fiber position. Input laser polarizations parallel to the interface maximize the coupling into DE modes (blue). For polarization states in-between (black arrows), both DE modes and modes with SPP character are excited, however, with reduced coupling efficiencies. The remarkably good correspondence between simulated (vertical dashed lines) and experimentally observed resonance positions for a set of modes with resonance wavelengths around 1550 nm together with the distinct Q-factor ranges of the modes allows for a preliminary mode classification. Taken from [85].

Positioning the fiber more toward the rotation axis of the resonator (r_F≈11.50 µm) and recording transmission spectra for the same three input polarizations (highlighted in orange in Fig. 5.13) provides further insight into the mode spectrum of the resonator. Whereas the spectrally sharp DE modes with a polarization parallel to the silver–polymer interface are still present in the normalized transmission spectra (black and blue curves), the spectrally broad resonances observed for the fiber positioned close the resonator edge (r_F≈13.75 µm) cannot be excited anymore. Instead, a new mode with intermediate linewidth and Q-factor around ∼900 appears (black and magenta curve). This mode is optimally excited for an input polarization perpendicular to the silver–polymer interface. From its SPP character, the intermediate Q-factor, and the fact that it is localized at smaller horizontal fiber positions r_F compared to the modes with SPP character observed at r_F≈13.75 µm (red curve), we assume that this mode is the HY1 mode.

To underpin this assumption and to make a first attempt to assign the experimentally observed resonances in Fig. 5.13 to the simulated ones, we exemplarily mark the simulated resonance positions for the SPP2, DE1, DE2, and HY1 modes around 1550 nm (see Fig. 5.10) by vertical dashed lines in Fig. 5.13. The remarkably good accordance between the simulated and the experimentally determined resonance positions suggests that the

resonances observed in the red spectra are the SPP2 modes, the resonances in the blue spectra the DE1 and the DE2 modes, and the resonance in the magenta spectrum the HY1 modes. SPP1 modes are not observed in the spectra shown in Fig. 5.13, as their excitation requires the tapered fiber being positioned even further toward the resonator edge.

The results presented here show that controlling the input laser polarization in fiber-coupling experiments plays a key role to discriminate between DE modes and modes with plasmonic character supported by the silver-coated microwedge. In combination with the distinct Q-factor ranges of the modes observed in fiber transmission spectra and the remarkably good correspondence between simulated and experimentally determined resonance positions a preliminary mode assignment is possible.

5.5.2 Selective excitation and classification of cavity eigenmodes using mode filtering

Due to uncertainties in the simulated resonance wavelengths and Q-factors (see section 5.4.2), we apply the experimental procedure proposed in section 5.4.3 to unambiguously identify the distinct eigenmodes supported by the silver-coated microwedge and confirm the mode assignment made in Fig. 5.13. I.e., we determine the coupling efficiencies c between the input fiber and the distinct cavity modes as a function of the horizontal fiber position r_{F}.
To this end, we first identify by means of the three selected normalized transmission spectra shown in Fig. 5.14(a) all distinct eigenmodes supported by the fabricated hybrid microwedge. Each spectrum is recorded with an input fiber polarization which maximizes the coupling into the respective cavity eigenmodes. The upper spectrum recorded with the exciting fiber field being polarized perpendicular to the silver–polymer interface is recorded close to the resonator edge ($r_{\mathrm{edge}}\approx$14.6 µm) at a fiber position $r_{\mathrm{F}}\approx$14 µm. In addition to the SPP2 mode (red) already observed in Fig. 5.13, a second weakly pronounced broad resonance with a low Q-factor of ∼350 (black) is observed, which is assumed to be the SPP1 mode. The spectra in the middle and the bottom of Fig. 5.14(a) are recorded at fiber positions $r_{\mathrm{F}}\approx$12 µm and $r_{\mathrm{F}}\approx$10 µm with the exciting fiber field being polarized parallel and perpendicular to the silver–polymer interface, respectively. These spectra reveal the DE1 (blue), DE2 (cyan), and HY1 mode (magenta) observed already in Fig. 5.13. In the following, we focus on the set of the five distinct modes highlighted in color in Fig. 5.14(a) with resonance wavelengths around 1550 nm, which are marked by vertical dashed lines.

To check whether the mode assignment in Fig. 5.13 is correct and to demonstrate that the distinct cavity modes can be selectively excited, we track the five selected modes while moving the input fiber stepwise from the resonator edge toward the rotation axis of the silver-coated microwedge. At each horizontal fiber position, the input laser polarization is switched between two specific polarization states corresponding to optimal coupling into DE modes and modes with SPP character and the respective fiber–resonator coupling efficiencies c are determined from the absolute dip depth of the resonances in the normalized

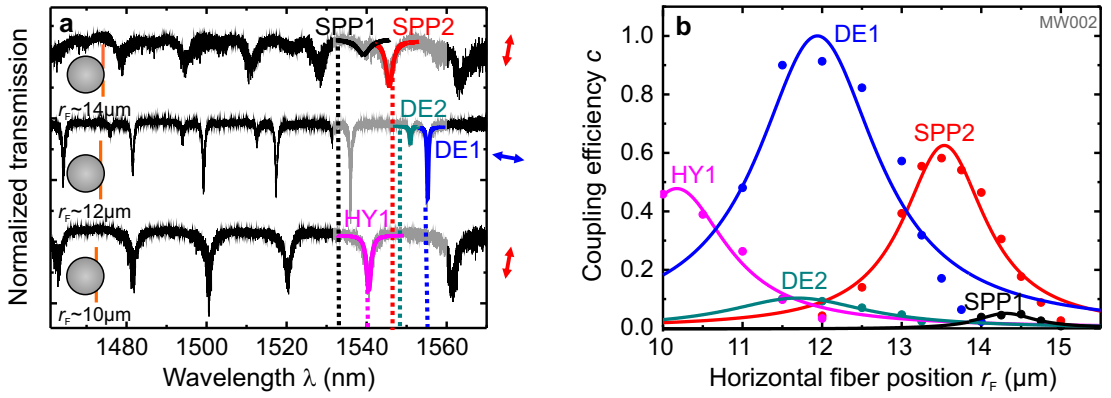

Figure 5.14: Experimental classification of resonator modes. (a) Normalized fiber transmission spectra recorded for horizontal fiber positions $r_F \approx 14\,\mu m$ (top), $12\,\mu m$ (middle), and $10\,\mu m$ (bottom). The three spectra provide an overview of all modes supported by the silver-coated microwedge and are recorded for an input laser polarization which maximizes the coupling into the respective modes (indicated by arrows). Simulated resonance positions for the set of modes highlighted in color with resonance wavelengths around 1550 nm are marked by vertical dashed lines. (b) Tracking the five distinct modes while tuning the horizontal fiber position results in a selective excitation of the various modes. The respective fiber-position-dependent coupling efficiencies c are plotted against the horizontal fiber position r_F (dots) and fitted with Lorentzian functions (solid lines). The excellent correspondence with the simulation results in Fig. 5.12(a) allows for an unambiguous mode classification. Adapted from [85].

transmission spectra (see section 3.3.2 for details).
Extracting the respective fiber–resonator coupling efficiencies c for all five modes under optimal coupling conditions as a function of the horizontal fiber position r_F and fitting the data with Lorentzian functions produces Fig. 5.14(b). As the experimentally determined coupling efficiency c is in first order approximations proportional to the transferred power P and as the fiber radius in the experiment is furthermore comparable to that in the FEM simulations [Fig. 5.12(a)], the experimental results presented in Fig. 5.14(b) can be directly compared with the simulation results shown in Fig. 5.12(a).
From the comparison it is obvious that the experimental results for the fiber-position dependent coupling efficiencies c are in excellent qualitative accordance with the predictions from the simulations. As expected, moving the fiber horizontally from the resonator edge toward the rotation axis of the resonator results in a selective excitation of the five distinct cavity eigenmodes, which is manifested through the five spatially separated Lorentzians in Fig. 5.14(b). According to their order of appearance when tuning the horizontal fiber position, the five Lorentzians corresponding to the modes highlighted in color in Fig. 5.14(a) can now be unambiguously associated with the SPP1, SPP2, DE1, DE2, and HY1 modes. For the input fiber positioned close to the resonator edge ($14\,\mu m < r_F < r_{edge}$), only the SPP1 and SPP2 modes significantly overlap with the evanescent field of the fiber mode and can be, hence, excited. As the SPP2 mode with an effective mode index $n_{SPP2}=1.40$ is better phase-matched to the fundamental fiber mode ($n_F=1.29$) as compared to the

SPP1 mode (n_{SPP1}=1.48), higher coupling efficiencies are obtained for the SPP2 mode. However, as phase matching is also for the SPP2 mode not perfectly fulfilled, the maximal coupling efficiency $c\approx$0.6 at the optimal horizontal fiber position $r_{\mathrm{F}}\approx$13.5 µm is notably below unity. Moving the input fiber toward smaller horizontal fiber positions r_{F} leads to a successive excitation of the DE1, DE2, and HY1 mode, as predicted. In the case of the DE1 mode (n_{DE1}=1.27) phase matching with the tapered-fiber eigenmode is almost perfectly fulfilled, thus, resulting in coupling efficiencies close to unity at $r_{\mathrm{F}}\approx$12 µm. In line with the simulation results, the DE2 mode with an effective refractive index n_{DE2}=1.20 is only weakly excited, which is reflected in the small maximal coupling efficiency $c\approx$0.1 at $r_{\mathrm{F}}\approx$11.75 µm. Contrary to the DE2 mode, the evanescent field of the HY1 mode exhibits a large overlap with the exciting fiber mode, which is why the maximal coupling efficiency is with $c\approx$0.5 at $r_{\mathrm{F}}\approx$10.25 µm notably increased compared to the DE2 mode – despite the comparatively low effective refractive index of the HY1 mode (n_{HY1}=1.10).

We'd like to emphasize that the fiber–resonator coupling efficiencies can be further increased by optimizing the radius of the tapered fiber in the coupling region. As the fiber radius determines the effective fiber mode index [see Fig. 5.3(b)], adjusting the fiber radius allows to perfectly phase-match the individual resonator modes to the tapered-fiber's eigenmode. Whereas input fibers with radii around 400 nm are optimal for exciting the low-index HY1 modes, phase-matching with the high-index SPP1 modes is best fulfilled for thicker input fibers with radii around ∼1.5 µm. Please note that as the distinct cavity eigenmodes notably differ in their effective refractive indices, phase matching can, however, not be simultaneously optimized for all cavity eigenmodes.

Conclusions

The experimental results presented in this section show that SPP, DE, and HY modes supported by the silver-coated microwedge can be unambiguously identified from fiber transmission spectra by following the mode filtering technique developed in section 5.4.3. Tuning the horizontal fiber position with respect to the resonator edge and controlling the input laser polarization is seen to result in a successive and selective excitation of the individual cavity eigenmodes, which allows to clearly and reliably assign the simulated resonances to the experimentally observed ones. Sufficient phase matching for the theoretically predicted SPP1, SPP2, DE1, DE2, and HY1 modes is demonstrated using an input fiber with a radius of ∼700 nm. As the phase-matching condition is perfectly fulfilled for the DE1 mode, coupling efficiencies close to unity are measured. Together with the fact that input power transfers exceeding 50% are recorded for the SPP2 and the HY1 modes, these results demonstrate that the cavity eigenmodes of differing nature cannot only be selectively, but also efficiently excited by means of a tapered optical fiber using pump wavelengths in the near-infrared. The fiber-coupling scheme has, hence, proven its strength in providing a comprehensive insight into the mode spectrum of a silver-coated polymeric microwedge.

5.6 Summary and conclusions

In this chapter, we proposed and characterized a silver-coated polymeric WGM resonator with wedge-like geometry which was carefully engineered to support distinct types of eigenmodes: purely plasmonic (SPP), purely dielectric (DE), and hybrid photonic-plasmonic (HY) modes with Q-factors exceeding a thousand and ultra-small mode volumes. Regarding the resonator design, special emphasis was put on the possibility to efficiently and selectively excite the distinct mode types via the evanescent field of a tapered optical fiber.

Studying the dispersion relation and physical properties of SPPs propagating along a plane metal–dielectric interface allowed deriving first basic guidelines for the design of metal-coated WGM resonators. Silver was identified as suitable coating metal for polymeric WGM resonators, as it enables a low-loss propagation of SPPs at optical frequencies. Furthermore, operational wavelengths in the near-infrared were shown to be indispensable to provide phase matching with a tapered-fiber eigenmode and, hence, allow for an efficient excitation of these surface modes. Based on these findings, numerically efficient finite-element method (FEM) simulations using a bent-waveguide approach were performed for wavelengths around 1500 nm to identify a WGM resonator template which fulfills the target requirements and can be fabricated on a polymer basis. Among different polymeric resonator types, only a WGM resonator with wedge-like geometry was shown to support SPP, DE, and HY modes when coated with a thin silver layer from the top. The inclined resonator edge of this specific resonator type was furthermore seen to be critical to provide a large evanescent field overlap of the individual resonator modes with the surrounding and to spatially separate their modal centers of gravity from each other. Both peculiarities were essential to efficiently and selective excite SPP, DE, and HY modes in silver-coated microwedges.
Simulating the mode spectrum of an experimentally implemented polymeric microwedge with a $\sim$100 nm thick silver coating confirmed the existence of SPP, DE, and HY modes and hinted to the largely disparate properties of the various types of eigenmodes, i.e. differences in Q-factor, mode volume, polarization, and mode localization. With Q-factors of almost two thousand and ultra-small mode volumes V=3.2 µm^3, the HY mode was shown to successfully combine the low-loss characteristic of DE modes with the light-focusing characteristic of SPP modes. Uncertainties in the simulated resonance wavelengths and the Q-factors of the various resonator modes, pointed out the need to develop a reliable experimental procedure to unambiguously identify resonances observed in fiber transmission spectra. Performing bent-waveguide simulations that explicitly include the coupling to an input fiber and applying coupled-mode theory, a mode classification scheme based on mode filtering was developed that exploits qualitative differences in the mode localization and propagation of the distinct cavity eigenmodes to reliably and unequivocally classify them. Computing the power transferred from the input fiber into the distinct cavity eigenmodes as a function of the horizontal fiber position showed that SPP, DE, and HY modes in silver-coated microwedges cannot only be efficiently, but also selectively excited using the horizontal fiber position as tuning parameter. This behavior enables a robust mode classification in the experiment.

Following the proposed mode filtering technique while controlling the input laser polarization, the existence of SPP, DE, and HY modes was demonstrated experimentally. The experimental results were seen to be in excellent compliance with the simulation results. Input power transfers exceeding 50% for all three distinct mode types hinted to the effectiveness of the fiber–excitation scheme, whose strength lies in effectively phase-matching the cavity eigenmodes to the fiber mode by optimizing the fiber thickness and the mode overlap.

The theoretical and experimental results presented in this chapter provide a comprehensive insight into the complex mode spectrum of silver-coated microwedges and show that the proposed mode filtering technique is a powerful tool to unambiguously identify resonances in fiber transmission spectra. The silver-coated microwedge developed in this work is expected to be highly promising for future works on optoplasmonic WGM microcavities where a clear identification of distinct mode types and a selective excitation is required.

Chapter 6

Summary and perspective

Enhancing light–matter interactions in optical whispering-gallery-mode (WGM) resonators is of great interest not only to reach unprecedented sensitivity in biosensing applications, but also to explore quantum effects in cavity quantum electrodynamics experiments. The goal of this thesis was to boost light–matter interactions in polymeric WGM resonators by hybridizing WGMs with plasmonic resonances sustained by metallic nanostructures coupled to the WGM resonator surface. To this end, two different types of hybrid photonic–plasmonic WGM resonators with promising optical properties were designed, experimentally implemented, and optically characterized: polymeric microdisks coated with densely packed spherical gold nanoparticles (NPs) and silver-coated polymeric WGM microwedges.

Summary and conclusions

The theoretical and experimental investigations of gold-NP-coated WGM resonators focused on answering the question whether the locally enhanced light–matter interactions in the vicinity of plasmonic NPs can be exploited to improve the performance of WGM resonators as bulk refractive index sensors. Providing a fundamental understanding of the interaction between plasmonic NPs and WGMs and deriving general design guidelines on how to maximize the sensitivity were central issues. The bulk refractive index sensitivity (BRIS), a measure for the spatial overlap of a mode with its surrounding, was used as a figure-of-merit to quantify the sensitivity of WGM resonators. The strategy to enhance the BRIS of WGM resonators relied on pushing the optical field distribution of WGMs further outside the resonator to increase the interaction with the surrounding.
To provide elementary insight into the coupling between WGMs and plasmonic resonances sustained by plasmonic NPs, a basic model of two coupled harmonic oscillators was introduced. It was shown that this simple model captures fundamental properties of hybrid NP–WGM resonators and succeeds in mapping out a strategy on how to boost the BRIS of WGM resonators. Both the optical properties and the sensitivity of WGMs were shown to

strongly depend on the resonance wavelength detuning between the plasmonic resonance and the operational WGM and the Q-factor of the plasmonic resonance. Depending on the relative detuning, the coupling between WGMs and plasmonic resonances was demonstrated to result either in an enhancement or a reduction in BRIS. A maximal BRIS enhancement was predicted for operational WGMs with resonance wavelengths slightly red detuned from the plasmonic resonance. The respective optimal detuning was the outcome of balancing between WGM linewidth broadening and sensitivity gain. A notable BRIS enhancement was predicted, however, only for plasmonic NPs with comparatively high-quality plasmonic resonances and high intrinsic sensitivities significantly exceeding that of the dielectric WGM resonator.

The results from the coupled harmonic oscillator model were verified using exact analytical calculations of the optical and sensing properties of an idealized hybrid system comprised of a small WGM microsphere coupled to a single artificial plasmonic NP made from a Drude-metal. Using the concept of a Drude-metal allowed to systematically study hybrid NP–WGM sensors. The multi-Mie simulations of the idealized hybrid system confirmed that the BRIS of WGM resonators can be enhanced via the coupling to plasmonic NPs, but demonstrated that the enhancement effects due to the coupling to a single plasmonic NP are small.

To assess the impact of the number density of plasmonic NPs on the BRIS enhancement, finite-element method (FEM) simulations of a hybrid system comprised of a state-of-the-art polymeric microdisk coated with a huge number of randomly distributed spherical gold NPs were performed. To efficiently simulate the hybrid system, the layer of gold NPs covering the microdisk was treated at the level of an effective medium, i.e., modeled as a homogeneous coating made from a medium with an effective permittivity. It was demonstrated that the effective permittivity of the plasmonic coating can be easily and widely tuned in the visible spectral range by simply adjusting the gold NP filling fraction in the shell. This property was the key to study the impact of huge numbers on gold NPs on the optical and sensing properties of WGMs. Again, a maximal BRIS enhancement was predicted for operational WGMs with resonance wavelengths slightly red detuned from the resonance of a single gold NP by approximately half the plasmonic resonance linewidth. The BRIS of the gold-NP-coated microdisks was shown to increase with increasing number density of gold NPs as a result of an increased mode overlap with the surrounding. However, the beneficial effect on the BRIS due to an increased number of gold NPs was accompanied by a strong Q-factor reduction, which drastically lowered the sensor's spectral resolution. It was judged that a proper sensing performance is guaranteed for hybrid microdisks with Q-factors >220 corresponding to gold NP filling fractions f<0.05 ($\sim$40 NPs/ µm^2). For this largest tolerable gold NP filling fraction, a BRIS enhancement by a factor of $\sim$2 was demonstrated. The optical and sensing properties of the gold-NP-coated microdisks were seen to be similar to those of microdisks coated with ultra-thin homogeneous gold films with thicknesses <20 nm.

Sensing experiments on gold-NP-coated poly(methyl methacrylate) (PMMA) microdisks with integrated laser dye pyrromethene 597 were conducted on a micro-photoluminescence spectroscopy setup to quantify the BRIS enhancement experimentally. To ensure a reliable sensing performance, the gold NPs were covalently attached to the microdisk surface

using an immobilization scheme based on chemical vapor deposition polymerization to activate the PMMA surface and self-assembly techniques. The improved spectral resolution of active microdisks compared to their passive counterparts when operated above the lasing threshold allowed to partly compensate for the linewidth broadening of WGMs induced by the coupling to the lossy gold-NP coating. The lasing performance of the hybrid microdisks was shown to strongly degrade with increasing number density of gold NPs on the resonator surface due to increased plasmonic losses. Lasing operation in water was possible up to a modest gold NP filling fraction $f \approx 0.009$ ($\sim 7\,\mathrm{NPs}/\,\mu\mathrm{m}^2$), imposing an upper bound on the achievable sensitivity enhancement in the experimental system. As the BRIS enhancement was even for the hybrid microdisk with the largest tolerable gold NP filling fraction quite small and on the order of the measurement error, the beneficial effect of the gold-NP coating on the BRIS of PMMA microdisks could not be verified experimentally.
The experimental and theoretical results combined made clear that the coupling of gold NPs to WGM microresonators is, so far, not beneficial to improve their performance as bulk refractive index sensors. Although theoretically a BRIS enhancement by a factor of ~ 2 was predicted for microdisks coated with densely packed gold NPs, this modest enhancement factor cannot compensate for the strong WGM Q-factor degradation induced by the lossy gold-NP coating. As the performance of a sensor is determined by the ratio of sensitivity to resonance linewidth, the proposed gold-NP-coated microdisks can, hence, not compete with their bare dielectric counterparts for what concerns bulk refractive index sensing.

Apart from gold-NP-coated WGM resonators, another type of hybrid photonic–plasmonic WGM resonator was developed and studied both theoretically and experimentally in this work: a silver-coated polymeric WGM resonator with wedge-like geometry. This novel type of resonator was carefully engineered to support modes of distinct nature, namely purely plasmonic (SPP), purely dielectric (DE), and hybrid photonic–plasmonic (HY) modes with high Q-factors and ultra-small mode volumes. Providing a comprehensive insight into its mode spectrum and developing a strategy on how to efficiently and selectively excite the individual cavity eigenmodes with the evanescent field of a tapered optical fiber was a key issue.
Based on the analysis of fundamental physical properties of surface plasmon polaritons (SPPs) sustained at a metal–polymer interface, first guidelines for the design of metal-coated WGM resonators were derived. Silver was identified as a suitable coating metal enabling a low-loss propagation of SPPs at optical frequencies. Operation wavelengths in the near-infrared were shown to be critical to fulfill phase matching between SPP modes and the fundamental mode of a tapered optical fiber. Optimizing the hybrid cavity design using numerically efficient FEM simulations based on a bent-waveguide approach pointed out the need for a silver-coated resonator with wedge-like geometry to efficiently and selectively excite SPP, DE and HY modes. The wedge-like cavity geometry provides a large evanescent field overlap of the resonator modes with the surrounding, as required for an efficient mode excitation using tapered fibers, and is responsible for spatially separating the centers of gravity of the different modes from each other. This peculiarity is the key

for a selective excitation of the individual cavity eigenmodes.
PMMA microwedges with an ultra-smooth cavity surface and Q-factors on the order of 10^5 were fabricated using electron beam lithography together with conventional etching techniques. A post-lithographic thermal reflow process was at the heart of the fabrication process. It transformed lithographically structured microdisks into the desired wedge-like geometry due to surface tension while simultaneously smoothening the resonator surface. Electron beam physical vapor deposition was used to coat the resonator templates from the top with an ultra-smooth $\sim$100 nm thick silver film, enabling the formation of high-Q SPP modes at the polymer–silver interface.
Simulating the mode spectrum of a fabricated silver-coated PMMA microwedge demonstrated the existence of DE, SPP, and HY modes with Q-factors exceeding a thousand and ultra-small mode volumes $V\approx$3.2 µm^3 and hinted to the largely disparate properties of the distinct cavity eigenmodes, i.e. differences in Q-factor, mode volume, polarization, and mode localization. Motivated by uncertainties in simulated spectral features, an experimental procedure based on mode filtering was developed to unambiguously classify the individual resonator modes observed in fiber transmission spectra. To this end, bent-waveguide simulations of the joint fiber–resonator system were performed and coupled-mode theory was applied to extract fiber-position-dependent coupling efficiencies between the individual cavity eigenmodes and a tapered-fiber eigenmode. It was demonstrated both theoretically and experimentally that SPP, DE, and HY modes in silver-coated polymeric microwedges can be selectively excited by tuning the fiber position relative to the resonator while controlling the polarization of the incoming laser light. Following this procedure allowed for an unambiguous classification of SPP, DE, and HY modes in fiber–coupling experiments. The experimental results were seen to be in excellent compliance with theory. Input power transfers exceeding 50% for all three mode types demonstrated the effectiveness of the fiber-excitation scheme, whose strength lies in effectively phase-matching the resonator and fiber eigenmodes by optimizing the fiber thickness and the mode overlap.

Recommendations for future research

As the high intrinsic absorption of gold ultimately limits the performance of gold-NP coated microdisks in bulk refractive index sensing, advances in material science are critical to make plasmonic-NP-coated WGM resonators competitive with their dielectric counterparts. In particular, the development of novel plasmonic nanostructures with notably higher-quality resonances and higher intrinsic BRIS values is needed to bridge the gap between hybrid and conventional WGM resonators. Combining conventional WGM resonators with such tailored plasmonic NPs is considered worthy of investigation. So far, silica–silver core–shell NPs with comparatively high-quality plasmonic resonances and nanocrescents [135] or shape- and dispersion-engineered Ag-Ti nanohelices [131], exhibiting one of the highest sensitivities measured to date, are among the most promising plasmonic nanostructures.
The gold-NP-coated WGM resonators developed in this work are expected to occupy a

privileged niche in ensemble-based sensing schemes where analytes specifically bind to the surface of the gold NPs. Contrary to bulk refractive index sensing where the beneficial effect of the gold NPs on the BRIS enhancement is modest due to the strong local confinement of plasmonic hotspots to the immediate vicinity of gold NPs, the greatly elevated field intensities at the gold NP surface can be directly exploited in such sensing schemes to boost WGM signals induced by adsorbing biomolecules by several orders of magnitude. WGM resonators coated with densely packed gold NPs or novel plasmonic NPs, thus, hold great potential in significantly lowering the detection limit compared to conventional WGM resonators in that field of application.
The FEM simulations of gold-NP-coated microdisks pointed out the possibility to mimick ultra-thin homogeneous gold coatings with thicknesses <20 nm by self-assembled gold-NP composites. Whereas the fabrication of ultra-thin gold coatings on curved dielectrics with the homogeneity and smoothness required for practical applications is a big challenge, a random assembly of gold NPs on arbitrarily shaped dielectrics can be achieved with ease using self-assembly techniques. The FEM simulation results, hence, provide powerful guidelines for the design of novel hybrid photonic–plasmonic devices whose performance was so far restricted by the achievable quality of ultra-thin gold coatings.

The silver-coated polymeric wedge-like WGM resonators are expected to be highly promising for future works on optoplasmonic WGM resonators where a clear identification and selective excitation of different mode types is demanded.
The differing dispersive characters of SPP, DE, and HY modes might be exploited, e.g., in sensing applications for self-referencing, enabling a direct determination of analyte concentrations from relative mode shifts.
Besides, the possibility to switch between dielectric and plasmonic excitation channels in a controlled manner might be of great interest in cavity quantum electrodynamics experiments, as it allows to tune the coupling between the resonator and an embedded quantum emitter. In this context, it might be useful to optimize silver-coated WGM microwedges with regard to a higher Q/V-ratio to further enhance the coupling strength between light and matter.

Appendix A

Immobilization of gold nanoparticles on polymeric WGM resonators

In the following, a protocol for the covalent immobilization of amine-functionalized spherical gold nanoparticles (NPs) (*NanopartzTM Inc., Loveland, CO, USA*) on PMMA resonators coated with a thin polymeric layer containing reactive pentafluorophenyl esters (PFP-ester) is given. The thin film coatings made from poly[(4-pentafluorophenyl ester-p-xylylene)-co-(p-xylylene)] were fabricated at the Institute of Functional Interfaces (Institut für Funktionelle Grenzflächen, IFG) at KIT by Dr. Meike König using chemical vapor deposition (CVD) polymerization. Details regarding their fabrication can be found in [90–93].

The provided parameters for the self-assembling of gold NPs refer to the fabrication of the gold-NP-coated WGM microdisk investigated in section 4.5 with labeling MD0039.
In a first step, the stock suspension (2,7 nM) containing the colloidal gold NPs was diluted in phosphate buffered saline (PBS) in a ratio of 1:150. The suspension was homogenized by ultrasonification for 5 minutes followed by 2 minutes vigorous vortex mixing to prevent the agglomeration of the gold NPs.
To covalently attach the amine-functionalized colloidal gold NPs to the CVD-modified PMMA microdisks, the sample was immersed in 1 ml of the diluted gold-NP solution for 24 hours and rinsed with distilled water afterwards. The self-assembly process resulted in a gold-NP surface density of $\sim$7 NPs/ µm^2. Varying the concentration of the colloidal gold NPs in the suspension or the immersion time allows to adjust the resulting NP surface density on the resonator surface.

Appendix B

Numerical modeling of fiber–resonator coupling

B.1 Bent-waveguide approach to simulate fiber–resonator system

To simulate the fiber–resonator coupling, the input fiber is positioned underneath the silver-free bottom surface of the silver-coated microwedge at sufficiently small distances to the resonator surface to ensure a large overlap of the evanescent fields of fiber and resonator modes. Since introducing a straight fiber, as used in the experiment, breaks the rotational symmetry of the system, full 3D calculations would be necessary to rigorously simulate the fiber–resonator coupling. However, for reasons already discussed in section 5.3.1, performing such calculations is out of the question due to tremendous computational costs.
To efficiently simulate the fiber–resonator coupling, thus, a strategy is needed to restore the cylindrical symmetry. Instead of considering a straight fiber, we, thus, consider a bent fiber in the FEM simulations which is positioned concentrically below the bottom surface of the resonator, as graphically illustrated in Fig. B.1. The problem of simulating the coupling between a straight fiber and the resonator is then reduced to simulating the coupling between two bent waveguides. With this approach, numerically efficient 2D simulations using the bent-waveguide approach presented in section 5.3.1 can be performed.
Please note that this idealized system differs from the experimental system in several aspects, which are detailed below and have to be kept in mind when mapping the simulation results to the real fiber–resonator system.

First, since the fiber in the FEM simulations is bent, its eigenmodes experience distortions – contrary to modes supported by a straight fiber. The smaller the radius of curvature of the bent fiber, the larger is the distortion effect and, hence, the error in the calculations.

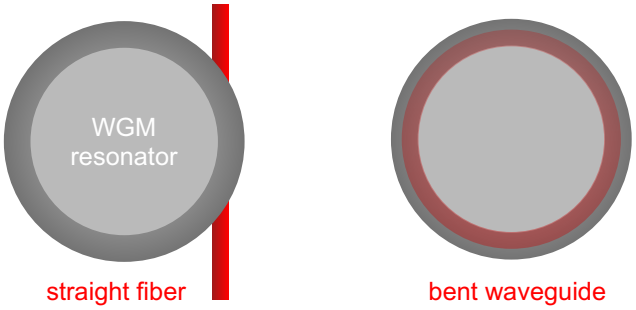

Figure B.1: Bent-waveguide approach for simulating the fiber–resonator coupling. *Left:* Coupling a straight fiber (red) to the silver-coated microwedge (grey) from below, as done in experiments, breaks the rotational symmetry. *Right:* To restore the symmetry and perform efficient 2D simulations, the hybrid microwedge is coupled to a closed bent waveguide which is positioned concentric to and underneath the resonator. Adapted from [85].

However, as WGMs are localized close to the resonator edge, bent fibers with radii large compared to the operational wavelength and large compared to the fiber's waist diameter are needed to efficiently excite the modes. In the investigated parameter regime, distortion effects are, thus, assumed to play a negligible role.

Second, as a further consequence of the bend, the eigenmodes of the bent fiber experience radiation losses – contrary to modes of a straight fiber. These losses enter the imaginary part of the bent fiber's effective mode index n_{eff}. Since they are nonphysical, only the real part of the effective fiber mode index containing the physical information is considered in the calculations.

Third, further deviations from the experimental system arise from the fact that the interaction length between the bent fiber and the microwedge is infinite while being finite in the case of a straight fiber coupled to the resonator. Due to the resulting infinite interaction time, the power transferred from the bent fiber to the resonator is significantly larger than for the straight-fiber case. This effect needs to be considered when extracting fiber–resonator coupling efficiencies for the experimental system from the bent-waveguide simulations.

Finally, and in contrast to straight waveguides, moving the bent fiber in the FEM simulations horizontally underneath the resonator affects the bent fiber's effective refractive index. This can be understood as follows: Contrary to straight fibers for which the effective fiber mode index is well-defined due to the translational symmetry of the guide, the lack of translational symmetry in bent fibers requires an alternative definition of the effective refractive index.
For this, we utilize the cylindrical symmetry of the system. Since the Lie group of rotations around an axis is parametrized by a single angle ϕ, the phase change $\delta\phi$ is given in analogy to the translationally symmetric case as $\delta\phi{=}\eta{\cdot}\phi$, where η can be interpreted as an angular wave number. Defining a reference radius r_{ref}, the phase change can be rewritten as a function of the propagation length l along a circular path of radius r_{ref} according

to: $\delta\phi{=}\eta/r_{\mathrm{ref}}{\cdot}l$. This is formally identical to the translational case when one identifies $n_{\mathrm{eff}}{=}\eta/r_{\mathrm{ref}}$. For sufficiently large radii of curvature r_{F} of the bent fiber, i.e. small fiber curvatures, we expect the wave number in the center of the fiber ($r_{\mathrm{ref}}{=}r_{\mathrm{F}}$) to be close to the value $n_{\mathrm{eff},0}$ of a straight fiber. This means that $\eta{\approx}n_{\mathrm{eff},0}{\cdot}r_{\mathrm{F}}{\propto}r_{\mathrm{F}}$. Therefore, for calculations relative to a fixed reference radius r_{ref}, we expect a linear relation between the fiber's radius and its effective refractive index.

B.2 Calculation of fiber-position-dependent coupling efficiencies

To verify that tuning the horizontal fiber position results in a selective excitation of the distinct eigenmodes supported by the silver-coated microwedge, we perform bent-waveguide simulations of the joint system for varying fiber positions [232].
To this end, the fiber in the simulations is moved horizontally from the resonator edge toward the rotation axis of the resonator at a constant vertical distance of 900 nm between the fiber axis and the bottom surface of the resonator (see Fig. 5.11). We focus on an input fiber with 700 nm radius and consider pump wavelengths $\lambda_{\mathrm{F}}{=}1500$ nm. The index F is used in the following to denote quantities related to the input fiber, the index R is used to label quantities related to the resonator.
Varying the horizontal fiber position r_{F} with respect to the resonator edge manifests an anticrossing of the effective refractive indices $n_{\mathrm{eff,F}}$ and $n_{\mathrm{eff,R}}$ of fundamental fiber and resonator modes, respectively. The splitting in the effective refractive indices is a signature of fiber–resonator coupling taking place and can be translated to a resonance frequency splitting $\Delta\omega$ by exploiting the phase-matching condition. As coupling requires the wavenumbers of fiber and resonator mode to match, i.e. $k_{\mathrm{F}}{=}k_{\mathrm{R}}$, the effective mode indices and resonance frequencies of both modes are related by:

$$n_{\mathrm{eff,R}} \cdot \omega_{\mathrm{R}} = n_{\mathrm{eff,F}} \cdot \omega_{\mathrm{F}}. \tag{B.1}$$

Using Eq. B.1 and defining the splitting in the effective refractive indices as $\Delta n_{\mathrm{eff}}{=}n_{\mathrm{eff,R}}{-}n_{\mathrm{eff,F}}$, the resonance frequency detuning $\Delta\omega{=}\omega_{\mathrm{R}}{-}\omega_{\mathrm{F}}$ between resonator and fiber mode can be expressed as follows:

$$\Delta\omega = -\frac{\Delta n_{\mathrm{eff}}}{n_{\mathrm{eff,R}}}\omega_{\mathrm{F}}. \tag{B.2}$$

The frequency detuning $\Delta\omega$ between the considered fiber eigenmode and a DE1 mode is plotted exemplarily in Fig. B.2 as a function of the horizontal fiber position r_{F} (red dots). The black dashed lines in Fig. B.2 denote the effective mode indices of fiber and DE1 mode in the absence of coupling. The upper (lower) branch corresponds to a state of the joint fiber–resonator system where the fields of fiber and DE1 mode are polarized antiparallel (parallel) to each other, as indicated by the arrows in the insets in Fig. B.2. The fiber eigenmode considered in Fig. B.2 exhibits a polarization parallel to the silver–polymer

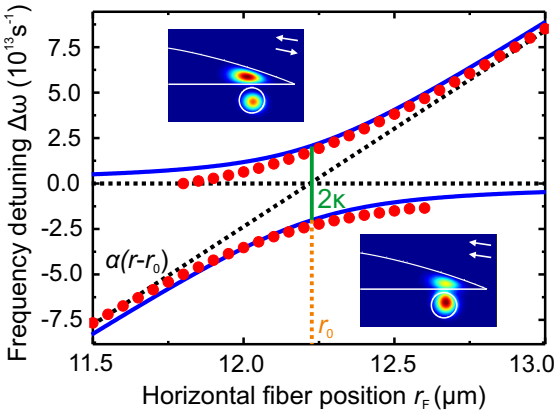

Figure B.2: Frequency splitting between a DE1 mode and an eigenmode of a tapered fiber with 700 nm radius. Tuning the horizontal fiber position r_{F} with respect to the resonator edge r_{edge} in the simulations reveals a splitting $\Delta\omega$ in the resonance frequencies of fiber and resonator mode, which is a signature of fiber–resonator coupling taking place. The simulation data (red dots) are fitted with Eq. B.2 (blue solid lines) to extract the fiber–resonator coupling efficiency κ [232]. The upper (lower) branch corresponds to a state, where the polarization vectors of fiber and resonator mode are antiparallel (parallel) to each other (see insets). The asymptotes representing the fiber and resonator states in the absence of coupling are indicated by black dashed lines. Adapted from [85].

interface, which maximizes the coupling to the DE1 mode. Since we consider eigenstates of the coupled fiber–resonator system, there exists also a second fiber eigenmode which is polarized orthogonal to the considered one. However, this fiber mode does not couple to the DE1 mode due to the polarization mismatch. We'd like to note that varying the input fiber polarization alters the relative excitation of the two fiber eigenmodes and, thus, affects the fiber–resonator coupling efficiency. In the following calculations, only input polarizations maximizing the coupling efficiency are considered.

To understand the anticrossing behavior and to understand how to extract fiber–resonator coupling efficiencies from the simulation results, we apply CMT.
Assuming weak coupling between the fiber and the resonator mode, the equations of motion for the coupled system read:

$$\frac{\mathrm{d}}{\mathrm{d}t}\begin{pmatrix} a_{\mathrm{F}} \\ a_{\mathrm{R}} \end{pmatrix} = \begin{pmatrix} 0 & -\mathrm{i}\kappa \\ -\mathrm{i}\kappa & -\mathrm{i}\Delta\omega \end{pmatrix} \cdot \begin{pmatrix} a_{\mathrm{F}} \\ a_{\mathrm{R}} \end{pmatrix}. \tag{B.3}$$

κ is the fiber–resonator mode coupling constant, a_{F} and a_{R} denote the mode amplitudes of fiber and resonator with natural frequencies ω_{F} and $\omega_{\mathrm{R}}{=}\omega_{\mathrm{F}}{+}\Delta\omega$, respectively. To solve for the natural frequencies of the coupled system, we insert the time-harmonic ansatz $a_{\mathrm{F,R}}{\propto}\exp(-i\omega_{\mathrm{F}}t)$ into Eq. B.3 and find the eigenvalues ω_+ and ω_-:

$$\omega_{\pm} = \frac{\Delta\omega}{2} \pm \sqrt{\left(\frac{\Delta\omega}{2}\right)^2 + \kappa^2}. \tag{B.4}$$

To fit the anticrossing data shown in Fig. B.2, Eq. B.4 must be expressed in terms of the horizontal fiber position r_F. From Eq. B.2 we know that the frequency detuning $\Delta\omega$ is proportional to Δn_eff and depends, hence, linearly on the fiber position r_F (see section B.1). Since the frequency detuning $\Delta\omega$ must furthermore vanish for $r_\mathrm{F}{=}r_0$, $\Delta\omega$ depends linearly on the radial detuning $\Delta r{=}r_\mathrm{F}{-}r_0$:

$$\Delta\omega = \alpha \cdot (r - r_0) \propto \Delta n_\mathrm{eff}, \tag{B.5}$$

With the aid of Eq. B.5, the fiber–resonator mode coupling constant κ can be determined by fitting Eq. B.4 to the anticrossing data shown in Fig. B.2 (blue solid lines). It is given by the splitting of the eigenvalues $\omega_\pm$ at the zero detuning position r_0:

$$2\kappa = \omega_+(r_0) - \omega_-(r_0). \tag{B.6}$$

Calculating the coupling constants κ for the different eigenmodes supported by the investigated silver-coated microwedge near the considered pump wavelength yields the following values:

$$\kappa_\mathrm{SPP1} = 1.10 \cdot 10^{13}\mathrm{s}^{-1}, \tag{B.7a}$$
$$\kappa_\mathrm{SPP2} = 1.33 \cdot 10^{13}\mathrm{s}^{-1}, \tag{B.7b}$$
$$\kappa_\mathrm{DE1} = 2.05 \cdot 10^{13}\mathrm{s}^{-1}, \tag{B.7c}$$
$$\kappa_\mathrm{DE2} = 4.61 \cdot 10^{12}\mathrm{s}^{-1}, \tag{B.7d}$$
$$\kappa_\mathrm{HY1} = 1.66 \cdot 10^{13}\mathrm{s}^{-1}. \tag{B.7e}$$

According to these results, the fiber–resonator coupling is strongest for the DE1 mode and weakest for the DE2 mode if an input fiber with 700 nm radius is used for mode excitation.

To map the simulation results to the experiment, we use a transfer-amplitude formalism and relate the calculated coupling constants κ to the power P transferred from the input fiber to the resonator eigenmodes. P serves as an experimentally observable quantity, as it is proportional to the dip depth of resonances observed in fiber transmission spectra. In a first step, the power transferred from the bent fiber into the individual cavity eigenmodes is computed. The results are then transferred to the straight-fiber case to make predictions about fiber-position-dependent coupling efficiencies in the experimental system.
Defining the normalized fiber and resonator states as:

$$|F\rangle := (1,0)^\mathrm{T}, \quad |R\rangle := (0,1)^\mathrm{T}, \tag{B.8}$$

and assuming that at the time $t{=}t_0{=}0$ only the fiber is excited, the initial state $|\Psi(t_0)\rangle$ of the coupled system can be expressed in terms of the normalized eigenstates $|\pm\rangle$ corresponding to the eigenvalues $\omega_\pm$ in Eq. B.4:

$$|\Psi(t_0)\rangle = |F\rangle = \langle +|\, F\, |+\rangle + \langle -|\, F\, |-\rangle\,, \tag{B.9}$$
$$|\pm\rangle = \frac{1}{\sqrt{\omega_\pm^2 + \kappa^2}}(\kappa, \omega_\pm)^\mathrm{T}. \tag{B.10}$$

The time-evolution of the system is described by the time-evolution operator $U(t)$=exp$(-iH(t-t_0)/\hbar)$ with eigenstates $|\pm\rangle$ and eigenvalues $\omega_\pm$. Applying $U(t)$ to the initial state $|\Psi(t_0)\rangle$ yields the eigenstate of the coupled system at any later time t:

$$|\Psi(t)\rangle = U(t)\,|F\rangle = e^{-i\omega_+ t}\,\langle +|\,F\,|+\rangle + e^{-i\omega_- t}\,\langle -|\,F\,|-\rangle\,. \tag{B.11}$$

To calculate the energy E transferred from the fiber mode into a resonator mode, we calculate the transfer amplitude T, i.e. we project the eigenstate $|\Psi(t)\rangle$ onto the resonator state $|R\rangle$:

$$T := \langle R|\,U(t)\,|F\rangle = \frac{\kappa\omega_+}{\omega_+^2+\kappa^2}\mathrm{e}^{-\mathrm{i}\omega_+ t} + \frac{\kappa\omega_-}{\omega_-^2+\kappa^2}\mathrm{e}^{-\mathrm{i}\omega_- t}. \tag{B.12}$$

Since the energy E transferred from the bent fiber into a specific eigenmode is proportional to the absolute square of the transfer amplitude T, it can be calculated from Eq. B.12 under the assumption that no light enters or leaves the system and by neglecting fast oscillating terms:

$$\begin{aligned} E \propto |T|^2 \approx & \frac{\kappa^2\omega_+^2}{\left(\omega_+^2+\kappa^2\right)^2} + \frac{\kappa^2\omega_-^2}{\left(\omega_-^2+\kappa^2\right)^2} \\ = & \frac{2\kappa^2}{(\Delta\omega)^2+(2\kappa)^2}. \end{aligned} \tag{B.13}$$

To transfer the result to the experimental system, we have to consider that the interaction length over which the fiber and resonator modes can exchange energy is finite for a straight fiber, while being infinite for a bent fiber. As a consequence, energy can be transferred from a straight fiber to the cavity eigenmodes only during a finite interaction time Δt=t_{int}, which significantly reduces the amount of transferred energy compared to the bent-fiber case. The reduction in transferred energy can be estimated from the change the resonator's mode amplitude a_{R} experiences during the finite interaction time t_{int} under optimal coupling conditions, i.e. $\Delta\omega$=0. Assuming that the coupling length L_{C}≈t_{int} for the straight fiber coupled to the resonator is much smaller than in the case of the bent fiber (t_{int}≪κ^{-1}), the change Δa_{R} in resonator amplitude can be calculated from the equations of motion (Eq. B.3) at resonance:

$$\Delta a_{\mathrm{R}} = a_{\mathrm{R}}(t+t_{\mathrm{int}}) - a_{\mathrm{R}}(t) \approx \kappa \cdot t_{\mathrm{int}} \cdot a_{\mathrm{F}}. \tag{B.14}$$

Pumping the fiber at constant power and assuming that the interaction time t_{int} is almost independent of the fiber position r_{F}, the power P transmitted from a straight fiber into a cavity eigenmode can be determined by combing Eq. B.13 with Eq. B.14:

$$P \propto (\Delta a_R)^2\,|T|^2 \propto \kappa^2\,|T|^2 \approx \frac{2\kappa^4}{(\Delta\omega)^2+(2\kappa)^2}. \tag{B.15}$$

From Eq. B.15 we see that the power P transferred from the straight input fiber into a specific cavity eigenmode has a Lorentzian line shape with a FWHM determined by the respective fiber–resonator coupling constant κ and is centered around the zero detuning position r_0.

List of Publications

Regular Articles

1. **Size-Optimized Polymeric Whispering Gallery Mode Lasers with Enhanced Sensing Performance**,
S. Krämmer, S. Rastjoo, T. Siegle, S. F. Wondimu, C. Klusmann, C. Koos, H. Kalt, *Optics Express* **25**, 7884–7894 (2017)

2. **Hybridizing whispering gallery modes and plasmonic resonances in a photonic metadevice for biosensing applications [Invited]**,
C. Klusmann, R. N. S. Suryadharma, J. Oppermann, C. Rockstuhl, and H. Kalt, *Journal of the Optical Society of America B* **34**, D46–D55 (2017)

3. **A Comparision of Various Excitation and Detection Schemes for Dye-Doped Polymeric Whispering Gallery Mode Micro-Lasers**,
T. Siegle, J. Kellerer, M. Bonenberger, S. Krämmer, C. Klusmann, M. Müller, H. Kalt, *Optics Express* **26**, 3579–3593 (2018)

4. **Identification of Dielectric, Plasmonic, and Hybrid Modes in Metal-Coated Whispering-Gallery-Mode Resonators**,
C. Klusmann, J. Oppermann, P. Forster, C. Rockstuhl, and H. Kalt, *ACS Photonics* **5**, 2365–2373 (2018)

5. **Strong Coupling between Molecular Ensembles and Whispering Gallery Mode Resonators**,
J. Oppermann, J. Straubel, K. Slowik, C. Lee, T. Siegle, C. Klusmann, H. Kalt, and C. Rockstuhl *manuscript in preparation*

Contributions to International Conferences with Proceedings

1. **Hybridizing whispering gallery modes and plasmonic resonances in a photonic meta-device for bio-sensing applications**,
C. Klusmann, R. N. S. Suryadharma, J. Oppermann, C. Rockstuhl, and H. Kalt, *Quantum Nano-Photonics, Erice, Italy (2017)*, Poster Presentation

NATO Science for Peace and Security Series B: Physics and Biophysics, Springer (2018)

Contributions to Workshops

1. **Hybridizing whispering gallery modes and plasmonic resonances in a photonic meta-device for bio-sensing applications**,
C. Klusmann, R. N. S. Suryadharma, J. Oppermann, C. Rockstuhl, and H. Kalt, *653. WE-Heraeus-Seminar on Optical Microcavities and Their Applications, Bad Honnef, Germany (2017)*, Poster Presentation

2. **Plasmonic, Dielectric and Hybrid modes in Whispering-Gallery-Mode Resonators**,
C. Klusmann, J. Oppermann, P. Forster, C. Rockstuhl, and H. Kalt, *Workshop on Photonic Devices, Berlin, Germany (2019)*, Talk

Contributions to DPG Spring Meetings

1. **Optical Modes in Photonic Molecules from Whispering-Gallery-Mode Microcavities**,
T. Siegle, S. Wiegele, C. Klusmann, T. Grossmann, T. Wienhold, U. Bog, S. Köber, and H. Kalt, *DPG spring meeting, Dresden (2014)*, Talk

2. **Quantum Dots and Lanthanides as cw-Emitters in Polymeric Microresonators**,
C. Klusmann, S. Wiegele, T. Siegle, T. Wienhold, S. Köber, C. Koos, and H. Kalt, *DPG spring meeting, Dresden (2014)*, Poster Presentation

3. **Plasmon-Enhanced Biosensing with Polymeric Whispering-Gallery-Mode Resonators**,
C. Klusmann, S. Krämmer, S. A. Schmid, T. Siegle, C. Rockstuhl, and H. Kalt, *DPG spring meeting, Regensburg (2016)*, Poster Presentation

4. **Effect of Different Excitation and Collection Geometries on the Lasing Threshold of PM597-Doped WGM Micro Disk Cavities**,
T. Siegle, M. Bonenberger, S. Krämmer, C. Klusmann, and H. Kalt, *DPG spring meeting, Regensburg (2016)*, Poster Presentation

5. **Whispering Gallery Mode Resonators with Varying Diameter and Thickness for Enhanced Sensitivity**,
S. Rastjoo, S. Krämmer, T. Siegle, C. Klusmann, and H. Kalt, *DPG spring meeting, Regensburg (2016)*, Poster Presentation

6. **The interplay of plasmonic nanoparticles and dielectric whispering gallery mode resonators**,
S. A. Schmid, R. N. S. Suryadharma, M. Fruhnert, C. Klusmann, H. Kalt, and C. Rockstuhl, *DPG spring meeting, Dresden (2017)*, Poster Presentation

7. **Enhancing the Sensitivity of Polymeric Whispering Gallery Mode Micro-Disks by Structuring Notches in the Outer Cavity Rim**,
M. Remmel, T. Siegle, S. Krämmer, C. Klusmann, H. Kalt, *DPG spring meeting, Dresden (2017)*, Poster Presentation

8. **Studying the interplay of plasmonic nanoparticles and polymeric whispering gallery mode resonators using a generalized Mie theory**,
C. Klusmann, S. A. Schmid, R. N. S. Suryadharma, C. Rockstuhl, and H. Kalt, *DPG spring meeting, Dresden (2017)*, Poster Presentation

9. **Properties of metal-coated polymeric whispering gallery mode resonators**,
P. Forster, C. Klusmann, J. Oppermann, C. Rockstuhl, and H. Kalt, *DPG spring meeting, Dresden (2017)*, Poster Presentation

10. **Hybrid photonic–plasmonic whispering-gallery-mode resonators**,
C. Klusmann, J. Oppermann, P. Forster, C. Rockstuhl, and H. Kalt, *DPG spring meeting, Berlin (2018)*, Talk

11. **Widely tunable polymer-based photonic devices**,
T. Siegle, J. Frank, S. Schierle, M. Remmel, M. Migeot, C. Klusmann, and H. Kalt, *DPG spring meeting, Berlin (2018)*, Talk

12. **Tuning of Polymeric Photonic Devices based on Liquid Crystal Elastomers**,
M. Migeot, C. Klusmann, S. Nocentini, D. Nuzhdin, D. Wiersma and H. Kalt, *DPG spring meeting, Berlin (2018)*, Poster Presentation

13. **Tunable Whispering-Gallery-Mode Resonators made from Liquid Crystal Elastomers**,
J. Hessenauer, C. Klusmann, S. Woska, M. Migeot, and H. Kalt, *DPG spring meeting, Regensburg (2019)*, Poster Presentation

14. **Wide Tunability of Coupled Whispering-Gallery-Mode Resonators Using Flexible Elastomer Substrates**,
S. Woska, L. Mall, J. Hessenauer, C. Klusmann, T. Siegle, and H. Kalt, *DPG spring meeting, Regensburg (2019)*, Poster Presentation

15. **Fabrication of Polymeric Whispering-Gallery-Mode Resonators on Tunable Liquid Crystal Elastomer Substrates using Deep-UV**,
L. Mall, S. Woska, J. Hessenauer, C. Klusmann, T. Siegle, and H. Kalt, *DPG spring meeting, Regensburg (2019)*, Poster Presentation

Bibliography

[1] T. H. Maiman, "Stimulated Optical Radiation in Ruby," Nature **187**, 493–494 (1960).

[2] I. Kaminow and T. Li, *Optical Fiber Telecommunications IV-A: Components*, Optics and Photonics (Elsevier Science, 2002).

[3] R. M. Verdaasdonk and C. F. P. van Swol, "Laser light delivery systems for medical applications," Physics in Medicine and Biology **42**, 869–894 (1997).

[4] P. B. Deotare and M. Loncar, *Photonic Crystal Nanobeam Cavities* (Springer Netherlands, Dordrecht, 2012).

[5] Y.-n. Zhang, Y. Zhao, and R.-q. Lv, "A review for optical sensors based on photonic crystal cavities," Sensors and Actuators A: Physical **233**, 374–389 (2015).

[6] T. M. Benson, S. V. Boriskina, P. Sewell, A. Vukovic, S. C. Greedy, and A. I. Nosich, *Micro-optical resonators for microlasers and integrated optoelectronics* (Springer Netherlands, Dordrecht, 2006).

[7] O. Painter, R. K. Lee, A. Scherer, A. Yariv, J. D. O'Brien, P. D. Dapkus, and I. Kim, "Two-Dimensional Photonic Band-Gap Defect Mode Laser," Science **284**, 1819–1821 (1999).

[8] Lefévre-Seguin, "Whispering-gallery mode lasers with doped silica microspheres," Optical Materials **11**, 153–165 (1999).

[9] D. Armani, T. J. Kippenberg, S. M. Spillane, and K. J. Vahala, "Ultra-High-Q Toroid Microcavity on a Chip," Nature **421**, 925–928 (2003).

[10] K. J. Vahala, "Optical microcavities," Nature **424**, 839–846 (2003).

[11] A. Polman, B. Min, J. Kalkman, T. J. Kippenberg, and K. J. Vahala, "Ultralow-threshold erbium-implanted toroidal microlaser on silicon," Applied Physics Letters **84**, 1037–1039 (2004).

[12] A. A. Savchenkov, V. S. Ilchenko, A. B. Matsko, and L. Maleki, "Kilohertz optical resonances in dielectric crystal cavities," Physical Review A **70**, 051804:1–051804:4 (2004).

[13] J. S. Foresi, P. R. Villeneuve, J. Ferrera, E. R. Thoen, G. Steinmeyer, S. Fan, J. D. Joannopoulos, L. C. Kimerling, H. I. Smith, and E. P. Ippen, "Photonic-bandgap microcavities in optical waveguides," Nature **390**, 143–145 (1997).

[14] H. Benisty, C. Weisbuch, D. Labilloy, M. Rattier, C. J. M. Smith, T. F. Krauss, R. M. De La Rue, R. Houdre, U. Oesterle, C. Jouanin, and D. Cassagne, "Optical and Confinement Properties of Two-Dimensional Photonic Crystals," Journal of Lightwave Technology **17**, 2063–2077 (1999).

[15] E. Chow, S. Y. Lin, S. G. Johnson, P. R. Villeneuve, J. D. Joannopoulos, J. R. Wendt, G. A. Vawter, W. Zubrzycki, H. Hou, and A. Alleman, "Three-dimensional control of light in a two-dimensional photonic crystal slab," Nature **407**, 983–986 (2000).

[16] J. M. Gérard, B. Sermage, B. Gayral, B. Legrand, E. Costard, and V. Thierry-Mieg, "Enhanced Spontaneous Emission by Quantum Boxes in a Monolithic Optical Microcavity," Physical Review Letters **81**, 1110–1113 (1998).

[17] A. Muller, E. B. Flagg, J. R. Lawall, and G. S. Solomon, "Ultrahigh-finesse, low-mode-volume Fabry-Pérot microcavity," Optics Letter **35**, 2293–2295 (2010).

[18] M. L. Gorodetsky, A. A. Savchenkov, and V. S. Ilchenko, "Ultimate Q of Optical Microsphere Resonators," Optics Letters **21**, 453–455 (1996).

[19] T. J. Kippenberg, S. M. Spillane, and K. J. Vahala, "Demonstration of ultra-high-Q small mode volume toroid microcavities on a chip," Applied Physics Letters **85**, 6113–6115 (2004).

[20] T. Aoki, B. Dayan, E. Wilcut, W. P. Bowen, A. S. Parkins, T. J. Kippenberg, K. J. Vahala, and H. J. Kimble, "Observation of strong coupling between one atom and a monolithic microresonator," Nature **443**, 671–674 (2006).

[21] P. Del'Haye, A. Schliesser, O. Arcizet, T. Wilken, R. Holzwarth, and T. J. Kippenberg, "Optical Frequency Comb Generation from a Monolithic Microresonator," Nature **450**, 1214–1217 (2007).

[22] T. Carmon and K. Vahala, "Visible Continuous Emission from a Silica Microphotonic Device by Third Harmonic Generation," Nature Physics **3**, 430–435 (2007).

[23] D. V. Strekalov, C. Marquardt, A. B. Matsko, H. G. L. Schwefel, and G. Leuchs, "Nonlinear and quantum optics with whispering gallery resonators," Journal of Optics **18**, 123002:1–123002:43 (2016).

[24] F. Vollmer and S. Arnold, "Whispering-Gallery-Mode Biosensing: Label-Free Detection Down to Single Molecules," Nature Methods **5**, 591–596 (2008).

[25] F. Vollmer, D. Braun, A. Libchaber, M. Khoshsima, I. Teraoka, and S. Arnold, "Protein Detection by Optical Shift of a Resonant Microcavity," Applied Physics Letters **80**, 4057–4059 (2002).

[26] S. Arnold, R. Ramjit, D. Keng, V. Kolchenko, and I. Teraoka, "MicroParticle Photophysics Illuminates Viral Bio-Sensing," Faraday Discussions **137**, 65–83 (2008).

[27] L. B. Shao, X. F. Jiang, X. C. Yu, B. B. Li, W. R. Clements, F. Vollmer, W. Wang, Y. F. Xiao, and Q. H. Gong, "Detection of Single Nanoparticles and Lentiviruses Using Microcavity Resonance Broadening," Advanced Materials **25**, 5616–5620 (2013).

[28] D. K. Gramotnev and S. I. Bozhevolnyi, "Plasmonics beyond the diffraction limit," Nature Photonics **4**, 83–91 (2010).

[29] A. G. Curto, G. Volpe, T. H. Taminiau, M. P. Kreuzer, R. Quidant, and N. F. van Hulst, "Unidirectional emission of a quantum dot coupled to a nanoantenna," Science **329**, 930–933 (2010).

[30] S. A. Maier, "Plasmonics: Metal Nanostructures for Subwavelength Photonic Devices," IEEE Journal of Selected Topics in Quantum Electronics **12**, 1214–1220 (2006).

[31] E. J. R. Vesseur, R. de Waele, H. J. Lezec, H. A. Atwater, F. J. García de Abajo, and A. Polman, "Surface plasmon polariton modes in a single-crystal Au nanoresonator fabricated using focused-ion-beam milling," Applied Physics Letters **92**, 083110:1–083110:10 (2008).

[32] H. Raether, ed., *Surface plasmons on smooth surfaces and on Gratings*, vol. 111 (Springer, 1988).

[33] V. R. Dantham, S. Holler, V. Kolchenko, Z. Wan, and S. Arnold, "Taking Whispering Gallery-Mode Single Virus Detection and Sizing to the Limit," Applied Physics Letters **101**, 043704:1–043704:4 (2012).

[34] M. A. Santiago-Cordoba, S. V. Boriskina, F. Vollmer, and M. C. Demirel, "Plasmonic Nanoparticle-based Protein Detection by Optical Shift of a Resonant Microcavity," Applied Physics Letters **99**, 073701:1–073701:3 (2011).

[35] J. D. Swaim, J. Knittel, and W. P. Bowen, "Detection limits in whispering gallery biosensors with plasmonic enhancement," Applied Physics Letters **99**, 243109:1–243109:3 (2011).

[36] M. A. Santiago-Cordoba, M. Cetinkaya, S. V. Boriskina, F. Vollmer, and M. C. Demirel, "Ultrasensitive detection of a protein by optical trapping in a photonic-plasmonic microcavity," Journal of Biophotonics **5**, 629–638 (2012).

[37] S. I. Shopova, R. Rajmangal, S. Holler, and S. Arnold, "Plasmonic enhancement of a whispering-gallery-mode biosensor for single nanoparticle detection," Applied Physics Letters **98**, 243104:1–243104:3 (2011).

[38] M. D. Baaske and F. Vollmer, "Optical observation of single atomic ions interacting with plasmonic nanorods in aqueous solution," Nature Photonics **10**, 733–739 (2016).

[39] B. Min, E. Ostby, V. Sorger, E. Ulin-Avila, L. Yang, X. Zhang, and K. Vahala, "High-Q surface plasmon-polariton whispering-gallery microcavity," Nature **457**, 455–459 (2009).

[40] J. Xavier, S. Vincent, F. Meder, and F. Vollmer, "Advances in optoplasmonic sensors - Combining optical nano/microcavities and photonic crystals with plasmonic nanostructures and nanoparticles," Nanophotonics **7**, 1–38 (2018).

[41] M. R. Foreman and F. Vollmer, "Level repulsion in hybrid photonic-plasmonic microresonators for enhanced biodetection," Physical Review A **88**, 023831:1–023831:6 (2013).

[42] Q. Lu, D. Chen, G. Wu, B. Peng, and J. Xu, "A hybrid plasmonic microresonator with high quality factor and small mode volume," Journal of Optics **14**, 125503:1–125503:5 (2012).

[43] S. Cai, Y. Xiang, Y. Miao, M. Li, Y. Peng, and Y. Song, "Mode coupling in metal-coated microsphere," Optics Express **24**, 13832–13838 (2016).

[44] Y. Yin, Y. Chen, E. Saei Ghareh Naz, X. Lu, S. Li, V. Engemaier, L. Ma, and O. G. Schmidt, "Silver Nanocap Enabled Conversion and Tuning of Hybrid Photon-Plasmon Modes in Microtubular Cavities," ACS Photonics **4**, 736–740 (2017).

[45] L. J. Kricka, "Microchips, Microarrays, Biochips and Nanochips: Personal Laboratories for the 21st Century," Clinica Chimica Acta **307**, 219–223 (2001).

[46] Ş. K. Özdemir, J. Zhu, X. Yang, B. Peng, H. Yilmaz, L. He, F. Monifi, S. H. Huang, G. L. Long, and L. Yang, "Highly sensitive detection of nanoparticles with a self-referenced and self-heterodyned whispering-gallery Raman microlaser," Proceedings of the National Academy of Sciences **111**, E3836–E3844 (2014).

[47] L. Yang, T. Lu, T. Carmon, B. Min, and K. J. Vahala, "A 4-Hz Fundamental Linewidth On-Chip Microlaser," in "Conference on Quantum Electronics and Laser Science Conference on Lasers and Electro-Optics, CLEO/QELS, San Jose, USA," (2007).

[48] J. Yang and L. Y. Guo, "Optical sensors based on active microcavities," IEEE Journal of Selected Topics in Quantum Electronics **12**, 143–147 (2006).

[49] L. He, Ş. K. Özdemir, J. Zhu, and L. Yang, "Ultrasensitive detection of mode splitting in active optical microcavities," Physical Review A **82**, 053810:1–053810:4 (2010).

[50] M. R. Foreman, J. D. Swaim, and F. Vollmer, "Whispering Gallery Mode Sensors," Advances in Optics and Photonics **7**, 168–240 (2015).

[51] S. Krämmer, S. Rastjoo, T. Siegle, S. F. Wondimu, C. Klusmann, C. Koos, and H. Kalt, "Size-optimized polymeric whispering gallery mode lasers with enhanced sensing performance," Optics Express **25**, 7884–7894 (2017).

[52] L. Rayleigh, "The Problem of the Whispering Gallery," Philosophical Magazine Series 6 **20**, 1001–1004 (1910).

[53] R. D. Richtmyer, "Dielectric Resonators," Journal of Applied Physics **10**, 391–398 (1939).

[54] G. Mie, "Beiträge zur Optik trüber Medien, speziell kolloidaler Metallösungen," Annalen der Physik **330**, 377–445 (1908).

[55] B. R. Johnson, "Theory of Morphology-Dependent Resonances – Shape Resonances and Width Formulas," Journal of the Optical Society of America A **10**, 343–352 (1993).

[56] H.-J. Moon, "Photon Tunneling Behavior in a Coated Cylindrical Microcavity Laser," Journal of the Optical Society of America B **27**, 512–517 (2010).

[57] J. D. Jackson, ed., *Klassische Elektrodynamik* (De Gruyter, Berlin, 2013).

[58] C. F. Bohren and D. R. Huffman, eds., *Absorption and Scattering of Light by Small Particles* (John Wiley & Sons, 2008).

[59] A. N. Oraevsky, "Whispering-gallery waves," Quantum Electronics **32**, 377–400 (2002).

[60] S. Balac and P. Féron, "Whispering gallery modes volume computation in optical micro-spheres," Research report, FOTON, UMR CNRS 6082 (2014).

[61] C. C. Lam, P. T. Leung, and K. Young, "Explicit asymptotic formulas for the positions, widths, and strengths of resonances in Mie scattering," Journal of the Optical Society of America B **9**, 1585–1592 (1992).

[62] M. Borselli, T. Johnson, and O. Painter, "Beyond the Rayleigh Scattering Limit in High-Q Silicon Microdisks: Theory and Experiment," Optics Express **13**, 1515–1530 (2005).

[63] A. W. Snyder and J. Love, *Optical Waveguide Theory* (Springer US, 2012).

[64] M. Hauser, "Mikroresonatoren aus Glas und Polymeren als optische Flüstergalerien," Ph.D. Thesis, Karlsruhe Institute of Technology (KIT) (2011).

[65] K. Okamoto, *Fundamentals of Optical Waveguides*, Electronics & Electrical (Elsevier Science, 2006).

[66] T. J. Kippenberg, S. M. Spillane, D. K. Armani, B. Min, L. Yang, and K. J. Vahala, "Fabrication, Coupling and Nonlinear Optics of Ultra-High-Q Micro-Sphere and Chip-Based Toroid Microcavities," in "Optical Microcavities," , K. J. Vahala, ed. (World Scientific, 2004).

[67] R. F. Oulton, V. J. Sorger, D. A. Genov, D. F. P. Pile, and X. Zhang, "A hybrid plasmon waveguide for subwavelength confinement and long-range propagation," Nature Photonics **2**, 496–500 (2008).

[68] L. D. Landau, L. P. Pitaevskii, and E. Lifshitz, *Electrodynamics of Continuous Media* (Butterworth-Heinemann, Oxford, 2002).

[69] J. R. Buck and H. J. Kimble, "Optimal sizes of dielectric microspheres for cavity QED with strong coupling," Physical Review A **67**, 033806:1–033806:11 (2003).

[70] G. C. Righini, Y. Dumeige, P. Féron, M. Ferrari, G. N. Conti, D. Ristic, and S. Soria, "Whispering Gallery Mode Microresonators: Fundamentals and Applications," Rivista del Nuovo Cimento **34**, 435–488 (2011).

[71] T. Großmann, "Whispering-Gallery-Mode Lasing in Polymeric Microcavities," Ph.D. Thesis, Karlsruhe Institute of Technology (KIT) (2012).

[72] M. Borselli, K. Srinivasan, P. E. Barclay, and O. Painter, "Rayleigh scattering, mode coupling, and optical loss in silicon microdisks," Applied Physics Letters **85**, 3693–3695 (2004).

[73] T. Grossmann, M. Hauser, T. Beck, C. Gohn-Kreuz, M. Karl, H. Kalt, C. Vannahme, and T. Mappes, "High-Q Conical Polymeric Microcavities," Applied Physics Letters **96**, 013303:1–013303:3 (2010).

[74] T. J. Kippenberg, J. Kalkman, A. Polman, and K. J. Vahala, "Demonstration of an erbium-doped microdisk laser on a silicon chip," Physical Review A **74**, 051802:1–051802:4 (2006).

[75] H. D. Reidenbach and F. Bodem, "Optical transmission of bulk plastic material and plastic lightguides at high optical powers," Optics & Laser Technology **7**, 131–133 (1975).

[76] A. M. Armani, A. Srinivasan, and K. J. Vahala, "Soft Lithographic Fabrication of High Q Polymer Microcavity Arrays," Nano Letters **7**, 1823–1826 (2007).

[77] M. A. Foster, J. S. Levy, O. Kuzucu, S. Kasturi, M. Lipson, and A. L. Gaeta, "Silicon-Based Monolithic Optical Frequency Comb Source," Optics Express **19**, 14233–14239 (2011).

[78] P. S. Kuo, J. Bravo-Abad, and G. S. Solomon, "Second-harmonic generation using quasi-phasematching in a GaAs whispering-gallery-mode microcavity," Nature Communications **5**, 3109:1–3109:7 (2014).

[79] K. Djordjev, S. J. Choi, S. J. Choi, and P. D. Dapkus, "High-Q vertically coupled InP microdisk resonators," IEEE Photonics Technology Letters **14**, 331–333 (2002).

[80] A. A. Savchenkov, A. B. Matsko, V. S. Ilchenko, I. Solomatine, D. Seidel, and L. Maleki, "Tunable Optical Frequency Comb with a Crystalline Whispering Gallery Mode Resonator," Physical Review Letters **101**, 093902:1–093902:4 (2008).

[81] B. E. Little, S. T. Chu, H. A. Haus, J. Foresi, and J.-P. Laine, "Microring resonator channel dropping filters," Journal of Lightwave Technology **15**, 998–1005 (1997).

[82] A. J. Maker and A. M. Armani, "Fabrication of Silica Ultra High Quality Factor Microresonators," Journal of Visualized Experiments **65**, e4164:1–e4164:6 (2012).

[83] Y. Takezawa, N. Taketani, S. Tanno, and S. Ohara, "Empirical Estimation Method of Intrinsic Loss Spectra in Transparent Amorphous Polymers for Plastic Optical Fibers," Journal of Applied Polymer Science **46**, 1835–1841 (1992).

[84] P. Forster, "Photonisch–plasmonische Hybridmoden in silberbeschichteten keilförmigen Flüstergalerie-Resonatoren," Master's Thesis, Karlsruhe Institute of Technology (KIT) (2017).

[85] C. Klusmann, J. Oppermann, P. Forster, C. Rockstuhl, and H. Kalt, "Identification of dielectric, plasmonic, and hybrid modes in metal-coated whispering-gallery-mode resonators," ACS Photonics **5**, 2365–2373 (2018).

[86] D. Daly, R. F. Stevens, M. C. Hutley, and N. Davies, "The manufacture of microlenses by melting photoresist," Measurement Science and Technology **1**, 759–766 (1990).

[87] T. R. Jay, M. B. Stern, and R. E. Knowlden, "Effect of refractive microlens array fabrication parameters on optical quality," Proceedings of SPIE **1751**, 236–245 (1993).

[88] P. Nussbaum, R. Völkel, H. P. Herzig, M. Eisner, and S. Haselbeck, "Design, fabrication and testing of microlens arrays for sensors and microsystems," Pure and Applied Optics **6**, 617–636 (1997).

[89] J. R. Schwesyg, T. Beckmann, A. S. Zimmermann, K. Buse, and D. Haertle, "Fabrication and characterization of whispering-gallery-mode resonators made of polymers," Optics Express **17**, 2573–2578 (2009).

[90] J. Lahann, I. S. Choi, J. Lee, K. F. Jensen, and R. Langer, "A new method toward microengineered surfaces based on reactive coating," Angewandte Chemie International Edition **40**, 3166–3169 (2001).

[91] X. Deng, T. W. Eyster, Y. Elkasabi, and J. Lahann, "Bio-orthogonal polymer coatings for co-presentation of biomolecules," Macromolecular Rapid Communications **33**, 640–645 (2012).

[92] F. Bally, K. Cheng, H. Nandivada, X. Deng, A. M. Ross, A. Panades, and J. Lahann, "Co-immobilization of biomolecules on ultrathin reactive chemical vapor deposition coatings using multiple click chemistry strategies," ACS Applied Materials & Interfaces **5**, 9262–9268 (2013).

[93] X. Deng and J. Lahann, "Orthogonal surface functionalization through bioactive vapor-based polymer coatings," Journal of Applied Polymer Science **131**, 40315:1–40315:9 (2014).

[94] K. K. Gleason, ed., *CVD Polymers: Fabrication of Organic Surfaces and Devices* (Wiley-VCH, 2015).

[95] K. S. S. Harsha, ed., *Principles of Physical Vapor Deposition of Thin Films* (Elsevier, Great Britain, 2006).

[96] Thin silver films were deposited onto polymeric microwedges using PVD by Patrick Forster during his master's thesis.

[97] F. P. Schäfer, ed., *Dye Lasers* (Springer, 1990).

[98] A. Diaspro, ed., *Nanoscopy and Multidimensional Optical Fluorescence Microscopy* (CRC Press, Taylor & Francis Group, 2010).

[99] C. Grivas and M. Pollnau, "Organic Solid-State Integrated Amplifiers and Lasers," Laser and Photonics Reviews **6**, 419–462 (2012).

[100] S. Krämmer, "Dye-Doped Polymeric Lasers for Sensing Applications," Ph.D. Thesis, Karlsruhe Institute of Technology (KIT) (2016).

[101] A. B. Matsko and V. S. Ilchenko, "Optical Resonators With Whispering-Gallery Modes — Part I: Basics," IEEE Journal of Selected Topics in Quantum Electronics **12**, 3–14 (2006).

[102] J. Zhu, Ş. K. Özdemir, H. Yilmaz, B. Peng, M. Dong, M. Tomes, T. Carmon, and L. Yang, "Interfacing whispering-gallery microresonators and free space light with cavity enhanced Rayleigh scattering." Scientific reports **4**, 6396:1–6396:7 (2014).

[103] M. L. Gorodetsky and V. S. Ilchenko, "High-Q optical whispering-gallery microresonators: precession approach for spherical mode analysis and emission patterns with prism couplers," Optics Communications **113**, 133–143 (1994).

[104] M. L. Gorodetsky and V. S. Ilchenko, "Optical microsphere resonators: optimal coupling to high-Q whispering gallery modes," Journal of the Optical Society of America B **16**, 147–154 (1999).

[105] J. C. Knight, G. Cheung, F. Jacques, and T. A. Birks, "Phase-matched excitation of whispering-gallery-mode resonances by a fiber taper," Optics Letters **22**, 1129–1131 (1997).

[106] M. Cai, O. Painter, and K. J. Vahala, "Observation of Critical Coupling in a Fiber Taper to a Silica-Microsphere Whispering-Gallery Mode System," Physical Review Letters **85**, 74–77 (2000).

[107] S. M. Spillane, T. J. Kippenberg, O. J. Painter, and K. J. Vahala, "Ideality in a fiber-taper-coupled microresonator system for application to cavity quantum electrodynamics," Physical Review Letters **91**, 043902:1–043902:4 (2003).

[108] T. Beck, "Polymer-Mikroresonatoren hoher Güte als optische Sensoren," Ph.D. Thesis, Karlsruhe Institute of Technology (KIT) (2013).

[109] G. Brambilla, F. Xu, and X. Feng, "Fabrication of Optical Fibre Nanowires and their Optical and Mechanical Characterisation," Electronics Letters **42**, 517–518 (2006).

[110] M. Choi, J. W. Choi, S. Kim, S. Nizamoglu, S. K. Hahn, and S. H. Yun, "Light-guiding hydrogels for cell-based sensing and optogenetic synthesis in vivo," Nature photonics **7**, 987–994 (2013).

[111] A. M. Ruminski, M. M. Moore, and M. J. Sailor, "Humidity-Compensating Sensor for Volatile Organic Compounds Using Stacked Porous Silicon Photonic Crystals," Advanced Functional Materials **18**, 3418–3426 (2008).

[112] N. Liu, M. Mesch, T. Weiss, M. Hentschel, and H. Giessen, "Infrared perfect absorber and its application as plasmonic sensor," Nano letters **10**, 2342–2348 (2010).

[113] K. M. Mayer and J. H. Hafner, "Localized Surface Plasmon Resonance Sensors," Chemical Reviews **111**, 3828–3857 (2011).

[114] J. Homola, "Surface Plasmon Resonance Sensors for Detection of Chemical and Biological Species," Chemical Reviews **108**, 462–493 (2008).

[115] M. S. Luchansky and R. C. Bailey, "High-Q Optical Sensors for Chemical and Biological Analysis," Analytical Chemistry **84**, 793–821 (2012).

[116] W. Lee, Y. Sun, H. Li, K. Reddy, M. Sumetsky, and X. Fan, "A Quasi-Droplet Optofluidic Ring Resonator Laser Using a Micro-Bubble," Applied Physics Letters **99**, 1–4 (2011).

[117] D. Gandolfi, F. Ramiro-Manzano, F. J. Aparicio Rebollo, M. Ghulinyan, G. Pucker, and L. Pavesi, "Role of edge inclination in an optical microdisk resonator for label-free sensing," Sensors **15**, 4796–4809 (2015).

[118] I. M. White and X. Fan, "On the performance quantification of resonant refractive index sensors," Optics Express **16**, 1020–1028 (2008).

[119] D. S. Weiss, V. Sandoghdar, J. Hare, V. Lefèvre-Seguin, J. M. Raimond, and S. Haroche, "Splitting of High-Q Mie Modes Induced by Light Backscattering in Silica Microspheres," Optics Letters **20**, 1835–1837 (1995).

[120] L. He, Ş. K. Özdemir, Z. J., W. Kim, and L. Yang, "Detecting single viruses and nanoparticles using whispering gallery microlasers," Nature Nanotechnology **6**, 428–432 (2011).

[121] J. Zhu, Ş. K. Ozdemir, Y.-F. Xiao, L. Li, L. He, D.-R. Chen, and L. Yang, "On-chip single nanoparticle detection and sizing by mode splitting in an ultrahigh-Q microresonator," Nature Photonics **4**, 46–49 (2010).

[122] F. Vollmer and L. Yang, "Label-free detection with high-Q microcavities: a review of biosensing mechanisms for integrated devices," Nanophotonics **1**, 267–291 (2012).

[123] R. W. P. Drever, J. L. Hall, F. V. Kowalski, J. Hough, G. M. Ford, A. J. Munley, and H. Ward, "Laser phase and frequency stabilization using an optical resonator," Applied Physics B **31**, 97–105 (1983).

[124] J. Su, A. F. G. Goldberg, and B. M. Stoltz, "Label-free detection of single nanoparticles and biological molecules using microtoroid optical resonators," Light: Science & Applications **5**, e16001:1–e16001:6 (2016).

[125] N. M. Hanumegowda, C. Stica, B. C. Patel, I. White, and X. Fan, "Refractometric sensors based on microsphere resonators," Applied Physics Letters **87**, 201107:1–201107:3 (2005).

[126] Y. Sun and X. Fan, "Optical ring resonators for biochemical and chemical sensing," Analytical and Bioanalytical Chemistry **399**, 205–211 (2011).

[127] K. De Vos, I. Bartolozzi, E. Schacht, P. Bienstman, and R. Baets, "Silicon-on-Insulator microring resonator for sensitive and label-free biosensing," Optics Express **15**, 7610–7615 (2007).

[128] G. A. Rodriguez, S. Hu, and S. M. Weiss, "Porous silicon ring resonator for compact, high sensitivity biosensing applications," Optics Express **23**, 7111–7119 (2015).

[129] M. Rex, F. E. Hernandez, and A. D. Campiglia, "Pushing the limits of mercury sensors with gold nanorods," Analytical chemistry **78**, 445–451 (2006).

[130] R. B. M. Schasfoort and A. J. Tudos, eds., *Handbook of Surface Plasmon Resonance* (The Royal Society of Chemistry, 2008).

[131] H. H. Jeong, A. G. Mark, M. Alarcón-Correa, I. Kim, P. Oswald, T. C. Lee, and P. Fischer, "Dispersion and shape engineered plasmonic nanosensors," Nature Communications **7**, 11331:1–11331:7 (2016).

[132] P. Pfeifer, U. Aldinger, G. Schwotzer, S. Diekmann, and P. Steinrücke, "Real time sensing of specific molecular binding using surface plasmon resonance spectroscopy," Sensors and Actuators B: Chemical **54**, 166–175 (1999).

[133] T. Chung, S.-Y. Lee, E. Y. Song, H. Chun, and B. Lee, "Plasmonic Nanostructures for Nano-Scale Bio-Sensing," Sensors **11**, 10907–10929 (2011).

[134] M. E. Stewart, C. R. Anderton, L. B. Thompson, J. Maria, S. K. Gray, J. A. Rogers, and R. G. Nuzzo, "Nanostructured plasmonic sensors," Chemical Reviews **108**, 494–521 (2008).

[135] R. Bukasov and J. S. Shumaker-Parry, "Highly Tunable Infrared Extinction Properties of Gold Nanocrescents," Nano Letters **7**, 1113–1118 (2007).

[136] A. U. Khan, S. Zhao, and G. Liu, "Key Parameter Controlling the Sensitivity of Plasmonic Metal Nanoparticles: Aspect Ratio," The Journal of Physical Chemistry C **120**, 19353–19364 (2016).

[137] K. A. Willets and R. P. Van Duyne, "Localized Surface Plasmon Resonance Spectroscopy and Sensing," Annual Review of Physical Chemistry **58**, 267–297 (2007). PMID: 17067281.

[138] I. Ament, J. Prasad, A. Henkel, S. Schmachtel, and C. Sönnichsen, "Single Unlabeled Protein Detection on Individual Plasmonic Nanoparticles," Nano Letters **12**, 1092–1095 (2012).

[139] P. Zijlstra, P. M. R. Paulo, and M. Orrit, "Optical Detection of Single Non-Absorbing Molecules Using the Surface Plasmon Resonance of a Gold Nanorod," Nature Nanotechnology **7**, 379–382 (2012).

[140] H. Ditlbacher, A. Hohenau, D. Wagner, U. Kreibig, M. Rogers, F. Hofer, F. R. Aussenegg, and J. R. Krenn, "Silver Nanowires as Surface Plasmon Resonators," Physical Review Letters **95**, 257403:1–257403:4 (2005).

[141] S. I. Bozhevolnyi, V. S. Volkov, E. Devaux, J.-Y. Laluet, and T. W. Ebbesen, "Channel plasmon subwavelength waveguide components including interferometers and ring resonators," Nature **440**, 508–511 (2016).

[142] H. T. Miyazaki and Y. Kurokawa, "Squeezing Visible Light Waves into a 3-nm-Thick and 55-nm-Long Plasmon Cavity," Physical Review Letters **96**, 067401:1–067401:4 (2006).

[143] A. Ramachandran, S. Wang, J. Clarke, S. J. Ja, D. Goad, L. Wald, E. M. Flood, E. Knobbe, J. V. Hryniewicz, S. T. Chu, D. Gill, W. Chen, O. King, and B. E. Little, "A universal biosensing platform based on optical micro-ring resonators," Biosensors and Bioelectronics **23**, 939–944 (2008).

[144] F. De Angelis, M. Patrini, G. Das, I. Maksymov, M. Galli, L. Businaro, L. C. Andreani, and E. Di Fabrizio, "A hybrid plasmonic-photonic nanodevice for label-free detection of a few molecules," Nano letters **8**, 2321–2327 (2008).

[145] M. Chamanzar, E. S. Hosseini, S. Yegnanarayanan, and A. Adibi, "Hybrid plasmonic-photonic resonators for sensing and spectroscopy," in "CLEO: 2011 - Laser Science to Photonic Applications," (IEEE, 2011), pp. 1–2.

[146] M. R. Foreman and F. Vollmer, "Theory of resonance shifts of whispering gallery modes by arbitrary plasmonic nanoparticles," New Journal of Physics **15**, 083006:1–083006:27 (2013).

[147] Y.-F. Xiao, C.-L. Zou, B.-B. Li, Y. Li, C.-H. Dong, Z.-F. Han, and Q. Gong, "High-Q Exterior Whispering-Gallery Modes in a Metal-Coated Microresonator," Physical Review Letters **105**, 153902:1–153902:4 (2010).

[148] M. Zhang, G. Wu, and D. Chen, "Silicon hybrid plasmonic microring resonator for sensing applications," Applied Optics **54**, 7131–7134 (2015).

[149] R. Ahmed, A. A. Rifat, A. K. Yetisen, M. S. Salem, S.-H. Yun, and H. Butt, "Optical microring resonator based corrosion sensing," RSC Advances **6**, 56127–56133 (2016).

[150] D. Urbonas, A. Balčytis, M. Gabalis, K. Vaškevičius, G. Naujokaitė, S. Juodkazis, and R. Petruškevičius, "Ultra-wide free spectral range, enhanced sensitivity, and removed mode splitting SOI optical ring resonator with dispersive metal nanodisks," Optics Letters **40**, 2977–2980 (2015).

[151] M. Chamanzar, M. Soltani, B. Momeni, S. Yegnanarayanan, and A. Adibi, "Hybrid photonic surface-plasmon-polariton ring resonators for sensing applications," Applied Physics B **101**, 263–271 (2010).

[152] H. Fan, C. Xia, L. Fan, L. Wang, and M. Shen, "Graphene-supported plasmonic whispering-gallery mode in a metal-coated microcavity for sensing application with ultrahigh sensitivity," Optics Communications **410**, 668–673 (2018).

[153] F. Zangeneh-Nejad, "A Graphene-Based THz Ring Resonator for Label-Free Sensing," IEEE Sensors Journal **16**, 4338–4344 (2016).

[154] X. Sun, D. Dai, L. Thylén, and L. Wosinski, "Double-Slot Hybrid Plasmonic Ring Resonator Used for Optical Sensors and Modulators," Photonics **2**, 1116–1130 (2015).

[155] E. Kim, M. D. Baaske, and F. Vollmer, "In Situ Observation of Single-Molecule Surface Reactions from Low to High Affinities," Advanced Materials **28**, 9941–9948 (2016).

[156] V. R. Dantham, S. Holler, C. Barbre, D. Keng, V. Kolchenko, and S. Arnold, "Label-Free Detection of Single Protein Using a Nanoplasmonic-Photonic Hybrid Microcavity," Nano Letters **7**, 3347–3351 (2013).

[157] S. Arnold, V. R. Dantham, C. Barbre, B. A. Garetz, and X. Fan, "Periodic plasmonic enhancing epitopes on a whispering gallery mode biosensor," Optics Express **20**, 26147–26159 (2012).

[158] S. A. Schmid, "Plasmonic Nanoparticles Coupled to Whispering Gallery Mode Resonators for Sensing Applications," Master's Thesis, Karlsruhe Institute of Technology (KIT) (2016).

[159] Y. S. Joe, A. M. Satanin, and C. S. Kim, "Classical analogy of Fano resonances," Physica Scripta **74**, 259–266 (2006).

[160] W. Frank and P. von Brentano, "Classical analogy to quantum mechanical level repulsion," American Journal of Physics **62**, 706–709 (1994).

[161] Calculations are based on a matlab code developed by Steffen A. Schmid during his master's thesis.

[162] S. Mühlig, "Towards Self-Assembled Metamaterials," Ph.D. Thesis, Friedrich Schiller Universität Jena (2014).

[163] R. N. S. Suryadharma, M. Fruhnert, I. Fernandez-Corbaton, and C. Rockstuhl, "Studying plasmonic resonance modes of hierarchical self-assembled meta-atoms based on their transfer matrix," Physical Review B **96**, 045406:1–045406:14 (2017).

[164] Y. lin Xu, "Electromagnetic scattering by an aggregate of spheres," Applied Optics **34**, 4573–4588 (1995).

[165] J. Boken, P. Khurana, S. Thatai, D. Kumar, and S. Prasad, "Plasmonic nanoparticles and their analytical applications: A review," Applied Spectroscopy Reviews **52**, 774–820 (2017).

[166] Simulations were performed by Steffen A. Schmid during his master's thesis.

[167] L. I. Deych, C. Schmidt, A. Chipouline, T. Pertsch, and A. Tünnermann, "Optical coupling of fundamental whispering-gallery modes in bispheres," Physical Review A **77**, 051801:1–051801:4 (2008).

[168] Y. Hu, L. Shao, S. Arnold, Y.-C. Liu, C.-Y. Ma, and Y.-F. Xiao, "Mode broadening induced by nanoparticles in an optical whispering-gallery microcavity," Physical Review A **90**, 043847:1–043847:10 (2014).

[169] M. R. Foreman, D. Keng, E. Treasurer, J. R. Lopez, and S. Arnold, "Whispering gallery mode single nanoparticle detection and sizing: the validity of the dipole approximation," Optics Letters **42**, 963–966 (2017).

[170] C. Klusmann, R. N. S. Suryadharma, J. Oppermann, C. Rockstuhl, and H. Kalt, "Hybridizing whispering gallery modes and plasmonic resonances in a photonic metadevice for biosensing applications [Invited]," Journal of the Optical Society of America B **34**, D46–D55 (2017).

[171] P. Malinský, P. Slepička, V. Hnatowicz, and V. Svorčík, "Early stages of growth of gold layers sputter deposited on glass and silicon substrates," Nanoscale research letters **7**, 241–248 (2012).

[172] S. Mühlig, C. Rockstuhl, V. Yannopapas, T. Bürgi, N. Shalkevich, and F. Lederer, "Optical properties of a fabricated self-assembled bottom-up bulk metamaterial," Optics express **19**, 9607–9616 (2011).

[173] A. Sihvola, "Mixing Rules with Complex Dielectric Coefficient," Subsurface Sensing Technologies and Applications **1**, 393–415 (2000).

[174] Calculation was performed by Radius N. S. Suryadharma.

[175] S. Mühlig, C. Menzel, C. Rockstuhl, and F. Lederer, "Multipole analysis of meta-atoms," Metamaterials **5**, 64 – 73 (2011). Metamaterials Congress - 2010.

[176] A. Derkachova, K. Kolwas, and I. N. Demchenko, "Dielectric Function for Gold in Plasmonics Applications: Size Dependence of Plasmon Resonance Frequencies and Damping Rates for Nanospheres," in "Plasmonics," (2016), pp. 941–951.

[177] P. B. Johnson and R. W. Christy, "Optical Constants of the Noble Metals," Physical Review B **6**, 4370–4379 (1972).

[178] U. Kreibig, "Electronic properties of small silver particles: the optical constants and their temperature dependence," Journal of Physics F: Metal Physics **4**, 999–1014 (1974).

[179] C. Bréchignac, P. Houdy, and M. Lahmani, *Nanomaterials and Nanochemistry* (Springer Berlin Heidelberg, 2008).

[180] U. Kreibig and M. Vollmer, eds., *Optical Properties of Metal Clusters* (Springer-Verlag, Berlin, Heidelberg, 1995).

[181] L. Novotny and B. Hecht, eds., *Principles of Nano-Optics* (Cambridge University Press, 2006).

[182] J. Pomplun, S. Burger, L. Zschiedrich, and F. Schmidt, "Adaptive finite element method for simulation of optical nano structures," Physica Status Solidi **244**, 3419–3434 (2007).

[183] C. Rockstuhl and T. Scharf, eds., *Amorphous Nanophotonics* (Springer, 2013).

[184] D.-S. Wang and C.-W. Lin, "Density-dependent optical response of gold nanoparticle monolayers on silicon substrates," Optics Letters **32**, 2128–2130 (2007).

[185] B. N. J. Persson, "Lateral interactions in small particle systems," Journal de Physique Colloques **44**, 409–420 (1983).

[186] Multi-Mie simulations of the hybrid microsphere used to verify the effective medium approach were performed by Radius N. S. Suryadharma.

[187] R. Hightower and C. Richardson, "Resonant mie scattering from a layered sphere," Appl. Optics **27**, 4850–4855 (1988).

[188] A. Hammiche, R. P. Webb, and I. H. Wilson, "A scanning tunnelling microscopy study of thin gold films evaporated on silicon," Vacuum **45**, 569–573 (1994).

[189] H. Qian, Y. Xiao, D. Lepage, L. Chen, and Z. Liu, "Quantum Electrostatic Model for Optical Properties of Nanoscale Gold Films," Nanophotonics **4**, 413–418 (2015).

[190] F. J. G. de Abajo, "Nonlocal Effects in the Plasmons of Strongly Interacting Nanoparticles, Dimers, and Waveguides," The Journal of Physical Chemistry C **112**, 17983–17987 (2008).

[191] M. M. Mazumder, G. Chen, R. K. Chang, and J. B. Gillespie, "Wavelength Shifts of Dye Lasing in Microdroplets: Effect of Absorption Change," Optics Letters **20**, 878–880 (1995).

[192] H.-J. Moon, Y.-T. Chough, J. B. Kim, K. An, J. Yi, and J. Lee, "Cavity-Q-Driven Spectral Shift in a Cylindrical Whispering-Gallery-Mode Microcavity Laser," Applied Physics Letters **76**, 3679–3681 (2000).

[193] T. Siegle, "Durchstimmbare photonische Bauelemente aus polymeren Flüstergalerie-Resonatoren," Ph.D. Thesis, Karlsruhe Institute of Technology (KIT) (2017).

[194] J. Oppermann, "Quantum Many-Body Phenomena in Optical Whispering Gallery Mode Resonators," Master's Thesis, Karlsruhe Institute of Technology (KIT) (2016).

[195] H. S. Hsu, C. Cai, and A. M. Armani, "Ultra-low-threshold Er:Yb sol-gel microlaser on silicon," Optics Express **17**, 23265–23271 (2009).

[196] V. Sandoghdar, F. Treussart, J. Hare, V. Lefèvre-Seguin, J.-M. Raimond, and S. Haroche, "Very low threshold whispering-gallery-mode microsphere laser," Physical Review A **54**, R1777–R1780 (1996).

[197] T. Wienhold, S. Kraemmer, S. F. Wondimu, T. Siegle, U. Bog, U. Weinzierl, S. Schmidt, H. Becker, H. Kalt, T. Mappes, S. Koeber, and C. Koos, "All-polymer photonic sensing platform based on whispering-gallery mode microgoblet lasers," Lab on a Chip **15**, 3800–3806 (2015).

[198] S. N. Chormaic, R. Madugani, S. Kasumie, J. Ward, and Y. Yang, "Whispering gallery resonators for nonlinear optics and optical manipulation," in "Progress in Electromagnetic Research Symposium (PIERS)," (2016), pp. 2619–2619.

[199] R. Castro-Beltrán, V. M. Diep, S. Soltani, E. Gungor, and A. M. Armani, "Plasmonically Enhanced Kerr Frequency Combs," ACS Photonics **4**, 2828–2834 (2017).

[200] S. M. Spillane, T. J. Kippenberg, K. J. Vahala, K. W. Goh, E. Wilcut, and H. J. Kimble, "Ultrahigh-Q toroidal microresonators for cavity quantum electrodynamics," Physical Review A **71**, 013817:1–013817:10 (2005).

[201] W. G. Farr, M. Goryachev, D. L. Creedon, and M. E. Tobar, "Strong Coupling between Whispering Gallery Modes and Chromium Ions in Ruby," Physical Review B **90**, 054409:1–054409:6 (2014).

[202] S. D. Gupta and G. S. Agarwal, "Strong coupling cavity physics in microspheres with whispering gallery modes," Optics Communications **115**, 597–605 (1995).

[203] W. Yoshiki, A. Chen-Jinnai, T. Tetsumoto, S. Fujii, and T. Tanabe, "Time-domain observation of strong coupling between counter-propagating ultra-high Q whispering gallery modes," SPIE Conference Proceedings **9727**, 97271T (2016).

[204] W. L. Barnes, A. Dereux, and T. W. Ebbesen, "Surface plasmon subwavelength optics," Nature **424**, 824–830 (2003).

[205] E. Ozbay, "Plasmonics: Merging Photonics and Electronics at Nanoscale Dimensions," Science **311**, 189–193 (2006).

[206] T. W. Ebbesen, H. J. Lezec, H. F. Ghaemi, T. Thio, and P. A. Wolff, "Extraordinary optical transmission through sub-wavelenght hole arrays," Nature **391**, 667–669 (1998).

[207] Y.-W. Hu, B.-B. Li, Y.-X. Liu, Y.-F. Xiao, and Q. Gong, "Hybrid photonic-plasmonic mode for refractometer and nanoparticle trapping," Optics Communications **291**, 380–385 (2013).

[208] A. Rottler, M. Bröll, S. Schwaiger, D. Heitmann, and S. Mendach, "Tailoring of high-Q-factor surface plasmon modes on silver microtubes," Optics Letters **36**, 1240–1242 (2011).

[209] J. Gu, Z. Zhang, M. Li, and Y. Song, "Mode characteristics of metal-coated microcavity," Physical Review A **90**, 013816:1–013816:6 (2014).

[210] Y. Yin, S. Li, V. Engemaier, S. Giudicatti, E. Saei Ghareh Naz, L. Ma, and O. G. Schmidt, "Hybridization of photon-plasmon modes in metal-coated microtubular cavities," Physical Review A **94**, 013832:1–013832:6 (2016).

[211] Y. Yin, S. Li, S. Giudicatti, C. Y. Jiang, L. B. Ma, and O. G. Schmidt, "Strongly hybridized plasmon-photon modes in optoplasmonic microtubular cavities," Physical Review B **92**, 241403:1–241403:4 (2015).

[212] A. Rottler, M. Harland, M. Bröll, M. Klingbeil, J. Ehlermann, and S. Mendach, "High-Q Hybrid Plasmon-Photon Modes in a Bottle Resonator Realized with a Silver-Coated Glass Fiber with a Varying Diameter," Physical Review Letters **111**, 253901:1–253901:5 (2013).

[213] Q. Wang, H. Zhao, X. Du, W. Zhang, M. Qiu, and Q. Li, "Hybrid photonic-plasmonic molecule based on metal/Si disks," Optics Express **21**, 11037–11047 (2013).

[214] S. A. Maier, ed., *Plasmonics: fundamentals and applications* (Springer Science & Business Media, 2017).

[215] P. Berini, "Plasmon-polariton waves guided by thin lossy metal films of finite width: Bound modes of symmetric structures," Physical Review B **61**, 10484–10503 (2000).

[216] R. H. Ritchie, E. T. Arakawa, J. J. Cowan, and R. N. Hamm, "Surface-Plasmon Resonance Effect in Grating Diffraction," Physical Review Letters **21**, 1530–1533 (1968).

[217] U. Fano, "The Theory of Anomalous Diffraction Gratings and of Quasi-Stationary Waves on Metallic Surfaces (Sommerfeld's Waves)," Journal of the Optical Society of America **31**, 213–222 (1941).

[218] E. Kretschmann and H. Raether, "Radiative Decay of Non Radiative Surface Plasmons Excited by Light," Zeitschrift fur Naturforschung A **3**, 2135–2136 (1968).

[219] A. Otto, "Excitation of nonradiative surface plasma waves in silver by the method of frustrated total reflection," Zeitschrift für Physik A Hadrons and nuclei **216**, 398–410 (1968).

[220] W. H. Weber and G. W. Ford, "Optical electric-field enhancement at a metal surface arising from surface-plasmon excitation," Optics Letters **6**, 122–124 (1981).

[221] W. L. Barnes, "Fluorescence near interfaces: The role of photonic mode density," Journal of Modern Optics **45**, 661–699 (1998).

[222] M. Blaber, M. Arnold, and M. Ford, "A review of the optical properties of alloys and intermetallics for plasmonics," Journal of Physics: Condensed Matter **22**, 143201 (2010).

[223] J. Čtyroký, L. Prkna, and M. Hubálek, "Guided-Wave Optical Microresonators: Calculation of Eigenmodes," Microresonators As Building Blocks For VLSI Photonics, AIP Conference Proceedings **709**, 72–90 (2004).

[224] M. K. Chin and S. T. Ho, "Design and Modeling of Waveguide-Coupled Single-Mode Microring Resonator," Journal of Lightwave Technology **16**, 1433–1446 (1998).

[225] M. Heiblum and J. H. Harris, "Analysis of Curved Optical Waveguides by Conformal Transformation," IEEE Journal of Quantum Electronics **11**, 75–83 (1975).

[226] G. Beadie, M. Brindza, R. A. Flynn, A. Rosenberg, and J. S. Shirk, "Refractive index measurements of poly (methyl methacrylate)(PMMA) from 0.4–1.6 µm," Applied Optics **54**, F139–F143 (2015).

[227] Simulations for the effective refractive indices were performed by Jens Oppermann, the simulations for the Q-factors by the author.

[228] Y. Jiang, S. Pillai, and M. A. Green, "Re-evaluation of literature values of silver optical constants," Optics Express **23**, 2133–2144 (2015).

[229] D. J. Nash and J. R. Sambles, "Surface plasmon-polariton study of the optical dielectric function of silver," Journal of Modern Optics **43**, 81–91 (1996).

[230] A. Masten and P. Wissmann, "Ellipsometric studies on thin silver films epitaxially grown on Si(111)," Thin Solid Films **343**, 187–190 (1999).

[231] V. P. Drachev, U. K. Chettiar, A. V. Kildishev, H. K. Yuan, W. S. Cai, and V. M. Shalaev, "The Ag dielectric function in plasmonic metamaterials," Optics Express **16**, 1186–1195 (2008).

[232] Bent-waveguide simulations of the joint fiber–resonator system were performed by Patrick Forster during his master's thesis. Fiber–resonator coupling efficiencies and transferred powers were computed from the simulation results by Jens Oppermann using coupled mode theory.

Closing words

The last pages of this thesis are dedicated to all the people who supported me during my PhD project and contributed to its success. Without the assistance of many colleagues and collaborators, the results presented in this work would not have been accomplished.

First and foremost, I want to thank Prof. Dr. Heinz Kalt for giving me the opportunity to work on this intriguing research project, for his patient guidance and his invaluable advice. Thanks for giving me the freedom to shape this project according to my own ideas and for the support concerning the participation in conferences.
In the same breath I'd like to express my deep gratitude to Prof. Dr. Carsten Rockstuhl, my co-examiner, for the great collaboration, the valuable discussions, his enthusiastic encouragement, interest and trust in this work.

Furthermore, special thanks goes to my master students Patrick Forster, Jannis Hessenauer, Matthias Migeot, and Steffen A. Schmid, who notably contributed to the success of this work. It was a pleasure for me to work with you. Thanks for your amazing engagement and the fruitful discussions! The same applies to my collaborators Radius N. S. Surydharma and Jens Oppermann from the Institute of Theoretical Solid State Physics (TFP) at KIT, without whom the results presented in this thesis could not have been achieved. Thanks for your ongoing support, for sharing your knowledge with me, and for the great discussions.
I also want to sincerely thank all members of the AG Kalt for the positive and enjoyable atmosphere, your steady helpfulness, and for the nice conversations both in- and outside university. Thanks to all the people who took their time for proof reading and helped reducing the number of errors in this thesis.

In addition, I would like to acknowledge all the people who were involved in the fabrication of WGM resonators. Thanks to Dr. Meike König from the Institute of Functional Interfaces (IFG) for coating WGM resonators with parylene. Thanks also to Dr. Uwe Bog, Dr. Tobias Wienhold, and Sentayehu Wondimu from the Institute of Microstructure Technology (IMT) for their assistance in sample preparation, their useful advice, and the constructive cooperation. A sincere thank you also goes to Dr. Silvia Diewald, Stefan Kühn, and Dr. Aina Quintilla for the lithographic structuring of WGM resonators via e-beam lithography and for their assistance in obtaining beautiful scanning electron micrographs. Thanks additionally to Patrice Brenner for his assistance in depositing smooth

and homogeneous silver films on polymeric microwedges and for performing focused ion beam cuts.

My gratitude furthermore goes to Heinz Leonhard for making technical drawings, and all the people from the electronics and fine mechanics workshop at the Institute of Applied Physics (APH) for their engaged and competent support in all technical concerns.
Thanks also to our secretaries for their helpfulness and their assistance in all kind of administrative matters.

I also want to thank the Karlsruhe School of Optics and Photonics (KSOP) for financial support and for giving me the opportunity to broaden my horizon in several technical and business modules.

Last but not least, I would like to express my deepest gratitude and appreciation to my family, Niclas, and my friends for their vigorous support, constant encouragement, and for having confidence in me.